Developing New Methodologies for the Analysis of Proteins by Native Top-Down Mass Spectrometry

by

Brock Ryan Juliano

A dissertation submitted in partial fulfillment
of the requirements for the degree of
Doctor of Philosophy
(Chemistry)
in the University of Michigan
2023

Doctoral Committee:

Professor Brandon T. Ruotolo, Chair
Professor Ryan C. Bailey
Professor Kristina I. Håkansson
Professor Robert T. Kennedy

Brock R. Juliano

bjuliano@umich.edu

ORCID iD: 0000-0001-6101-3890

Dedication

This dissertation is dedicated to Scott Sokolic, Megan Lucidi, Colleen Fitzgerald, and Marilyn Brahms, science teachers at Woodbury Junior-Senior High School, who worked tirelessly under challenging, resource-limited conditions to deliver a quality science education to me and all of their students.

Acknowledgments

Firstly, I would like to begin by thanking my supervisor, Brandon Ruotolo for mentoring me both as an undergraduate and graduate student. Your guidance and support have pushed me to become a better scientist than I could have ever dreamed of becoming when I first set foot in your lab. It has been a pleasure to watch how much our lab has grown so remarkably in the past several years, from having only three mass spectrometry platforms to now having access to over six systems, which is truly a testament to your hard work and scientific expertise. I would also like to thank all of my committee members: Professors Bob Kennedy, Kicki Håkansson, Ryan Bailey and Phil Andrews, for their guidance and support throughout this process. It has been a pleasure to be able to learn from you all.

I would also like to thank the members of the Ruotolo Lab, both past and present, for making the lab a supportive and enjoyable place to learn. I would like to especially thank Dan Polasky for mentoring me twice and giving me the skillset necessary to succeed in my top-down endeavors. I also would like to thank Suggie Dixit, Cara D'Amico and Sarah Fantin for welcoming me into the lab, helping me to and sharing their tips on how to succeed in grad school and most importantly for their friendship. Kristine Parson was my first friend in the lab, as we bonded over learning how use the needle puller, and I could not have asked for a more supportive lab mate and friend to navigate this experience with me. I'd also like to thank Carolina Rojas-Ramírez and Yilin Han who were both such a positive and enthusiastic lab member and friends. I'd also like to thank Chae Jeon for commiserating over our cohort deadlines with me and for always being ready to go to a brewery or to go to Windsor for a

Canadian shopping haul. I would also like to acknowledge Iliana Levesque for sharing the highs and lows of membrane protein research with me as we trauma bonded over detergent exchange and for setting a strong example in the lab with her positivity, resilience, kindness, and strength. I would also like to thank Rosie Villafuerte-Vega for always making me laugh even if I didn't want to and for being my fellow chismoso. I would also like to acknowledge Anna Anders for always helping me to troubleshoot the 6560c, introducing me to the wonderful world of oligonucleotides and for being such a good leader in lab. I would also like to thank Nicole Rivera-Fuentes for being such a kind and caring lab member and for always checking on me in lab. I also must acknowledge Addison Bergman for being so enthusiastic in lab, you will be a wonderful addition to our lab and I am excited to see you slay on the cyclic. Finally, I would also like to thank the two undergraduate students I had the pleasure of mentoring, Joe Keating and Henry Li, for all of their help in making the research in Chapters 2 and 6 possible.

I also would like to thank all of the members of the Håkansson lab past and present, especially Carson Szot, for their help in troubleshooting the 6560c and maintaining the CO_2 laser on the Lumos. I would also like to acknowledge Hye-Kyong Kweon and Russ Bornschein for their assistance in supporting my research with the resources in the departmental Mass Spectrometry Facility. I would especially like to acknowledge the laboratories of Chuck Sanders of Vanderbilt University and Randy Stockbridge of the Department of Molecular , Cellular, and Developmental Biology for generously providing the membrane protein stock samples that I used to complete several of my chapters. I would also like to acknowledge my collaborators Varun Gadkari, Chris Mallis, Jody May, Ruwan Kurulugama, John Fjeldsted, Dave Russell and John McLean for their assistance in conducting the interlaboratory CIU project. I would also like to thank Zhuoer Xie of Amgen for providing the siRNA duplex that I used in my RapidFire work. Finally, I would also like to thank my collaborators Sammy Schon and Sue Hammoud of the Departments of Human Genetics, Urology, Obstetrics and Gynecology for giving me an interesting system to explore with my top-down methods with the human protamines project and Haley Brown and Nicole Koropatkin of the Department of Microbiology and Immunology for giving me the opportunity to learn more about the importance of metal ligand coordination in the gut microbiome with the $\text{BoGH13A}_{\text{Sus}}$ project. I would especially like to thank Bryan Miller and Peter Rye at Agilent for their generosity in supporting me as I was at long last able to lift the RapidFire project off the ground.

Outside of lab, I would like to thank the village of friends and family whose support and faith in me have enabled me to achieve this great milestone. I would especially like to thank Vivian Crum, my oldest friend in Ann Arbor, for always supporting me throughout our shared undergraduate and graduate endeavors and for being my most trusted friend and confidante. I would also like to acknowledge Professors Keri Colabroy and Amy Hark of Muhlenberg College for mentoring me as an undergraduate and helping me to grow into a competent scientist.

Finally, I would like to thank my entire family, especially my parents, for their love and support in completing this degree. Even though I moved away further than they would have liked, we have managed to stay close throughout these five years through shared vacations and visits and through those months in 2020 when I was a remote graduate student at home. I could not have asked more supportive or loving parents, who have always nurtured my curiosity and learning, and whose sacrifices have enabled me to be living a life of opportunity of which I could scarcely have dreamed. This dissertation is as much a credit to both of their love and support as it is to me.

Table of Contents

List of Tables

List of Figures

List of Appendices

Abstract

Proteins are critical mediators of physiological function and human health. The complexity of the human proteome, which contains over 1 million individual proteoforms, presents a daunting challenge for modern measurement science. Such proteoforms are recruited into myriad multi-protein complexes, many of which remain refractory to standard functional and structural assays. Native proteomics seeks to deploy tools, such as native mass spectrometry (nMS) to identify and a characterize such complexes, but current nMS methods struggle to rapidly quantify closely related proteoforms and to sequence many important assemblies. To advance our understanding of biochemistry, new nMS methodologies are needed to improve the throughput and information content of nMS assays.

MPs are challenging targets for nMS due to their hydrophobicity. Current nMS methods yield limited sequence coverages for MPs (< 20%). In Chapter 2, we explore the use of infrared (IR) photoactivation to improve the sequence coverage that can be obtained for MPs. We discovered that IR photoactivation can selectively liberate proteins from detergent micelles, dissociate detergent and lipid clusters, and ultimately enable greater sequence coverages to be obtained (40-60%).

Native proteomics methodologies targeting MPs rely upon detergent exchange methodologies to prepare samples for nMS analysis but have yet to be evaluated quantitatively. In Chapter 3, we analyze the efficiency of standard detergent exchange methodologies to identify optimal approaches for native proteomics. Our results highlight the inability of current methods to completely exchange samples into a desired detergent. Furthermore, we note that exchange

efficiency depends strongly upon the starting detergent, exchange method, and the MP contained within the sample. Furthermore, we were able to improve detergent exchange efficiencies by increasing the number of exchanges performed or by increasing the concentration of the target surfactant.

Collision induced unfolding (CIU) is methodology based in ion mobility-mass spectrometry (IM-MS) capable of rapidly distinguishing between closely related protein isoforms and assessing their stabilities. In Chapter 4, we conduct an interlaboratory assessment of CIU reproducibility by partnering with three laboratories housing of the same IM-MS instrumentation. Using selected standard proteins prepared in our lab and shipped to our collaborators, we found CIU to be highly reproducible (~4-5% RMSD) across laboratories.

Chapter 5 explores the first use of CIU for quantitative measurements to assess isomass pairs of biotherapeutics and sequence homologues in both standard and biological matrices that are indistinguishable by IM-MS alone. Our results cover three antibody pairs and include examples of mixed therapies that are provided to patients. Our CIU assays produce calibration curves with correlation coefficients ranging from 0.92- 0.99, limits of detection ranging from 300-5000 nM and sensitivities ranging from $8.7\text{x}10^{-5}$ nM $^{-1}$ –$6\text{x}10^{-3}$ μM $^{-1}$.

Despite the wide adoption of CIU, it has generally remained a throughput limited technology. In Chapter 6, we explore the use of a RapidFire$^{\text{TM}}$ robotic system to automate and increase the throughput of CIU. We developed an automated, online desalting procedure, evaluate its efficiency, and develop methods to collect CIU in as little as 30 seconds for a variety of standard proteins, protein complexes, biotherapeutic antibodies, and RNA samples.

The work described in this thesis greatly expands the potential applications of nMS by developing new approaches that allow for nMS to be better deployed for challenging targets, to be used for novel applications such as quantitation, whilst also creating methods that vastly improve the throughput of these technologies.

Chapter 1 Introduction

1.1 Motivation

Proteins constitute the majority of the cellular machinery necessary to sustain life[1]. As such, identifying the structures, functions and interactions of each of these proteins has emerged as a major area of research in medicine over the past several decades in order to gain insight to the roles that changes in protein structure can have in the etiology of disease states[2–4]. The Human Genome Project, completed in 2003, revealed that there are approximately 20000 protein encoding genes within the genome[5]. However, recent work in proteomics has revealed that proteins can be significantly modified, yielding multiple discrete forms of a protein known as proteoforms. The modifications can be created by single nucleotide polymorphisms that alter protein structure pre-translationally, and post-translational modifications (PTM) like glycations and phosphorylations that are added to the protein structure enzymatically after translation (Figure 1-1).

While the human genome encodes for only 20000 proteins, there are estimated to be approximately 1000000 proteoforms within the human proteome, which includes all the potential variants of these 20000 proteins[6]. Developing methodologies to rapidly identify these proteoforms and assay their structures remains a significant analytical challenge[7–10]. Beyond the roles of proteins *in vivo*, they have also emerged as an especially promising class of biotherapeutics. In particular, monoclonal antibodies (mAbs) are an important therapeutic modality, due to their ability to specifically target specific epitopes, allowing for the precise delivery of drugs to particular cellular targets[11]. Mass spectrometry (MS) has emerged as a powerful technique to identify protein structure and sequence and can be adroitly leveraged to study a variety of protein archetypes[12]. New MS based methods are required in order to be better suited for diverse applications such as proteomic sequencing, structural biology assays and the characterization of protein biotherapeutics.

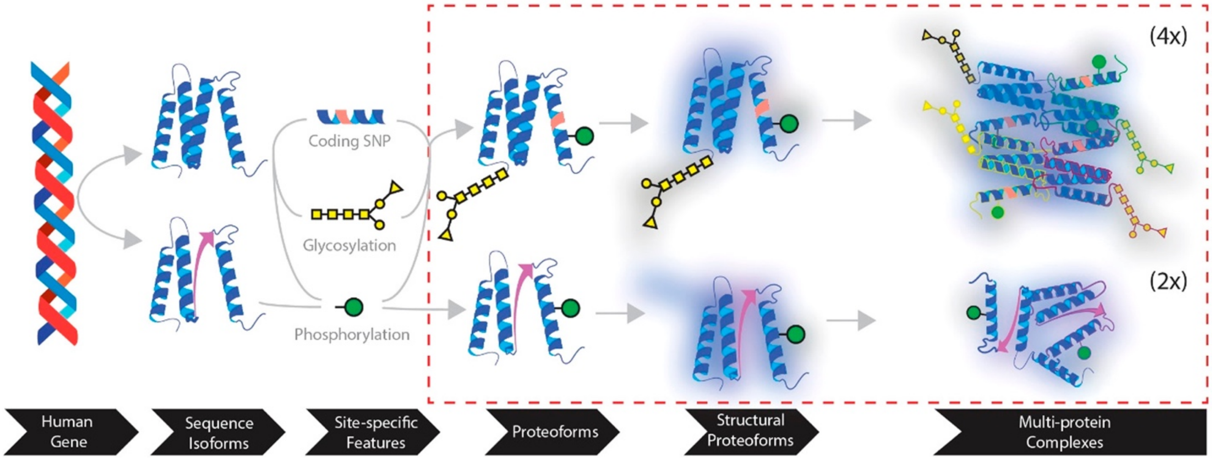

Figure 1-1 The creation of multiple proteoforms from a single protein encoding gene. Single nucleotides polymorphisms and post-translational modifications, give rise to multiple proteoforms from this gene. The proteoforms can vary further in their structural conformations and can give rise to even more variable protein complexes. Reproduced with permission from Ruotolo, B. T. Collision Cross Sections for Native Proteomics: Challenges and Opportunities. J. Proteome Res. **2022**, 21 (1), 2–8. https://doi.org/10.1021/acs.jproteome.1c00686. Copyright, American Chemical Society, 2022.

1.2 Structural Biology Techniques for Proteome Analysis

Given the biological paradigm that protein structure begets function, determining accurate representations of protein structure is of critical importance for structural biology, medicine, and drug design[14,15]. Ideally, it would be possible to predict the structure of a protein directly from its sequence, without the need for a direct, experimental measurement. Some success has been had for the prediction of the structure of well-ordered, small proteins from their primary sequences, and newer methodologies that function based in artificial intelligence have had more success with larger, more complex protein systems[16–18]. The use of AlphaFold, an AI based tool, to elucidate biomolecular structure, is rapidly expanding, with AlphaFold data now available for the majority of putative proteins in the human proteome[19]. However, these systems, such as AlphaFold, remain nascent and have numerous limitations. Namely, systems like AlphaFold are highly dependent on the quality of their training data to generate their predictions, whilst continuing to experience limitations in their ability to predict the structures of protein complexes and large macromolecular assemblies. As such, direct structural measurement remains the gold standard in academe and in industry.

There are several well-established marquee techniques by which structural biologists generate three-dimensional structures of proteins and protein complexes, a survey of which can be found in Figure 1-2. X-ray crystallography remains the most commonly deployed technique for the structural determination of proteins[19]. X-ray crystallography can achieve atomic-level resolution for crystallized biomolecular samples and has been used to generate structures for large protein complexes such as ribosomal subunits and RNA polymerase[20–22]. Despite the wide deployment of X-ray crystallography in structural biology, X-ray crystallography has several drawbacks. Namely, X-ray crystallography requires the formation of crystals for diffraction to occur, requiring large amounts of highly pure and concentrated

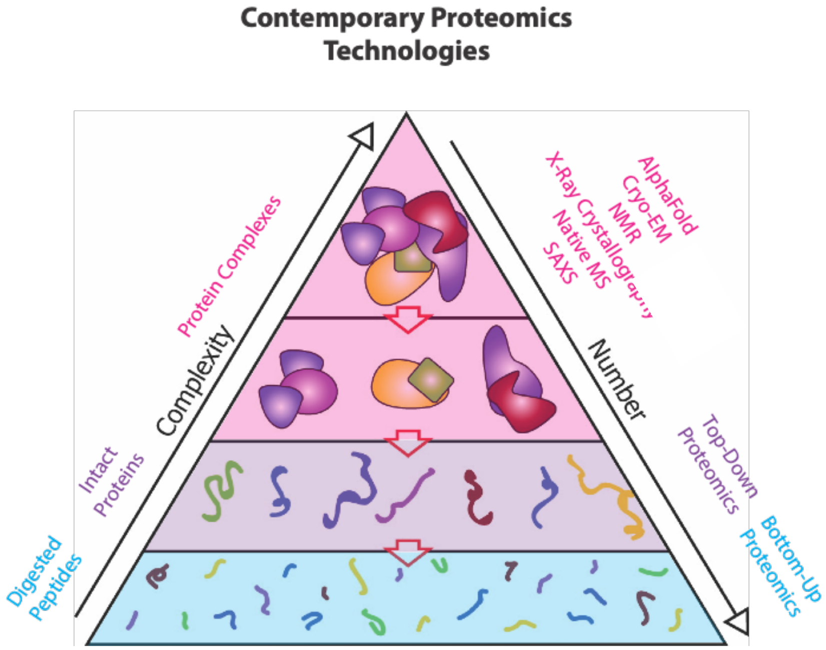

Figure 1-2 An overview of methods for the analysis of protein sequence and structure, from intact protein complexes to protein fragmentsMS based approaches can assay both protein sequence and structure, ranging from digested peptides to intact complexes. Other structural techniques such as NMR and X-Ray crystallography exist to assay protein structure. Adapted with permission from Benesch, J. L. P.; Ruotolo, B. T.; Simmons, D. A.; Robinson, C. V. Protein Complexes in the Gas Phase: Technology for Structural Genomics and Proteomics. Chem. Rev. **2007**, 107 (8), 3544–3567. https://doi.org/10.1021/cr068289b. Copyright American Chemical Society 2007.

protein, as well as a great deal of time to identity the conditions that are most conducive to crystal formation[23]. Additionally, the crystallized form of the protein is not necessarily in its native state, given the overwrought and specific conditions that yield crystallization[24]. X-ray crystallography is also incompatible with proteins that are highly disordered, as crystallography is unable to assay dynamic regions of these proteins[25].

Nuclear magnetic resonance (NMR) is another structural technique that can achieve atomic resolution and is more tolerant of dynamics than X-ray crystallography[26]. However, NMR is generally limited to being deployed for smaller biomolecules, that are below 50 kDa in molecular weight, and also requires highly pure samples for successful data to be obtained[27]. Cryo-electron microscopy (Cryo-EM) is another technique that is deployed in order to achieve atomic resolution[28]. However, cryo-EM is best deployed for larger systems that are greater than 150 kDa in molecular weight, such as intact viruses, and has substantial sample preparation requirements than limit its throughput[29,30]. While atomic resolution is often ideal as it provides the greatest amount of information content regarding the system of interest, there are additional lower resolution structural techniques that are available as well. For example, circular dichroism (CD) which can provide information about the secondary structure of the protein[31]. Meanwhile, small angle x-ray scattering (SAXS) can be used to provide limited insight into protein tertiary structure and secondary structure[32,33]. These techniques are advantageous in that they require less sample preparation and have faster acquisition times than other techniques such as X-Ray crystallography and cryo-EM.

In addition, protein stability can be a key metric to assay structure and function. For example, differences in protein melting temperature could be correlated to differences in protein stability[34]. Most often, calorimetry is used to performs these assays, either by differential scanning calorimetry (DSC) or isothermal titration calorimetry (ITC)[35,36]. These measurements provide global measurements of protein stability, without the ability to probe specific proteoforms of interest. Additionally, these calorimetry techniques require large amounts of purified samples to complete and require acquisition times in the tens of minutes. The limitations of each of these technologies necessitates the development of additional techniques to be used in the arsenal of structural biology. An ideal technique to complement some of the limitations of these existing technologies would be one that is tolerant of sample heterogeneity, one that does not require chemical labeling, whilst also requiring minimal acquisition and data analysis times.

1.3 Native Mass Spectrometry Methodologies

Native mass spectrometry (nMS) has emerged as powerful technique to study the structural biology of a variety biomolecular systems of interest[12,37]. nMS differs from other forms of mass spectrometry in that the experimental conditions are carefully tuned and optimized such that the native-like structure of the biomolecule of interest is preserved as the biomolecules are transferred from the solution phase to the gas phase for measurement. In this way, nMS can provide greater levels of structural insight into the systems of interest when compared to standard MS assays which often occur under denaturing conditions. nMS has been deployed to study the structures of oligonucleotide complexes[38,39], mAbs[40–42], membrane proteins (MPs) [43–46], large protein complexes like chaperones[47,48] and intact viral capsids[49,50]. In these experiments biomolecules are prepared in solution with non-denaturing, volatile solvents, such as ammonium acetate at physiological pH[51–53]. Biomolecules are then delivered as intact biomolecules into the gas phase through electrospray ionization. Electrospray ionization (ESI) is advantageous in that it can transfer biomolecules into the gas phase without fragmenting them, while producing multiple charge states of the molecule of interest[54–57]. In a positive polarity ESI experiment, an electric voltage is applied to an emitter, which generates charged cationic droplets at the tip. Due to the presence of a strong electric field, the sample becomes polarized and then generates a Taylor cone which emits fine, charged droplets[58]. These micrometer sized droplets are then desolvated, due the application of heat or gas flow in the source. As the droplets become smaller, the droplets reach their Rayleigh limit and underogfission, and this process is repeated until the smallest possible droplets are formed[59]. A depiction of ESI can be found in Figure 1-3.

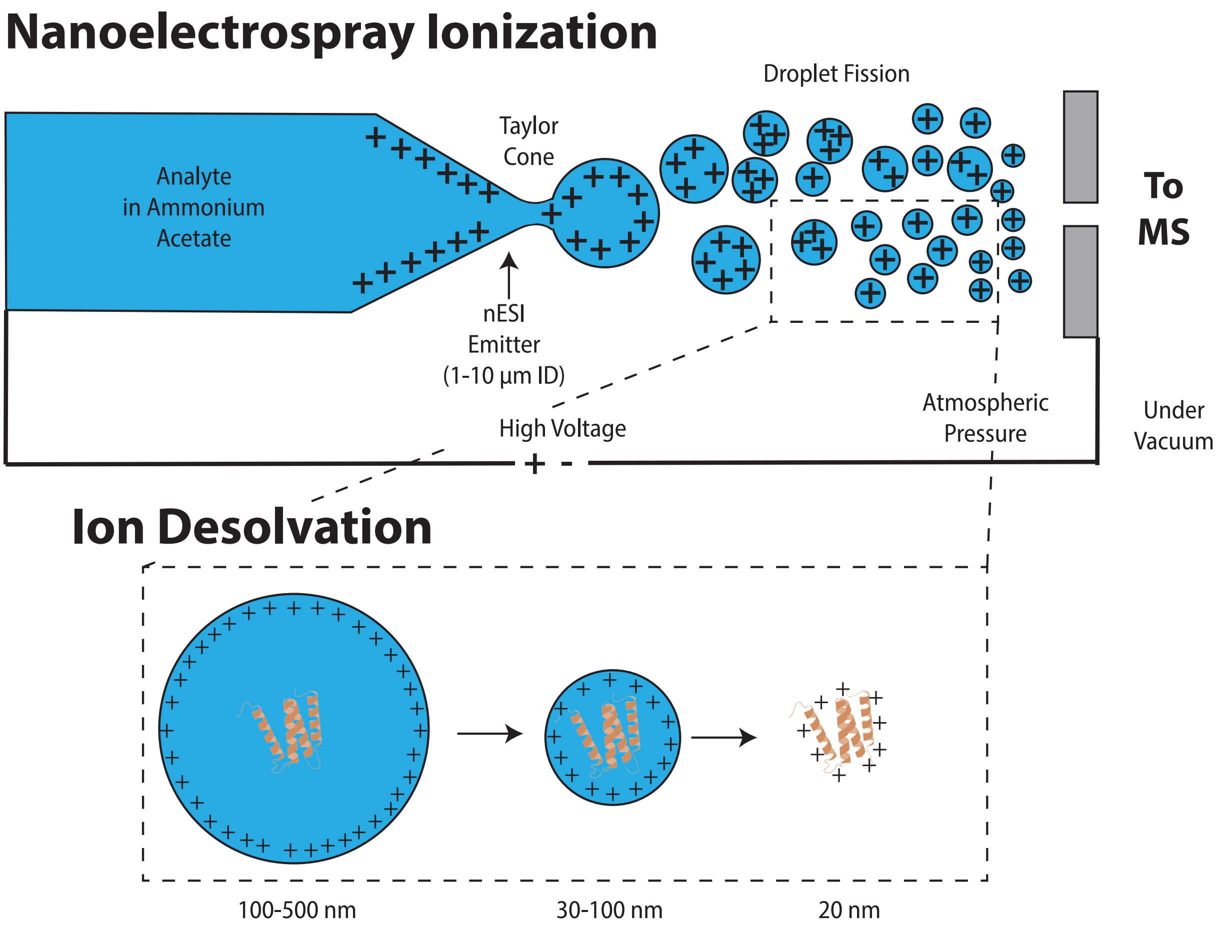

Figure 1-3 A rendering of nanoelectrospray ionization as it occurs in positive polarity. The voltage applied to the capillary generates the formation of a Taylor Cone and charged droplets. These droplets subsequently undergo multiple fission events during the desolvation process, ultimately yielding charge analytes that then enter the MS for detection.

Several models exist to explain how charge becomes deposited on large analytes during ESI. However, the charged residue model (CRM) is the most widely accepted mechanism for this process[60,61]. In CRM, solvent molecules in droplets are evaporated until the droplet contains a single protein ion, with the charge of the protein being proportional to the surface area of the system. Recent evidence suggests that larger protein systems may proceed by a related bead ejection model, wherein ordered regions of the protein undergo CRM, while more disordered linkers undergo the chain ejection mechanism[62]. Most often, nMS samples are ionized with nanoelectrospray ionization (nESI) which uses a nanometer sized emitter tip that produces smaller droplets that require less energy to be desolvated, and thereby are better able to preserve the native-like structure of the analyte during the ionization process, including noncovalent complexes (Figure 1-3)[63,64]. However, data in Chapters 4 and 6 suggest that, when carefully tuned, larger emitters, such as those that are 50 μm in diameter, can be used for microelectrospray ionization experiments that can produce native ion populations that are comparable to data collected with nESI. While the extent to which proteins remain native-like after undergoing ESI remains an active area of inquiry, evidence from ion mobility, computation modeling, and soft-landing experiments suggests that, in many cases, the structures of these proteins remain remarkably similar to protein structures elucidated by other methods[65–68].

1.4 Ion Mobility Separations

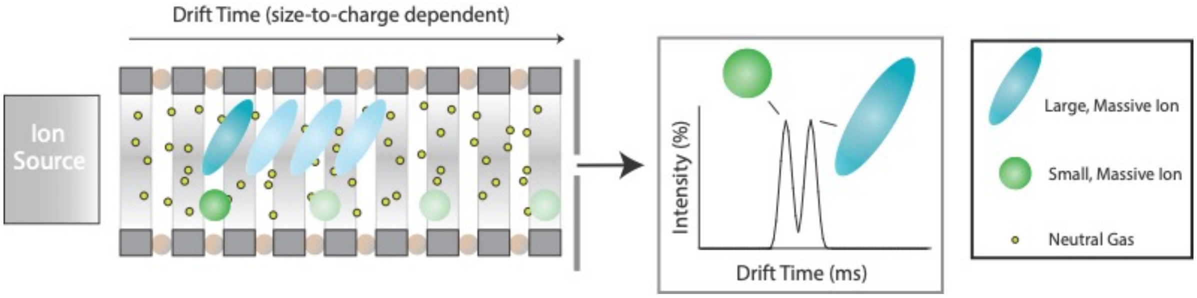

Figure 1-4 A schematic of a drift tube ion mobility separation. Collisions with a neutral bath gas can separate a larger ion from a smaller ion. The smaller ion traverses the drift tube more quickly as it collides less with the bath gas. The differences in drift time are then able to be visualized in an arrival time distribution plot, which represents the distinct drift times of both species.

Ion mobility (IM) can be leveraged as a separation technique that separates proteins on a millisecond time scale based on their size, shape and charge[69,70]. As ions are driven through an electric field, they collide with inert gas molecules, typically N_2. Ions that possess larger surface areas will experience more collisions with the gas, and, as a result, take longer to traverse the separator when compared to smaller and more compact ions[70]. An example of a basic IM separation can be viewed in Figure 1-4. While the drift times reported in ion mobility experiments are often not directly comparable across instruments, they can be calibrated with tune mix to report collision cross section values (CCS) based on the terms of the Mason-Schamp equation[71,72]. CCS values are three-dimensional, rotationally averaged measurements of the size of the ion, and can be compared directly to structural measurements collected with other techniques, making them particularly valuable experimental measurements[70].

Multiple configurations exist for ion mobility separations. Two of the most common forms of ion mobility separators are drift tube ion mobility separators and traveling wave ion mobility separators (TWIMS)[70]. The simplest form is that of a drift tube separation. In a drift tube, a linear electric gradient is applied across the entirety of the drift tube, propelling ions to traverse the drift tube as they collide with the background gas.[70] As opposed to drift tube IM, in a TWIMS device, electric waveforms are generated instead of a linear voltage gradient[73]. Ions initially are carried by the waves, until they crest over the waves and roll over in the trough. Larger ions roll over the waves more frequently, and thereby take longer to traverse the separator[73]. TWIMS requires lower voltages to be applied and are more compact than drift tube devices[73]. Recent innovations in IM separations have yielded cyclic IM (cIM) devices and structures for lossless IM (SLIM) devices that make it possible to do tandem IM^n separations[74–76]. Other forms of IM such as trapped ion mobility (TIM)[77,78] and high-field asymmetric-waveform IM (FAIMS)[79] also are commercially available. IM paired with MS can be a particularly powerful technology for structural biology, as the IM data provides greater insight into the structural conformations of the ions[80]. When coupled with nMS, IM has been deployed to gain increased structural insight into a wide variety of systems of interest, including mAbs[41,81], kinases[82,83] and membrane proteins[84,85].

1.5 Collision Induced Unfolding

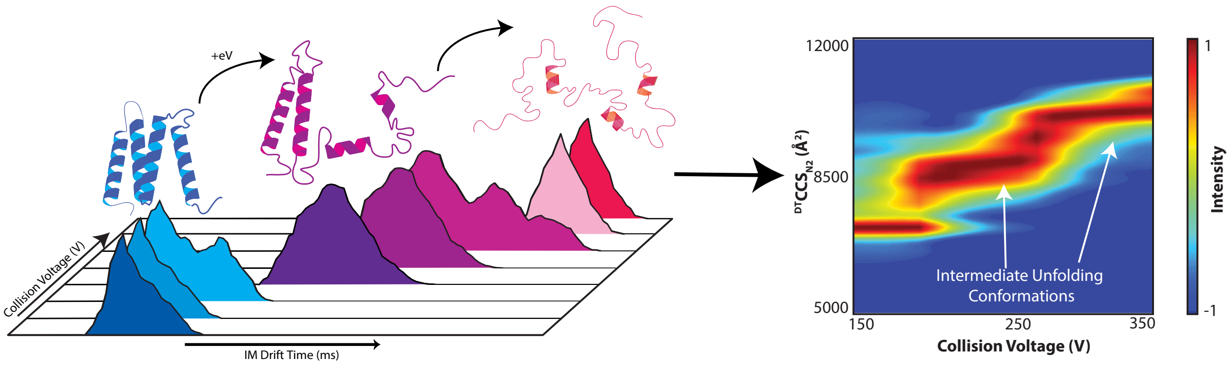

Figure 1-5 An illustration of the collision induced unfolding process. As proteins are collisionally activated, they generally adopt more extended conformations that have large drift times. These differences in drift time, or CCS, can then be represented as a function of collision voltage in the form of a heat plot known as a CIU fingerprint. CIU fingerprints also depict the relatively intensity of the different features.

Collision Induced Unfolding is a powerful application of native IM-MS (nIM-MS) that tracks changes in ion conformation as a function of collisional activation[86]. Oftentimes, a single CCS value is insufficient to provide significant structural insight into a biomolecule, limiting the amount of information that can be obtained from a standard nIM-MS experiment[87]. CIU aims to leverage nIM-MS to obtain more information about the analyte's structure by collisionally activating the biomolecule with an inert background gas to cause it to unfold in the gas phase[86] (Figure 1-5). In this way, CIU experiments capture the full gas phase unfolding trajectory of the system of interest. As biomolecules unfold, they adopt different, extended structural conformations that can be sampled by IM.

In many ways, CIU can be understood as a gas phase form of DSC, as it can be deployed to measure subtle differences in the structural stability of the biomolecules. CIU has several advantages over DSC in that it is more tolerant of sample heterogeneity, does not require highly pure sample and that it can sample individual proteoforms as opposed to doing a coarse, bulk measurement[88]. CIU data are visualized as heat maps that are referred to as CIU fingerprints[89]. Slopeless regions are known as features, and are areas in which the analyte exists as a single conformation before unfolding into another conformer[89]. The transitions between features are known as CIU50s and occur at the voltage at which half to the intensity of one feature progresses into another feature[89]. CIU data can be analyzed in a software package known as CIUSuite 2. CIUSuite2 can analyze IM-MS data from a variety of vendors and can be used to extract and plot CIU data. The most important features of CIUSuite2 include its ability to average and compare CIU fingerprints, to smooth data using Savitsky-Golay approaches, to identify features and CIU50s, to perform Gaussian fitting, denoising, and interpolation[89]. In this way, CIU data can be compared and analyzed in a more quantitative and rigorous manner.

CIU data have been deployed to gain further insight into a variety of systems of interest including mAbs[41,42,81], kinases[82,90], intrinsically disordered proteins[91,92] and MPs[43,84]. CIU has been leveraged to identify subtle shifts in stability that occur upon ligand or drug binding, which can alter the CIU50s that exist between certain features[93]. CIUSuite2 can also calculate the root mean square deviation (RMSD) between two fingerprints, which can be used as a mathematical representation of their sameness[89]. In fact, using artificial intelligence, CIU can characterize the ligand binding effects on analyte as being agonistic or antagonistic, and even further classify the ligands according to their binding modality[90]. CIU of ligand-bound proteins can also be deployed to further annotate CIU data to gain insight into which domains are correlated to the unfolding features that are present[94]. Similarly, CIU can be combined with electron capture dissociation (ECD) to annotate which region of the protein become unfolded, by tracking differences in fragmentation patterns at different levels of collisional activation[95]. As CIU technologies continue to be adopted and developed in the structural MS community, new approaches are needed to increase the throughput of CIU measurements to make CIU more applicable to high throughput screening in biopharma, which will be explored in Chapter 6. Additionally, the reproducibility of CIU measurements between platforms and laboratories needs to be benchmarked in order to evaluate the suitability CIU data for inclusion into a structural biology database. This will be discussed in Chapter 4. While CIU is primarily deployed as a structural assay, Chapter 5 will explore the development of CIU methodologies to quantitate isomass species that are unable to be quantitated using standard approaches.

1.6 Tandem Mass Spectrometry

MS has emerged as the premier technology for proteomics experimentation. Other techniques for protein sequencing such as Edman degradation, are quite slow and are unable to identify PTMs, and are relatively démodé, having been displaced by MS in in the late twentieth century[96,97]. MS-based proteomics experiments can be categorized into three main experimental archetypes: bottom-up, middle-down and top-down. In a bottom-up experiment, proteins are enzymatically digested prior to MS experiment with enzymes that cleave the peptide bond, such as trypsin, pepsin and endoproteinase Lys-C[98]. The peptides that are formed are then typically separated by liquid chromatography (LC)-MS, prior to introduction to the mass spectrometer, where they can be further fragmented in the gas phase[98]. Middle-down experiments are similar to bottom-up experiments; however, the proteins are not fully digested, but rather digested into slightly smaller subunits, such as the Fc domain of a mAb, or an individual histone, before being fragmented within the instrument[99,100]. Top-down experiments are different wherein proteins are not digested before being introduced into the mass spectrometer, rather they are sprayed intactly into the instrument and fragmented once in the gas phase[101].

Top-down proteomics has several advantages over bottom-up proteomics. By fragmenting the protein directly in the mass spectrometer, the peptide fragments can be traced directly to their proteoform of origin[102]. This eliminates some of the ambiguity that can occur when analyzing multiple proteoforms of the same protein by bottom-up analysis, as the digested peptides from each proteoform are scrambled together, making it difficult to directly identify which PTMs are occurring together to confidently assign the presence of discrete proteoforms[103] (Figure 1-6). However, typical top-down experiments are conducted under denaturing conditions, limiting the amount of structural information than can be extrapolated from these experiments. Rather, by conducting a native top-down experiment that preserves the native-like structure of the protein of interest, one can capture a richer and more comprehensive dataset that provides insight into the stability, stoichiometry, ligand binding, and oligomeric states of the protein, as opposed to solely reporting on the sequence of the protein[104]. Top-down

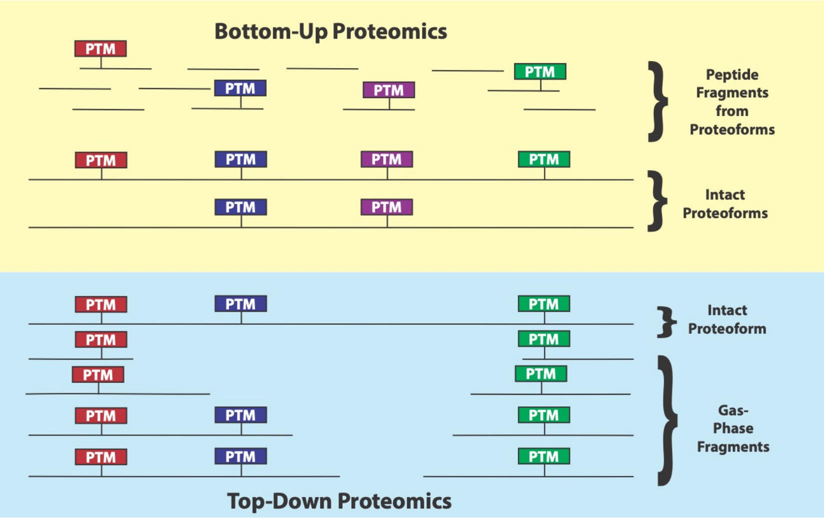

Figure 1-6 A comparison of top-down and bottom-up proteomics approaches. In a bottom-up experiment, multiple proteoforms may be digested together, yielding peptides. Since the peptides from each proteoform are detected together, this creates ambiguity in identifying how various PTMs occur together to yield discrete proteoforms. Top-down approaches eliminate the ambiguity by fragmenting only one proteoform at a time, allowing for more confident proteoform assignment.

mass spectrometry has been deployed to gain insight into a variety of target proteins, including challenging systems such as membrane proteins[44,105], mAbs[106,107], and histones[108,109]. Chapter 2 will explore the develop new methods for the native top-down of MPs.

Top-down mass spectrometry can be particularly powerful when coupled to native separations. Given the large number of fragments that are generated in a top-down experiment, it is often advantageous to couple a separation to the analysis to resolve the resultant peptides and increase the experimental peak capacity. LC-MS is typically used for this, but often requires the usage of denaturing solvents for these separations[110,111]. However, native separations based on hydrophobic interaction chromatography (HIC)[112] or size exclusion chromatography (SEC)[113,114] have been developed for native top-down LC-MS. Other separation techniques such as capillary zone electrophoresis coupled can be used as a separation for native top-down experimentation as well, with the advantage of being faster than typical LC separations[114,115]. IM is also commonly deployed as a native separation coupled to mass spectrometry for top-down experiments. Ion mobility can be particularly advantageous given its ability to resolve isobaric peptides, increasing the number of fragments that are able to be identified in the experiment[13].

There are multiple means of inducing fragmentation of a protein into peptides in a mass spectrometer. The most common mode of fragmentation is collision induced dissociation (CID)[116]. CID utilizes collisions with a background gas to activate the protein, intramolecular vibrational energy redistribution (IVR) causes the energy to fragment the most labile bond, the peptide bond[116]. Subsequently, N-terminal and C-terminal fragment ions are formed that are known as b and y ions respectively. Beam-type CID on orbitrap platforms is referred to as higher-energy collisional dissociation (HCD) to contrast with CID that occurs in ion traps[117].

CID has drawbacks, however; it is often not ideal for labile PTMs such as glycations or phosphorylations as these PTMs can be lost during collisional activation[118].

To improve the sequence coverage of native top-down experiments, other fragmentation methods have been deployed. ECD[119] and electron transfer dissociation (ETD)[120] have been deployed in native top-down experiments to fragment the N-C_α bond, producing c and z ions at the N and C termini, respectively. These electron-based methods occur on a much faster time scale than CID, bettering preserving labile PTMs[121]. Two main mechanisms exist to describe the process of ECD, the Cornell mechanism, and the Utah-Washington mechanism[119]. The Cornell mechanism suggests that ECD is a nonergodic process by which IVR is avoided, better preserving labile PTMs[119]. The Utah-Washington mechanisms suggests that IVR occurs, but that the neutralization of the radical ion formed is sufficiently quick to dissociatiate of the N-C_α bond without the loss of labile PTMs[119]. Other photoactivation-based methods deploy lasers have been used to improve sequence coverage in native top-down experiments included infrared multiphoton dissociation (IRMPD)[122] and ultraviolet photodissociation (UVPD)[123] have also been used to improve the sequence coverage obtained in these experiments. Oftentimes, it is advantageous to combine multiple fragmentation methods at once in order to achieve the highest sequence coverage obtainable, in experiments such as activated-ion ETD[124] and EThcD[125] . Other approaches to increasing sequence coverage in native top-down experiments include the use of covalent labeling tags to fix charged to certain residues in CID experiments to improve the sequence coverages obtained[126]. Additionally, the use of covalent TEMPO tagging can be used to enable free radical based sequencing that can produce c and z ions upon collision activation to improve sequence coverage[127].

1.7 Instrumentation

nMS experiments can be accomplished on a variety of instrument platforms. While several mass detectors exist, data for this thesis was collected exclusively on time-of-flight (TOF) and orbitrap based systems. TOF-MS instruments were predominate in early native MS work; however, orbitrap systems are becoming better established for nMS work, especially as the mass range of commercial orbitrap system continues to improve[128]. Data collected for this thesis were taken from several platforms: two TWIM-MS systems, a drift tube IM-MS system and an orbitrap system. The membrane protein work discussed within this thesis in Chapters 2 and 3 was collected on a modified Orbitrap Fusion Lumos (ThermoFisher, San Jose, CA) system. The Lumos consists of a nESI source, a quadrupole, and two mass analyzers: an ion trap and an orbitrap. The Lumos also has been modified with a 60 W CO_2 laser that can irradiate the ion trap with 10.6 μm light for IR photoactivation. The Lumos is also able to perform CID, in the ion trap and the ion routing multipole, and ETD.

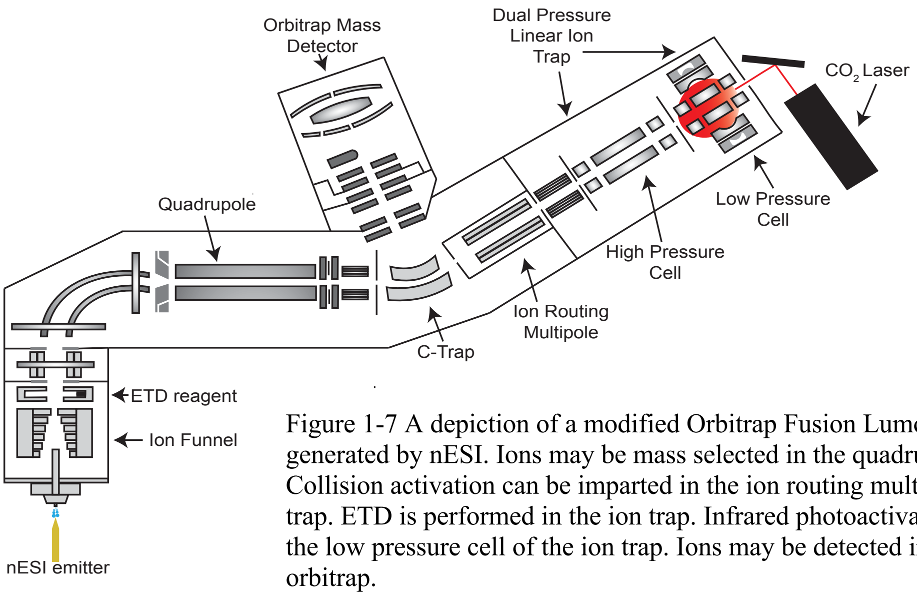

Figure 1-7 A depiction of a modified Orbitrap Fusion Lumos. Analyte ions are generated by nESI. Ions may be mass selected in the quadrupole and ion trap. Collision activation can be imparted in the ion routing multipole and in the ion trap. ETD is performed in the ion trap. Infrared photoactivation can be titrated into the low pressure cell of the ion trap. Ions may be detected in the ion trap and the orbitrap.

The two traveling wave systems that were used in this thesis are the Synapt G2 and the Select Series IMS (Waters, Milford, MA) (Figure 1-8). The Synapt G2 contains a nESI source, a

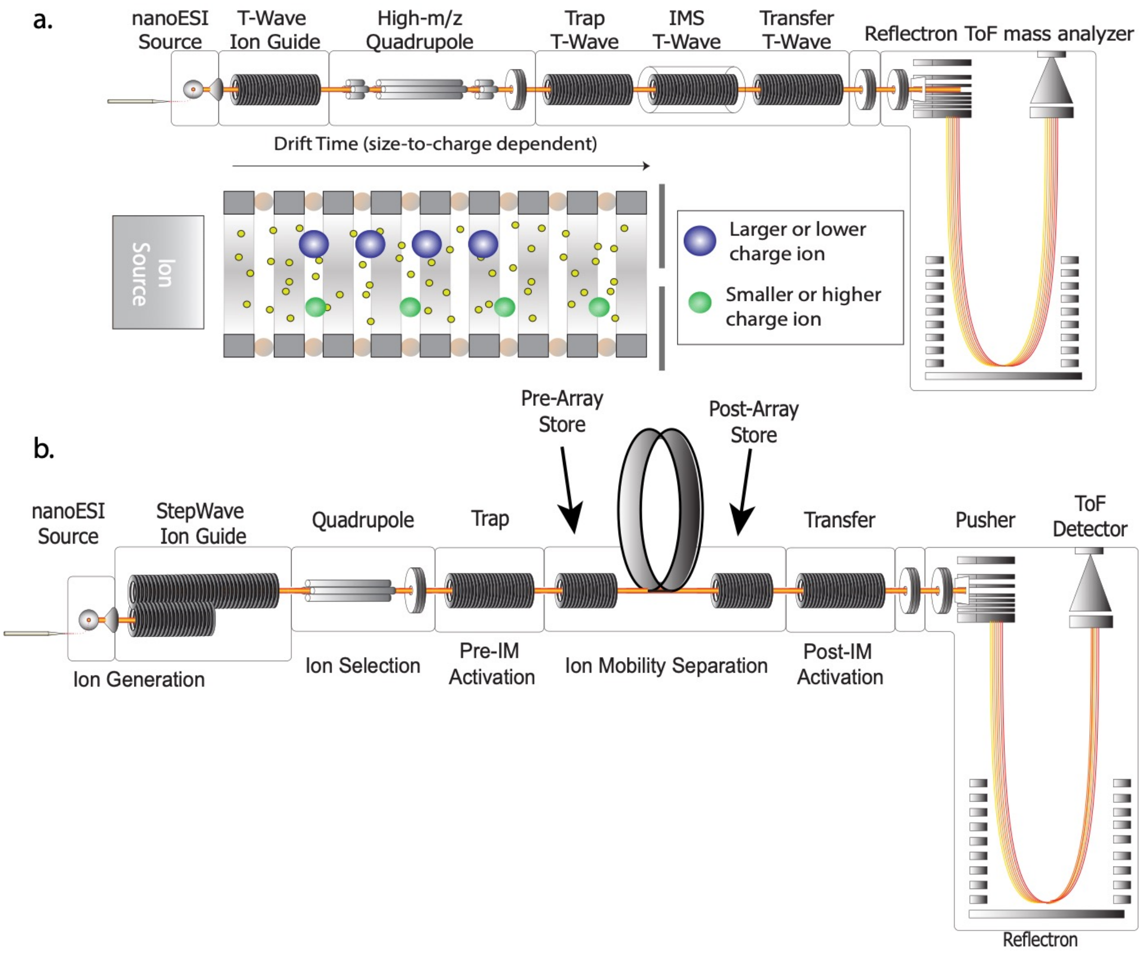

Figure 1-8 Schematics of a Synapt G2 (a) and a Select Series Cyclic IMS (b). Both systems are TWIM-MS platforms that generate ions by nESI. Ions then can be mass selected in the quadrupole, then passing through the trap where they may be collisionally activated. Analytes are then separated in the TWIM cell before passing through the transfer region to the TOF for mass detection. Notable differences between the platforms are that the cyclic has a non-linear ion guide, as opposed to the linear ion guide of the G2. Additionally, the cyclic ion mobility separator is non-linear and allows for IM^n separations that are impossible to perform on the linear TWIM cell of the G2.

quadrupole, an TWIM separator as well as a time-of-flight (TOF) mass analyzer. Collisional activation for CID and CIU can be performed in the trap and transfer regions; however, collisional activation is most often performed in the trap region to IM separate the resultant ion populations. The Select Series IMS is a cyclic ion mobility platform. Like the G2, it contains a nESI source, quadrupole, cyclic TWIM separator and a TOF detector. The stepwave on the cIM is not linear, unlike the linear traveling wave ion guide on the G2. The non-linear stepwave allows for neutral ions to be lost at this stage. Additionally, the design of the cyclic TWIM separator allows for certain ions to be selectively trapped and excluded from the experiment, as well as for discreet populations of ions to be subjected to additional rounds of separations and supplementary collisional activation[74]. The additional pathlength of the cyclic TWIM separator enables higher resolution IM separations when compared to the TWIM separation of the G2[74].

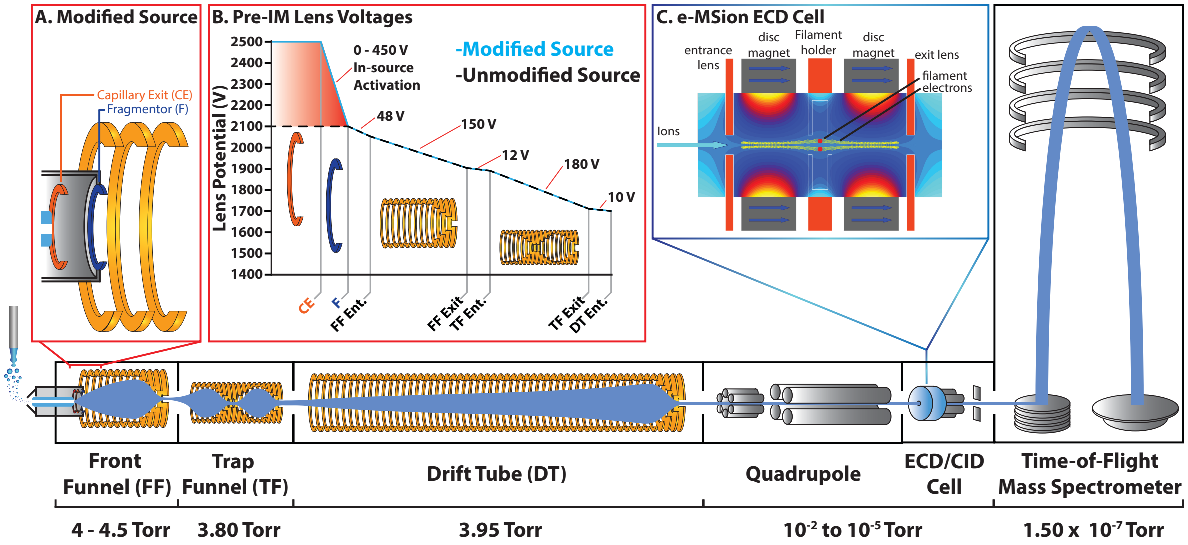

Figure 1-9 A schematic of the Agilent 6560c IM-Q-TOF platform. Ions are generated by microelectrospray ionization. Analytes can then be collisionally activated for CIU in the front funnel with the capillary exit lens (Panels A and B). Ions then pass through the trap funnel before being separated in the drift tube. The analytes can subsequently be mass selected in the quadrupole before undergoing ECD (Panel C) or CID in the collision cell before being detected in the TOF. Reproduced with permission from Gadkari, V. V.; Ramírez, C. R.; Vallejo, D. D.; Kurulugama, R. T.; Fjeldsted, J. C.; Ruotolo, B. T. Enhanced Collision Induced Unfolding and Electron Capture Dissociation of Native-like Protein Ions. Anal. Chem. 2020, 92 (23), 15489–15496. Copyright, American Chemical Society, 2020.

Like the Synapt G2 and the cIM systems, the Agilent 6560c (Santa Clara, CA) is an IM-MS platform. However, the 6560c, unlike those platforms, is a drift tube IM system, with the IM separation occurring prior to the quadrupole (Figure 1-9). The 6560c was specifically developed for nMS applications and CIU experimentation, as it contains an additional capillary exit lens in the front funnel to enable the collisional activation of proteins for CIU[95]. The 6560c can perform CID both in the front funnel and the collision cell; however, it is often advantageous to perform CID in the front funnel to IM separate the resultant fragments. The presence of an ExD cell (eMSion, Corvallis, OR) allows for ECD experiments to be performed in the collision cell as well, but these fragments are unable to be IM separated[95,118]. The design of the of 6560c allows for CIU experiments to be coupled to ECD experiments, which can allow for the unfolding of a protein to be annotated based on differences in ECD fragmentation before and after unfolding[95].

1.8 Target Systems

nMS is widely applicable to a variety of challenging and complex protein and oligonucleotide systems. While there are several standard proteins that have emerged to benchmark the performance of new methodologies in nMS, in this work, several specific target systems, including membrane proteins and mAbs, have been studied to develop new methodologies which expand the scope of nMS applications.

1.8.1 Membrane Proteins (MPs)

MPs constitute a third of the human proteome, but only a 3% of the structures within the Protein Data Bank[129]. Despite this MPs, constitute over 60% of current pharmaceutical targets[130]. This gap between the importance of MPs and the amount of structural information that is available regarding MPs is due to the inherent difficulties with performing experimentation with MPs[129]. MPs are particularly challenging to study given their low purification yields, their instability, and their high hydrophobic content[131]. To prevent MPs from precipitating in solution when out of the membrane, membrane mimetics are used. There are a wide variety of membrane mimetics that have been develop and are also compatible with nMS (Figure 1-10). The most common mimetic is a detergent micelle[132]. Detergents are amphipathic, like MPs, and the hydrophobic portions of these molecules can protect the hydrophobic portions of the MP,

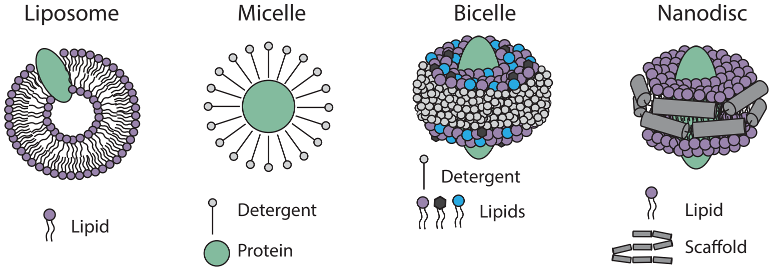

Figure 1-10 A representation of several common membrane mimetics and their components. All these mimetics were employed to solubilize proteins presented in this work.

allowing for it to be solubilized in solution. Typically, nonionic detergents are preferred for MS, in order to reduce the amount of noise that the detergent creates in the mass spectrometer[133]. Detergents can be exchanged prior to MS analysis to select for detergents that are more amenable to nMS. Detergent exchange methodologies will be further discussed in Chapter 3.

Other mimetics have been created to resemble the native environment of cellular membranes more closely. Bicelles are constituted of detergents and lipids, with lipids forming a bilayer and the detergents molecules positioned at the edge of the bilayer[134]. The lipid content of bicelles is tunable, enabling the study of the structural effects that different lipids can have on membrane protein stability[135]. Nanodiscs are constructed with a scaffold, either a scaffolding protein or a peptide, that holds together a lipid bilayer[136]. Nanodiscs are quite tunable, with the lipid composition and size of the nanodisc being able to be adjusted to accommodate the incorporation of the system of interest[137]. Additional, less commonly used bilayer-mimetics include small maleic acid lipid particles[138], amphipols[139], lipid vesicles[140] and liposomes[141]. Recent work has also been performed wherein nMS analysis of MPs has been performed with proteins ejected directly from the cellular membrane[45].

nMS of MPs typically requires some fashion of collisional activation to liberate the membrane protein from its mimetic, once ionized in the mass spectrometer[133]. Most often, this is accomplished by collisionally activating the mimetic complex until the protein is completely liberated, but not so activated that it unfolds and fragments[133]. However, the liberation from the mimetic creates significant noise in the spectra from the detergents, lipids and scaffolds that were released upon liberation. Alternate approaches to reduce the amount of noise that is created in these experiments, have included the development of photocleavable surfactants that can be broken down with the application of ultraviolet light, as opposed to collisional activation[142,143].

Chapter 1 will explore the use of infrared photoactivation for improved nMS methods with MPs, by using photoactivation to liberate proteins from a variety of mimetic environments. Despite these challenges, native mass spectrometry has been successfully used to study membrane protein structure and function[43,44,85]. In this way, nMS has revealed information about the oligomeric states of MPs[144] and their structural stability[84]. For example, CIU has been successfully deployed to evaluate structural differences upon ligand binding to translocator protein (TSPO)[145], as well as evaluating the destabilizing effects that mutations have upon peripheral myelin protein 22 (PMP22)[43]. Native top-down MS has also been conducted to obtain information regarding MP structure and sequence[44,146].

1.8.2 Monoclonal Antibodies (mAbs)

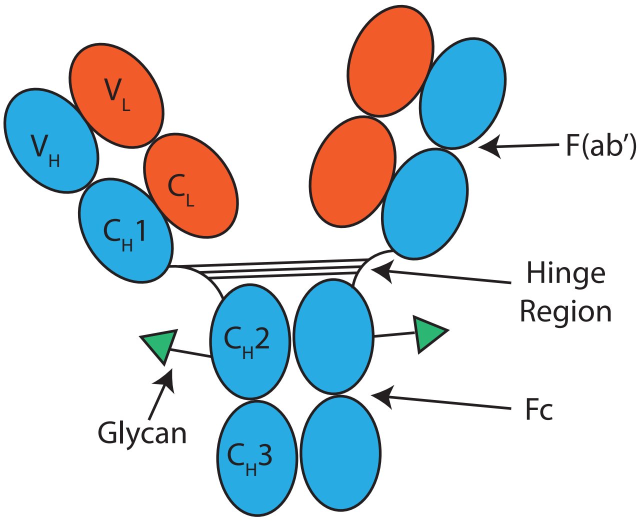

Figure 1-11 . A representation of the structure of IgG, highlighting its structural components, such as the hinge region and the Fc domain.

mAbs have emerged as an important class of biotherapeutics. Since their initial approval in the 1980s, their use in the pharmaceutical industry has expanded greatly, now comprising over half of all pharmaceutical sales[147]. Their growth is due in part to their high specificity, allowing for mAbs to bind their targets with high affinity, reducing the resultant side effects from off target binding[147]. Immunoglobulin Gs (IgG) are the most dominant subclass of mAb biotherapeutics[148]. IgGs are about 150 kDa and consist of several subclasses that differ the number of disulfide bonds that are present within the hinge region. An overview of the structure of IgG is provided in Figure 1-11. The variable regions of the heavy (V_H) and light chains of the mAb (V_L) constitute the hypervariable loops of the antibody which provides its high specificity for its epitope[148]. The V_H and V_L regions of the IgG combine with the constant domains (C_H1 and C_L) to constitute the antigen binding fragment ($F(ab')_2$)[148]. The remaining constant domains (C_H2 and C_H3) make up the fragment crystallizable (Fc) region of the mAb, where glycosylation can occur as a PTM[148]. The $F(ab')_2$ and Fc domains of the mAb are connected via the hinge region, which contains disulfide bonds, the number of which vary between different IgG subclasses[149].

IgG biotherapeutics are typically produced through genetic recombination and expressed in humanized constructs via overexpression in CHO cells (Chinese Hamster ovary, *Cricetulus griseus)*[150]. As such, these biotherapeutics are subject to a variety of biological processes, such as modification by PTMs, such as glycosylations. While non-biological changes experienced by mAbs during manufacturing include oxidation, deamidation and disulfide bond reshuffling[151]. These changes can impact the stability and function of the mAb therapeutic, making it critical to have analytical assays to measure and understand these changes as a part of quality control. nIM-MS and CIU have been widely deployed to evaluate mAb structure and the effects that PTMs and stress can have upon biotherapeutic stability[41,152,153]. Additionally, as the patents for many innovator biologics expire, biosimilars, which are substantially similar to the innovator mAb but not identical, continue to be developed[147]. Over 30 biosimilars have been approved by regulatory agencies such as the Food and Drug Administration, Health Canada, and the European Medicines Agency in the last decade[154]. Subtle differences in production can lead to structural changes in the biosimilar mAb, making methodologies like CIU important to rapidly characterize the structure of these biosimilars and their relative similarity to innovators[34,155]. Such analyses highlight the breadth of applications for the nMS of mAbs in industry, although work is still needed to further extend the applications of these technologies and their throughput. In this vein, Chapters 4, 5, and 6 will each discuss the application of nMS and CIU for monoclonal antibody targets.

1.9 Dissertation Overview

The aim of this dissertation is to develop and validate new methodologies for native ion-mobility mass spectrometry. Emphasis was placed in three core areas: developing new techniques for membrane protein analysis by nMS, validating and extending applications of CIU, and the development of high-throughput methodologies for nIM-MS. Additional work that will be discussed in the appendix include the application of native mass spectrometry to a metalloprotein and to proteoforms of a human protein obtained from clinical samples. The appendix will also discuss top-down data collected on the cyclic MS system and the 6560c.

Chapter 2 will focus on the development infrared photoactivation based methodologies for the native top-down MS of transmembrane proteins. Infrared activation applied by a 60 W CO_2 laser in the linear ion trap of an orbitrap can successfully liberate MPs from a variety of mimetic environments. The liberation process is selective, with the photoactivation dissociating the mimetic without perturbing native oligomeric structure or ligand binding. Liberating MPs from detergent micelles prior to top-down fragmentation by HCD significantly increases the sequence coverage that can be obtained, due to the reduction in detergent noise, as opposed to canonical experiments that use collisional activation to fragment and liberate protein simultaneously. Infrared photoactivation can preserve protein oligomeric states whilst also allowing for the identification of specific proteoforms within the protein. The work is undergoing peer review as: **Juliano, B. R.; Keating, J.W.; Ruotolo, B. T. Infrared Photoactivation Enables Improved Native Top-Down Mass Spectrometry of Transmembrane Proteins.**

***Anal. Chem.* 2023.** Data collection for this chapter was assisted by Joe Keating, a former undergraduate student in the lab.

Chapter 3 is a critical analysis of existing detergent exchange methodologies. The studies in Chapter 2 revealed that substantial amounts of the original detergent that the MP was purified into remain even after following established exchange procedures. To investigate the efficacy of the detergent exchange procedures that have been published in the literature, several model MPs were exchanged into a variety of different detergents by several methodologies. In all cases, detergent exchange was found to be incomplete, suggesting that existing methodologies must be revised. Of all the methodologies, SEC by fast protein liquid chromatography (FPLC) was the most effective. Potential solutions include increasing the number of exchange processes by performing iterative exchanges by SEC. It is important to better characterize the detergent exchange process to better understand the true chemical environment that the MPs exist in when being assayed by nMS experimentations. This work was completed with close collaboration with Iliana Levesque and Kristine Parson in the Ruotolo lab who assisted in data collection and analysis, especially with the dynamic light scattering data.

Chapter 4 focuses on benchmarking the reproducibility of CIU measurements across the same platform at geographically distinct locations. Such a study was necessary to better understand the factors that influence the reproducibility of CIU measurements as well as to identify the feasibility of including CIU measurements in a structural database for protein identification. The study revealed that for data collected with standard proteins that were prepared and analyzed identically between laboratories, the subsequent CIU measurements that were generated were remarkably similar. The features of the fingerprint were reproducible within 3% RSD in all cases observed. However, the transitions between the features were found to be less reproducible. To overcome this limitation, a new prototype of the source CIU hardware was developed according to stricter engineering controls. CIU data collected with this hardware produced transitions that more similar. The work has been published previously as: **Gadkari, V. V.; Juliano, B. R.; Mallis, C. S.; May, J. C.; Kurulugama, R. T.; Fjeldsted, J. C.; McLean, J. A.; Russell, D. H.; Ruotolo, B. T. Performance Evaluation of In-Source Ion Activation Hardware for Collision-Induced Unfolding of Proteins and Protein Complexes on a Drift Tube Ion Mobility-Mass Spectrometer. *Analyst* 2023, 148 (2), 391–401.** This work was done in close collaboration with Varun Gadkari, a former postdoc in the Ruotolo laboratory. Additional collaborators included the laboratory of David Russell at Texas A&M University, the laboratory of John McLean at Vanderbilt University and John Fjeldsted and Ruwan Kurulugama at Agilent Technologies who all participated in data collection and analysis.

Chapter 5 seeks to develop CIU methodologies for the quantitation of isomass species. Under typical, quantitative MS approaches isomass species are unable to be quantitated, as they overlap in m/z space. As IM can separate these species, it can then be deployed to develop quantitative methodologies for these otherwise intractable isomass molecules. CIU was used to identify differences in drift time for pairs of isomass sequence homologues and biotherapeutics at discreet collision voltages. For all systems involved, this quantitative CIU approach was able to produce linear calibration curves for all systems studied with nanomolar limits of detection, in both standard and complex matrices. Potential applications of this work include the use of a quantitative CIU approach to calculate effective dosages of isomass mAb biotherapeutics in the clinic.

Finally, Chapter 6 revolves around the development of automated, nMS and CIU workflows that are compatible with high-throughput experimentation. The Agilent RapidFire^{TM}

400 is a high throughput mass spectrometry robotic system that can rapidly aspirate samples from a well plate onto a cartridge for pre-MS cleanup prior to elution onto the MS for detection. The RF needed to have its plumbing modified to be compatible with an SEC cartridge for online desalting. Additionally, the flow rates had to be reduced to be compatible with microelectrospray ionization, which was previously demonstrated to be comparable to nanoelectrospray ionization for nMS in Chapter 4. RF-MS data is highly similar to other nMS data, with similar charge state distributions being observed for the resultant ions when compared to standard nMS approaches and with CCS values that are within 3% RSD of previously published nMS values. RF-MS can be applied for CIU experimentation by programming a voltage ramp to run as biomolecules elute off the RF. CIU data collected with the RF are collected in 30 seconds, which are among the fastest CIU data collected to date. RF-MS can be widely applied to a variety of systems of interest for nMS including protein complexes, monoclonal antibodies, and oligonucleotides. This work was performed in collaboration with Joe Keating and Henry Li, former undergraduate students whom I mentored in the lab, and who assisted me with data collection. Anna Anders assisted with optimizing instrument conditions for oligonucleotides, and Zhuoer Xie of Amgen provided the siRNA duplex.

The appendices detail work done to apply nMS to various protein systems. Appendix I highlights the application of nMS to identify differences in protamine proteoform populations in discrete clinical populations. This work was done in collaboration with Samantha Schon and Sue Hammoud in the departments of Human Genetics, Urology and Obstetrics and Gynecology Appendix II details the use of nMS and inductively coupled plasma (ICP)-MS to identify an unknown metal ion ligand bound to a bacterial amylase. This work has undergone peer review and has recently been accepted for publication as **Brown, H.A.; DeVeaux, A.L.; Juliano, B.R.;**

Photenhauer, A.L., Boulinguiez, M.; Bornschein, R.E.; Wawrzak, Z.; Ruotolo, B.T.; Terrapon, N.; Koropatkin, N.M. SusG from *Bacteroides ovatus* Represents a Novel α-amylase Used for *Bacteroides* Starch Breakdown in the Human Gut. *Cell. Mol. Life Sci.* 2023. This work was performed in collaboration with the laboratory of Nicole Koropatkin in the department of Molecular, Cellular and Developmental Biology. The remainder of the appendices contain supporting material for Chapters 2-6.

The development of the novel methodologies described in this thesis will enable improved applications of nMS techniques for a wide variety of target systems. The method described in Chapter 2 offers significant improvements over current methodologies for native proteomics by nMS, allowing for more informative sequence coverage to be generated for a variety of MP targets in the future. The evaluation of detergent exchange procedures in Chapter 3 will allow for practitioners in the field to use improved methodologies for detergent exchange, whilst also highlighting the need for improved methodologies in that space to enable more quantitative control over detergent exchange. The careful study of interlaboratory reproducibility of CIU measurements in Chapter 4 lays the groundwork for the development of CIU fingerprint data base, that could identify analytes according to the CCS values of their unique features. The work described in Chapter 5 will allow for CIU to now be deployed for quantitative approaches, allowing for previously intractable isomass species to be quantified using nIM-MS. Finally, the automated desalting procedure in Chapter 6 will allow for nIM-MS data to be collected with a significantly enhanced throughput and allows for nIM-MS to be better deployed for high throughput screening applications in academic and industrial settings. As such, the work described in this thesis is a valuable contribution to the nMS community, as it expands the applications of nMS in several discrete experimental areas and will be of broad interest within the community.

1.10 References

(1) Robinson, C. V.; Sali, A.; Baumeister, W. The Molecular Sociology of the Cell. *Nature* **2007**, *450* (7172), 973–982. https://doi.org/10.1038/nature06523.

(2) Legrain, P.; Aebersold, R.; Archakov, A.; Bairoch, A.; Bala, K.; Beretta, L.; Bergeron, J.; Borchers, C. H.; Corthals, G. L.; Costello, C. E.; Deutsch, E. W.; Domon, B.; Hancock, W.; He, F.; Hochstrasser, D.; Marko-Varga, G.; Salekdeh, G. H.; Sechi, S.; Snyder, M.; Srivastava, S.; Uhlén, M.; Wu, C. H.; Yamamoto, T.; Paik, Y.-K.; Omenn, G. S. The Human Proteome Project: Current State and Future Direction. *Molecular & Cellular Proteomics* **2011**, *10* (7). https://doi.org/10.1074/mcp.M111.009993.

(3) Omenn, G. S.; Lane, L.; Overall, C. M.; Cristea, I. M.; Corrales, F. J.; Lindskog, C.; Paik, Y.-K.; Van Eyk, J. E.; Liu, S.; Pennington, S. R.; Snyder, M. P.; Baker, M. S.; Bandeira, N.; Aebersold, R.; Moritz, R. L.; Deutsch, E. W. Research on the Human Proteome Reaches a Major Milestone: >90% of Predicted Human Proteins Now Credibly Detected, According to the HUPO Human Proteome Project. *J. Proteome Res.* **2020**, *19* (12), 4735–4746. https://doi.org/10.1021/acs.jproteome.0c00485.

(4) Bhowmick, A.; Brookes, D. H.; Yost, S. R.; Dyson, H. J.; Forman-Kay, J. D.; Gunter, D.; Head-Gordon, M.; Hura, G. L.; Pande, V. S.; Wemmer, D. E.; Wright, P. E.; Head-Gordon, T. Finding Our Way in the Dark Proteome. *J. Am. Chem. Soc.* **2016**, *138* (31), 9730–9742. https://doi.org/10.1021/jacs.6b06543.

(5) Collins, F. S.; Morgan, M.; Patrinos, A. The Human Genome Project: Lessons from Large-Scale Biology. *Science* **2003**, *300* (5617), 286–290. https://doi.org/10.1126/science.1084564.

(6) Aebersold, R.; Agar, J. N.; Amster, I. J.; Baker, M. S.; Bertozzi, C. R.; Boja, E. S.; Costello, C. E.; Cravatt, B. F.; Fenselau, C.; Garcia, B. A.; Ge, Y.; Gunawardena, J.; Hendrickson, R. C.; Hergenrother, P. J.; Huber, C. G.; Ivanov, A. R.; Jensen, O. N.; Jewett, M. C.; Kelleher, N. L.; Kiessling, L. L.; Krogan, N. J.; Larsen, M. R.; Loo, J. A.; Ogorzalek Loo, R. R.; Lundberg, E.; MacCoss, M. J.; Mallick, P.; Mootha, V. K.; Mrksich, M.; Muir, T. W.; Patrie, S. M.; Pesavento, J. J.; Pitteri, S. J.; Rodriguez, H.; Saghatelian, A.; Sandoval, W.; Schlüter, H.; Sechi, S.; Slavoff, S. A.; Smith, L. M.; Snyder, M. P.; Thomas, P. M.; Uhlén, M.; Van Eyk, J. E.; Vidal, M.; Walt, D. R.; White, F. M.; Williams, E. R.; Wohlschlager, T.; Wysocki, V. H.; Yates, N. A.; Young, N. L.; Zhang, B. How Many Human Proteoforms Are There? *Nat Chem Biol* **2018**, *14* (3), 206–214. https://doi.org/10.1038/nchembio.2576.

(7) Schaffer, L. V.; Millikin, R. J.; Miller, R. M.; Anderson, L. C.; Fellers, R. T.; Ge, Y.; Kelleher, N. L.; LeDuc, R. D.; Liu, X.; Payne, S. H.; Sun, L.; Thomas, P. M.; Tucholski, T.; Wang, Z.; Wu, S.; Wu, Z.; Yu, D.; Shortreed, M. R.; Smith, L. M. Identification and Quantification of Proteoforms by Mass Spectrometry. *PROTEOMICS* **2019**, *19* (10), 1800361. https://doi.org/10.1002/pmic.201800361.

(8) Toby, T. K.; Fornelli, L.; Kelleher, N. L. Progress in Top-Down Proteomics and the Analysis of Proteoforms. *Annu Rev Anal Chem (Palo Alto Calif)* **2016**, *9* (1), 499–519. https://doi.org/10.1146/annurev-anchem-071015-041550.

(9) Schachner, L. F.; Jooß, K.; Morgan, M. A.; Piunti, A.; Meiners, M. J.; Kafader, J. O.; Lee, A. S.; Iwanaszko, M.; Cheek, M. A.; Burg, J. M.; Howard, S. A.; Keogh, M.-C.; Shilatifard, A.; Kelleher, N. L. Decoding the Protein Composition of Whole Nucleosomes with Nuc-MS. *Nat Methods* **2021**, *18* (3), 303–308. https://doi.org/10.1038/s41592-020-01052-9.

(10) Ives, A. N.; Dunn, H. A.; Afsari, H. S.; Seckler, H. dos S.; Foroutan, M. J.; Chavez, E.; Melani, R. D.; Fellers, R. T.; LeDuc, R. D.; Thomas, P. M.; Martemyanov, K. A.; Kelleher, N. L.; Vafabakhsh, R. Middle-Down Mass Spectrometry Reveals Activity-Modifying Phosphorylation Barcode in a Class C G Protein-Coupled Receptor. *J. Am. Chem. Soc.* **2022**, *144* (50), 23104–23114. https://doi.org/10.1021/jacs.2c10697.

(11) Castelli, M. S.; McGonigle, P.; Hornby, P. J. The Pharmacology and Therapeutic Applications of Monoclonal Antibodies. *Pharmacology Research & Perspectives* **2019**, *7* (6), e00535. https://doi.org/10.1002/prp2.535.

(12) Karch, K. R.; Snyder, D. T.; Harvey, S. R.; Wysocki, V. H. Native Mass Spectrometry: Recent Progress and Remaining Challenges. *Annu Rev Biophys* **2022**, *51*, 157–179. https://doi.org/10.1146/annurev-biophys-092721-085421.

(13) Ruotolo, B. T. Collision Cross Sections for Native Proteomics: Challenges and Opportunities. *J. Proteome Res.* **2022**, *21* (1), 2–8. https://doi.org/10.1021/acs.jproteome.1c00686.

(14) Westbrook, J. D.; Burley, S. K. How Structural Biologists and the Protein Data Bank Contributed to Recent FDA New Drug Approvals. *Structure* **2019**, *27* (2), 211–217. https://doi.org/10.1016/j.str.2018.11.007.

(15) Batool, M.; Ahmad, B.; Choi, S. A Structure-Based Drug Discovery Paradigm. *International Journal of Molecular Sciences* **2019**, *20* (11), 2783. https://doi.org/10.3390/ijms20112783.

(16) Binder, J. L.; Berendzen, J.; Stevens, A. O.; He, Y.; Wang, J.; Dokholyan, N. V.; Oprea, T. I. AlphaFold Illuminates Half of the Dark Human Proteins. *Current Opinion in Structural Biology* **2022**, *74*, 102372. https://doi.org/10.1016/j.sbi.2022.102372.

(17) Varadi, M.; Velankar, S. The Impact of AlphaFold Protein Structure Database on the Fields of Life Sciences. *PROTEOMICS* **2022**, *n/a* (n/a), 2200128. https://doi.org/10.1002/pmic.202200128.

(18) Roney, J. P.; Ovchinnikov, S. State-of-the-Art Estimation of Protein Model Accuracy Using AlphaFold. *Phys. Rev. Lett.* **2022**, *129* (23), 238101. https://doi.org/10.1103/PhysRevLett.129.238101.

(19) Subramaniam, S.; Kleywegt, G. J. A Paradigm Shift in Structural Biology. *Nat Methods* **2022**, *19* (1), 20–23. https://doi.org/10.1038/s41592-021-01361-7.

(20) Dobson, C. M. Biophysical Techniques in Structural Biology. *Annu Rev Biochem* **2019**, *88*, 25–33. https://doi.org/10.1146/annurev-biochem-013118-111947.

(21) Cate, J. H.; Yusupov, M. M.; Yusupova, G. Zh.; Earnest, T. N.; Noller, H. F. X-Ray Crystal Structures of 70S Ribosome Functional Complexes. *Science* **1999**, *285* (5436), 2095–2104. https://doi.org/10.1126/science.285.5436.2095.

(22) Cramer, P.; Bushnell, D. A.; Kornberg, R. D. Structural Basis of Transcription: RNA Polymerase II at 2.8 Ångstrom Resolution. *Science* **2001**, *292* (5523), 1863–1876. https://doi.org/10.1126/science.1059493.

(23) Chayen, N. E.; Saridakis, E. Protein Crystallization: From Purified Protein to Diffraction-Quality Crystal. *Nat Methods* **2008**, *5* (2), 147–153. https://doi.org/10.1038/nmeth.f.203.

(24) Bakhtiari, M.; Konermann, L. Protein Ions Generated by Native Electrospray Ionization: Comparison of Gas Phase, Solution, and Crystal Structures. *J. Phys. Chem. B* **2019**, *123* (8), 1784–1796. https://doi.org/10.1021/acs.jpcb.8b12173.

(25) Charlier, C.; Bouvignies, G.; Pelupessy, P.; Walrant, A.; Marquant, R.; Kozlov, M.; De Ioannes, P.; Bolik-Coulon, N.; Sagan, S.; Cortes, P.; Aggarwal, A. K.; Carlier, L.; Ferrage, F. Structure and Dynamics of an Intrinsically Disordered Protein Region That Partially Folds upon Binding by Chemical-Exchange NMR. *J. Am. Chem. Soc.* **2017**, *139* (35), 12219–12227. https://doi.org/10.1021/jacs.7b05823.

(26) Markwick, P. R. L.; Malliavin, T.; Nilges, M. Structural Biology by NMR: Structure, Dynamics, and Interactions. *PLOS Computational Biology* **2008**, *4* (9), e1000168. https://doi.org/10.1371/journal.pcbi.1000168.

(27) Hu, Y.; Cheng, K.; He, L.; Zhang, X.; Jiang, B.; Jiang, L.; Li, C.; Wang, G.; Yang, Y.; Liu, M. NMR-Based Methods for Protein Analysis. *Anal. Chem.* **2021**, *93* (4), 1866–1879. https://doi.org/10.1021/acs.analchem.0c03830.

(28) Yip, K. M.; Fischer, N.; Paknia, E.; Chari, A.; Stark, H. Atomic-Resolution Protein Structure Determination by Cryo-EM. *Nature* **2020**, *587* (7832), 157–161. https://doi.org/10.1038/s41586-020-2833-4.

(29) Weissenberger, G.; Henderikx, R. J. M.; Peters, P. J. Understanding the Invisible Hands of Sample Preparation for Cryo-EM. *Nat Methods* **2021**, *18* (5), 463–471. https://doi.org/10.1038/s41592-021-01130-6.

(30) Sirohi, D.; Chen, Z.; Sun, L.; Klose, T.; Pierson, T. C.; Rossmann, M. G.; Kuhn, R. J. The 3.8 Å Resolution Cryo-EM Structure of Zika Virus. *Science* **2016**, *352* (6284), 467–470. https://doi.org/10.1126/science.aaf5316.

(31) Greenfield, N. J. Using Circular Dichroism Spectra to Estimate Protein Secondary Structure. *Nat Protoc* **2006**, *1* (6), 2876–2890. https://doi.org/10.1038/nprot.2006.202.

(32) Hura, G. L.; Menon, A. L.; Hammel, M.; Rambo, R. P.; Poole II, F. L.; Tsutakawa, S. E.; Jenney Jr, F. E.; Classen, S.; Frankel, K. A.; Hopkins, R. C.; Yang, S.; Scott, J. W.; Dillard, B. D.; Adams, M. W. W.; Tainer, J. A. Robust, High-Throughput Solution Structural Analyses by Small Angle X-Ray Scattering (SAXS). *Nat Methods* **2009**, *6* (8), 606–612. https://doi.org/10.1038/nmeth.1353.

(33) Brosey, C. A.; Tainer, J. A. Evolving SAXS Versatility: Solution X-Ray Scattering for Macromolecular Architecture, Functional Landscapes, and Integrative Structural Biology. *Current Opinion in Structural Biology* **2019**, *58*, 197–213. https://doi.org/10.1016/j.sbi.2019.04.004.

(34) Pisupati, K.; Benet, A.; Tian, Y.; Okbazghi, S.; Kang, J.; Ford, M.; Saveliev, S.; Sen, K. I.; Carlson, E.; Tolbert, T. J.; Ruotolo, B. T.; Schwendeman, S. P.; Schwendeman, A. Biosimilarity under Stress: A Forced Degradation Study of Remicade® and Remsima™. *mAbs* **2017**, *9* (7), 1197–1209. https://doi.org/10.1080/19420862.2017.1347741.

(35) Velázquez Campoy, A.; Freire, E. ITC in the Post-Genomic Era…? Priceless. *Biophysical Chemistry* **2005**, *115* (2), 115–124. https://doi.org/10.1016/j.bpc.2004.12.015.

(36) Ibarra-Molero, B.; Naganathan, A. N.; Sanchez-Ruiz, J. M.; Muñoz, V. Chapter Twelve - Modern Analysis of Protein Folding by Differential Scanning Calorimetry. In *Methods in Enzymology*; Feig, A. L., Ed.; Calorimetry; Academic Press, 2016; Vol. 567, pp 281–318. https://doi.org/10.1016/bs.mie.2015.08.027.

(37) Boeri Erba, E.; Petosa, C. The Emerging Role of Native Mass Spectrometry in Characterizing the Structure and Dynamics of Macromolecular Complexes. *Protein Science* **2015**, *24* (8), 1176–1192. https://doi.org/10.1002/pro.2661.

(38) D'Atri, V.; Gabelica, V. DNA and RNA Telomeric G-Quadruplexes: What Topology Features Can Be Inferred from Ion Mobility Mass Spectrometry? *Analyst* **2019**, *144* (20), 6074–6088. https://doi.org/10.1039/C9AN01216H.

(39) Marchand, A.; Gabelica, V. Native Electrospray Mass Spectrometry of DNA G-Quadruplexes in Potassium Solution. *J. Am. Soc. Mass Spectrom.* **2014**, *25* (7), 1146–1154. https://doi.org/10.1007/s13361-014-0890-3.

(40) Tian, Y.; Ruotolo, B. T. Collision Induced Unfolding Detects Subtle Differences in Intact Antibody Glycoforms and Associated Fragments. *International Journal of Mass Spectrometry* **2018**, *425*, 1–9. https://doi.org/10.1016/j.ijms.2017.12.005.

(41) Vallejo, D. D.; Jeon, C. K.; Parson, K. F.; Herderschee, H. R.; Eschweiler, J. D.; Filoti, D. I.; Ruotolo, B. T. Ion Mobility–Mass Spectrometry Reveals the Structures and Stabilities of Biotherapeutic Antibody Aggregates. *Anal. Chem.* **2022**, *94* (18), 6745–6753. https://doi.org/10.1021/acs.analchem.2c00160.

(42) Botzanowski, T.; Erb, S.; Hernandez-Alba, O.; Ehkirch, A.; Colas, O.; Wagner-Rousset, E.; Rabuka, D.; Beck, A.; Drake, P. M.; Cianférani, S. Insights from Native Mass Spectrometry Approaches for Top- and Middle- Level Characterization of Site-Specific Antibody-Drug Conjugates. *mAbs* **2017**, *9* (5), 801–811. https://doi.org/10.1080/19420862.2017.1316914.

(43) Fantin, S. M.; Parson, K. F.; Yadav, P.; Juliano, B.; Li, G. C.; Sanders, C. R.; Ohi, M. D.; Ruotolo, B. T. Ion Mobility–Mass Spectrometry Reveals the Role of Peripheral Myelin Protein Dimers in Peripheral Neuropathy. *Proceedings of the National Academy of Sciences* **2021**, *118* (17), e2015331118.

(44) Sipe, S. N.; Patrick, J. W.; Laganowsky, A.; Brodbelt, J. S. Enhanced Characterization of Membrane Protein Complexes by Ultraviolet Photodissociation Mass Spectrometry. *Anal. Chem.* **2020**, *92* (1), 899–907. https://doi.org/10.1021/acs.analchem.9b03689.

(45) Chorev, D. S.; Baker, L. A.; Wu, D.; Beilsten-Edmands, V.; Rouse, S. L.; Zeev-Ben-Mordehai, T.; Jiko, C.; Samsudin, F.; Gerle, C.; Khalid, S.; Stewart, A. G.; Matthews, S. J.; Grünewald, K.; Robinson, C. V. Protein Assemblies Ejected Directly from Native Membranes Yield Complexes for Mass Spectrometry. *Science* **2018**, *362* (6416), 829–834. https://doi.org/10.1126/science.aau0976.

(46) Allison, T. M.; Reading, E.; Liko, I.; Baldwin, A. J.; Laganowsky, A.; Robinson, C. V. Quantifying the Stabilizing Effects of Protein–Ligand Interactions in the Gas Phase. *Nat Commun* **2015**, *6* (1), 8551. https://doi.org/10.1038/ncomms9551.

(47) Giska, F.; Mariappan, M.; Bhattacharyya, M.; Gupta, K. Deciphering the Molecular Organization of GET Pathway Chaperones through Native Mass Spectrometry. *Biophysical Journal* **2022**, *121* (7), 1289–1298. https://doi.org/10.1016/j.bpj.2022.02.026.

(48) Gault, J.; Lianoudaki, D.; Kaldmäe, M.; Kronqvist, N.; Rising, A.; Johansson, J.; Lohkamp, B.; Laín, S.; Allison, T. M.; Lane, D. P.; Marklund, E. G.; Landreh, M. Mass Spectrometry Reveals the Direct Action of a Chemical Chaperone. *J. Phys. Chem. Lett.* **2018**, *9* (14), 4082–4086. https://doi.org/10.1021/acs.jpclett.8b01817.

(49) Uetrecht, C.; Barbu, I. M.; Shoemaker, G. K.; van Duijn, E.; Heck, A. J. R. Interrogating Viral Capsid Assembly with Ion Mobility–Mass Spectrometry. *Nature Chem* **2011**, *3* (2), 126–132. https://doi.org/10.1038/nchem.947.

(50) Snijder, J.; Rose, R. J.; Veesler, D.; Johnson, J. E.; Heck, A. J. R. Studying 18 MDa Virus Assemblies with Native Mass Spectrometry. *Angew Chem Int Ed Engl* **2013**, *52* (14), 4020–4023. https://doi.org/10.1002/anie.201210197.

(51) Konermann, L. Addressing a Common Misconception: Ammonium Acetate as Neutral PH “Buffer” for Native Electrospray Mass Spectrometry. *J. Am. Soc. Mass Spectrom.* **2017**, *28* (9), 1827–1835. https://doi.org/10.1007/s13361-017-1739-3.

(52) Heck, A. J. R. Native Mass Spectrometry: A Bridge between Interactomics and Structural Biology. *Nat Methods* **2008**, *5* (11), 927–933. https://doi.org/10.1038/nmeth.1265.

(53) Xia, Z.; B. DeGrandchamp, J.; R. Williams, E. Native Mass Spectrometry beyond Ammonium Acetate: Effects of Nonvolatile Salts on Protein Stability and Structure. *Analyst* **2019**, *144* (8), 2565–2573. https://doi.org/10.1039/C9AN00266A.

(54) Yamashita, M.; Fenn, J. B. Electrospray Ion Source. Another Variation on the Free-Jet Theme. *J. Phys. Chem.* **1984**, *88* (20), 4451–4459. https://doi.org/10.1021/j150664a002.

(55) Ganem, B.; Li, Y. T.; Henion, J. D. Observation of Noncovalent Enzyme-Substrate and Enzyme-Product Complexes by Ion-Spray Mass Spectrometry. *J. Am. Chem. Soc.* **1991**, *113* (20), 7818–7819. https://doi.org/10.1021/ja00020a085.

(56) Katta, V.; Chait, B. T. Observation of the Heme-Globin Complex in Native Myoglobin by Electrospray-Ionization Mass Spectrometry. *J. Am. Chem. Soc.* **1991**, *113* (22), 8534–8535. https://doi.org/10.1021/ja00022a058.

(57) Light-Wahl, K. J.; Schwartz, B. L.; Smith, R. D. Observation of the Noncovalent Quaternary Associations of Proteins by Electrospray Ionization Mass Spectrometry. *J. Am. Chem. Soc.* **1994**, *116* (12), 5271–5278. https://doi.org/10.1021/ja00091a035.

(58) Taylor, G. I. Disintegration of Water Drops in an Electric Field. *Proceedings of the Royal Society of London. Series A. Mathematical and Physical Sciences* **1997**, *280* (1382), 383–397. https://doi.org/10.1098/rspa.1964.0151.

(59) Rayleigh, Lord. XX. On the Equilibrium of Liquid Conducting Masses Charged with Electricity. *The London, Edinburgh, and Dublin Philosophical Magazine and Journal of Science* **1882**, *14* (87), 184–186. https://doi.org/10.1080/14786448208628425.

(60) Dole, M.; Hines, R. L.; Mack, L. L.; Mobley, R. C.; Ferguson, L. D.; Alice, M. B. Gas Phase Macroions. *Macromolecules* **1968**, *1* (1), 96–97. https://doi.org/10.1021/ma60001a017.

(61) Kebarle, P.; Verkerk, U. H. Electrospray: From Ions in Solution to Ions in the Gas Phase, What We Know Now. *Mass Spectrometry Reviews* **2009**, *28* (6), 898–917. https://doi.org/10.1002/mas.20247.

(62) Khristenko, N.; Rosu, F.; Largy, E.; Haustant, J.; Mesmin, C.; Gabelica, V. Native Electrospray Ionization of Multi-Domain Proteins via a Bead Ejection Mechanism. *J. Am. Chem. Soc.* **2023**, *145* (1), 498–506. https://doi.org/10.1021/jacs.2c10762.

(63) Wilm, M.; Mann, M. Analytical Properties of the Nanoelectrospray Ion Source. *Anal. Chem.* **1996**, *68* (1), 1–8. https://doi.org/10.1021/ac9509519.

(64) Leney, A. C.; Heck, A. J. R. Native Mass Spectrometry: What Is in the Name? *J Am Soc Mass Spectrom* **2017**, *28* (1), 5–13. https://doi.org/10.1007/s13361-016-1545-3.

(65) Breuker, K.; McLafferty, F. W. Stepwise Evolution of Protein Native Structure with Electrospray into the Gas Phase, 10^{-12} to 10^{2} s. *Proc. Natl. Acad. Sci. U.S.A.* **2008**, *105* (47), 18145–18152. https://doi.org/10.1073/pnas.0807005105.

(66) Jurneczko, E.; Barran, P. E. How Useful Is Ion Mobility Mass Spectrometry for Structural Biology? The Relationship between Protein Crystal Structures and Their Collision Cross

Sections in the Gas Phase. *Analyst* **2011**, *136* (1), 20–28. https://doi.org/10.1039/C0AN00373E.

(67) Westphall, M. S.; Lee, K. W.; Salome, A. Z.; Lodge, J. M.; Grant, T.; Coon, J. J. Three-Dimensional Structure Determination of Protein Complexes Using Matrix-Landing Mass Spectrometry. *Nat Commun* **2022**, *13* (1), 2276. https://doi.org/10.1038/s41467-022-29964-4.

(68) Rolland, A. D.; Prell, J. S. Computational Insights into Compaction of Gas-Phase Protein and Protein Complex Ions in Native Ion Mobility-Mass Spectrometry. *TrAC Trends in Anal. Chem.* **2019**, *116*, 282–291. https://doi.org/10.1016/j.trac.2019.04.023.

(69) Gabelica, V.; Marklund, E. Fundamentals of Ion Mobility Spectrometry. *Current Opinion in Chemical Biology* **2018**, *42*, 51–59. https://doi.org/10.1016/j.cbpa.2017.10.022.

(70) Dodds, J. N.; Baker, E. S. Ion Mobility Spectrometry: Fundamental Concepts, Instrumentation, Applications, and the Road Ahead. *J. Am. Soc. Mass Spectrom.* **2019**, *30* (11), 2185–2195. https://doi.org/10.1007/s13361-019-02288-2.

(71) Haler, J. R. N.; Kune, C.; Massonnet, P.; Comby-Zerbino, C.; Jordens, J.; Honing, M.; Mengerink, Y.; Far, J.; De Pauw, E. Comprehensive Ion Mobility Calibration: Poly(Ethylene Oxide) Polymer Calibrants and General Strategies. *Anal. Chem.* **2017**, *89* (22), 12076–12086. https://doi.org/10.1021/acs.analchem.7b02564.

(72) Stow, S. M.; Causon, T. J.; Zheng, X.; Kurulugama, R. T.; Mairinger, T.; May, J. C.; Rennie, E. E.; Baker, E. S.; Smith, R. D.; McLean, J. A.; Hann, S.; Fjeldsted, J. C. An Interlaboratory Evaluation of Drift Tube Ion Mobility–Mass Spectrometry Collision Cross Section Measurements. *Anal. Chem.* **2017**, *89* (17), 9048–9055. https://doi.org/10.1021/acs.analchem.7b01729.

(73) Cumeras, R.; Figueras, E.; Davis, C. E.; Baumbach, J. I.; Gràcia, I. Review on Ion Mobility Spectrometry. Part 1: Current Instrumentation. *Analyst* **2015**, *140* (5), 1376–1390. https://doi.org/10.1039/C4AN01100G.

(74) Giles, K.; Ujma, J.; Wildgoose, J.; Pringle, S.; Richardson, K.; Langridge, D.; Green, M. A Cyclic Ion Mobility-Mass Spectrometry System. *Anal. Chem.* **2019**, *91* (13), 8564–8573. https://doi.org/10.1021/acs.analchem.9b01838.

(75) M. Ibrahim, Y.; M. Hamid, A.; Deng, L.; B. Garimella, S. V.; K. Webb, I.; S. Baker, E.; D. Smith, R. New Frontiers for Mass Spectrometry Based upon Structures for Lossless Ion Manipulations. *Analyst* **2017**, *142* (7), 1010–1021. https://doi.org/10.1039/C7AN00031F.

(76) Deng, L.; Webb, I. K.; Garimella, S. V. B.; Hamid, A. M.; Zheng, X.; Norheim, R. V.; Prost, S. A.; Anderson, G. A.; Sandoval, J. A.; Baker, E. S.; Ibrahim, Y. M.; Smith, R. D. Serpentine Ultralong Path with Extended Routing (SUPER) High Resolution Traveling Wave Ion Mobility-MS Using Structures for Lossless Ion Manipulations. *Anal. Chem.* **2017**, *89* (8), 4628–4634. https://doi.org/10.1021/acs.analchem.7b00185.

(77) Borotto, N. B.; Osho, K. E.; Richards, T. K.; Graham, K. A. Collision-Induced Unfolding of Native-like Protein Ions Within a Trapped Ion Mobility Spectrometry Device. *J. Am. Soc. Mass Spectrom.* **2022**, *33* (1), 83–89. https://doi.org/10.1021/jasms.1c00273.

(78) Jeanne Dit Fouque, K.; Garabedian, A.; Leng, F.; Tse-Dinh, Y.-C.; Ridgeway, M. E.; Park, M. A.; Fernandez-Lima, F. Trapped Ion Mobility Spectrometry of Native Macromolecular Assemblies. *Anal. Chem.* **2021**, *93* (5), 2933–2941. https://doi.org/10.1021/acs.analchem.0c04556.

(79) Schweppe, D. K.; Prasad, S.; Belford, M. W.; Navarrete-Perea, J.; Bailey, D. J.; Huguet, R.; Jedrychowski, M. P.; Rad, R.; McAlister, G.; Abbatiello, S. E.; Woulters, E. R.;

Zabrouskov, V.; Dunyach, J.-J.; Paulo, J. A.; Gygi, S. P. Characterization and Optimization of Multiplexed Quantitative Analyses Using High-Field Asymmetric-Waveform Ion Mobility Mass Spectrometry. *Anal. Chem.* **2019**, *91* (6), 4010–4016. https://doi.org/10.1021/acs.analchem.8b05399.

(80) Christofi, E.; Barran, P. Ion Mobility Mass Spectrometry (IM-MS) for Structural Biology: Insights Gained by Measuring Mass, Charge, and Collision Cross Section. *Chem. Rev.* **2023**, *123* (6), 2902–2949. https://doi.org/10.1021/acs.chemrev.2c00600.

(81) Deslignière, E.; Ehkirch, A.; Botzanowski, T.; Beck, A.; Hernandez-Alba, O.; Cianférani, S. Toward Automation of Collision-Induced Unfolding Experiments through Online Size Exclusion Chromatography Coupled to Native Mass Spectrometry. *Anal. Chem.* **2020**, *92* (19), 12900–12908. https://doi.org/10.1021/acs.analchem.0c01426.

(82) Rabuck, J. N.; Hyung, S.-J.; Ko, K. S.; Fox, C. C.; Soellner, M. B.; Ruotolo, B. T. Activation State-Selective Kinase Inhibitor Assay Based on Ion Mobility-Mass Spectrometry. *Anal. Chem.* **2013**, *85* (15), 6995–7002. https://doi.org/10.1021/ac4012655.

(83) Rabuck-Gibbons, J. N.; Keating, J. E.; Ruotolo, B. T. Collision Induced Unfolding and Dissociation Differentiates ATP-Competitive from Allosteric Protein Tyrosine Kinase Inhibitors. *International Journal of Mass Spectrometry* **2018**, *427*, 151–156. https://doi.org/10.1016/j.ijms.2017.12.002.

(84) Fantin, S. M.; Huang, H.; Sanders, C. R.; Ruotolo, B. T. Collision-Induced Unfolding Differentiates Functional Variants of the KCNQ1 Voltage Sensor Domain. *J. Am. Soc. Mass Spectrom.* **2020**, *31* (11), 2348–2355. https://doi.org/10.1021/jasms.0c00288.

(85) Liu, Y.; Cong, X.; Liu, W.; Laganowsky, A. Characterization of Membrane Protein–Lipid Interactions by Mass Spectrometry Ion Mobility Mass Spectrometry. *J. Am. Soc. Mass Spectrom.* **2017**, *28* (4), 579–586. https://doi.org/10.1007/s13361-016-1555-1.

(86) Dixit, S. M.; Polasky, D. A.; Ruotolo, B. T. Collision Induced Unfolding of Isolated Proteins in the Gas Phase: Past, Present, and Future. *Current Opinion in Chemical Biology* **2018**, *42*, 93–100. https://doi.org/10.1016/j.cbpa.2017.11.010.

(87) Nash, S.; Vachet, R. W. Gas-Phase Unfolding of Protein Complexes Distinguishes Conformational Isomers. *J. Am. Chem. Soc.* **2022**, *144* (48), 22128–22139. https://doi.org/10.1021/jacs.2c09573.

(88) Vallejo, D. D.; Rojas Ramírez, C.; Parson, K. F.; Han, Y.; Gadkari, V. V.; Ruotolo, B. T. Mass Spectrometry Methods for Measuring Protein Stability. *Chem Rev* **2022**, *122* (8), 7690–7719. https://doi.org/10.1021/acs.chemrev.1c00857.

(89) Polasky, D. A.; Dixit, S. M.; Fantin, S. M.; Ruotolo, B. T. CIUSuite 2: Next-Generation Software for the Analysis of Gas-Phase Protein Unfolding Data. *Anal. Chem.* **2019**, *91* (4), 3147–3155. https://doi.org/10.1021/acs.analchem.8b05762.

(90) Polasky, D. A.; Dixit, S. M.; Vallejo, D. D.; Kulju, K. D.; Ruotolo, B. T. An Algorithm for Building Multi-State Classifiers Based on Collision-Induced Unfolding Data. *Anal. Chem.* **2019**, *91* (16), 10407–10412.

(91) Lieblein, T.; Zangl, R.; Martin, J.; Hoffmann, J.; Hutchison, M. J.; Stark, T.; Stirnal, E.; Schrader, T.; Schwalbe, H.; Morgner, N. Structural Rearrangement of Amyloid-β upon Inhibitor Binding Suppresses Formation of Alzheimer's Disease Related Oligomers. *eLife* **2020**, *9*, e59306. https://doi.org/10.7554/eLife.59306.

(92) Bhoite, S. S.; Han, Y.; Ruotolo, B. T.; Chapman, M. R. Mechanistic Insights into Accelerated α-Synuclein Aggregation Mediated by Human Microbiome-Associated

Functional Amyloids. *Journal of Biological Chemistry* **2022**, *298* (7). https://doi.org/10.1016/j.jbc.2022.102088.

(93) Niu, S.; Ruotolo, B. T. Collisional Unfolding of Multiprotein Complexes Reveals Cooperative Stabilization upon Ligand Binding. *Protein Science* **2015**, *24* (8), 1272–1281. https://doi.org/10.1002/pro.2699.

(94) Eschweiler, J. D.; Martini, R. M.; Ruotolo, B. T. Chemical Probes and Engineered Constructs Reveal a Detailed Unfolding Mechanism for a Solvent-Free Multidomain Protein. *J. Am. Chem. Soc.* **2017**, *139* (1), 534–540. https://doi.org/10.1021/jacs.6b11678.

(95) Gadkari, V. V.; Ramírez, C. R.; Vallejo, D. D.; Kurulugama, R. T.; Fjeldsted, J. C.; Ruotolo, B. T. Enhanced Collision Induced Unfolding and Electron Capture Dissociation of Native-like Protein Ions. *Anal. Chem.* **2020**, *92* (23), 15489–15496. https://doi.org/10.1021/acs.analchem.0c03372.

(96) Edman, P. A Method for the Determination of Amino Acid Sequence in Peptides. *Arch Biochem* **1949**, *22* (3), 475.

(97) Wilm, M.; Shevchenko, A.; Houthaeve, T.; Breit, S.; Schweigerer, L.; Fotsis, T.; Mann, M. Femtomole Sequencing of Proteins from Polyacrylamide Gels by Nano-Electrospray Mass Spectrometry. *Nature* **1996**, *379* (6564), 466–469. https://doi.org/10.1038/379466a0.

(98) Miller, R. M.; Smith, L. M. Overview and Considerations in Bottom-up Proteomics. *Analyst* **2023**, *148* (3), 475–486. https://doi.org/10.1039/D2AN01246D.

(99) Sidoli, S.; Schwämmle, V.; Ruminowicz, C.; Hansen, T. A.; Wu, X.; Helin, K.; Jensen, O. N. Middle-down Hybrid Chromatography/Tandem Mass Spectrometry Workflow for Characterization of Combinatorial Post-Translational Modifications in Histones. *PROTEOMICS* **2014**, *14* (19), 2200–2211. https://doi.org/10.1002/pmic.201400084.

(100) Fornelli, L.; Srzentić, K.; Huguet, R.; Mullen, C.; Sharma, S.; Zabrouskov, V.; Fellers, R. T.; Durbin, K. R.; Compton, P. D.; Kelleher, N. L. Accurate Sequence Analysis of a Monoclonal Antibody by Top-Down and Middle-Down Orbitrap Mass Spectrometry Applying Multiple Ion Activation Techniques. *Anal. Chem.* **2018**, *90* (14), 8421–8429. https://doi.org/10.1021/acs.analchem.8b00984.

(101) Zhou, H.; Ning, Z.; E. Starr, A.; Abu-Farha, M.; Figeys, D. Advancements in Top-Down Proteomics. *Anal. Chem.* **2012**, *84* (2), 720–734. https://doi.org/10.1021/ac202882y.

(102) Garcia, B. A. What Does the Future Hold for Top Down Mass Spectrometry? *J Am Soc Mass Spectrom* **2010**, *21* (2), 193–202. https://doi.org/10.1016/j.jasms.2009.10.014.

(103) Cui, W.; W. Rohrs, H.; L. Gross, M. Top-down Mass Spectrometry : Recent Developments, Applications and Perspectives. *Analyst* **2011**, *136* (19), 3854–3864. https://doi.org/10.1039/C1AN15286F.

(104) Liu, R.; Xia, S.; Li, H. Native Top-down Mass Spectrometry for Higher-Order Structural Characterization of Proteins and Complexes. *Mass Spectrometry Reviews n/a* (n/a), e21793. https://doi.org/10.1002/mas.21793.

(105) Ro, S. Y.; Schachner, L. F.; Koo, C. W.; Purohit, R.; Remis, J. P.; Kenney, G. E.; Liauw, B. W.; Thomas, P. M.; Patrie, S. M.; Kelleher, N. L.; Rosenzweig, A. C. Native Top-down Mass Spectrometry Provides Insights into the Copper Centers of Membrane-Bound Methane Monooxygenase. *Nat Commun* **2019**, *10*, 2675. https://doi.org/10.1038/s41467-019-10590-6.

(106) Lodge, J. M.; Schauer, K. L.; Brademan, D. R.; Riley, N. M.; Shishkova, E.; Westphall, M. S.; Coon, J. J. Top-Down Characterization of an Intact Monoclonal Antibody Using

Activated Ion Electron Transfer Dissociation. *Anal. Chem.* **2020**, *92* (15), 10246–10251. https://doi.org/10.1021/acs.analchem.0c00705.

(107) Larson, E. J.; Roberts, D. S.; Melby, J. A.; Buck, K. M.; Zhu, Y.; Zhou, S.; Han, L.; Zhang, Q.; Ge, Y. High-Throughput Multi-Attribute Analysis of Antibody-Drug Conjugates Enabled by Trapped Ion Mobility Spectrometry and Top-Down Mass Spectrometry. *Anal. Chem.* **2021**, *93* (29), 10013–10021. https://doi.org/10.1021/acs.analchem.1c00150.

(108) Greer, S. M.; Brodbelt, J. S. Top-Down Characterization of Heavily Modified Histones Using 193 Nm Ultraviolet Photodissociation Mass Spectrometry. *J. Proteome Res.* **2018**, *17* (3), 1138–1145. https://doi.org/10.1021/acs.jproteome.7b00801.

(109) Siuti, N.; Kelleher, N. L. Decoding Protein Modifications Using Top-down Mass Spectrometry. *Nat Methods* **2007**, *4* (10), 817–821. https://doi.org/10.1038/nmeth1097.

(110) Donnelly, D. P.; Rawlins, C. M.; DeHart, C. J.; Fornelli, L.; Schachner, L. F.; Lin, Z.; Lippens, J. L.; Aluri, K. C.; Sarin, R.; Chen, B.; Lantz, C.; Jung, W.; Johnson, K. R.; Koller, A.; Wolff, J. J.; Campuzano, I. D. G.; Auclair, J. R.; Ivanov, A. R.; Whitelegge, J. P.; Paša-Tolić, L.; Chamot-Rooke, J.; Danis, P. O.; Smith, L. M.; Tsybin, Y. O.; Loo, J. A.; Ge, Y.; Kelleher, N. L.; Agar, J. N. Best Practices and Benchmarks for Intact Protein Analysis for Top-down Mass Spectrometry. *Nat Methods* **2019**, *16* (7), 587–594. https://doi.org/10.1038/s41592-019-0457-0.

(111) Cai, W.; Tucholski, T. M.; Gregorich, Z. R.; Ge, Y. Top-down Proteomics: Technology Advancements and Applications to Heart Diseases. *Expert Rev Proteomics* **2016**, *13* (8), 717–730. https://doi.org/10.1080/14789450.2016.1209414.

(112) Chen, B.; Peng, Y.; Valeja, S. G.; Xiu, L.; Alpert, A. J.; Ge, Y. Online Hydrophobic Interaction Chromatography–Mass Spectrometry for Top-Down Proteomics. *Anal. Chem.* **2016**, *88* (3), 1885–1891. https://doi.org/10.1021/acs.analchem.5b04285.

(113) Cai, W.; Tucholski, T.; Chen, B.; Alpert, A. J.; McIlwain, S.; Kohmoto, T.; Jin, S.; Ge, Y. Top-Down Proteomics of Large Proteins up to 223 KDa Enabled by Serial Size Exclusion Chromatography Strategy. *Anal. Chem.* **2017**, *89* (10), 5467–5475. https://doi.org/10.1021/acs.analchem.7b00380.

(114) Shen, X.; Kou, Q.; Guo, R.; Yang, Z.; Chen, D.; Liu, X.; Hong, H.; Sun, L. Native Proteomics in Discovery Mode Using Size-Exclusion Chromatography–Capillary Zone Electrophoresis–Tandem Mass Spectrometry. *Anal. Chem.* **2018**, *90* (17), 10095–10099. https://doi.org/10.1021/acs.analchem.8b02725.

(115) Jooß, K.; McGee, J. P.; Melani, R. D.; Kelleher, N. L. Standard Procedures for Native CZE-MS of Proteins and Protein Complexes up to 800 KDa. *Electrophoresis* **2021**, *42* (9–10), 1050–1059. https://doi.org/10.1002/elps.202000317.

(116) Mitchell Wells, J.; McLuckey, S. A. Collision-Induced Dissociation (CID) of Peptides and Proteins. In *Methods in Enzymology*; Biological Mass Spectrometry; Academic Press, 2005; Vol. 402, pp 148–185. https://doi.org/10.1016/S0076-6879(05)02005-7.

(117) McAlister, G. C.; Phanstiel, D. H.; Brumbaugh, J.; Westphall, M. S.; Coon, J. J. Higher-Energy Collision-Activated Dissociation Without a Dedicated Collision Cell. *Mol Cell Proteomics* **2011**, *10* (5), O111.009456. https://doi.org/10.1074/mcp.O111.009456.

(118) Beckman, J. S.; Voinov, V. G.; Hare, M.; Sturgeon, D.; Vasil'ev, Y.; Oppenheimer, D.; Shaw, J. B.; Wu, S.; Glaskin, R.; Klein, C.; Schwarzer, C.; Stafford, G. Improved Protein and PTM Characterization with a Practical Electron-Based Fragmentation on Q-TOF

Instruments. *J Am Soc Mass Spectrom* **2021**, *32* (8), 2081–2091. https://doi.org/10.1021/jasms.0c00482.

(119) Lermyte, F.; Valkenborg, D.; Loo, J. A.; Sobott, F. Radical Solutions: Principles and Application of Electron-Based Dissociation in Mass Spectrometry-Based Analysis of Protein Structure. *Mass Spectrometry Reviews* **2018**, *37* (6), 750–771. https://doi.org/10.1002/mas.21560

(120) Syka, J. E. P.; Coon, J. J.; Schroeder, M. J.; Shabanowitz, J.; Hunt, D. F. Peptide and Protein Sequence Analysis by Electron Transfer Dissociation Mass Spectrometry. *Proceedings of the National Academy of Sciences* **2004**, *101* (26), 9528–9533. https://doi.org/10.1073/pnas.0402700101.

(121) Doll, S.; Burlingame, A. L. Mass Spectrometry-Based Detection and Assignment of Protein Posttranslational Modifications. *ACS Chem. Biol.* **2015**, *10* (1), 63–71. https://doi.org/10.1021/cb500904b.

(122) Little, D. P.; Speir, J. Paul.; Senko, M. W.; O'Connor, P. B.; McLafferty, F. W. Infrared Multiphoton Dissociation of Large Multiply Charged Ions for Biomolecule Sequencing. *Anal. Chem.* **1994**, *66* (18), 2809–2815. https://doi.org/10.1021/ac00090a004.

(123) Shaw, J. B.; Li, W.; Holden, D. D.; Zhang, Y.; Griep-Raming, J.; Fellers, R. T.; Early, B. P.; Thomas, P. M.; Kelleher, N. L.; Brodbelt, J. S. Complete Protein Characterization Using Top-Down Mass Spectrometry and Ultraviolet Photodissociation. *J. Am. Chem. Soc.* **2013**, *135* (34), 12646–12651. https://doi.org/10.1021/ja4029654.

(124) Riley, N. M.; Westphall, M. S.; Coon, J. J. Activated Ion-Electron Transfer Dissociation Enables Comprehensive Top-Down Protein Fragmentation. *J. Proteome Res.* **2017**, *16* (7), 2653–2659. https://doi.org/10.1021/acs.jproteome.7b00249.

(125) Brunner, A. M.; Lössl, P.; Liu, F.; Huguet, R.; Mullen, C.; Yamashita, M.; Zabrouskov, V.; Makarov, A.; Altelaar, A. F. M.; Heck, A. J. R. Benchmarking Multiple Fragmentation Methods on an Orbitrap Fusion for Top-down Phospho-Proteoform Characterization. *Anal Chem* **2015**, *87* (8), 4152–4158. https://doi.org/10.1021/acs.analchem.5b00162.

(126) Polasky, D. A.; Lermyte, F.; Nshanian, M.; Sobott, F.; Andrews, P. C.; Loo, J. A.; Ruotolo, B. T. Fixed-Charge Trimethyl Pyrilium Modification for Enabling Enhanced Top-down Mass Spectrometry Sequencing of Intact Protein Complexes. *Anal. Chem.* **2018**, *90* (4), 2756–2764.

(127) Rojas Ramírez, C.; Murtada, R.; Gao, J.; Ruotolo, B. T. Free Radical-Based Sequencing for Native Top-Down Mass Spectrometry. *J. Am. Soc. Mass Spectrom.* **2022**, *33* (12), 2283–2290. https://doi.org/10.1021/jasms.2c00252.

(128) Tamara, S.; den Boer, M. A.; Heck, A. J. R. High-Resolution Native Mass Spectrometry. *Chem. Rev.* **2022**, *122* (8), 7269–7326. https://doi.org/10.1021/acs.chemrev.1c00212.

(129) Choy, B. C.; Cater, R. J.; Mancia, F.; Pryor, E. E. A 10-Year Meta-Analysis of Membrane Protein Structural Biology: Detergents, Membrane Mimetics, and Structure Determination Techniques. *Biochimica et Biophysica Acta (BBA) - Biomembranes* **2021**, *1863* (3), 183533. https://doi.org/10.1016/j.bbamem.2020.183533.

(130) Overington, J. P.; Al-Lazikani, B.; Hopkins, A. L. How Many Drug Targets Are There? *Nat Rev Drug Discov* **2006**, *5* (12), 993–996. https://doi.org/10.1038/nrd2199.

(131) Marty, M. T.; Hoi, K. K.; Robinson, C. V. Interfacing Membrane Mimetics with Mass Spectrometry. *Acc. Chem. Res.* **2016**, *49* (11), 2459–2467. https://doi.org/10.1021/acs.accounts.6b00379.

(132) Reading, E.; Liko, I.; Allison, T. M.; Benesch, J. L. P.; Laganowsky, A.; Robinson, C. V. The Role of the Detergent Micelle in Preserving the Structure of Membrane Proteins in the Gas Phase. *Angewandte Chemie International Edition* **2015**, *54* (15), 4577–4581. https://doi.org/10.1002/anie.201411622.

(133) Laganowsky, A.; Reading, E.; Hopper, J. T. S.; Robinson, C. V. Mass Spectrometry of Intact Membrane Protein Complexes. *Nat Protoc* **2013**, *8* (4), 639–651. https://doi.org/10.1038/nprot.2013.024.

(134) Frey, L.; Lakomek, N.-A.; Riek, R.; Bibow, S. Micelles, Bicelles, and Nanodiscs: Comparing the Impact of Membrane Mimetics on Membrane Protein Backbone Dynamics. *Angewandte Chemie International Edition* **2017**, *56* (1), 380–383. https://doi.org/10.1002/anie.201608246.

(135) Hutchison, J. M.; Shih, K.-C.; Scheidt, H. A.; Fantin, S. M.; Parson, K. F.; Pantelopulos, G. A.; Harrington, H. R.; Mittendorf, K. F.; Qian, S.; Stein, R. A.; Collier, S. E.; Chambers, M. G.; Katsaras, J.; Voehler, M. W.; Ruotolo, B. T.; Huster, D.; McFeeters, R. L.; Straub, J. E.; Nieh, M.-P.; Sanders, C. R. Bicelles Rich in Both Sphingolipids and Cholesterol and Their Use in Studies of Membrane Proteins. *J. Am. Chem. Soc.* **2020**, *142* (29), 12715–12729. https://doi.org/10.1021/jacs.0c04669.

(136) Sligar, S. G.; Denisov, I. G. Nanodiscs: A Toolkit for Membrane Protein Science. *Protein Science* **2021**, *30* (2), 297–315. https://doi.org/10.1002/pro.3994.

(137) Keener, J. E.; Jayasekera, H. S.; Marty, M. T. Investigating the Lipid Selectivity of Membrane Proteins in Heterogeneous Nanodiscs. *Anal. Chem.* **2022**.

(138) Postis, V.; Rawson, S.; Mitchell, J. K.; Lee, S. C.; Parslow, R. A.; Dafforn, T. R.; Baldwin, S. A.; Muench, S. P. The Use of SMALPs as a Novel Membrane Protein Scaffold for Structure Study by Negative Stain Electron Microscopy. *Biochimica et Biophysica Acta (BBA) - Biomembranes* **2015**, *1848* (2), 496–501. https://doi.org/10.1016/j.bbamem.2014.10.018.

(139) Calabrese, A. N.; Watkinson, T. G.; Henderson, P. J. F.; Radford, S. E.; Ashcroft, A. E. Amphipols Outperform Dodecylmaltoside Micelles in Stabilizing Membrane Protein Structure in the Gas Phase. *Anal. Chem.* **2015**, *87* (2), 1118–1126. https://doi.org/10.1021/ac5037022.

(140) Chorev, D. S.; Tang, H.; Rouse, S. L.; Bolla, J. R.; von Kügelgen, A.; Baker, L. A.; Wu, D.; Gault, J.; Grünewald, K.; Bharat, T. A. M.; Matthews, S. J.; Robinson, C. V. The Use of Sonicated Lipid Vesicles for Mass Spectrometry of Membrane Protein Complexes. *Nat Protoc* **2020**, *15* (5), 1690–1706. https://doi.org/10.1038/s41596-020-0303-y.

(141) Frick, M.; Schwieger, C.; Schmidt, C. Liposomes as Carriers of Membrane-Associated Proteins and Peptides for Mass Spectrometric Analysis. *Angewandte Chemie International Edition* **2021**, *60* (20), 11523–11530. https://doi.org/10.1002/anie.202101242.

(142) Brown, K. A.; Chen, B.; Guardado-Alvarez, T. M.; Lin, Z.; Hwang, L.; Ayaz-Guner, S.; Jin, S.; Ge, Y. A Photocleavable Surfactant for Top-down Proteomics. *Nat Methods* **2019**, *16* (5), 417–420. https://doi.org/10.1038/s41592-019-0391-1.

(143) Brown, K. A.; Tucholski, T.; Eken, C.; Knott, S.; Zhu, Y.; Jin, S.; Ge, Y. High-Throughput Proteomics Enabled by a Photocleavable Surfactant. *Angewandte Chemie* **2020**, *132* (22), 8484–8488. https://doi.org/10.1002/ange.201915374.

(144) Keener, J. E.; Zambrano, D. E.; Zhang, G.; Zak, C. K.; Reid, D. J.; Deodhar, B. S.; Pemberton, J. E.; Prell, J. S.; Marty, M. T. Chemical Additives Enable Native Mass Spectrometry Measurement of Membrane Protein Oligomeric State within Intact

Nanodiscs. *J. Am. Chem. Soc.* **2019**, *141* (2), 1054–1061. https://doi.org/10.1021/jacs.8b11529.

(145) Fantin, S. M.; Parson, K. F.; Niu, S.; Liu, J.; Polasky, D. A.; Dixit, S. M.; Ferguson-Miller, S. M.; Ruotolo, B. T. Collision Induced Unfolding Classifies Ligands Bound to the Integral Membrane Translocator Protein. *Anal. Chem.* **2019**, *91* (24), 15469–15476. https://doi.org/10.1021/acs.analchem.9b03208.

(146) Konijnenberg, A.; Bannwarth, L.; Yilmaz, D.; Koçer, A.; Venien-Bryan, C.; Sobott, F. Top-down Mass Spectrometry of Intact Membrane Protein Complexes Reveals Oligomeric State and Sequence Information in a Single Experiment. *Protein Science* **2015**, *24* (8), 1292–1300. https://doi.org/10.1002/pro.2703.

(147) Ecker, D. M.; Jones, S. D.; Levine, H. L. The Therapeutic Monoclonal Antibody Market. *mAbs* **2015**, *7* (1), 9–14. https://doi.org/10.4161/19420862.2015.989042.

(148) Irani, V.; Guy, A. J.; Andrew, D.; Beeson, J. G.; Ramsland, P. A.; Richards, J. S. Molecular Properties of Human IgG Subclasses and Their Implications for Designing Therapeutic Monoclonal Antibodies against Infectious Diseases. *Molecular Immunology* **2015**, *67* (2, Part A), 171–182. https://doi.org/10.1016/j.molimm.2015.03.255.

(149) Liu, H.; May, K. Disulfide Bond Structures of IgG Molecules. *mAbs* **2012**, *4* (1), 17–23. https://doi.org/10.4161/mabs.4.1.18347.

(150) Liu, H. F.; Ma, J.; Winter, C.; Bayer, R. Recovery and Purification Process Development for Monoclonal Antibody Production. *mAbs* **2010**, *2* (5), 480–499. https://doi.org/10.4161/mabs.2.5.12645.

(151) Wang, Y.; Li, X.; Liu, Y.-H.; Richardson, D.; Li, H.; Shameem, M.; Yang, X. Simultaneous Monitoring of Oxidation, Deamidation, Isomerization, and Glycosylation of Monoclonal Antibodies by Liquid Chromatography-Mass Spectrometry Method with Ultrafast Tryptic Digestion. *mAbs* **2016**, *8* (8), 1477–1486. https://doi.org/10.1080/19420862.2016.1226715.

(152) Kerr, R. A.; Keire, D. A.; Ye, H. The Impact of Standard Accelerated Stability Conditions on Antibody Higher Order Structure as Assessed by Mass Spectrometry. *mAbs* **2019**, *11* (5), 930–941. https://doi.org/10.1080/19420862.2019.1599632.

(153) Tian, Y.; Han, L.; Buckner, A. C.; Ruotolo, B. T. Collision Induced Unfolding of Intact Antibodies: Rapid Characterization of Disulfide Bonding Patterns, Glycosylation, and Structures. *Anal. Chem.* **2015**, *87* (22), 11509–11515. https://doi.org/10.1021/acs.analchem.5b03291.

(154) Niazi, S. K. The Coming of Age of Biosimilars: A Personal Perspective. *Biologics* **2022**, *2* (2), 107–127. https://doi.org/10.3390/biologics2020009.

(155) Vallejo, D. D.; Kang, J.; Coghlan, J.; Ramírez, C. R.; Polasky, D. A.; Kurulugama, R. T.; Fjeldsted, J. C.; Schwendeman, A. A.; Ruotolo, B. T. Collision-Induced Unfolding Reveals Stability Differences in Infliximab Therapeutics under Native and Heat Stress Conditions. *Anal. Chem.* **2021**, *93* (48), 16166–16174. https://doi.org/10.1021/acs.analchem.1c03946.

Chapter 2 Infrared Photoactivation Enables Improved Native Top-Down Mass Spectrometry of Transmembrane Proteins

Brock R. Juliano, Joseph W. Keating, Brandon T. Ruotolo

2.1 Abstract

Membrane proteins are often challenging targets for native top-down mass spectrometry experimentation. The requisite use of membrane mimetics to solubilize such proteins necessitates the application of supplementary activation methods to liberate protein ions prior to sequencing, which typically limits the sequence coverage achieved. Recently, infrared photoactivation has an emerged as an alternative to collisional activation for the liberation of membrane proteins from surfactant micelles. However, much remains unknown regarding the mechanism by which IR activation liberates membrane proteins ions from such micelles, the extent to which such methods can improve membrane protein sequence coverage, and degree to which such approaches can be extended to support native proteomics. Here, we describe experiments designed to evaluate and probe infrared photoactivation for membrane protein sequencing, proteoform identification and native proteomics applications. Our data reveal that infrared photoactivation can dissociate micelles comprised of a variety of detergent classes, without the need for a strong IR chromophore by leveraging the relatively weak association energies of such detergent clusters in the gas-phase. Additionally, our data illustrates how IR photoactivation can be extended to include membrane mimetics beyond micelles, and liberate proteins from nanodiscs, liposomes and bicelles. Finally, our data quantifies the improvements in membrane

protein sequence coverage produced through the use of IR photoactivation, which typically leads to membrane protein sequence coverage values ranging from 40-60%.

2.2 Introduction

Membrane proteins (MP) are critical mediators of a variety of cellular processes. Their physiological importance is highlighted by the fact that MPs account for over 60% of current pharmaceutical drug targets[1,2]. Despite their clear importance, MPs remain under characterized, with membrane proteins currently constituting only 3% of the structures in the Protein Data Bank[3]. This is due in part to the inherent challenges associated with purifying, separating, and biophysically analyzing MPs. For instance, most structural biology workflows require significant modifications to accommodate amphipathic MPs. Often this is achieved by inserting MPs into a membrane mimetic, such as micelles, bicelles, amphipols and nanodiscs, that act to solubilize the MP[4–11]. Beyond these initial challenges, MPs can also be difficult to express and purify and can be particularly unstable[3]. Novel methodologies are needed to improve our ability to provide a more complete understanding of MP structure and function.

Native mass spectrometry (nMS) has emerged as a useful technique for the study of MPs[12,13]. In a nMS experiment, MPs are ionized directly within a mimetic and are then liberated by activation methods applied within the mass spectrometer[4,14,15]. This approach has been utilized in the past to reveal information regarding the oligomeric states[16–18], complex organization[19,20], lipid [17,21–23] and ligand[24,25] binding interactions for a variety of membrane proteins.

Top-down mass spectrometry (TDMS) has been employed to evaluate the protein composition within complex samples of biological origins for several decades[26–29]. TDMS has advantages over commonly deployed bottom-up approaches in that TDMS is able to capture the proteoform populations present within system of interest. It is estimated that there are about one million proteoforms in the human proteome[30], with many proteoforms of high clinical relevance[31], making it an important analytical challenge to comprehensively identify all of the proteoforms present within a sample.

TDMS experiments are typically performed under conditions designed to denature protein analytes in order to maximize the sequence information obtained[32]. Such conditions also make the collection of information pertaining to protein-protein complexes and 3D structure challenging. As such, native TMDS (nTDMS) experiments have been developed that preserve native protein structures prior to fragmentation[33–37]. Such nTDMS experiments have been conducted with a variety of fragmentation methods such as collision induced dissociation (CID/HCD)[37,38], electron based methods, such as electron capture dissociation (ECD)[35,39] and electron transfer dissociation (ETD)[33,40,41], and ultraviolet photodissociation (UVPD)[34,42,43]. Often these experiments are combined with separation tools such as ion mobility[37,44,45], capillary electrophoresis[46–48] and liquid chromatography[49–53]. However, for nTDMS of MPs, such studies have often resulted in modest sequence coverages, with values of less than 25% being typical[36,54]. Recently, alternative ion activation methods, such as UVPD, have been shown to substantially improve the nTDMS sequence coverage of MPs[55].

Often, nMS experiments targeting MPs use collisional activation to liberate the MP ions from associated membrane mimetics[4,56]. In a MP nTDMS experiment, this activation step often coincides with collision induced dissociation (CID). This presents a challenge in nTDMS data analysis, as the chemical noise resulting from dissociated mimetic molecules can make the resultant spectra difficult to deconvolute and interpret, limiting the amount of sequence coverage that can be confidently assigned. Recent work has shown that the use of a photocleavable surfactant can be one way of addressing this challenge[57,58]. Alternatively, infrared (IR) photoactivation can be utilized to liberate membrane proteins from detergent micelles, with prior reports focusing primarily on the acquisition of nMS data[59,60]. Additional work has demonstrated that IR photoactivation can be deployed to decluster protein complexes in order to better resolve these analytes[61,62]. In addition, prior work focusing on TDMS of soluble proteins has demonstrated the benefits of IR photoactivation to improve the sequence coverages obtained via electron transfer dissociation (ETD)[40,53,63]. Furthermore, IR photoactivation can be used to induce infrared multiphoton dissociation (IRMPD), in which the peptide bond of protein is fragmented into N- and C- terminal fragments similar to those produced by CID[64,65].

In this manuscript, we demonstrate for the first time that IR photoactivation can be used to liberate membrane proteins from detergent micelles prior to fragmentation by HCD to yield improved sequence coverage. We evaluate our methods using two model MPs. Peripheral Myelin Protein 22 (PMP22) and Guanidinium transporter (GDX) were used as transmembrane protein model systems for this research. PMP22 is a tetraspan transmembrane protein that is involved in the myelination of Schwann cells[66]. PMP22 is also known to have multiple pathogenic proteoforms in humans that play roles in the etiology of hereditary neuropathies[18,67]. GDX is a small multidrug resistant transmembrane protein that is functionally active as a dimer in bacteria that serves to efflux guanidium from bacterial cells[68–70]. Our data indicates that IR photoactivation can selectively break down detergent clusters, while preserving native MP oligomeric states. The IR photoactivation imparted by the laser is deployed to enhance the liberation of proteins from these clusters and mimetics; however, we do not fragment the proteins by IRMPD. By comprehensively recording MS/MS data as a function of IR laser energy, alongside FT-IR spectroscopy data, we reveal that the apparent selectivity of gas-phase IR photoactivation towards detergent micelles results from the relatively weak intermolecular interactions that constitute non-covalent detergent clusters commonly observed in MP nMS data, rather than the presence of IR chromophores within detergent structures. Thus, the enhanced declustering imparted by IR photoactivation serves to improve top-down sequencing by HCD. Furthermore, we extend our IR photoactivation methods to liberate MPs from a variety of common mimetics, including bicelles, nanodiscs, and liposomes. Finally, we evaluate the ability of our IR-based methodology to improve MP sequence coverage values obtained from nTDMS. In the case of PMP22, we observe a 16% increase in sequence coverage across all charge states when IR photoactivation is used rather than HCD to liberate the MP from detergent micelles. In the case of GDX, similar sequence coverage values for monomers were observed across standard and IR-photoactivation methods, but the latter allowed for the observation and sequencing of GDX dimers that were not observed without the use of IR photoactivation. We conclude by discussing future applications of IR-enabled modes of operation in nTDMS workflows.

2.3 Materials and Methods

2.3.1 Materials

PMP22 was purified from *Escherichia coli* using previously publish protocols[62]. Octaethylene glycol monododecyl ether (C12E8), β-n-decyl maltoside (DM) and lauryl maltose neopentyl glycol (LMPG) were purchased from Anatrace (Maumee, OH). Deoxycholic acid (DC) and ammonium acetate were sourced from MilliporeSigma (St. Louis, MO). PMP22 was 50 μM was buffer and detergent exchanged from 50 mM TRIS buffer (pH=8.0), 0.15% DM, 1mM TCEP buffer, 15 mM imidazole, and into 200 mM ammonium acetate (pH=8) and 0.01% C12E8, at two times the critical micelle concentration (CMC), to a final protein concentration of less than 25 μM in 200 mM ammonium acetate (pH=8.0) using 10 kDa Amicon Ultra 0.5 mL ultracentrifugal filter units (MilliporeSigma). GDX was also obtained from overexpression in *E. coli* cells. Prior to nMS experiments, GDX was buffer and detergent exchange simultaneously from 10 mM HEPES (pH=8.0), 100 mM NaCl, 4 mM DM into 200 mM ammonium acetate (pH=8.0) and 0.01% C12E8.

2.3.2 Preparation of lipid/detergent bicelles

PMP22 was purified from *Escherichia coli* using previously publish protocols[67]. Octaethylene glycol monododecyl ether (C12E8), β-n-decyl maltoside (DM) and lauryl maltose neopentyl glycol (LMPG) were purchased from Anatrace (Maumee, OH). Deoxycholic acid (DC) and ammonium acetate were sourced from MilliporeSigma (St. Louis, MO). PMP22 (50 µM) was buffer and detergent exchanged from 50 mM TRIS buffer (pH=8.0), 0.15% DM, 1mM TCEP buffer, 15 mM imidazole, and into 200 mM ammonium acetate (pH=8) and 0.01% C12E8, at two times the critical micelle concentration (CMC), to a final protein concentration of less than 25 µM in 200 mM ammonium acetate (pH=8.0) using 10 kDa Amicon Ultra 0.5 mL ultracentrifugal filter units (MilliporeSigma). GDX was also obtained from overexpression in *E. coli* cells. Prior to nMS experiments, GDX was buffer and detergent exchange simultaneously from 10 mM HEPES (pH=8.0), 100 mM NaCl, 4 mM DM into 200 mM ammonium acetate (pH=8.0) and 0.01% C12E8.

2.3.3 Preparation of Lipid/Detergent Bicelles

β-n-Dodecyl melibioside (DDMB) and 1-Palmitoyl-2-oleoylphosphatidylcholine (POPC) were purchased from Anatrace. POPC was dissolved in a mixture of benzene and ethanol (95:5 v/v). After dissolution, the solvent was evaporated at 45 degrees. The mixture was frozen and lyophilized overnight to remove excess solvent. A 15% (wt) solution of DDMB in water was added to the lyophilized POPC to create the desired POPC-DDMB ratio of 4%. The mixture was vortexed and flash frozen, prior to sonication at ambient temperature. This cycle of agitation was repeated until the mixture became clear. The POPC bicelles were flash frozen and stored at -80 prior to use. POPC in chloroform was dried under house nitrogen, prior to solvent evaporation under vacuum overnight. A buffer containing sodium cholate (MilliporeSigma) was used to dilute the POPC by two-fold. The sample was then vortexed and heated, prior to sonication. Membrane Scaffolding Protein (MSP) (MilliporeSigma) was added in a 1:65 ratio with POPC. Detergent cholate was then removed by SM-2 BioBeads (Bio-Rad, Hercules, CA). 800 mg of BioBeads were added for each milliliter of solution, and the suspension was incubated for 4 hours on a shaker. The nanodiscs were then incubated with protein, and separated with a FPLC ÄKTA system (Cytiva, Marlborough, MA) over a Superdex 200 size exclusion column (Cytiva), in order to separate empty nanodiscs from those containing protein cargo.

2.3.4 Preparation of Liposomes

Liposomes were formed from *E. coli* Polar Lipid mixture (Avanti, Alabaster, AL), containing a mixture of phosphatidylethanolamine (PE), phosphatidylglycerol (PG) and cardiolipin with 200 nanograms of protein for each milliliter of solution that was dialyzed against 200 mM NaCl, 20 mM HEPES (pH=7.5), which constituted the intraliposomal solution. Liposomes with protein were stored at -80° in aliquots prior to MS analyses.

2.3.5 Conditions of nMS Experiments

All mass spectrometry data were collected on an Orbitrap Fusion Lumos (ThermoFisher, San Jose, CA) that was modified with a 10.6 μm 60 W CO_2 laser (Synrad, Mukilteo, WA) that irradiates the linear ion trap. A schematic of the Lumos can be viewed in Figure III-1. Samples were infused via direct infusion using the NanoSpray Flex ion source (ThermoFisher) operated in positive mode. For membrane protein and detergent data, 1 kV of in-source activation was applied, and the temperature of the transfer tube was increased to 325 degrees to assist in liberation from the mimetics. 1.8 kV of capillary voltage was applied to the nESI emitter which was made of borosilicate glass coated in gold and prepared in house using a P-97 pipette puller (Sutter Instruments, Novato, CA). IR photoactivation was titrated into the ion trap in 200 ms pulses to liberate the proteins from the mimetics. Laser power was modulated directly through a digital controller. Data were collected with a resolution of 120000 at 200 Th. This instrument was operated with an extended mass range greater than 2000 Th with the source RF operated with a 30% amplitude. Protein ions were also collisionally activated in the ion routing multipole by higher-energy collisional dissociation (HCD) with collision energies between 10-30%.

2.3.6 Infrared Spectroscopy

FT-IR data were collected on a Nicolet iS50 FTIR Spectrometer (ThermoFisher) using the attenuated total reflectance accessory. Spectra were collected with detergents at 2x CMC. FTIR data were collected, visualized, and exported as csv files using Omnic (ThermoFisher).

2.3.7 Data Analysis

Raw mass spectra were viewed and analyzed using FreeStyle (ThermoFisher) and UniDec[66]. Fragmentation data were analyzed using a variety of software packages, including BioPharma Finder (ThermoFisher) and ProSight Lite[67]. Mass cutoffs of 20 ppm were used to identify peptide fragments. OriginPro (OriginLab, Northampton, MA) was also used to visualize data and to perform statistical analyses.

2.4 Results and Discussions

2.4.1 Infrared Photoactivation of Micelles

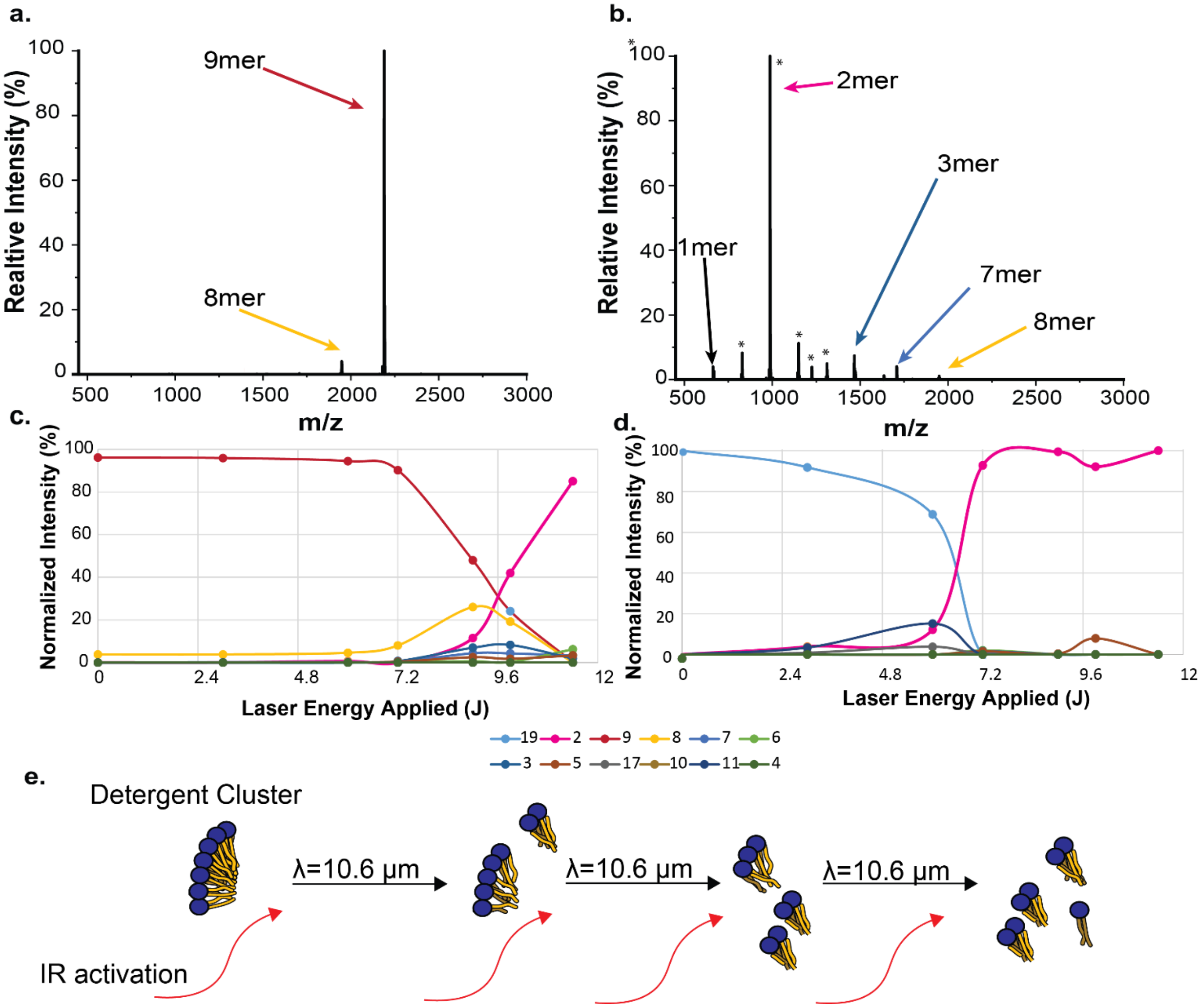

Figure 2-1 The mass spectrum from quadrupole selected DM 9mer after 0 J (a) and 9 J (b) of energy had been applied to the cluster. The peaks labeled with asterisks in panel b are annotated in more detail in Figure S5a. The normalized intensities of quadrupole selected DM 9mer (c) and 19mer (d) and their products as infrared photoactivation was applied. The clusters are color coded according to the legend shown. A schematic (e) of the proposed mechanism by which IR photoactivation dissociates detergent clusters into charged dimers.

FT-IR spectra were collected in order to evaluate the detergent clusters produced from samples containing DC, DM and LMPG to evaluate their response to IR photoactivation in the absence of MPs. The detergents were selected for the different functional groups they possess. The FT-IR data in Figure III-2 shows maximal absorbance around 1085 cm^{1} for all three of the detergents, resulting from the C-O stretches in their ether linkages. It is important to note, however, that the IR laser used in our gas-phase MP photoactivation experiments operates at 950 cm^{-1}. Of the molecules screened in this report, only LMPG exhibits strong absorbance at 950 cm^{-1} due to the P-O stretches present in its phosphate group. Despite this, when clusters of DM, DC and LMPG of various sizes were activated in the gas-phase with IR light, all of three exhibited facile dissociation, producing a range of smaller cluster ions, as shown in Figure III-3. This suggests that detergent molecules do not require a particular chromophore that absorbs strongly at 950 cm^{-1} to undergo activation sufficient to produce cluster fragmentation. When comparing the amount of energy required to liberate detergent ions from clusters of various sizes, we observe that larger clusters generally require significantly less energy to undergo dissociation when compared to smaller clusters for all three detergents evaluated in this report, as indicated by the trends shown in Figure III-3. The IR50 metric calculated here is defined as the energy at which half of the detergent cluster has undergone dissociation into smaller clusters or individual detergent ions.

Our data reveal that, as IR laser irradiation is increased, detergent clusters break down into an array of intermediate states prior to ultimately yielding charged detergent dimers. In the case of the DM 9mer, as in Figure 2-1a, initially the 9mer predominates at low IR laser energy, with a small amount of 8mer present, suggesting that monomeric DM may be lost as a neutral. However, at an energy of ~9 J, relatively low intensity signals for intermediate cluster ions such as 6mers and 7mers appear before charged dimers become the most intense signal observed (for more details, see Figures 2-1c, III-4, III-5a). We observe evidence of some charge partitioning during detergent cluster fragmentation, whereby the 2mer, 3mer, 5mer and 6mer fragments adopt +1 charge states when produced from 2+ precursor ions. To account for variability between spectra, we tracked the normalized intensities of the ion clusters reported in these experiments. Similar trends can be found for other DM clusters, such as 19mers (Figure III-5b) and 8mers, as demonstrated in Figures 2-1b,d, and III-6. LMPG and DC clusters dissociate similarly to those comprised of DM, wherein larger clusters proceed through a series of minor fragmentation channels characterized by individual detergent loss events before ultimately yielding charged dimers in large quantities (Figure III-7).

As such, the mechanism for IR based fission of detergent micelles appear to proceed very similarly to the CID based fission of detergent micelles, suggesting a linked mechanism[68]. Specifically, we propose a mechanism for IR-based detergent cluster breakdown as depicted in Figure 1e, wherein detergent clusters are gradually dissociated into intermediate sizes before ultimately yielding a population primarily comprised of dimeric cluster ions. Taken together, our results indicate that detergent clusters are only weakly coupled to the IR radiation used in our experiments, and the dissociation observed is a product of the relatively weak association energies between individual detergent dimers. Thus, the weak absorption exhibited by DM and DC in at 10.6 μm is evidently more than sufficient to dissociate these clusters due to the weakness of the intermolecular attractions holding the detergent clusters together. The evident weakness of these intermolecular interactions explains why a particular chromophore, such as a phosphate group that absorbs 10.6 μm photons strongly, is not needed for the fission of these clusters by IR photoactivation. This observation is consistent with the manner in which IR activation disrupts weak non-covalent interactions in other IR photoactivation based methodologies[61,63]. Altogether, our data suggests that detergent clusters commonly deployed for membrane protein MS, such as DM, are only weakly coupled to the IR radiation used in our experiments, and their dissociation is instead driven by relatively weak intra-molecular association energies between detergent dimer units within the cluster ions observed.

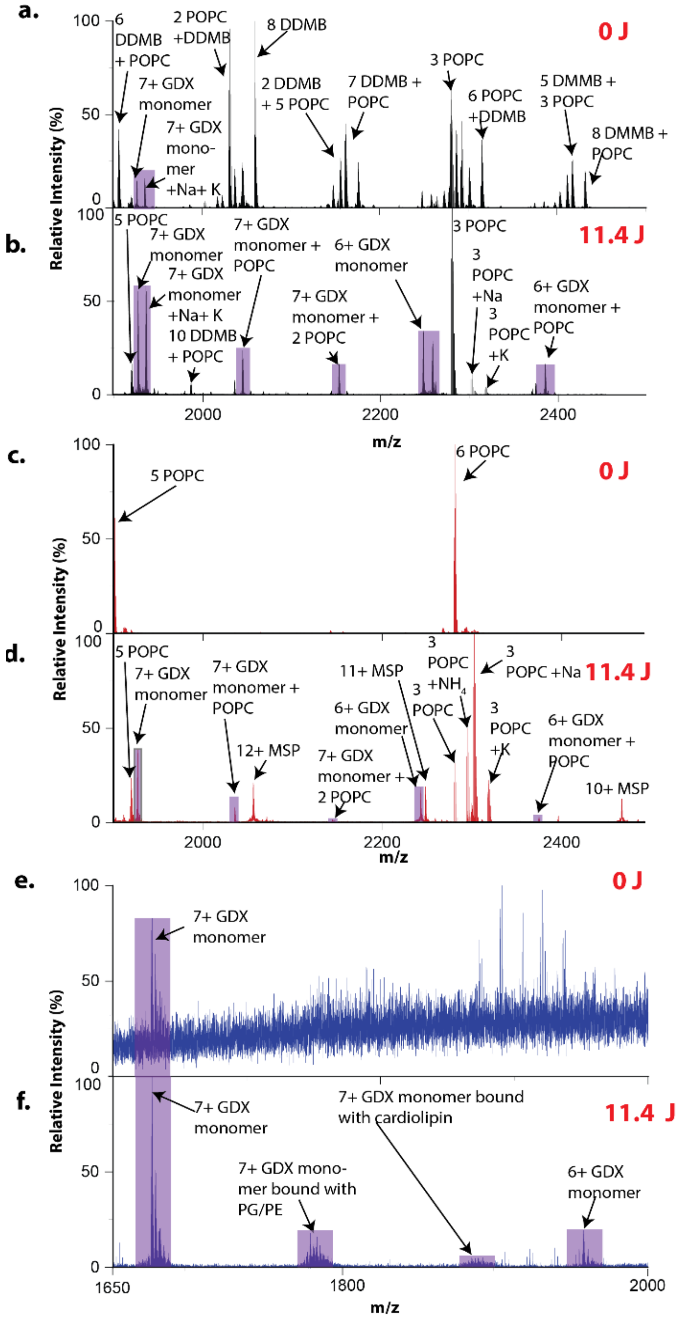

Figure 2-2 GDX inserted into bicelles prior to IR photoactivation (a) and after 11.4 J of IR laser energy was applied (b). GDX inserted into lipid nanodiscs prior to IR photoactivation (c) and after 11.4 J of IR laser energy was applied (d). GDX inserted into liposomes prior to IR photoactivation (e) and after 11.4 J of IR laser energy was applied (f). Panels a and f are annotated in greater detail in Figure III-8.

2.4.2 Infrared Photoactivation of Other Mimetics

We then moved to evaluate the ability of IR photoactivation to liberate MPs from a range of widely used membrane mimetics. For example, nMS data collected from samples containing GDX inserted into lipid bicelles constructed from DDMB and POPC reveals that GDX can indeed be ejected from this mimetic for subsequent mass measurements. Prior to any IR photoactivation, the nMS spectra is predominated by a variety of cluster ions assigned to mixed detergent and lipid populations, with some 7+ monomer barely visible (Figure 2-2a, III-8a). Following 11.4 J of IR photoactivation, we observe the appearance of signals associated with GDX in a manner correlated with the decrease in intensity for signals associated with lipid and detergent signals, with only POPC 3mer ion signal remaining (Figure 2-2b). Importantly, the data also reveal the presence of and 6 and 7+ monomers of GDX bound to POPC, suggesting that IR photoactivation is gentle enough to preserve lipid bound MP species following activation. Similar trends are observed with samples where we inserted GDX into lipid nanodiscs (Figure 2-2c,d). In this instance, the nanodiscs were assembled with membrane scaffolding protein (MSP) and POPC. Prior to IR photoactivation, the only signal that we observe corresponds to POPC cluster ions. As described above for GDX/bicelle samples, when 11.4 J of IR laser energy is is applied, signals identified as the 7+ and 6+ monomeric GDX charge states are detected, along with GDX bound to POPC. Similarly to our bicelle experiments targeting GDX, low intensity signals for the POPC 3mer persists at this laser energy, along with several charge states of MSP. Previous work[60] has demonstrated that IR photoactivation can be utilized to simplify spectra of empty nanodiscs to better determine lipid incorporation levels; however, this study is the first to demonstrate the liberation of native protein from a nanodisc by IR photoactivation.

Unlike samples using nanodiscs or bicelles to solubilize MPs, insertion of GDX into liposomes produces a signal for 7+ GDX monomers at low SNR values, prior to IR photoactivation (Figure 2-2e). However, after 11.4 J of IR energy is applied, a wide range of GDX signals are revealed (Figure 2-2f, III-8b). Specifically, we observe signals corresponding to GDX bound to all three lipids used to construct the liposome used in our experiments: PG, PE, and cardiolipin.

Unlike the detergents screened in our micelle-based experiments described above, many common lipids are phosphorylated and often used in the construction of bicelles, nanodiscs and liposomes. Given that 10.6 µm photons used in our experiments are strongly absorbed by P-O stretching modes found within all of the lipids utilized in our studies, it stands to reason that these phosphorylated moieties act as chromophores in order to drive an increase of internal energy in the gas-phase mimetics in our experiments, thus producing mimetic dissociation and GDX ion ejection. This appears to occur in selective manner, wherein nonspecific phospholipids are dissociated upon IR photoactivation, and lipid binding to the MP is preserved, in a manner similar to collisional activation[69]. However, the tunability of IR photoactivation is a significant advantage here, as the MP can be liberated from its mimetic environment, while preserving native, specific lipid bound states, without the potential to overactivate the MP and disrupt its native structure. Ejection of proteins from more complex mimetics, such as bicelles and nanodiscs, requires much higher energies from collisional activation, potentially disrupting native oligomeric and ligand bound states[70]. Beyond these advantages, the ability to mass select particular species of interest in the linear ion trap for additional experimentation in a MS^3 approach, is another advantage over typical methods that are limited to solely using collisional activation to eject MPs from mimetic environments.

2.4.3 Infrared Photoactivation Improves Native Top-Down Mass Spectrometry

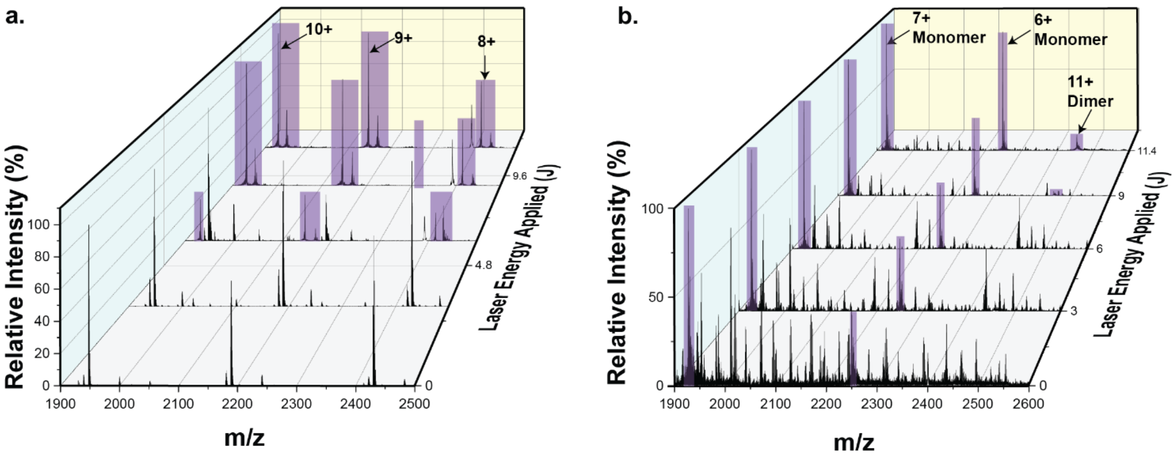

Figure 2-3 Mass spectra for samples containing the MPs PMP22 (a) and GDX (b) in surfactant after being subjected to increasing IR laser energy (Laser Energy Applied, J). Relevant protein peaks are highlighted in purple for each protein. All other signals correspond to detergent cluster ions and are discussed in Figure III-9.

As discussed above, a key challenge in the nTDMS analysis of MPs stems from the chemical noise produced by ions associated with solubilization agents and mimetic building blocks. Following our experiments aimed at assessing the mechanism and feasibility of IR photoactivation for the nMS of MPs, we extended our work to include the evaluation of sequence informative fragment ions captured directly from the MP complex ions observed in our experiments following IR irradiation (Figures 2-3 and 2-4). For example, prior to IR photoactivation, the only signals we observe in the MS data recorded for samples containing PMP22 and DM detergent correspond to detergent cluster ions (Figure III-9a). As the IR laser energy is increased, the DM cluster ions decrease in intensity, revealing the 8, 9 and 10+ charge states of PMP22, including a known sequence variant which has been identified previously[18] (Figure 2-3a). A detailed assessment of this process for the 10+ charge state is shown in Figure S10. Following IR photoactivation, the resulting MP ions can then be mass selected in the ion trap and then sent to the ion routing multipole for fragmentation by HCD. When comparing the sequence coverage obtained with and without IR photoactivation, the sequence coverage obtained is significantly enhanced in the latter case (Figure 2-4a). Specifically, when IR photoactivation is applied prior to HCD, PMP22 sequence coverages reaches an average of 61% when all charge states are sampled, as opposed to 43% when only using HCD to both liberate and fragment PMP22. An additional advantage of IR photoactivation specific to the instrument configuration used in our studies is that individual charge states can be selected for nTDMS fragmentation, which is not possible when using HCD to both liberate and fragment MP ions. PMP22 sequence coverage data acquired individually for 8, 9 and 10+ charge states are all ~60%, a result that is consistent with our sequencing data integrated across all PMP22 charge states. Representative fragmentation maps acquired of all PMP22 charge states, alongside similar maps developed for individual charge states are presented in Figure III-11.

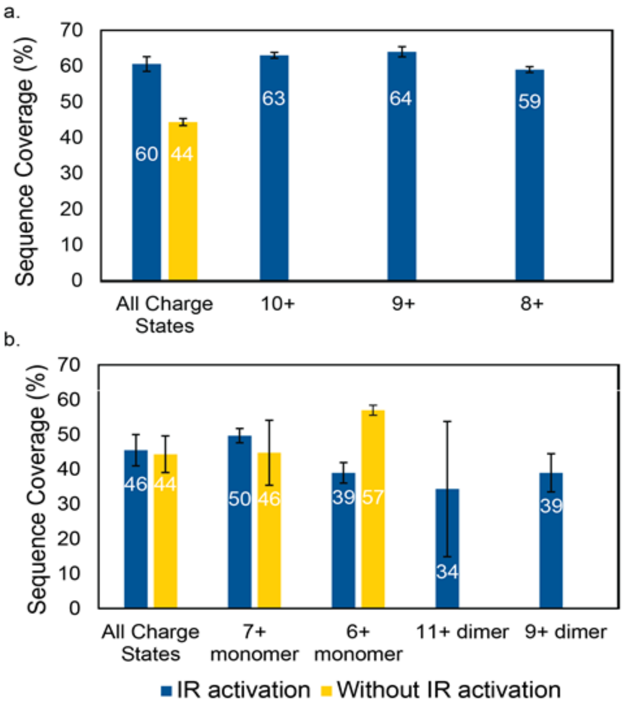

Figure 2-4 A comparison of sequence coverage values obtained with (blue) and without (yellow) IR photoactivation for a variety of charge states of PMP22 (a) and GDX (b) MPs. The average sequence coverage obtained for each experimental condition is labeled within their respective bars.

As in the case of PMP22, the nTDMS data acquired for GDX also improves significantly through the application of IR photoactivation. Our GDX data differs from the PMP22 data described above, in that prior to the application of any IR photoactivation, we observe MP signals corresponding to 6 and 7+ GDX monomer, as well as chemical noise for DM and C12E8 clusters of various ratios (Figure 2-3b, III-9b, III-12). Despite this, as IR laser energy is increased, the amount of detergent-related chemical noise observed in the resultant MS spectra decreases significantly, revealing signal for 11+ dimer at IR laser energies above 6 J

(Figure 2-3b, III-13). Sequence coverage values obtained across our GDX monomer data are within 5% of one another (Figure 2-4b), with the exception of our GDX 7+ monomer sequence data. It is important to emphasize that the native functional state of GDX is as a dimer, which can only be detected in our data following IR irradiation.

Sequence coverage values ranging from 34-39% are obtained from our GDX dimer data, which compare favorably to prior reports of MP nTDMS experiments targeting similar MPs (typically<25%)[36,54]. Representative fragmentation maps for GDX under the different experimental conditions described above are presented in Figure III-14. Importantly, the sequence coverage that we receive here is inclusive of the key residues of GDX (W16, E13, S42, W62) that are involved in ligand binding[70].

Upon close inspection of our GDX nTDMS sequencing data, we observed several fragment ions that exhibited a nominal mass increase of ~28 Da relative to their predicted sequence mass values (Figure III-15a). To determine the identity of this modification, we selected a number of nTDMS peptide fragment ions for interrogation by MS^3. Specifically, when we acquired MS^3 data for the b_3 GDX fragment ion, we were able to identify the modification as a formylation on the N-terminal Met residue of the protein (Figure III-15b). Such fMet modifications are commonly found for initiator methionine residues in bacterial membrane proteins like GDX[20,27,72,73]. This example underscores the ability of IR photoactivation, in combination with high resolution nTDMS to detect proteoform populations within native protein complexes.

2.5 Conclusions

In summary, we have demonstrated that IR photoactivation can used as a versatile and effective tool nTDMS of MPs. We analyzed several detergents having different functional groups and found that IR photoactivation can be broadly deployed to liberate proteins from a variety of detergent micelles, without the need for a strong IR chromophore. We interpret this result as indicating that the detergent cluster ions that act as chemical noise in our nTDMS for MPs are weakly associated, needing only low-level activation to undergo dissociation, eventually decaying into dimer detergent ions far removed from the m/z range typically occupied by most nTDMS signals of interest. In addition, we used IR photoactivation to liberate MPs from three other membrane mimetics commonly used in nMS, suggesting that IR photoactivation can be employed more generally for the liberation of MPs enabling a wider range of nTDMS assays.

Finally, we evaluated the sequence coverages obtained from nTDMS experiments both with and without the use of IR photoactivation. Compared to methods where CID/HCD is utilized throughout, the tunability of IR photoactivation, especially in a manner where small increases in ion internal energy can be achieved, appears to provide the ability to both liberate MPs from mimetics and dissociate cluster ions originating from solubilization agents that typically overlap with nTDMS fragment ion signals. In the cases of PMP22 and GDX, we demonstrate that IR photoactivation gives rise to advantages over the standard nTDMS approaches for MPs. Specifically, for PMP22, IR photoactivation methods provided significantly greater sequence coverage values when compared to equivalent experiments that used collisional activation. This increase in MP sequence information is provided, in part, by enabling the selection of individual MP charge states prior to HCD fragmentation in a manner that could not be accessed by methods lacking IR photoactivation. In addition, our GDX nTDMS demonstrates that while IR photoactivation does not seem to offer significant advantages when targeting sequence information from GDX monomers, IR photoactivation is essential for both detecting and sequencing GDX dimer ions. While only HCD was used in this study our primary nTDMS activation method, future work may well combine IR photoactivation with other ion activation methods to provide further increases in MP sequence coverage[35]. The improvements in sequence coverage here could be impactful in pharmaceutical research regarding MPs. MPs play key roles in mediating the etiology of cancer and other disease states[74,75],. Improvements in sequence coverage would help to more confidently reveal additional PTMs and proteoforms that could play key roles in the etiology of these diseases, especially as many proteoforms are of high clinical relevance[31], offering insights into how better to identify therapeutics that may modulate these effects. Taken together, our data provides insights into the mechanistic underpinnings and capabilities of IR photoactivation for future MP nTDMS experiments.

2.6 References

(1) Nicolson, G. L. The Fluid—Mosaic Model of Mem-brane Structure: Still Relevant to Understanding the Structure, Function and Dynamics of Biological Membranes after More than 40years. Biochimica et Biophysica Acta (BBA) - Biomembranes 2014, 1838 (6), 1451–1466. https://doi.org/10.1016/j.bbamem.2013.10.019.
(2) Choy, B. C.; Cater, R. J.; Mancia, F.; Pryor, E. E. A 10-Year Meta-Analysis of Membrane Protein Structural Biology: Detergents, Membrane Mimetics, and Structure Determination Techniques. Biochimica et Biophysica Acta (BBA) - Biomem-branes 2021, 1863 (3), 183533. https://doi.org/10.1016/j.bbamem.2020.183533.
(3) Shimizu, K.; Cao, W.; Saad, G.; Shoji, M.; Terada, T. Comparative Analysis of Membrane Protein Structure Data-bases. Biochimica et Biophysica Acta (BBA) - Biomembranes 2018, 1860 (5), 1077–1091. https://doi.org/10.1016/j.bbamem.2018.01.005.
(4) Laganowsky, A.; Reading, E.; Hopper, J. T. S.; Rob-inson, C. V. Mass Spectrometry of Intact Membrane Protein Complexes. Nat Protoc 2013, 8 (4), 639–651. https://doi.org/10.1038/nprot.2013.024.
(5) Sanders, C. R.; Landis, G. C. Reconstitution of Mem-brane Proteins into Lipid-Rich Bilayered Mixed Micelles for NMR Studies. Biochemistry 1995, 34 (12), 4030–4040. https://doi.org/10.1021/bi00012a022.
(6) Lee, D.; Walter, K. F. A.; Brückner, A.-K.; Hilty, C.; Becker, S.; Griesinger, C. Bilayer in Small Bicelles Revealed by Lipid−Protein Interactions Using NMR Spectroscopy. J. Am. Chem. Soc. 2008, 130 (42), 13822–13823. https://doi.org/10.1021/ja803686p.
(7) Bayburt, T. H.; Carlson, J. W.; Sligar, S. G. Reconstitution and Imaging of a Membrane Protein in a Nanometer-Size Phospholipid Bilayer. J Struct Biol 1998, 123 (1), 37–44. https://doi.org/10.1006/jsbi.1998.4007.
(8) Glück, J. M.; Wittlich, M.; Feuerstein, S.; Hoffmann, S.; Willbold, D.; Koenig, B. W. Integral Membrane Proteins in Nanodiscs Can Be Studied by Solution NMR

Spectroscopy. J Am Chem Soc 2009, 131 (34), 12060–12061. https://doi.org/10.1021/ja904897p.

(9) Calabrese, A. N.; Watkinson, T. G.; Henderson, P. J. F.; Radford, S. E.; Ashcroft, A. E. Amphipols Outperform Do-decylmaltoside Micelles in Stabilizing Membrane Protein Structure in the Gas Phase. Anal. Chem. 2015, 87 (2), 1118–1126. https://doi.org/10.1021/ac5037022.

(10) Sligar, S. G.; Denisov, I. G. Nanodiscs: A Toolkit for Membrane Protein Science. Protein Science 2021, 30 (2), 297–315. https://doi.org/10.1002/pro.3994.

(11) Nath, A.; Atkins, W. M.; Sligar, S. G. Applications of Phospholipid Bilayer Nanodiscs in the Study of Membranes and Membrane Proteins. Biochemistry 2007, 46 (8), 2059–2069. https://doi.org/10.1021/bi602371n.

(12) Barrera, N. P.; Robinson, C. V. Advances in the Mass Spectrometry of Membrane Proteins: From Individual Proteins to Intact Complexes. Annu Rev Biochem 2011, 80, 247–271. https://doi.org/10.1146/annurev-biochem-062309-093307.

(13) Konijnenberg, A.; van Dyck, J. F.; Kailing, L. L.; Sobott, F. Extending Native Mass Spectrometry Approaches to Integral Membrane Proteins. Biol Chem 2015, 396 (9–10), 991–1002. https://doi.org/10.1515/hsz-2015-0136.

(14) Marty, M. T.; Hoi, K. K.; Robinson, C. V. Interfacing Membrane Mimetics with Mass Spectrometry. Acc. Chem. Res. 2016, 49 (11), 2459–2467. https://doi.org/10.1021/acs.accounts.6b00379.

(15) Marty, M. T.; Zhang, H.; Cui, W.; Blankenship, R. E.; Gross, M. L.; Sligar, S. G. Native Mass Spectrometry Character-ization of Intact Nanodisc Lipoprotein Complexes. Analytical chemistry 2012, 84 (21), 8957–8960.

(16) Keener, J. E.; Zambrano, D. E.; Zhang, G.; Zak, C. K.; Reid, D. J.; Deodhar, B. S.; Pemberton, J. E.; Prell, J. S.; Marty, M. T. Chemical Additives Enable Native Mass Spectrometry Measurement of Membrane Protein Oligomeric State within Intact Nanodiscs. J. Am. Chem. Soc. 2019, 141 (2), 1054–1061. https://doi.org/10.1021/jacs.8b11529.

(17) Gupta, K.; Donlan, J. A. C.; Hopper, J. T. S.; Uz-davinys, P.; Landreh, M.; Struwe, W. B.; Drew, D.; Baldwin, A. J.; Stansfeld, P. J.; Robinson, C. V. The Role of Interfacial Li-pids in Stabilizing Membrane Protein Oligomers. Nature 2017, 541 (7637), 421–424. https://doi.org/10.1038/nature20820.

(18) Fantin, S. M.; Parson, K. F.; Yadav, P.; Juliano, B.; Li, G. C.; Sanders, C. R.; Ohi, M. D.; Ruotolo, B. T. Ion Mobility–Mass Spectrometry Reveals the Role of Peripheral Myelin Pro-tein Dimers in Peripheral Neuropathy. Proceedings of the National Academy of Sciences 2021, 118 (17), e2015331118.

(19) Chorev, D. S.; Baker, L. A.; Wu, D.; Beilsten-Edmands, V.; Rouse, S. L.; Zeev-Ben-Mordehai, T.; Jiko, C.; Samsudin, F.; Gerle, C.; Khalid, S.; Stewart, A. G.; Matthews, S. J.; Grünewald, K.; Robinson, C. V. Protein Assemblies Ejected Directly from Native Membranes Yield Complexes for Mass Spectrometry. Science 2018, 362 (6416), 829–834. https://doi.org/10.1126/science.aau0976.

(20) Lippens, J. L.; Nshanian, M.; Spahr, C.; Egea, P. F.; Loo, J. A.; Campuzano, I. D. G. Fourier Transform-Ion Cyclo-tron Resonance Mass Spectrometry as a Platform for Character-izing Multimeric Membrane Protein Complexes. J Am Soc Mass Spectrom 2018, 29 (1), 183–193. https://doi.org/10.1007/s13361-017-1799-4.

(21) Liko, I.; Degiacomi, M. T.; Lee, S.; Newport, T. D.; Gault, J.; Reading, E.; Hopper, J. T. S.; Housden, N. G.; White, P.; Colledge, M.; Sula, A.; Wallace, B. A.; Kleanthous, C.; Stansfeld, P. J.; Bayley, H.; Benesch, J. L. P.; Allison, T. M.; Robinson, C. V. Lipid Binding Attenuates Channel Closure of the Outer Membrane Protein OmpF. Proceedings of the Na-tional Academy of Sciences 2018, 115 (26), 6691–6696. https://doi.org/10.1073/pnas.1721152115.

(22) Marty, M. T.; Hoi, K. K.; Gault, J.; Robinson, C. V. Probing the Lipid Annular Belt by Gas-Phase Dissociation of Membrane Proteins in Nanodiscs. Angew Chem Int Ed Engl 2016, 55 (2), 550–554. https://doi.org/10.1002/anie.201508289.

(23) Keener, J. E.; Jayasekera, H. S.; Marty, M. T. Investi-gating the Lipid Selectivity of Membrane Proteins in Hetero-geneous Nanodiscs. Analytical Chemistry 2022.

(24) Fantin, S. M.; Parson, K. F.; Niu, S.; Liu, J.; Polasky, D. A.; Dixit, S. M.; Ferguson-Miller, S. M.; Ruotolo, B. T. Col-lision Induced Unfolding Classifies Ligands Bound to the Integral Membrane Translocator Protein. Anal. Chem. 2019, 91 (24), 15469–15476. https://doi.org/10.1021/acs.analchem.9b03208.

(25) Gault, J.; Liko, I.; Landreh, M.; Shutin, D.; Bolla, J. R.; Jefferies, D.; Agasid, M.; Yen, H.-Y.; Ladds, M. J. G. W.; Lane, D. P.; Khalid, S.; Mullen, C.; Remes, P. M.; Huguet, R.; McAlister, G.; Goodwin, M.; Viner, R.; Syka, J. E. P.; Robin-son, C. V. Combining Native and “omics” Mass Spectrometry to Identify Endogenous Ligands Bound to Membrane Proteins. Nat Methods 2020, 17 (5), 505–508. https://doi.org/10.1038/s41592-020-0821-0.

(26) Fearnley, I. M.; Walker, J. E. Analysis of Hydropho-bic Proteins and Peptides by Electrospray Ionization MS. Bio-chemical Society Transactions 1996, 24 (3), 912–917. https://doi.org/10.1042/bst0240912.

(27) Whitelegge, J. P.; Zhang, H.; Aguilera, R.; Taylor, R. M.; Cramer, W. A. Full Subunit Coverage Liquid Chromatog-raphy Electrospray Ionization Mass Spectrometry (LCMS+) of an Oligomeric Membrane Protein: Cytochrome B6f Complex From Spinach and the Cyanobacterium Mastigocladus Lam-inosus* S. Molecular & Cellular Proteomics 2002, 1 (10), 816–827. https://doi.org/10.1074/mcp.M200045-MCP200.

(28) Whitelegge, J. P.; Laganowsky, A.; Nishio, J.; Souda, P.; Zhang, H.; Cramer, W. A. Sequencing Covalent Modifica-tions of Membrane Proteins. Journal of Experimental Botany 2006, 57 (7), 1515–1522. https://doi.org/10.1093/jxb/erj163.

(29) Cohn, W.; Huguet, R.; Zabrouskov, V.; Whitelegge, J. Dissociation Strategies to Maximize Coverage of α-Helical Domains in Top-Down Mass Spectrometry of Integral Mem-brane Proteins. Journal of the American Society for Mass Spectrometry 2021, 32 (6), 1380–1387.

(30) Aebersold, R.; Agar, J. N.; Amster, I. J.; Baker, M. S.; Bertozzi, C. R.; Boja, E. S.; Costello, C. E.; Cravatt, B. F.; Fenselau, C.; Garcia, B. A.; Ge, Y.; Gunawardena, J.; Hendrickson, R. C.; Hergenrother, P. J.; Huber, C. G.; Ivanov, A. R.; Jensen, O. N.; Jewett, M. C.; Kelleher, N. L.; Kiessling, L. L.; Krogan, N. J.; Larsen, M. R.; Loo, J. A.; Ogorzalek Loo, R. R.; Lundberg, E.; MacCoss, M. J.; Mallick, P.; Mootha, V. K.; Mrksich, M.; Muir, T. W.; Patrie, S. M.; Pesavento, J. J.; Pitteri, S. J.; Rodriguez, H.; Saghatelian, A.; Sandoval, W.; Schlüter, H.; Sechi, S.; Slavoff, S. A.; Smith, L. M.; Snyder, M. P.; Thomas, P. M.; Uhlén, M.; Van Eyk, J. E.; Vidal, M.; Walt, D. R.; White, F. M.; Williams, E. R.; Wohlschlager, T.; Wysocki, V. H.; Yates, N. A.; Young, N. L.; Zhang, B. How Many

Human Proteoforms Are There? Nat Chem Biol 2018, 14 (3), 206–214. https://doi.org/10.1038/nchembio.2576.

(31) Kelleher, N. L.; Thomas, P. M.; Ntai, I.; Compton, P. D.; LeDuc, R. D. Deep and Quantitative Top-down Proteomics in Clinical and Translational Research. Expert Rev Proteomics 2014, 11 (6), 649–651. https://doi.org/10.1586/14789450.2014.976559.

(32) Siuti, N.; Kelleher, N. L. Decoding Protein Modifica-tions Using Top-down Mass Spectrometry. Nat Methods 2007, 4 (10), 817–821. https://doi.org/10.1038/nmeth1097.

(33) Zhou, M.; Lantz, C.; A. Brown, K.; Ge, Y.; Paša-Tolić, L.; A. Loo, J.; Lermyte, F. Higher-Order Structural Characteri-sation of Native Proteins and Complexes by Top-down Mass Spectrometry. Chemical Science 2020, 11 (48), 12918–12936. https://doi.org/10.1039/D0SC04392C.

(34) Greisch, J.-F.; Tamara, S.; A. Scheltema, R.; R. Maxwell, H. W.; D. Fagerlund, R.; C. Fineran, P.; Tetter, S.; Hilvert, D.; R. Heck, A. J. Expanding the Mass Range for UVPD-Based Native Top-down Mass Spectrometry. Chemical Science 2019, 10 (30), 7163–7171. https://doi.org/10.1039/C9SC01857C.

(35) Wongkongkathep, P.; Han, J. Y.; Choi, T. S.; Yin, S.; Kim, H. I.; Loo, J. A. Native Top-Down Mass Spectrometry and Ion Mobility MS for Characterizing the Cobalt and Manganese Metal Binding of α-Synuclein Protein. J. Am. Soc. Mass Spectrom. 2018, 29 (9), 1870–1880. https://doi.org/10.1007/s13361-018-2002-2.

(36) Ro, S. Y.; Schachner, L. F.; Koo, C. W.; Purohit, R.; Remis, J. P.; Kenney, G. E.; Liauw, B. W.; Thomas, P. M.; Pa-trie, S. M.; Kelleher, N. L.; Rosenzweig, A. C. Native Top-down Mass Spectrometry Provides Insights into the Copper Centers of Membrane-Bound Methane Monooxygenase. Nat Commun 2019, 10, 2675. https://doi.org/10.1038/s41467-019-10590-6.

(37) Polasky, D. A.; Lermyte, F.; Nshanian, M.; Sobott, F.; Andrews, P. C.; Loo, J. A.; Ruotolo, B. T. Fixed-Charge Trime-thyl Pyrilium Modification for Enabling Enhanced Top-down Mass Spectrometry Sequencing of Intact Protein Complexes. Analytical chemistry 2018, 90 (4), 2756–2764.

(38) Hale, O. J.; Cooper, H. J. Native Mass Spectrometry Imaging and In Situ Top-Down Identification of Intact Pro-teins Directly from Tissue. J. Am. Soc. Mass Spectrom. 2020, 31 (12), 2531–2537. https://doi.org/10.1021/jasms.0c00226.

(39) Zhang, H.; Cui, W.; Wen, J.; Blankenship, R. E.; Gross, M. L. Native Electrospray and Electron-Capture Disso-ciation FTICR Mass Spectrometry for Top-Down Studies of Protein Assemblies. Anal. Chem. 2011, 83 (14), 5598–5606. https://doi.org/10.1021/ac200695d.

(40) Riley, N. M.; Westphall, M. S.; Coon, J. J. Activated Ion-Electron Transfer Dissociation Enables Comprehensive Top-Down Protein Fragmentation. J. Proteome Res. 2017, 16 (7), 2653–2659. https://doi.org/10.1021/acs.jproteome.7b00249.

(41) Dyachenko, A.; Wang, G.; Belov, M.; Makarov, A.; de Jong, R. N.; van den Bremer, E. T. J.; Parren, P. W. H. I.; Heck, A. J. R. Tandem Native Mass-Spectrometry on Anti-body–Drug Conjugates and Submillion Da Antibody–Antigen Protein Assemblies on an Orbitrap EMR Equipped with a High-Mass Quadrupole Mass Selector. Anal. Chem. 2015, 87 (12), 6095–6102. https://doi.org/10.1021/acs.analchem.5b00788.

(42) Macias, L. A.; Sipe, S. N.; Santos, I. C.; Bashyal, A.; Mehaffey, M. R.; Brodbelt, J. S. Influence of Primary Structure on Fragmentation of Native-Like Proteins by Ultraviolet

Pho-todissociation. J. Am. Soc. Mass Spectrom. 2021, 32 (12), 2860–2873. https://doi.org/10.1021/jasms.1c00269.

(43) O'Brien, J. P.; Li, W.; Zhang, Y.; Brodbelt, J. S. Char-acterization of Native Protein Complexes Using Ultraviolet Photodissociation Mass Spectrometry. J. Am. Chem. Soc. 2014, 136 (37), 12920–12928. https://doi.org/10.1021/ja505217w.

(44) Larson, E. J.; Roberts, D. S.; Melby, J. A.; Buck, K. M.; Zhu, Y.; Zhou, S.; Han, L.; Zhang, Q.; Ge, Y. High-Throughput Multi-Attribute Analysis of Antibody-Drug Conjugates Enabled by Trapped Ion Mobility Spectrometry and Top-Down Mass Spectrometry. Anal. Chem. 2021, 93 (29), 10013–10021. https://doi.org/10.1021/acs.analchem.1c00150.

(45) Gerbasi, V. R.; Melani, R. D.; Abbatiello, S. E.; Bel-ford, M. W.; Huguet, R.; McGee, J. P.; Dayhoff, D.; Thomas, P. M.; Kelleher, N. L. Deeper Protein Identification Using Field Asymmetric Ion Mobility Spectrometry in Top-Down Prote-omics. Anal. Chem. 2021, 93 (16), 6323–6328. https://doi.org/10.1021/acs.analchem.1c00402.

(46) McCool, E. N.; Lubeckyj, R. A.; Shen, X.; Chen, D.; Kou, Q.; Liu, X.; Sun, L. Deep Top-Down Proteomics Using Capillary Zone Electrophoresis-Tandem Mass Spectrometry: Identification of 5700 Proteoforms from the Escherichia Coli Proteome. Anal. Chem. 2018, 90 (9), 5529–5533. https://doi.org/10.1021/acs.analchem.8b00693.

(47) Jooß, K.; Schachner, L. F.; Watson, R.; Gillespie, Z. B.; Howard, S. A.; Cheek, M. A.; Meiners, M. J.; Sobh, A.; Licht, J. D.; Keogh, M.-C.; Kelleher, N. L. Separation and Characterization of Endogenous Nucleosomes by Native Ca-pillary Zone Electrophoresis–Top-Down Mass Spectrometry. Anal. Chem. 2021, 93 (12), 5151–5160. https://doi.org/10.1021/acs.analchem.0c04975.

(48) Mehaffey, M. R.; Xia, Q.; Brodbelt, J. S. Uniting Na-tive Capillary Electrophoresis and Multistage Ultraviolet Pho-todissociation Mass Spectrometry for Online Separation and Characterization of Escherichia Coli Ribosomal Proteins and Protein Complexes. Anal. Chem. 2020, 92 (22), 15202–15211. https://doi.org/10.1021/acs.analchem.0c03784.

(49) Durbin, K. R.; Fornelli, L.; Fellers, R. T.; Doubleday, P. F.; Narita, M.; Kelleher, N. L. Quantitation and Identifica-tion of Thousands of Human Proteoforms below 30 KDa. J. Proteome Res. 2016, 15 (3), 976–982. https://doi.org/10.1021/acs.jproteome.5b00997.

(50) Roberts, D. S.; Mann, M.; Melby, J. A.; Larson, E. J.; Zhu, Y.; Brasier, A. R.; Jin, S.; Ge, Y. Structural O-Glycoform Heterogeneity of the SARS-CoV-2 Spike Protein Receptor-Binding Domain Revealed by Top-Down Mass Spectrometry. J. Am. Chem. Soc. 2021, 143 (31), 12014–12024. https://doi.org/10.1021/jacs.1c02713.

(51) Cai, W.; Tucholski, T.; Chen, B.; Alpert, A. J.; McIl-wain, S.; Kohmoto, T.; Jin, S.; Ge, Y. Top-Down Proteomics of Large Proteins up to 223 KDa Enabled by Serial Size Exclu-sion Chromatography Strategy. Anal. Chem. 2017, 89 (10), 5467–5475. https://doi.org/10.1021/acs.analchem.7b00380.

(52) Ansong, C.; Wu, S.; Meng, D.; Liu, X.; Brewer, H. M.; Deatherage Kaiser, B. L.; Nakayasu, E. S.; Cort, J. R.; Pevzner, P.; Smith, R. D.; Heffron, F.; Adkins, J. N.; Paša-Tolić, L. Top-down Proteomics Reveals a Unique Protein S-Thiolation Switch in Salmonella Typhimurium in Response to Infection-like Conditions. Proceedings of the National Academy of Sciences 2013, 110 (25), 10153–10158. https://doi.org/10.1073/pnas.1221210110.

(53) Riley, N. M.; Sikora, J. W.; Seckler, H. S.; Greer, J. B.; Fellers, R. T.; LeDuc, R. D.; Westphall, M. S.; Thomas, P. M.; Kelleher, N. L.; Coon, J. J. The Value of Activated Ion

Elec-tron Transfer Dissociation for High-Throughput Top-Down Characterization of Intact Proteins. Anal. Chem. 2018, 90 (14), 8553–8560. https://doi.org/10.1021/acs.analchem.8b01638.

(54) Konijnenberg, A.; Bannwarth, L.; Yilmaz, D.; Koçer, A.; Venien-Bryan, C.; Sobott, F. Top-down Mass Spectrometry of Intact Membrane Protein Complexes Reveals Oligomeric State and Sequence Information in a Single Experiment. Pro-tein Science 2015, 24 (8), 1292–1300. https://doi.org/10.1002/pro.2703.

(55) Sipe, S. N.; Patrick, J. W.; Laganowsky, A.; Brodbelt, J. S. Enhanced Characterization of Membrane Protein Com-plexes by Ultraviolet Photodissociation Mass Spectrometry. Anal. Chem. 2020, 92 (1), 899–907. https://doi.org/10.1021/acs.analchem.9b03689.

(56) Chorev, D. S.; Baker, L. A.; Wu, D.; Beilsten-Edmands, V.; Rouse, S. L.; Zeev-Ben-Mordehai, T.; Jiko, C.; Samsudin, F.; Gerle, C.; Khalid, S.; Stewart, A. G.; Matthews, S. J.; Grünewald, K.; Robinson, C. V. Protein Assemblies Ejected Directly from Native Membranes Yield Complexes for Mass Spectrometry. Science 2018, 362 (6416), 829–834. https://doi.org/10.1126/science.aau0976.

(57) Brown, K. A.; Chen, B.; Guardado-Alvarez, T. M.; Lin, Z.; Hwang, L.; Ayaz-Guner, S.; Jin, S.; Ge, Y. A Photo-cleavable Surfactant for Top-down Proteomics. Nat Methods 2019, 16 (5), 417–420. https://doi.org/10.1038/s41592-019-0391-1.

(58) Brown, K. A.; Tucholski, T.; Eken, C.; Knott, S.; Zhu, Y.; Jin, S.; Ge, Y. High-Throughput Proteomics Enabled by a Photocleavable Surfactant. Angewandte Chemie 2020, 132 (22), 8484–8488. https://doi.org/10.1002/ange.201915374.

(59) Mikhailov, V. A.; Liko, I.; Mize, T. H.; Bush, M. F.; Benesch, J. L. P.; Robinson, C. V. Infrared Laser Activation of Soluble and Membrane Protein Assemblies in the Gas Phase. Anal. Chem. 2016, 88 (14), 7060–7067. https://doi.org/10.1021/acs.analchem.6b00645.

(60) Campuzano, I. D. G.; Li, H.; Bagal, D.; Lippens, J. L.; Svitel, J.; Kurzeja, R. J. M.; Xu, H.; Schnier, P. D.; Loo, J. A. Native MS Analysis of Bacteriorhodopsin and an Empty Nanodisc by Orthogonal Acceleration Time-of-Flight, Or-bitrap and Ion Cyclotron Resonance. Anal. Chem. 2016, 88 (24), 12427–12436. https://doi.org/10.1021/acs.analchem.6b03762.

(61) El-Faramawy, A.; Guo, Y.; Verkerk, U. H.; Thomson, B. A.; Siu, K. W. M. Infrared Irradiation in the Collision Cell of a Hybrid Tandem Quadrupole/Time-of-Flight Mass Spec-trometer for Declustering and Cleaning of Nanoelectrosprayed Protein Complex Ions. Anal. Chem. 2010, 82 (23), 9878–9884. https://doi.org/10.1021/ac102351m.

(62) Lee, K. W.; Harrilal, C. P.; Fu, L.; Eakins, G. S.; McLuckey, S. A. Digital Ion Trap Mass Analysis of High Mass Protein Complexes Using IR Activation Coupled with Ion/Ion Reactions. International Journal of Mass Spectrometry 2020, 458, 116437. https://doi.org/10.1016/j.ijms.2020.116437.

(63) Riley, N. M.; Westphall, M. S.; Coon, J. J. Activated Ion Electron Transfer Dissociation for Improved Fragmenta-tion of Intact Proteins. Anal. Chem. 2015, 87 (14), 7109–7116. https://doi.org/10.1021/acs.analchem.5b00881.

(64) Madsen, J. A.; Gardner, M. W.; Smith, S. I.; Ledvina, A. R.; Coon, J. J.; Schwartz, J. C.; Stafford, G. C. Jr.; Brodbelt, J. S. Top-Down Protein Fragmentation by Infrared Multiphoton Dissociation in a Dual Pressure Linear Ion Trap. Anal. Chem. 2009, 81 (21), 8677–8686. https://doi.org/10.1021/ac901554z.

(65) Little, D. P.; Speir, J. Paul.; Senko, M. W.; O’Connor, P. B.; McLafferty, F. W. Infrared Multiphoton Dissociation of Large Multiply Charged Ions for Biomolecule Sequencing. Anal. Chem. 1994, 66 (18), 2809–2815. https://doi.org/10.1021/ac00090a004.

(66) Mittendorf, K. F.; Marinko, J. T.; Hampton, C. M.; Ke, Z.; Hadziselimovic, A.; Schlebach, J. P.; Law, C. L.; Li, J.; Wright, E. R.; Sanders, C. R.; Ohi, M. D. Peripheral Myelin Protein 22 Alters Membrane Architecture. Sci Adv 2017, 3 (7), e1700220. https://doi.org/10.1126/sciadv.1700220.

(67) Schlebach, J. P.; Narayan, M.; Alford, C.; Mittendorf, K. F.; Carter, B. D.; Li, J.; Sanders, C. R. Conformational Sta-bility and Pathogenic Misfolding of the Integral Membrane Protein PMP22. J. Am. Chem. Soc. 2015, 137 (27), 8758–8768. https://doi.org/10.1021/jacs.5b03743.

(68) Kermani, A. A.; Macdonald, C. B.; Gundepudi, R.; Stockbridge, R. B. Guanidinium Export Is the Primal Function of SMR Family Transporters. Proceedings of the National Academy of Sciences 2018, 115 (12), 3060–3065. https://doi.org/10.1073/pnas.1719187115.

(69) Kermani, A. A.; Macdonald, C. B.; Burata, O. E.; Ben Koff, B.; Koide, A.; Denbaum, E.; Koide, S.; Stockbridge, R. B. The Structural Basis of Promiscuity in Small Multidrug Resistance Transporters. Nat Commun 2020, 11 (1), 6064. https://doi.org/10.1038/s41467-020-19820-8.

(70) Kermani, A. A.; Burata, O. E.; Koff, B. B.; Koide, A.; Koide, S.; Stockbridge, R. B. Crystal Structures of Bacterial Small Multidrug Resistance Transporter EmrE in Complex with Structurally Diverse Substrates. eLife 2022, 11, e76766. https://doi.org/10.7554/eLife.76766.

(71) Borysik, A. J.; Robinson, C. V. Formation and Dis-sociation Processes of Gas-Phase Detergent Micelles. Langmuir 2012, 28 (18), 7160–7167. https://doi.org/10.1021/la3002866.

(72) Plöscher, M.; Granvogl, B.; Zoryan, M.; Reisinger, V.; Eichacker, L. A. Mass Spectrometric Characterization of Mem-brane Integral Low Molecular Weight Proteins from Photosys-tem II in Barley Etioplasts. PROTEOMICS 2009, 9 (3), 625–635. https://doi.org/10.1002/pmic.200800337.

(73) Dong, M. S.; Bell, L. C.; Guo, Z.; Phillips, D. R.; Blair, I. A.; Guengerich, F. P. Identification of Retained N-Formylmethionine in Bacterial Recombinant Mammalian Cytochrome P450 Proteins with the N-Terminal Sequence MALLLAVFL...: Roles of Residues 3-5 in Retention and Membrane Topology. Biochemistry 1996, 35 (31), 10031–10040. https://doi.org/10.1021/bi960873z.

(74) Boes, D. M.; Godoy-Hernandez, A.; McMillan, D. G. G. Peripheral Membrane Proteins: Promising Therapeutic Tar-gets across Domains of Life. Membranes 2021, 11 (5), 346. https://doi.org/10.3390/membranes11050346.

(75) Almasi, S.; El Hiani, Y. Exploring the Therapeutic Potential of Membrane Transport Proteins: Focus on Cancer and Chemoresistance. Cancers (Basel) 2020, 12 (6), 1624. https://doi.org/10.3390/cancers12061624.

Chapter 3 A Critical Evaluation of Detergent Exchange Procedures for Membrane Proteins Native Mass Spectrometry

Brock R. Juliano*, Iliana Levesque*, Kristine F. Parson, Brandon T. Ruotolo
*These authors contributed equally to this work

3.1 Abstract

Membrane proteins (MP) play many critical roles in cellular physiology and constitute the majority of current pharmaceutical targets. However, MPs are comparatively understudied relative to soluble proteins due to the challenges associated with their solubilization in membrane mimetics. Native Mass Spectrometry (nMS) has emerged as a useful technique to probe the structures of MPs. Typically, nMS studies using MPs have used detergent micelles to solubilize the MP. Oftentimes, the detergent micelle that the MP was purified into will be exchanged to another detergent prior to analysis by nMS. While methodologies for performing detergent exchange have been described in prior reports extensively, the effectiveness of these protocols remains understudied. Here, we present a critical analysis of detergent exchange efficacy using several model transmembrane proteins and a variety of commonly used detergents, evaluating the completeness of the exchange using a battery of existing protocols. Our dataset includes results for octyl glucoside (OG), octaethylene glycol monododecyl ether (C12E8), tetraethylene glycol monooctyl ether (C8E4), and demonstrates that existing protocols are insufficient and yield incomplete exchange for the proteins and under the conditions probed here. In some cases, our data indicates that up to 99% of the detergent remaining samples after detergent exchange corresponds to the original, pre-exchange detergent. We conclude by discussing the need for new

detergent exchange methodologies alongside improved exchange yield expectations for studying the potential influence of detergents upon MP structures.

3.2 Introduction

MPs are critical mediators of myriad cellular processes. Given their positions either within or associated with the cellular membrane, these proteins play important roles in facilitating cellular signaling, bulk trafficking, and other functions[1]. The significance of MPs to cellular physiology is underscored by the fact that these proteins make up approximately 60% of current pharmaceutical drug targets[1]. Despite this, MPs make up less than 3% of the structures in the Protein Data Bank[2]. This gap is due, in part, to the difficulties surrounding performing experiments with MPs due to their hydrophobicity. This makes MPs incompatible with standard protocols which have been developed for water soluble proteins. Beyond this initial hurdle of solubilization, MPs are often difficult to purify, and they can also be particularly unstable[3]. Generally, MPs must be preserved within a mimetic in order to preserve their structural integrity[4,5]. Typically, MPs are placed into a detergent micelle, wherein their hydrophobic portions are shielded by detergent molecules[6]. Other mimetics can be used, including bicelles, nanodiscs, liposomes, lipodisqs and amphipols[7–10]. Specifically, bicelles are constituted out of a mixture of detergents and lipids[11,12], nanodiscs are made of lipids that are held together by a protein or peptide based belt[13,14], liposomes are bilayers formed from mixtures of lipids[15], while lipodisqs and amphipols are made of polymers[10,16]. Alternatively, recent work has also demonstrated that nMS data can be collected with proteins ejected directly from the cellular membrane[17,18].

Native MS (nMS) has emerged as a transformational technology for the study of MP structural biology. Generally, nMS carefully tunes both solution and gas phase conditions to preserve the native-like structure of the protein or protein complex for duration of the experiment in order for the structure of the protein system to be interrogated[19,20]. Such nMS analyses typically use nanoelectrospray ionization (nESI) to produce native-like ions[21,22]. Prior reports have used nMS analyses to probe a variety of MPs, including both integral[23–26] and peripheral[15,27] protein systems. These prior reports have demonstrated that nMS is advantageous for such MP studies, as it allows for the preservation of native-like MP structures and allows for the rapid acquisition of such structural information[28]. Accordingly, nMS studies have been deployed to study the stoichiometry of membrane protein oligomers[13,14,24], lipid and drug binding,[29–31] and membrane protein stability[23,24,32]. Importantly, nMS allows for the MP to be preserved within a membrane mimetic until it is liberated by additional activation within the mass spectrometer[6,28].

Several detergent classes are commonly used to produce micelles for nMS experiments. For nMS studies, nonionic detergents are preferred as they tend to produce less chemical noise during analysis[28]. Commonly used detergents for nMS experimentation include maltosides, glucosides and polyoxyethylene glycols[2,33]. Novel detergents have also been developed, which are designed for more facile gas-phase cleavage and which more closely resemble native lipid environments[34–37]. Maltosides are the most commonly used detergents; however, as up to 137 detergents have been reported to be used for solubilizing MPs in the literature since 2010[33]. Guidelines regarding the use of detergents for nMS applications remain scarce. Not all detergents are compatible with all membrane protein systems, leaving users to strike a tenuous balance between structural stability and solubilization efficiency[5]. Oftentimes, MPs may not be purified directly in nMS compatible detergents and subsequently may require the use of detergent exchange procedures in order to replace the original detergent micelle with a micelle with properties desirable for nMS[6,28]. Three main methodologies exist for such detergent exchange procedures: spin columns packed with SEC resin, standard fast protein liquid chromatography (FPLC), or Amicon ultracentrifugal filters[28,38]. These buffer exchange methodologies operate under the principle that diluting the starting detergent below its critical micelle concentration (CMC) in the presence of the new detergent at least two times its CMC will facilitate the exchange of the protein into the desired micelle, as the old micelle will dissociate as its concentration falls below the CMC. These methodologies have been widely deployed in the nMS community for a variety of MP systems[32,39–41].

Despite the widespread use of these methods, the efficacy of standard detergent exchange methodologies remain understudied. Such information is critically needed to quantitatively capture and understand the effects of specific detergents and cofactors on MPs of interest. Prior work has clearly indicated that different detergents can have divergent structural effects on MPs, further highlighting the need to quantify detergent exchange efficiencies for nMS[42–47]. Here we present detailed biophysical studies using both nMS and dynamic light scattering (DLS) which suggest that, in nearly all cases, commonly used detergent exchange procedures yield incomplete detergent exchange. The proteins peripheral myelin protein 22 (PMP22), guanidium transporter (GDX) and the amyloid precursor protein (C99) were used as model systems to study the efficacy of detergent exchange. Each of these proteins has been studied previously by nMS[11,24]. PMP22 is a 22 kDa transmembrane protein that is involved in the myelination of Schwann cells and has been implicated in the etiology of several neuropathies[,48]. GDX is a 13 kDa transmembrane protein found in bacteria that serves to efflux guanidinium from those cells[49]. C99 is a 14 kDa protein that plays a role in the development of amyloid β oligomers[11,50]. Of the three main methodologies, we find that FPLC is the most efficient method, albeit still yielding incomplete exchange in most cases. DLS data demonstrate that some of the detergents, such as octaethylene glycol monododecyl ether (C12E8), do not form micelles under nMS buffer conditions at concentrations twice the published CMC for detergent. Furthermore, we have observed that exchanges from a detergent exhibiting a low CMC into another detergent possessing a higher CMC leads to more efficient exchange when compared with scenarios in which an exchange is performed from a detergent possessing a higher CMC to a detergent with a lower CMC, suggesting that ease of micelle formation is a key component of predicting successful detergent exchange. We conclude by discussing the future of detergent exchange procedures for nMS.

3.3 Materials and Methods

3.3.1 Materials

Ammonium acetate was obtained from MilliporeSigma (St. Louis, MO). C12E8, tetraethylene glycol monooctyl ether (C8E4), n-Octyl-β-D-glucopyranoside (OG), β-n-decyl maltoside (DM) and lyso-myristoylphosphatidylglycerol (LMPG) were purchased from Anatrace (Maumee, OH). PMP22 (50 µM) was expressed and purified from *Escherichia coli* using previously published protocols into DM micelles (0.15%), 1 mM TCEP, 15 mM imidazole and 50 mM TRIS (pH=8.0) according to previously described protocols[48]. GDX was also purified from *E. coli* into DM micelles (4 mM), 100 mM NaCl, and 10 mM HEPES (pH=8.0)[49]. C99 was purified and expressed from *E. coli* cultures into LMPG micelles (10%), 100 mM imidazole and 2 mM EDTA (pH=6.5)[51].

3.3.2 BioSpin Detergent Exchange

Micro BioSpin P-6 columns (Bio-Rad, Hercules, CA) were used to perform buffer exchange. The storage buffer was eluted through the column at 1 g for 2 minutes. The column was then washed with the new buffer, containing 2X CMC of the new detergent in 200 mM ammonium acetate (pH=7.4) for 4 times at 1 g for 1 minute, followed by a final wash at 1 g for 4 minutes. 50 μM of sample was then loaded onto the column and eluted at 1 g for 4 minutes prior to MS analysis.

3.3.3 Centrifugal Filter Detergent Exchange

50 μL of protein were added to 450 μL of 200 mM ammonium acetate (pH=7.4) with 2X CMC of the detergent into which the protein was being exchanged. The sample was incubated on ice for 30 minutes. The sample was then loaded on to a 10 kDa MWCO Amicon 0.5 mL ultracentrifugal unit (MilliporeSigma) and centrifuged at 6 g in 6 minute intervals until the volume remaining within the filter fell below 100 μL. The eluent was discarded.

3.3.4 Size Exclusion Chromatography

FPLC enabled 100 uL of protein to be simultaneously buffer and detergent exchanged using Size Exclusion Chromatography (SEC) with a Superdex S200 column (Cytiva, Marlborough, MA) in 200 mM Ammonium Acetate (pH=7.4) with 2X CMC of the detergent into which the protein was exchanged. After loading and eluting the protein, fractions with protein signal were pooled and concentrated with a 10 kDa MWCO Amicon 0.5 mL ultracentrifugal unit (MilliporeSigma) and centrifuged at 6 g at 6 minute intervals until the volume remaining within the filter was 100 μL.

3.3.5 Dynamic Light Scattering

Dynamic Light Scattering (DLS) measurements of protein incorporated detergent micelles were obtained using DynaPro NanoStar (Wyatt Technology, Santa Barbara, CA) to evaluate detergent micelle diameter size. Samples were prepared by the detergent exchange methods outlined above and filtered using 0.22 µM (MilliporeSigma) filters. 10 µL of sample was loaded onto a disposable DLS cuvette, and measurements were taken in triplicate. Measurements were taken at 25°C, with 5 second acquisition collections, and with 10 total acquisitions. The apparent radius was calculated with the DLS Dynamics 7 software (Wyatt Technology).

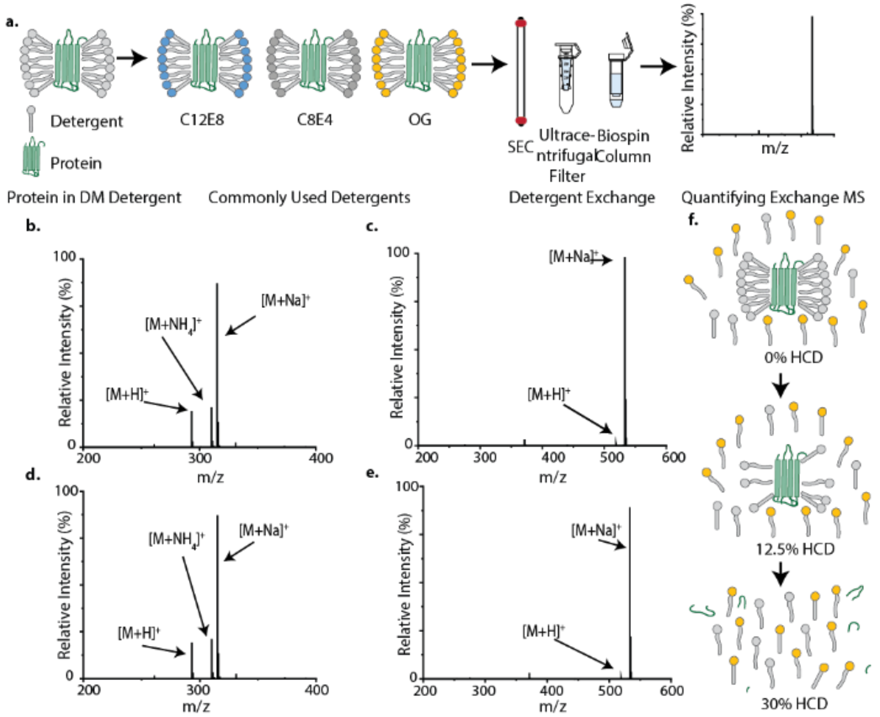

Figure 3-1 Overview of detergent exchange methodology (a) A target MP initially solubilized in its primary detergent micelles is exchanged into various secondary detergents with each of the three common nMS detergent exchange methods followed by nMS analysis for quantification of the exchange. Empty detergent micelles were run as controls and nMS spectra of C12E8 at b) 0% HCD and (c) 30% HCD showed no fragmentation as well as nMS spectra of OG at (d) 0% HCD and (e) 30% HCD. Controls were used to identify peaks following exchange. (f) at 0% HCD detergent molecules are not being activated and therefore have not been removed from the MP, while at 12.5% HCD detergent molecules begin dissociating off leaving the MP undisturbed and at 30% HCD all detergent molecules that encapsulated the MP can be seen.

3.3.6 nMS Data Acquisition

nMS data were collected on an Orbitrap Fusion Lumos (ThermoFisher, San Jose, CA). Samples were infused directly onto the MS using a NanoSpray Flex ion source (ThermoFisher) in positive polarity. 100 kV of in-source dissociation was employed to aid in the liberation of proteins from micelles, and the temperature of the transfer tube was also raised to 325 degrees to augment demicellization. 1.8 kV of capillary voltage was applied to a borosilicate emitter coated in gold, which was fabricated in house using a P-97 pitter puller (Sutter Instruments, Novato, CA). Data was collected with a resolution of 120000 at 300 Th. The instrument was operated with an extended mass range up to 4000 Th with an RF amplitude of 30%. Protein ions were collisionally activated with higher energy collisional dissociation (HCD) energies up to 30% in the ion-routing multipole. MS data were analyzed using FreeStyle (ThermoFisher). The ionization efficiency of each detergent molecule was measured on the Lumos to ensure that variations in efficiency did not significantly alter our analysis.

3.4 Results and Discussion

3.4.1 Quantifying Detergent Exchange Efficiency

To investigate detergent exchange efficiency across multiple MPs, PMP22 and GDX were selected for our initial analysis. These proteins were both originally expressed and purified in DM[33], one of the most common detergents employed for MP purification. C12E8, C8E4, and OG were selected for detergent exchange due to their shared nonionic and nondenaturing properties, combined with their prevalence in nMS workflows[14]. PMP22 and GDX were each exchanged using three methodologies: Amicon ultracentrifugal devices[28], BioSpin columns[6,38], and FPLC[6]. The efficacy of these exchanges was quantified by manually identifying the primary detergent peaks (DM) and subsequently identifying the peaks of detergent into the secondary detergent in which it was exchanged. From there, the signals from the primary detergent were summed against the total signal of the secondary detergent, yielding a percentage that we used to quantify the relative amount of each detergent remaining in the sample (Figure 3-1a).

Control samples were acquired for all secondary detergents using empty detergent micelles to identify detergent signals and verify that no detergent fragmentation was occurring under our instrument conditions (Figure 3-1b-e), as well as to evaluate the ionization efficiencies and ion suppression properties of each surfactant (Table IV-1) These findings supported the validity of including all detergent signals in the calculations to determine exchange efficiency. Salt adduction was consistently observed in our dataset, an observation reflected in prior reports.[6] We hypothesized that by using increasing the activation energy settings from 0, 12.5, and 30% HCD energy, the demicellization process of the MPs could be tracked. During demicellization, detergent molecules are stripped away from the MP through collisional activation, whilst leaving protein complexes intact.[52] At 0% HCD, we observe no detectable signals corresponding to protein ions, with the only observable signals in the spectra corresponding to free detergents in the sample, as without applying HCD activation, the MP is likely still ensconced within the gas-phase micelle. (Figure IV-1, IV-2) When we apply an HCD activation level of 12.5%, low intensity protein signals are observed, with charge state distributions indicative of compact native-like ions. (Figure IV-3a,b) The persistence of detergent signals suggests that some protein-micelle complexes continue to exist under these conditions. Finally, at an HCD activation level of 30%, we detect signals for MP fragments and detergent ions, with the latter appearing at higher abundance (Figure 3-2), indicating that these detergent ions represent a population of molecules the last to be ejected from the protein-micelle by virtue of strong intermolecular interactions with the MP. Thereby, we view MS data collected at 30% HCD energy is the best indicator of detergent exchange success, as these data are more likely to correspond to the detergent population bound to the MP (Figure 3-1e).

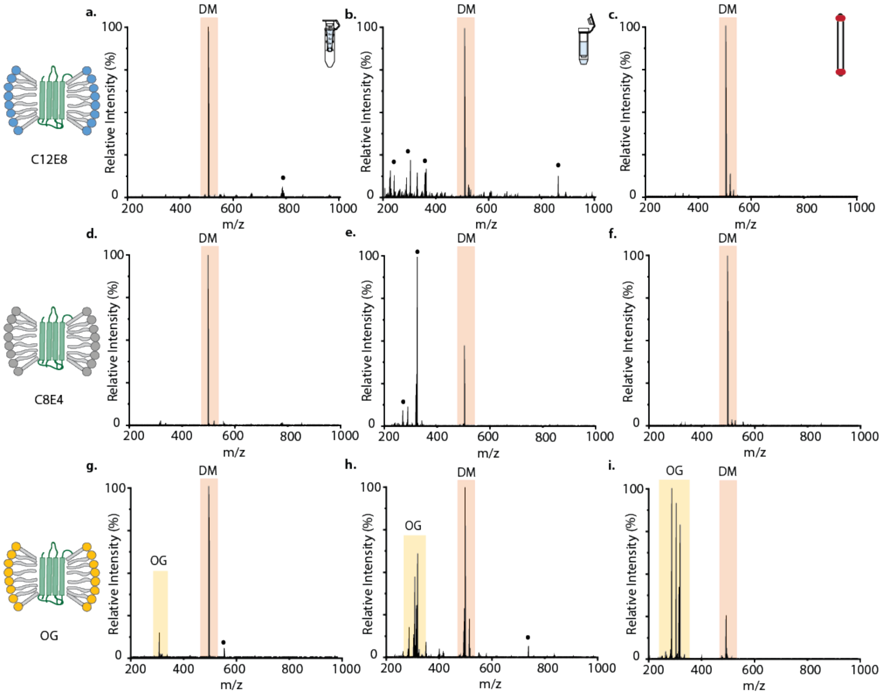

Figure 3-2 nMS spectra of PMP22 detergent exchanged from DM into C12E8 (a-c), C8E4 (d-f) and OG (g-i) by Amicon, BioSpin, and SEC methods each (left to right) at 30% HCD. DM signals are highlighted in orange. C12E8 and C8E4 signals are not apparent in the spectra due to their relatively low abundance in comparison to DM signals, while OG signals can be observed and are highlighted in yellow. Additional signals seen in the spectra that are annotated with a circle can be found in the supporting information. (Table IV-2)

3.4.2 Critical Micelles Concentration is the Most Significant Property Affecting Exchange Efficiency

Although the published physical properties of each detergent in our study vary widely, existing detergent exchange guidelines require all detergents to be used at a concentration equivalent to twice (2X) its published CMC in solution[28]. Taken as a whole, our data clearly indicate that the CMC of each detergent significantly impacts the efficacy of the exchange. For example, our PMP22 exchange data from DM to C12E8, which has a 2X CMC of 0.02 mM, reveals little evidence of exchange regardless of the exchange method employed. Similarly, our PMP22 exchange data from DM into C8E4, which has a 2X CMC of 16 mM, exhibited a greater exchange efficiency when compared to our C12E8 data described above. The most efficient exchanges occurred when proteins were exchanged into OG, which has a 2X CMC of 40 mM, the highest CMC out of all three detergents tested in this study. For PMP22 samples containing DM, exchange into OG is strongly method dependent, with Amicon filters providing the least exchange, BioSpin columns generating intermediate efficiencies, and FPLC methods providing the most complete amount of detergent exchange (Figure 3-2). These results further indicate that, in addition to CMC, the methodology chosen directly impacts detergent exchange efficiency. Similar data collected using GDX and C99 reveal similar trends, and the corresponding nMS spectra can be found in Appendix IV (Figure IV-3,4).

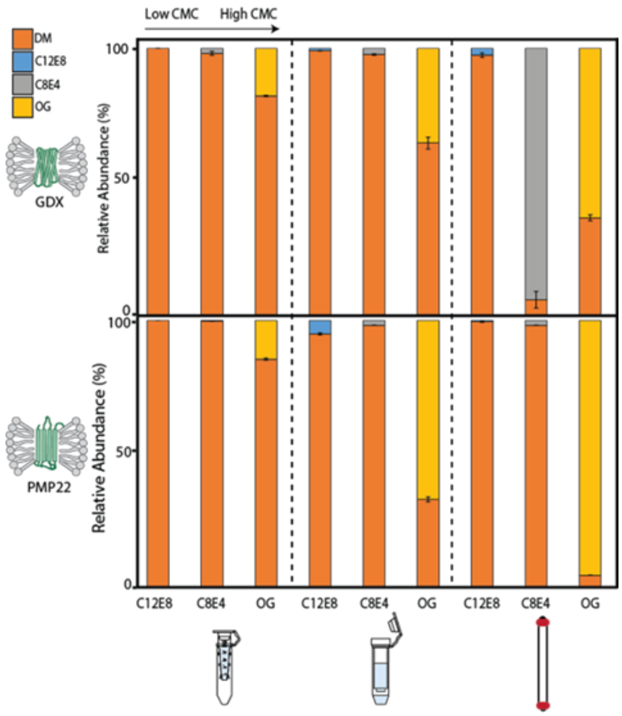

Figure 3-3 GDX (top) and PMP22(bottom) in DM as the primary detergent micelles, detergent exchanged into respective secondary detergents listed on the independent axis (2X CMC C12E8, C8E4, and OG) along with various exchange methods: Amicon, BioSpin, and FPLC (N=3). In the case of detergent exchanges with all three methods, GDX and PMP22 see minimal (0-5%) exchange of the pre-existing DM detergent with C12E8. Similar results are observed in C8E4, Amicon and BioSpin method exchanges (0-2%) but a surprising 94% exchange with FPLC (GDX) and only 2% (PMP22). Exchange with OG produced the most successful exchanges and an observable increasing trend throughout Amicon (14-17%), BioSpin (35-67%), and FPLC (63-96%) corresponding to OG signals.

We continued to quantify the detergent exchange observed in our data. This data (Figure 3-3), collected using GDX and PMP22, reveal minimal detergent exchange overall when DM is used as the starting surfactant. For example, exchange of MPs from DM to C12E8 yields values that range between 0-5% of C12E8 present in the final sample when Amicon filters are used. Similar results were obtained for C8E4, where we observe between 0-2% of C8E4 in the exchanged sample.

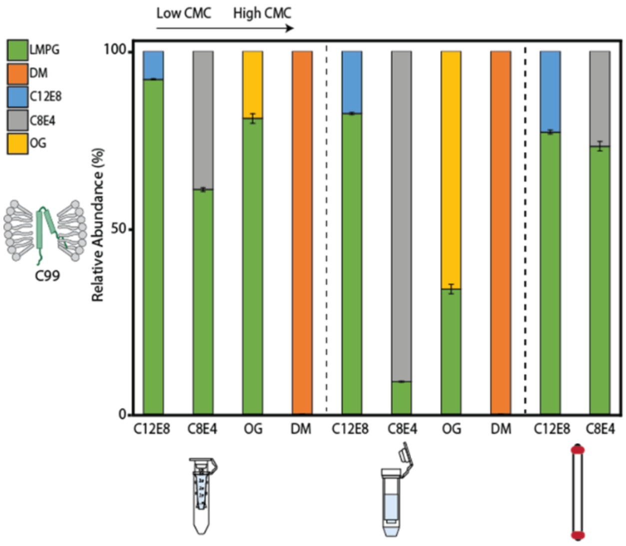

Figure 3-4 C99 in LMPG as the primary detergent micelles, detergent exchanged into secondary detergents listed on the independent axis (2X CMC C12E8, C8E4, OG, and DM) along with various exchange methods: Amicon, Biospin, and SEC (N=3). Although OG and DM were deemed incompatible with C99, C12E8 and C8E4 saw an increase in efficiency in C12E8 exchanges with Amicon, BioSpin, and SEC (8%, 17%, and 22%), meanwhile C8E4 resulted in 38%, 91%, and 26% with Amicon, BioSpin, and FPLC methods.

Exchange from DM to OG produced the most efficient exchange for both GDX and PMP22, with Amicon filters producing OG signals accounting for 14-17% of detergent signals recorded by MS in exchanged samples. BioSpin columns produced more efficient OG exchange, resulting in efficiency values ranging between 35-67%. The most efficient OG exchange was achieved using FPLC, yielding an exchange from DM samples with efficiencies ranging between 63-97% for the GDX and PMP22 samples tested here. Most of our detergent exchange experiments involving C8E4 resulted in a highly inefficient exchange, with the exception of those involving DM containing GDX samples exchanged using FPLC, which resulted in an exchange efficiency of 96%. This outlier data can most likely be attributed to an apparent affinity between GDX and C8E4 detergent, and further illustrates the need to evaluate a wide range of surfactants for MP nMS[28].

To determine if the low exchange efficiencies discussed above were primarily a product of the presence of DM surfactant in all the pre-exchanged samples studied in Figure 3-3, the repeated the experiments described above using C99 purified and stored in LMPG (Figure IV-3c, IV-4). Results were consistent with the low exchange efficiencies tracked in Figure 3-3 for DM containing samples, identifying C12E8 as exhibiting the lowest exchange efficiency compared to other detergents studied here. However, compared to GDX and PMP22 exchange data discussed above, we noted improved exchange into C12E8 for the LMPG samples containing C99 throughout all the methods screened here, yielding exchange efficiency values ranging from 8-22% with Amicon filters providing the least efficient exchange and FPLC providing the most efficient exchange. We observe an increase in exchange efficiency for LMPG samples exchanged into C8E4, producing efficiencies ranging from 38-91%. Interestingly, the most efficient exchange observed for LMPG C99 samples into C8E4 was achieved using Biospin columns rather than FPLC. Finally, we observe notably less efficient exchange values for LMPG C99 samples into OG when compared to C8E4. (Figure 3-4) This is likely due to the incompatibility between C99 and OG, as C99 was observed to precipitate out of solution upon exposure to OG in several of our experiments and precluded the collection of FPLC data for the relevant OG C99 samples.

To further examine if exchange efficiencies are predetermined in part by the starting surfactant, we made a number of attempts to exchange C99 from LMPG into DM. Following these exchanges, the only detectable signals corresponded to DM. (Figure 3-4) However, like with OG, C99 appears to be incompatible with DM, as C99 precipitates when incubated with DM over a short period of time. The incompatibility of C99 with both OG and DM was further verified when multiple attempts to purify and store C99 in these detergents failed due to precipitation of the protein. Overall, the results from our LMPG C99 samples support the low overall exchange efficiencies, alongside the method and protein dependencies observed for our DM exchange experiments described in Figure 3-3. In addition, LMPG exchange data leads to larger overall exchange efficiencies when compared to DM samples, indicating a dependence on the starting detergent that dictates the overall exchange efficiency achieved.

To determine if an increase in detergent concentration would improve the efficiency of detergent exchange observed, we exchanged DM containing PMP22 into 100X CMC C12E8 using the Amicon filter method. Results for this experiment indicated incomplete exchange, yielding DM MS signals corresponding to 26% of the total ion current recorded, with the remaining 74% of signals corresponded to C12E8 (Figure IV-5). When compared with our results for DM containing PMP22 exchanged into 2X CMC C12E8 (Figure 3-3), which produced 100% of signals recorded related to DM, the 50X increase in C12E8 concentration resulted in a significant increase in detergent exchange. While these results support the observation that exchange efficiency is correlated with the CMC, and thus concentration, of final intended detergent, such high detergent concentrations do not provide a route toward an improved detergent exchange protocol for nMS, as they typically lead to untenable levels of adduction and chemical noise.

In order to evaluate the state of the micelle populations produced under typical nMS conditions, we conducted DLS analysis of all detergents in 200 mM Ammonium Acetate solutions. Our data demonstrates that C12E8 does not form micelles in solution at 2X CMC under our experimental conditions. Overall, detergent stocks at several concentrations were tested (0.5X, 1X, 2X and 10X CMC) and it was observed that at 0.5X CMC C12E8 and C8E4 and DM did not form observable micelles, whereas OG, DM, and LMPG formed ~8 nm micelles. In addition, at 1X CMC we detected no micelles for C12E8 and C8E4, and observed micellar formation for OG, LMPG, and DM. At 2X CMC no micellar formation was observed for C12E8, and micelles were detected for OG, LMPG, DM, and C8E4. Finally, at 10X CMC all

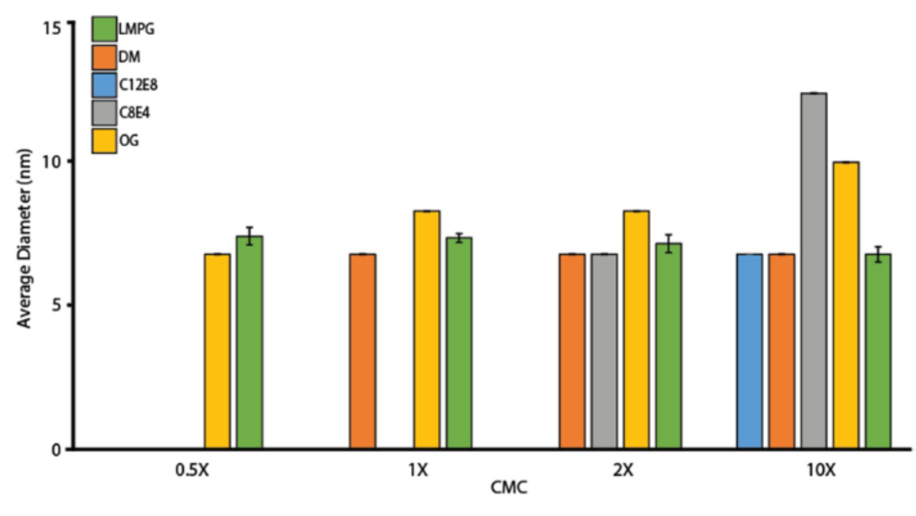

Figure 3-5 Average Diameter (nm) of C12E8, DM, C8E4, and OG at 0.5X, 1X, 2X and 10X CMC measured with DLS. Missing bars indicate that no micelles were detected under the conditions indicated.

detergents formed micelles, (Figure 3-5) Taken together, these findings confirm that the non-ionic detergents studied here that possess lower CMCs do not form micelles in ammonium acetate, which provides an explanation for the low exchange efficiencies observed in Figures 3-2, 3-3, and 3-4

3.4.3 BioSpin P-6 Columns Increase Exchange Efficiency

Standard FPLC utilizes a longer path length and thus should result in more efficient detergent exchange. While FPLC is often the most efficient exchange method tested in our dataset, we also observed exceptions to this expectation in the context of C12E8 and C8E4 detergent exchange. In order better evaluate the influence of the effective column path length on our detergent exchange efficiency results, we chose to employ serial BioSpin centrifugal column exchanges, testing the level of exchange after each successive BioSpin column is used (Figure 3-6). We performed sequential rounds of such detergent exchange using BioSpin columns using DM GDX samples, exchanged into C12E8, C8E4, and OG. The results indicate that with one additional round of exchange, the primary DM surfactant is removed from the sample at least two-fold more efficiently when compared to one round of exchange. Following one exchange

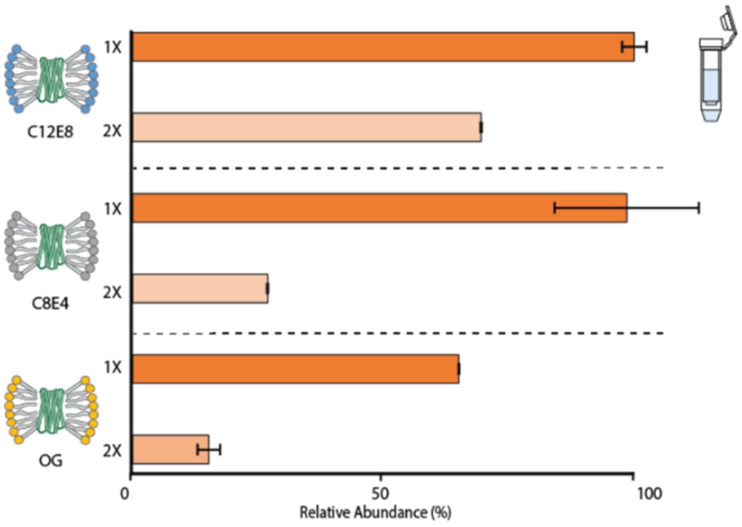

Figure 3-6 Percent DM remaining after detergent exchange of GDX with 2X CMC C12E8, C8E4, and OG performed with the BioSpin method. After 1 round (dark orange) of exchange, we observed 64-99% DM remains in the samples. Following 2 rounds (light orange) of exchanges we observed significantly improved exchange with 15-68% DM remaining in the samples.

with C12E8, DM signals account for 99% of the signals detected, following two C12E8 exchanges, this value decreased to 69%. Similarly, after completing one BioSpin exchange into C8E4, 98% of detected MS signals are related to DM, whereas this value decreases to 27% following two Biospin exchange steps. Lastly, when DM GDX samples are subjected to one exchange with OG, 64% of observed MS ion current is carried by DM signals, and this value drops to 15% following a subsequent BioSpin exchange. These results are consistent with previous observations that exchange efficiency qualitatively increases following subsequent exchange operations. Although the primary surfactant is never fully removed in our experiments, our data indicates that more than one round of detergent exchange is likely required in MP sample preparation workflows for nMS to ensure sufficiently efficient detergent exchange.

3.5 Conclusions

Here, this critical analysis of the efficiencies of existing detergent exchange methodologies were probed, revealing that these methodologies often yield incomplete exchange. In all the experiments we conducted, across several commonly used detergents and MP archetypes, no instances of complete detergent exchange were observed. FPLC was the most efficient means of detergent exchange tested here; however, FPLC is often impractical for routine nMS experiments, as it can take up to 90 min to conduct and requires large amounts (~1 L) of detergent. FPLC is likely more effective due to its larger number of theoretical plates when compared to shorter centrifugal columns and filters. Detergent exchange efficiency can be improved by increasing the number of exchanges performed, such as doing multiple rounds of BioSpin buffer exchange. (Figure 6)

The lack of complete detergent exchange observed in our dataset could be due to several factors. DLS data collected across the detergents screened here indicates that micelle formation in ammonium acetate occurs at concentrations far in excess of published CMCs for a number of detergents, such as C12E8. Additionally, mixed micelles may be forming with the primary and secondary detergents. Previous studies have shown that mixed detergent mimetic environments can be formed during detergent exchange, and that the resulting mixed mimetic environment can influence the stability of the MP studied,[47,53,54] thus highlighting the importance of maintaining quantitative control over the detergent environment when MP structure data is pursued by nMS and associated methods.

Understanding the detergent exchange process is critical for the careful study of MP structure and function. While existing protocols do adequately allow for MPs to be observed by nMS, they do not account for the likelihood of incomplete exchange, which leads to micelles of mixed compositions or largely composed of the starting detergent in most cases. Detergents can contribute to chemical noise populations, influencing the nMS analysis of small MPs[30]. As such, control of the detergent populations is critical for controlling such noise in nMS experiments. In addition, multiple studies have demonstrated that detergents can influence MP structure and stability, indicating that the detergent environment deployed to study an MP should be carefully accounted for when performing nMS experiments[42–47]. The data presented here provides nMS practitioners tools that can be used to reduce the ambiguity underlying current detergent exchange methods.

3.6 References

(1) Nicolson, G. L. The Fluid—Mosaic Model of Membrane Structure: Still Relevant to Understanding the Structure, Function and Dynamics of Biological Membranes after More than 40years. Biochimica et Biophysica Acta (BBA) - Biomembranes 2014, 1838 (6), 1451–1466. https://doi.org/10.1016/j.bbamem.2013.10.019.
(2) Choy, B. C.; Cater, R. J.; Mancia, F.; Pryor, E. E. A 10-Year Meta-Analysis of Membrane Protein Structural Biology: Detergents, Membrane Mimetics, and Structure Determination Techniques. Biochimica et Biophysica Acta (BBA) - Biomembranes 2021, 1863 (3), 183533. https://doi.org/10.1016/j.bbamem.2020.183533.
(3) Shimizu, K.; Cao, W.; Saad, G.; Shoji, M.; Terada, T. Comparative Analysis of Membrane Protein Structure Databases. Biochimica et Biophysica Acta (BBA) - Biomembranes 2018, 1860 (5), 1077–1091. https://doi.org/10.1016/j.bbamem.2018.01.005.
(4) Seddon, A. M.; Curnow, P.; Booth, P. J. Membrane Proteins, Lipids and Detergents: Not Just a Soap Opera. Biochimica et Biophysica Acta (BBA) - Biomembranes 2004, 1666 (1), 105–117. https://doi.org/10.1016/j.bbamem.2004.04.011.
(5) Ratkeviciute, G.; Cooper, B. F.; Knowles, T. J. Methods for the Solubilisation of Membrane Proteins: The Micelle-Aneous World of Membrane Protein Solubilisation. Biochemical Society Transactions 2021, 49 (4), 1763–1777. https://doi.org/10.1042/BST20210181.
(6) Keener, J. E.; Zhang, G.; Marty, M. T. Native Mass Spectrometry of Membrane Proteins. Anal. Chem. 2021, 93 (1), 583–597. https://doi.org/10.1021/acs.analchem.0c04342.
(7) Marty, M. T.; Hoi, K. K.; Robinson, C. V. Interfacing Membrane Mimetics with Mass Spectrometry. Acc. Chem. Res. 2016, 49 (11), 2459–2467. https://doi.org/10.1021/acs.accounts.6b00379.
(8) Thoma, J.; Burmann, B. M. Fake It 'Till You Make It—The Pursuit of Suitable Membrane Mimetics for Membrane Protein Biophysics. International Journal of Molecular Sciences 2021, 22 (1), 50. https://doi.org/10.3390/ijms22010050.
(9) Frey, L.; Lakomek, N.-A.; Riek, R.; Bibow, S. Micelles, Bicelles, and Nanodiscs: Comparing the Impact of Membrane Mimetics on Membrane Protein Backbone Dynamics. Angewandte Chemie International Edition 2017, 56 (1), 380–383. https://doi.org/10.1002/anie.201608246.
(10) Hoi, K. K.; Bada Juarez, J. F.; Judge, P. J.; Yen, H.-Y.; Wu, D.; Vinals, J.; Taylor, G. F.; Watts, A.; Robinson, C. V. Detergent-Free Lipodisq Nanoparticles Facilitate High-Resolution Mass Spectrometry of Folded Integral Membrane Proteins. Nano Lett. 2021, 21 (7), 2824–2831. https://doi.org/10.1021/acs.nanolett.0c04911.
(11) Hutchison, J. M.; Shih, K.-C.; Scheidt, H. A.; Fantin, S. M.; Parson, K. F.; Pantelopulos, G. A.; Harrington, H. R.; Mittendorf, K. F.; Qian, S.; Stein, R. A.; Collier, S. E.; Chambers, M. G.; Katsaras, J.; Voehler, M. W.; Ruotolo, B. T.; Huster, D.; McFeeters, R. L.; Straub, J. E.; Nieh, M.-P.; Sanders, C. R. Bicelles Rich in Both Sphingolipids and Cholesterol and Their Use in Studies of Membrane Proteins. J. Am. Chem. Soc. 2020, 142 (29), 12715–12729. https://doi.org/10.1021/jacs.0c04669.

(12) Lee, D.; Walter, K. F. A.; Brückner, A.-K.; Hilty, C.; Becker, S.; Griesinger, C. Bilayer in Small Bicelles Revealed by Lipid−Protein Interactions Using NMR Spectroscopy. J. Am. Chem. Soc. 2008, 130 (42), 13822–13823. https://doi.org/10.1021/ja803686p.

(13) Henrich, E.; Peetz, O.; Hein, C.; Laguerre, A.; Hoffmann, B.; Hoffmann, J.; Dötsch, V.; Bernhard, F.; Morgner, N. Analyzing Native Membrane Protein Assembly in Nanodiscs by Combined Non-Covalent Mass Spectrometry and Synthetic Biology. Elife 2017, 6, e20954. https://doi.org/10.7554/eLife.20954.

(14) Keener, J. E.; Zambrano, D. E.; Zhang, G.; Zak, C. K.; Reid, D. J.; Deodhar, B. S.; Pemberton, J. E.; Prell, J. S.; Marty, M. T. Chemical Additives Enable Native Mass Spectrometry Measurement of Membrane Protein Oligomeric State within Intact Nanodiscs. J. Am. Chem. Soc. 2019, 141 (2), 1054–1061. https://doi.org/10.1021/jacs.8b11529.

(15) Frick, M.; Schwieger, C.; Schmidt, C. Liposomes as Carriers of Membrane-Associated Proteins and Peptides for Mass Spectrometric Analysis. Angewandte Chemie International Edition 2021, 60 (20), 11523–11530. https://doi.org/10.1002/anie.202101242.

(16) Calabrese, A. N.; Watkinson, T. G.; Henderson, P. J. F.; Radford, S. E.; Ashcroft, A. E. Amphipols Outperform Dodecylmaltoside Micelles in Stabilizing Membrane Protein Structure in the Gas Phase. Anal. Chem. 2015, 87 (2), 1118–1126. https://doi.org/10.1021/ac5037022.

(17) Chorev, D. S.; Baker, L. A.; Wu, D.; Beilsten-Edmands, V.; Rouse, S. L.; Zeev-Ben-Mordehai, T.; Jiko, C.; Samsudin, F.; Gerle, C.; Khalid, S.; Stewart, A. G.; Matthews, S. J.; Grünewald, K.; Robinson, C. V. Protein Assemblies Ejected Directly from Native Membranes Yield Complexes for Mass Spectrometry. Science 2018, 362 (6416), 829–834. https://doi.org/10.1126/science.aau0976.

(18) Chen, S.; Getter, T.; Salom, D.; Wu, D.; Quetschlich, D.; Chorev, D. S.; Palczewski, K.; Robinson, C. V. Capturing a Rhodopsin Receptor Signalling Cascade across a Native Membrane. Nature 2022, 604 (7905), 384–390. https://doi.org/10.1038/s41586-022-04547-x.

(19) Karch, K. R.; Snyder, D. T.; Harvey, S. R.; Wysocki, V. H. Native Mass Spectrometry: Recent Progress and Remaining Challenges. Annu Rev Biophys 2022, 51, 157–179. https://doi.org/10.1146/annurev-biophys-092721-085421.

(20) Vallejo, D. D.; Rojas Ramírez, C.; Parson, K. F.; Han, Y.; Gadkari, V. V.; Ruotolo, B. T. Mass Spectrometry Methods for Measuring Protein Stability. Chem Rev 2022, 122 (8), 7690–7719. https://doi.org/10.1021/acs.chemrev.1c00857.

(21) Mehmood, S.; Allison, T. M.; Robinson, C. V. Mass Spectrometry of Protein Complexes: From Origins to Applications. Annu Rev Phys Chem 2015, 66, 453–474. https://doi.org/10.1146/annurev-physchem-040214-121732.

(22) Barth, M.; Schmidt, C. Native Mass Spectrometry—A Valuable Tool in Structural Biology. Journal of Mass Spectrometry 2020, 55 (10), e4578. https://doi.org/10.1002/jms.4578.

(23) Fantin, S. M.; Huang, H.; Sanders, C. R.; Ruotolo, B. T. Collision-Induced Unfolding Differentiates Functional Variants of the KCNQ1 Voltage Sensor Domain. J. Am. Soc. Mass Spectrom. 2020, 31 (11), 2348–2355. https://doi.org/10.1021/jasms.0c00288.

(24) Fantin, S. M.; Parson, K. F.; Yadav, P.; Juliano, B.; Li, G. C.; Sanders, C. R.; Ohi, M. D.; Ruotolo, B. T. Ion Mobility–Mass Spectrometry Reveals the Role of Peripheral Myelin Protein Dimers in Peripheral Neuropathy. Proceedings of the National Academy of Sciences 2021, 118 (17), e2015331118.

(25) Konijnenberg, A.; van Dyck, J. F.; Kailing, L. L.; Sobott, F. Extending Native Mass Spectrometry Approaches to Integral Membrane Proteins. Biol Chem 2015, 396 (9–10), 991–1002. https://doi.org/10.1515/hsz-2015-0136.

(26) Cong, X.; Liu, Y.; Liu, W.; Liang, X.; Russell, D. H.; Laganowsky, A. Determining Membrane Protein–Lipid Binding Thermodynamics Using Native Mass Spectrometry. J. Am. Chem. Soc. 2016, 138 (13), 4346–4349. https://doi.org/10.1021/jacs.6b01771.

(27) Sahin, C.; Reid, D. J.; Marty, M. T.; Landreh, M. Scratching the Surface: Native Mass Spectrometry of Peripheral Membrane Protein Complexes. Biochemical Society Transactions 2020, 48 (2), 547–558. https://doi.org/10.1042/BST20190787.

(28) Laganowsky, A.; Reading, E.; Hopper, J. T. S.; Robinson, C. V. Mass Spectrometry of Intact Membrane Protein Complexes. Nat Protoc 2013, 8 (4), 639–651. https://doi.org/10.1038/nprot.2013.024.

(29) Yen, H.-Y.; Liko, I.; Song, W.; Kapoor, P.; Almeida, F.; Toporowska, J.; Gherbi, K.; Hopper, J. T. S.; Charlton, S. J.; Politis, A.; Sansom, M. S. P.; Jazayeri, A.; Robinson, C. V. Mass Spectrometry Captures Biased Signalling and Allosteric Modulation of a G-Protein-Coupled Receptor. Nat. Chem. 2022, 1–8. https://doi.org/10.1038/s41557-022-01041-9.

(30) Fantin, S. M.; Parson, K. F.; Niu, S.; Liu, J.; Polasky, D. A.; Dixit, S. M.; Ferguson-Miller, S. M.; Ruotolo, B. T. Collision Induced Unfolding Classifies Ligands Bound to the Integral Membrane Translocator Protein. Anal. Chem. 2019, 91 (24), 15469–15476. https://doi.org/10.1021/acs.analchem.9b03208.

(31) Gupta, K.; Donlan, J. A. C.; Hopper, J. T. S.; Uzdavinys, P.; Landreh, M.; Struwe, W. B.; Drew, D.; Baldwin, A. J.; Stansfeld, P. J.; Robinson, C. V. The Role of Interfacial Lipids in Stabilizing Membrane Protein Oligomers. Nature 2017, 541 (7637), 421–424. https://doi.org/10.1038/nature20820.

(32) Townsend, J. A.; Keener, J. E.; Miller, Z. M.; Prell, J. S.; Marty, M. T. Imidazole Derivatives Improve Charge Reduction and Stabilization for Native Mass Spectrometry. Anal. Chem. 2019, 91 (22), 14765–14772. https://doi.org/10.1021/acs.analchem.9b04263.

(33) Stetsenko, A.; Guskov, A. An Overview of the Top Ten Detergents Used for Membrane Protein Crystallization. Crystals 2017, 7 (7), 197. https://doi.org/10.3390/cryst7070197.

(34) Urner, L. H. Advances in Membrane Mimetics and Mass Spectrometry for Understanding Membrane Structure and Function. Current Opinion in Chemical Biology 2022, 69, 102157. https://doi.org/10.1016/j.cbpa.2022.102157.

(35) Lee, H. J.; Lee, H. S.; Youn, T.; Byrne, B.; Chae, P. S. Impact of Novel Detergents on Membrane Protein Studies. Chem 2022, 8 (4), 980–1013. https://doi.org/10.1016/j.chempr.2022.02.007.

(36) Brown, K. A.; Chen, B.; Guardado-Alvarez, T. M.; Lin, Z.; Hwang, L.; Ayaz-Guner, S.; Jin, S.; Ge, Y. A Photocleavable Surfactant for Top-down Proteomics. Nat Methods 2019, 16 (5), 417–420. https://doi.org/10.1038/s41592-019-0391-1.

(37) Brown, K. A.; Gugger, M. K.; Yu, Z.; Moreno, D.; Jin, S.; Ge, Y. Nonionic, Cleavable Surfactant for Top-Down Proteomics. Anal. Chem. 2023, 95 (3), 1801–1804. https://doi.org/10.1021/acs.analchem.2c03916.

(38) Gault, J.; Liko, I.; Landreh, M.; Shutin, D.; Bolla, J. R.; Jefferies, D.; Agasid, M.; Yen, H.-Y.; Ladds, M. J. G. W.; Lane, D. P.; Khalid, S.; Mullen, C.; Remes, P. M.; Huguet, R.; McAlister, G.; Goodwin, M.; Viner, R.; Syka, J. E. P.; Robinson, C. V. Combining Native and "omics" Mass Spectrometry to Identify Endogenous Ligands Bound to Membrane Proteins. Nat Methods 2020, 17 (5), 505–508. https://doi.org/10.1038/s41592-020-0821-0.

(39) Ambrose, S.; Housden, N. G.; Gupta, K.; Fan, J.; White, P.; Yen, H.-Y.; Marcoux, J.; Kleanthous, C.; Hopper, J. T. S.; Robinson, C. V. Native Desorption Electrospray Ionization Liberates Soluble and Membrane Protein Complexes from Surfaces. Angewandte Chemie International Edition 2017, 56 (46), 14463–14468. https://doi.org/10.1002/anie.201704849.

(40) Borysik, A. J.; Hewitt, D. J.; Robinson, C. V. Detergent Release Prolongs the Lifetime of Native-like Membrane Protein Conformations in the Gas-Phase. J. Am. Chem. Soc. 2013, 135 (16), 6078–6083. https://doi.org/10.1021/ja401736v.

(41) Urner, L. H.; Liko, I.; Yen, H.-Y.; Hoi, K.-K.; Bolla, J. R.; Gault, J.; Almeida, F. G.; Schweder, M.-P.; Shutin, D.; Ehrmann, S.; Haag, R.; Robinson, C. V.; Pagel, K. Modular Detergents Tailor the Purification and Structural Analysis of Membrane Proteins Including G-Protein Coupled Receptors. Nat Commun 2020, 11 (1), 564. https://doi.org/10.1038/s41467-020-14424-8.

(42) Yang, Z.; Wang, C.; Zhou, Q.; An, J.; Hildebrandt, E.; Aleksandrov, L. A.; Kappes, J. C.; DeLucas, L. J.; Riordan, J. R.; Urbatsch, I. L.; Hunt, J. F.; Brouillette, C. G. Membrane Protein Stability Can Be Compromised by Detergent Interactions with the Extramembranous Soluble Domains. Protein Science 2014, 23 (6), 769–789. https://doi.org/10.1002/pro.2460.

(43) Lee, S.; Mao, A.; Bhattacharya, S.; Robertson, N.; Grisshammer, R.; Tate, C. G.; Vaidehi, N. How Do Short Chain Nonionic Detergents Destabilize G-Protein-Coupled Receptors? J. Am. Chem. Soc. 2016, 138 (47), 15425–15433. https://doi.org/10.1021/jacs.6b08742.

(44) Mouhib, M.; Benediktsdottir, A.; Nilsson, C. S.; Chi, C. N. Influence of Detergent and Lipid Composition on Reconstituted Membrane Proteins for Structural Studies. ACS Omega 2021, 6 (38), 24377–24381. https://doi.org/10.1021/acsomega.1c02542.

(45) Kurauskas, V.; Hessel, A.; Ma, P.; Lunetti, P.; Weinhäupl, K.; Imbert, L.; Brutscher, B.; King, M. S.; Sounier, R.; Dolce, V.; Kunji, E. R. S.; Capobianco, L.; Chipot, C.; Dehez, F.; Bersch, B.; Schanda, P. How Detergent Impacts Membrane Proteins: Atomic-Level Views of Mitochondrial Carriers in Dodecylphosphocholine. J. Phys. Chem. Lett. 2018, 9 (5), 933–938. https://doi.org/10.1021/acs.jpclett.8b00269.

(46) Zhou, H.-X.; Cross, T. A. Influences of Membrane Mimetic Environments on Membrane Protein Structures. Annu Rev Biophys 2013, 42, 361–392. https://doi.org/10.1146/annurev-biophys-083012-130326.

(47) Schlebach, J. P.; Cao, Z.; Bowie, J. U.; Park, C. Revisiting the Folding Kinetics of Bacteriorhodopsin. Protein Sci 2012, 21 (1), 97–106. https://doi.org/10.1002/pro.766.

(48) Schlebach, J. P.; Narayan, M.; Alford, C.; Mittendorf, K. F.; Carter, B. D.; Li, J.; Sanders, C. R. Conformational Stability and Pathogenic Misfolding of the Integral Membrane Protein PMP22. J. Am. Chem. Soc. 2015, 137 (27), 8758–8768. https://doi.org/10.1021/jacs.5b03743.

(49) Kermani, A. A.; Macdonald, C. B.; Gundepudi, R.; Stockbridge, R. B. Guanidinium Export Is the Primal Function of SMR Family Transporters. Proceedings of the National Academy of Sciences 2018, 115 (12), 3060–3065. https://doi.org/10.1073/pnas.1719187115.

(50) Song, Y.; Mittendorf, K. F.; Lu, Z.; Sanders, C. R. Impact of Bilayer Lipid Composition on the Structure and Topology of the Transmembrane Amyloid Precursor C99 Protein. J. Am. Chem. Soc. 2014, 136 (11), 4093–4096. https://doi.org/10.1021/ja4114374.

(51) Barrett, P. J.; Song, Y.; Van Horn, W. D.; Hustedt, E. J.; Schafer, J. M.; Hadziselimovic, A.; Beel, A. J.; Sanders, C. R. The Amyloid Precursor Protein Has a Flexible Transmembrane

Domain and Binds Cholesterol. Science 2012, 336 (6085), 1168–1171. https://doi.org/10.1126/science.1219988.

(52) Yen, H.-Y.; Abramsson, M. L.; Agasid, M. T.; Lama, D.; Gault, J.; Liko, I.; Kaldmäe, M.; Saluri, M.; Qureshi, A. A.; Suades, A.; Drew, D.; Degiacomi, M. T.; Marklund, E. G.; Allison, T. M.; Robinson, C. V.; Landreh, M. Electrospray Ionization of Native Membrane Proteins Proceeds via a Charge Equilibration Step. RSC Adv. 2022, 12 (16), 9671–9680. https://doi.org/10.1039/D2RA01282K.

(53) Kotov, V.; Bartels, K.; Veith, K.; Josts, I.; Subhramanyam, U. K. T.; Günther, C.; Labahn, J.; Marlovits, T. C.; Moraes, I.; Tidow, H.; Löw, C.; Garcia-Alai, M. M. High-Throughput Stability Screening for Detergent-Solubilized Membrane Proteins. Sci Rep 2019, 9 (1), 10379. https://doi.org/10.1038/s41598-019-46686-8.

(54) Tribet, C.; Diab, C.; Dahmane, T.; Zoonens, M.; Popot, J.-L.; Winnik, F. M. Thermodynamic Characterization of the Exchange of Detergents and Amphipols at the Surfaces of Integral Membrane Proteins. Langmuir 2009, 25 (21), 12623–12634. https://doi.org/10.1021/la9018772

Chapter 4 Performance Evaluation of In-source Ion Activation Hardware for Collision-Induced Unfolding of Proteins and Protein Complexes on a Drift Tube Ion Mobility-Mass Spectrometer

Adapted with permission from: Gadkari, V. V.; Juliano, B. R.; Mallis, C. S.; May, J. C.; Kurulugama, R. T.; Fjeldsted, J. C.; McLean, J. A.; Russell, D. H.; Ruotolo, B. T. Performance Evaluation of In-Source Ion Activation Hardware for Collision-Induced Unfolding of Proteins and Protein Complexes on a Drift Tube Ion Mobility-Mass Spectrometer. *Analyst* 2023, 148 (2), 391–401.

4.1 Abstract

Native ion mobility-mass spectrometry (IM-MS) has emerged as an information-rich technique for gas phase protein structure characterization; however, IM resolution is currently insufficient for the detection of subtle structural differences in large biomolecules. This challenge has spurred the development of collision-induced unfolding (CIU) which utilizes incremental gas phase activation to unfold a protein in order to expand the number of measurable descriptors available for native protein ions. Although CIU is now routinely used in native mass spectrometry studies, the interlaboratory reproducibility of CIU has not been established. Here we evaluate the reproducibility of the CIU data produced across three laboratories (University of Michigan, Texas A&M University, and Vanderbilt University). CIU data were collected for a variety of protein ions ranging from 8.6–66 kDa. Within the same laboratory, the CIU fingerprints were found to be repeatable with root mean square deviation (RMSD) values of less than 5%. Collision cross section (CCS) values of the CIU intermediates were consistent across the laboratories, with most features exhibiting an interlaboratory reproducibility of better than 1%. In contrast, the activation potentials required to induce protein CIU transitions varied between the three laboratories. To address these differences, three source assemblies were

constructed with an updated ion activation hardware design utilizing higher mechanical tolerance specifications. The production-grade assemblies were found to produce highly consistent CIU data for intact antibodies, exhibiting high precision ion CCS and CIU transition values, thus opening the door to establishing databases of CIU fingerprints to support future biomolecular classification efforts.

4.2 Introduction

Native mass spectrometry (MS) has rapidly grown as a robust technique for making measurements of proteins and their complexes.[1]Samples are prepared in aqueous, pH-adjusted electrolyte solutions of volatile salt (usually ammonium acetate) and ionized gently, preserving transient, non-covalent interactions from solution to the gas phase. Improvements in ionization[2,3] and instrumentation[4–11]have expanded the accessible mass range, enabling routine analysis of larger proteins such as intact antibodies,[12–15] membrane protein complexes,[16–22] protein chaperones,[9,10,23–25] and complete viral particles.[26] The coupling of ion mobility (IM) with native MS has spurred the field of native ion mobility-mass spectrometry (IM-MS) wherein ions are separated by size, shape, and charge prior to MS analysis. For uniform field drift tubes, ion arrival times can be converted to a rotationally averaged collision cross section (CCS) *via*the low-field IM relationship prescribed by the Mason–Schamp equation.[27] Such CCS values can facilitate structural comparisons with other experimentally measured or otherwise estimated CCS values corresponding to available 3-dimensional structures.[28–38]

Previous drift tube IM-MS (DTIM-MS) studies have shown that CCS measurements can be obtained within 0.3% RSD for small and medium sized molecules,[39] and within ~0.4% for larger native-like protein ions.[9] While these results established the reproducibility of such IM measurements, in the context of protein structure, IM-MS alone remains unable to resolve many

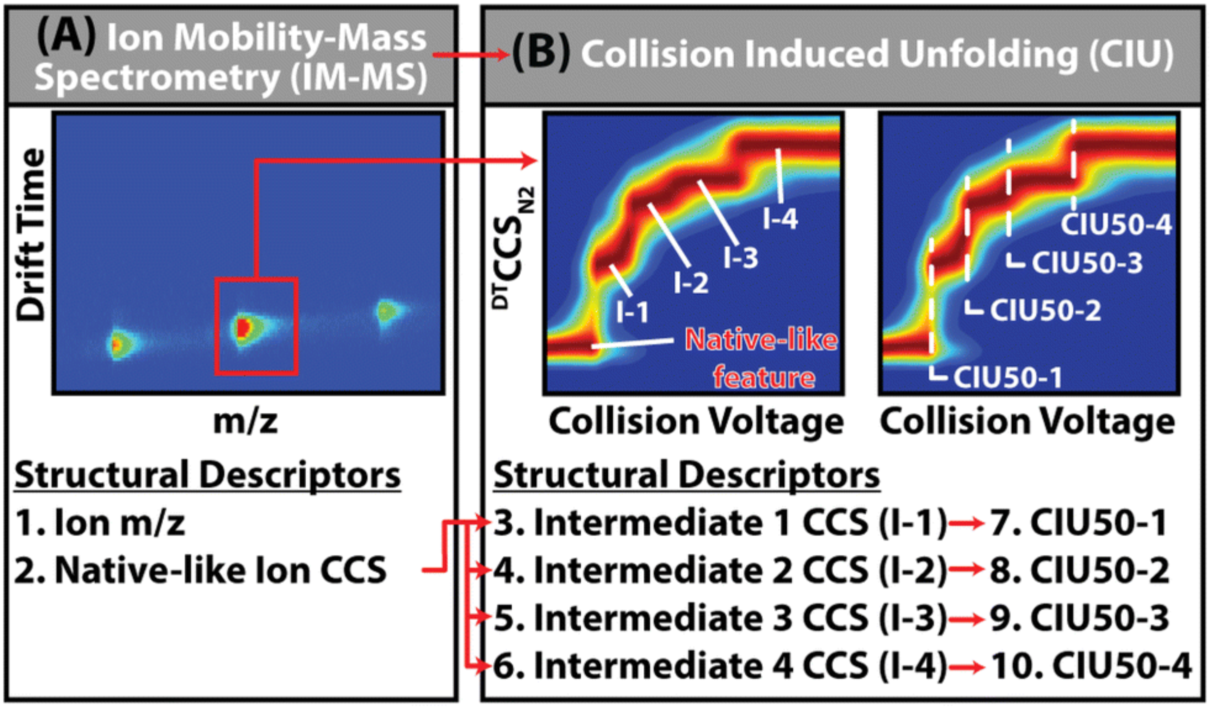

Figure 4-1 Expanding gas phase ion structure descriptors. (A) Typical IM-MS analysis of proteins yields two structural descriptors per ion, the m/z and collision cross sections recorded for native-like ions, however the resolution of these measurements alone is not currently sufficient to differentiate critically important structural microstates that dictate much of protein function. (B) CIU expands the structural descriptors of protein ions to include unfolding intermediates (I-1, -2, -3, -4 etc.) in addition to the native like CCS (N), and the activation voltages necessary to achieve these unfolding events (CIU50-1, -2, -3, -4 etc.), scaling the number of available structural descriptors 2- to 5-fold. Using this expanded set of structural descriptors, analytes can be differentiated based on subtle structural differences which are not captured by IM-MS alone.

key conformational states critical for biomolecular function. At its core, the native IM-MS experiment provides two key descriptors for differentiating protein states: the mass-to-charge (*m*/*z*) ratio of the ion and its CCS (Fig. 4-1A). The inherent complexity of proteins results in broad structural ensembles, and the IM resolution of IM-MS instruments is often insufficient to detect subtle but biologically relevant structural variations based on CCS alone. To overcome these limitations, the gradual and controlled collisional activation of gas-phase protein ions can be used to induce structural changes *via* collision-induced unfolding (CIU). CIU generates a wide range of non-native intermediate states corresponding to unfolded gas-phase protein ions (Fig. 4-1B).[40] By correlating the CCS distributions of ions against the instrument potentials applied, activation-correlated CCS plots (CIU fingerprints) can be generated. Most native-like globular protein ions exhibit a single, monomodal CCS distribution at low activation energy across all charge states observed. However, CIU fingerprints contain information regarding additional non-native, unfolded, and collisionally activated conformer populations and the accelerating potentials necessary to induce each transition (CIU50) detected, thus expanding the pool of structural descriptors 2–5 fold (Fig. 1). Using this expanded set of structural descriptors, CIU can be used to detect subtle changes in protein structure that are otherwise unresolvable by standard IM techniques alone. To date, CIU has been deployed in the analysis of various protein classes including kinases,[41] membrane proteins,[19–21] metalloproteins,[42,43] and biotherapeutics.[12,13,44]

In support of the rapidly growing applications of CIU, we have previously described our development of several modified DTIM-MS instruments equipped with prototype high-energy source hardware capable of increased in-source activation necessary for CIU experiments. To date, our work has demonstrated the ability of this IM-MS platform to produce CIU data similar to those reported previously[9,5,15,45,46]. In this study, we present the reproducibility of CIU fingerprints on three geographically distinct DTIM-MS instruments each equipped with prototype high- energy source hardware of the same design. Furthermore, we improved upon previously described methods, achieving higher-energy CIU of large proteins and protein complexes using a standard ESI source without the requisite addition of heavier dopant gases (*i.e.* sulfur hexafluoride).[9] We demonstrate that CCS measurements of CIU features observed across all laboratories are highly reproducible (<1% RSD), although CIU50 values vary significantly between datasets. Finally, we compare our interlaboratory CIU results with CIU data collected across multiple production-grade high-energy source hardware designed using higher-tolerance specifications and observe excellent reproducibility across both CIU features and CIU50 values. Establishing the reproducibility of CIU data obtained across multiple production-grade hardware assemblies alludes to the possibility of comparing CIU data acquired in different laboratories. Ultimately, this, and future work support the curation of a CIU fingerprint database with potential applications in proteomics, structural biology, and the pharmaceutical sciences.

4.3 Materials and Methods

4.3.1 Sample Preparation

Ammonium acetate, triethylammonium acetate, and lyophilized protein standards of bovine erythrocyte ubiquitin, equine heart myoglobin, Streptomyces avidinii streptavidin, bovine serum albumin (BSA), and universal monoclonal antibody standard (IgG1), were obtained from MilliporeSigma (St. Louis, MO). Product numbers for these standards are included in Table V-1. Low Concentration Tune Mix was obtained from Agilent Technologies (Santa Clara, CA). The protein standards for the interlaboratory investigation were reconstituted to 5 µM in 200 mM ammonium acetate at pH ~7.2. Aliquots (150 µL) of each protein solution were flash frozen prior to being distributed to each laboratory. Myoglobin, BSA and IgG1 samples were desalted in 200 mM ammonium acetate by Micro BioSpin P-6 columns (Bio-Rad, Hercules, CA) immediately prior to IM-MS analysis. Streptavidin samples were prepared by desalting into 160 mM ammonium acetate supplemented with 40 mM triethylammonium acetate to facilitate charge reduction. Ubiquitin samples were not desalted to avoid sample loss in the desalting columns. From each sample, the highest intensity ion signals, exhibiting both unimodality and native-like CCS values were chosen for subsequent collision- induced unfolding experiments.

4.3.2 Ion Mobility-Mass Spectrometry

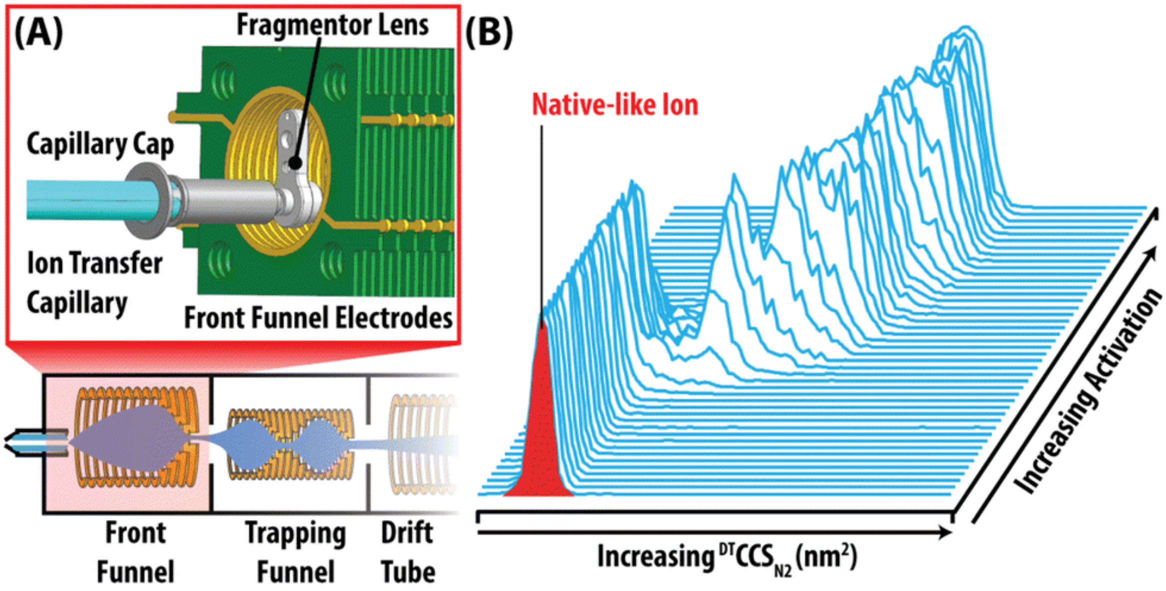

Figure 4-2 Source modifications enabling collision induced unfolding. (A) Schematic of the modified Agilent 6560 Source Region (full instrument diagram in Figure 1-9). The expanded red box depicts a CAD rendition of the high energy source optics. (B) Collision induced unfolding (CIU) occurs when native-like ions are gradually activated by increasing amounts of in-source activation, resulting in ion unfolding. Ion unfolding is monitored by an increase in CCS relative to the initial CCS. The ion CCS is plotted versus in-source activation to visualize gas phase unfolding.

Instruments at all sites were tuned to optimize transmission of native-like, compact ions using parameters compiled from several previous studies utilizing this instrument platform for intact protein analyses.[9,47–49] We collaboratively cross-examined native IM-MS spectra acquired at all sites and determined the optimal tuning conditions to ensure similar native-like ions were generated and measured at all sites. Samples were introduced via direct infusion into an electrospray ionization (ESI) source (Agilent Jet Stream) of a DTIM-MS (6560 IM-QTOF, Agilent Technologies) equipped with a prototype desolvation assembly consisting of high-energy in-source ion activation hardware (Fig. V-1, Fig. V-2A). The sources were equipped with a micronebulizer assembly which supports low sample flow rates (2-5 µL/min). The following ESI settings were used: Ion transfer capillary voltage, 2.5-3.5 kV; ion focusing nozzle voltage, 1-2 kV; drying gas flow, 5 L/min; drying gas temperature, 140 °C; sheath gas flow, 11 L/min; sheath gas temperature 140 °C. The use of lower sheath gas temperature compared to those employed in under standard Agilent Jet Stream ESI operation (325 °C) is likely due to the lower flow rates enabled by the microflow nebulizer. In addition, for BSA and IgG1 samples, drying gas temperature was maintained at 250 °C. The source and ion transfer conditions were optimized for each protein to minimize activation and best preserve native MS conditions. Similar tuning conditions were used for myoglobin, streptavidin, and BSA. Ubiquitin, the smallest protein studied here, required lowered radio frequency voltages (RF) and electric fields in the pre- IM region to prevent unintentional ion activation. In contrast, SigmaMAb the largest protein in this study required higher pre-IM RFs and electric fields to improve ion transmission. Detailed tuning conditions can be found in Table V-2. The high-pressure funnel, ion trap funnel, and drift tube were operated with high purity N_2 at 4.80 ± 0.10 Torr, 3.800 ± 0.025 Torr, and 3.950 ± 0.005 Torr (autoregulated by a gas flow controller) respectively, unless otherwise noted. The drift tube was operated at ambient temperature at an electric field of ~18 V/cm. The maximum drift time was set to 90 ms for all analytes, and the trap fill and release times were set to 80 ms and 1 ms, respectively. All post-IM tune settings used default values determined by performing a "System Tune" in the MassHunter Acquisition software. The post-IM settings used on the UM 6560 platform varied slightly due to the presence of a linear ExD cell (eMSion, Corvalis, OR); however, the ability of this instrument to perform native protein measurements has been extensively characterized previously.[9] Representative native mass spectra of all proteins used in the interlaboratory evaluation are available in Figure V-2.

All collision cross sections were measured using the single-field calibration method ($^{DT}CCS_{N2}$), which is a previously described linear calibration approach derived from the Mason-Schamp equation.[39] This approach incorporates instrument specific coefficients (β and t_{fix}) that are obtained via linear regression analysis of arrival time measurements from Agilent tune mix ions (m/z 622- 2722). Previous studies established that the single- field method produces CCS measurements within ~1.6% of the standard stepped-field method for a range of small molecules, metabolites, and proteins up to ~800 kDa.[9,39]

4.3.3 Collision Induced Unfolding

CIU has been previously demonstrated on the 6560 DTIM-MS platform previously. Data contained in this report was acquired on three such instruments located in laboratories at University of Michigan (UM), Texas A&M University (TAMU), and Vanderbilt University (VU). Each instrument was equipped with prototype high-energy source hardware to enable ion activation prior to IM-MS analysis. The modified source includes the addition of an ion lens element (termed the fragmentor lens) positioned at the exit of the ion transfer capillary and the entrance to first ion funnel (Figure 4-2A). Ramping the potential difference between the ion transfer capillary exit and the fragmentor lens up to 450 V (depending on specific hardware) when operating in high purity N_2, enables sufficient activation to achieve protein unfolding prior to IM separation (Figure 4-2B). A fourth instrument at the Agilent Technologies Research & Development Laboratory was used to evaluate new in-source ion activation hardware assemblies built to final commercial specifications (production-grade). The three identical production-grade hardware assemblies were evaluated to assess the CIU experiment reproducibility and performance. All instruments were also upgraded with QTOF firmware to enable time-of-flight mass spectrometer tuning and operation up to m/z 20,000.

Our CIU data acquisition methods were designed using the time segment feature in MassHunter Acquisition software 10.0 (Agilent Technologies), enabling the collection of multiple activation steps in a single data file. All IM-MS data were analyzed and calibrated for

CCS in IM-MS Browser 10.0 (Agilent Technologies), and the activation-resolved IM data were extracted and analyzed using CIUSuite2.[50] CIU fingerprints were generated by plotting $^{DT}CCS_{N2}$ distributions as a function of increasing applied collision voltage, referred to as "in-source collision energy" (In-source CE) in MassHunter Acquisition (Agilent Technologies). Additional CIUSuite2 fitting parameters are included in Table V-3. To assess reproducibility, all CIU fingerprint data were obtained in triplicate from each laboratory, and averaged fingerprints and corresponding RMSD values were obtained using software features currently available in CIUSuite2.

4.4 Results and Discussion

4.4.1 Interlaboratory CIU Results for Small Proteins

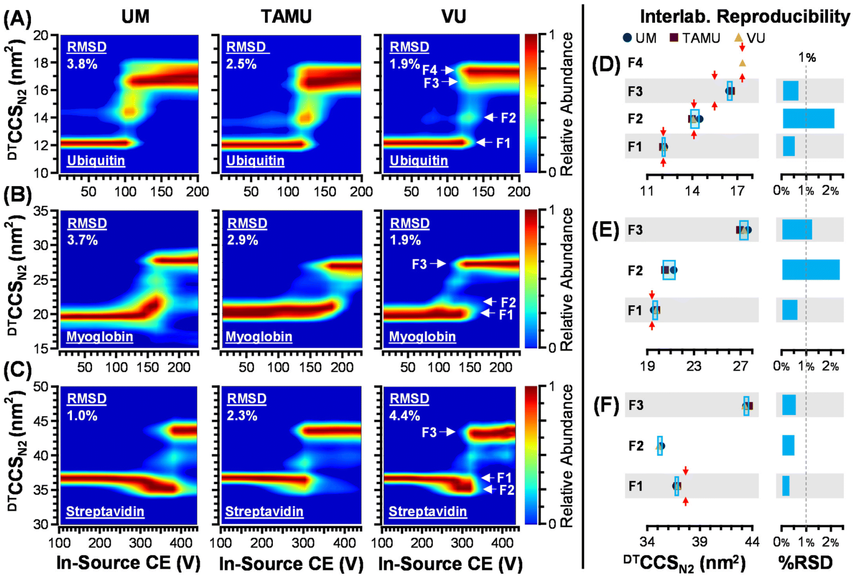

Figure 4-3 Interlaboratory CIU fingerprints and feature CCS reproducibility. (A) Ubiquitin +6, (B) myoglobin +8, and (C) streptavidin +11. Significant spectral features identified by CIUSuite2 (F1, F2, etc.) are annotated in the VU fingerprints (third column). Interlaboratory reproducibility of feature CCS measurements for each protein are summarized, delineated into distinct spectral features (F1, F2, etc.). (D–F) The interlaboratory standard deviations are indicated with the light blue boxes, and previous literature values ($^{DT}CCS_{N2}$), when available, are indicated with red arrows. The interlaboratory relative standard deviations (RSDs) for most (67%) CCS measurements, are within 1%. (D) Ubiquitin, (E) myoglobin, (F) streptavidin.

Figure 4-3 presents the CIU fingerprints for the three lowest molecular weight proteins investigated in this study: ubiquitin (+6, $[M+6H]^{+6}$), myoglobin (+8, $[M+8H]^{+8}$), and streptavidin (+11, $[M+11H]^{+11}$), panels (A) - (C), respectively. Each CIU fingerprint is an average of three intralaboratory repeats (technical replicates) and the corresponding RMSDs are provided at the upper left corner of each fingerprint as well as summarized in Table V-4. In general, the Intralaboratory CIU reproducibility was excellent, with all proteins analyzed producing CIU data with RMSD <4.5% in all laboratories. Importantly, the CIU fingerprints obtained for each protein are qualitatively similar across the different laboratories, in that all proteins sample similar intermediate CIU features, supporting the use of CIU fingerprints to support proteoform identification.[51]

While these CIU fingerprints were found to be highly reproducible within each laboratory, there are interlaboratory differences observed in the CIU fingerprints we recorded, particularly with respect to various stable intermediate structural families, referred to as CIU "features" (F). For example, ubiquitin (+6) exhibits a clear population of intermediate conformers (~14 nm^2 CCS) which appear with different degrees of prominence across all three laboratory datasets (Figure 4-3A). Ubiquitin (+6) also exhibits two unfolded features (F3 and F4) that vary in abundance in the CIU fingerprints. For myoglobin (+8), two low-abundance intermediate features can be observed: (1) a feature exhibiting slightly larger CCS than native-like ions (F2, ~21 nm^2), observed in two out of three fingerprints (UM & TAMU), and (2) a set of intermediate CIU features (~25 nm^2) observed in all three fingerprints, but not in sufficient abundance to be labeled as a feature in these data (Figure 4-3B). Likewise, for streptavidin (+11), at least two intermediate features are observed: (1) a feature with a CCS likely corresponding to a collapsed state of the tetramer adopting a smaller CCS than the value measured for the ion population observed at lowest activation energies (F2, ~35 nm^2), observed in two out of three fingerprints (UM & VU), and (2) a low- abundance feature between the compact and fully-extended states, with a CCS value of ~40 nm^2 (Figure 4-3C). The transient nature of these intermediate features ultimately limits the cross-laboratory reproducibility of CIU fingerprints using prototype in- source activation hardware.

The CCS measurements obtained for all CIU features observed are summarized in Figure 4-3D-F, Figure V-3 and Table V-5, with criteria used for feature identification provided in Table V-3. For those protein features which appear in sufficient abundance across all laboratories, the CCS measurement reproducibility was found to be excellent, with the majority of features (6/9, 67%) exhibiting an interlaboratory RSD of less than 1%. In addition, one feature exhibits a reproducibility just above this arbitrary 1% threshold (myoglobin F3, 1.3%). The remaining features have an interlaboratory RSD of ~2%. Overall, this work presents the remarkable reproducibility of CIU feature CCS values especially when considering that these features correspond to transient gas-phase protein unfolding intermediates (Figure 4-3D-F). Previously reported drift tube CCS measurements are available of the CIU features studied here (Table V-5) and the average literature $^{DT}CCS_{N2}$ values are indicated in Figure 4-3D-F. The CCS measurements presented in this study generally agree with previous reports, with significant deviations noted for one extended state of ubiquitin (F3, our value is 6.2% larger), as well as the starting native- like state sampled for streptavidin (F1, our value is 2.1% smaller). The four other CCS measurements for which literature values were available exhibited a relative bias of less than 2%, and in two cases (ubiquitin F1, F4) the interlaboratory CCS measurements were within 0.5% of the averaged literature values.

While the interlaboratory reproducibility of native-like protein ion CCS has been evaluated before, this work is the first to report the interlaboratory reproducibility of transient, gas-phase protein unfolding intermediates, establishing that the CCS of CIU features can be reliably used as structural descriptors when differentiating gas phase protein ions. Despite the high degree of reproducibility observed for CIU feature CCS, larger differences were observed in the levels of activation required to achieve CIU, commonly referred to as "CIU50" values. CIU50 voltages varied significantly between laboratories for the small proteins measured. Despite the excellent intralaboratory RMSDs (<4.5%) for all proteins measured by CIU, the interlaboratory RMSDs were ~18-40% (Table V-4) driven primarily by CIU50 variation found when using the prototype hardware assemblies located at UM, TAMU, and VU.

4.4.2 Intralaboratory CIU Results for BSA

Interlaboratory CIU comparisons of bovine serum albumin (BSA), a protein previously established as a CIU standard,[9] produced similar results as those observed for ubiquitin, myoglobin, and streptavidin. Comparisons of the CIU fingerprints from all laboratories demonstrate that similar unfolding pathways were observed for the BSA +16 ion, with the protein starting in a natively structured form (F1) with a CCS of ~45 nm^2. As the in-source CE is increased, the +16 ion gradually unfolds and populates several stable intermediate structures (F2, F3, F4) en route to a fully unfolded state (F5) (Figure 4-4A-C). The three hardware assemblies were able to reproduce the fingerprints with an intralaboratory reproducibility of <3% RMSD (3 replicates). The interlaboratory reproducibility for the CCSs of each of the observable features of BSA +16 was also found to be excellent (≤1.3% RSD). The most notable difference detected in our data was the pronounced variation in CIU feature intensity, resulting in a "missing" second

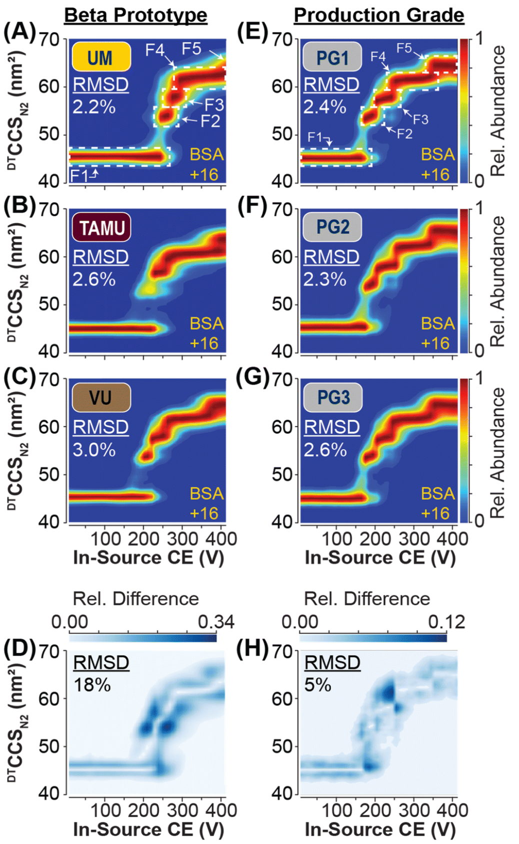

Figure 4-4 Interlaboratory CIU fingerprints of BSA (+16) and development of production-grade source hardware. Average CIU fingerprint of BSA (+16) ions acquired on three independent beta prototype DTIM-MS instruments located at (A) UM, (B) TAMU, and (C) VU. Intralaboratory CIU reproducibility is indicated by RMSD in the top left corner of each fingerprint. (D) CIU difference plot indicating the areas of greatest difference between the CIU fingerprints from the three laboratories (A–C), resulting in an interlaboratory RMSD of 18%. CIU of BSA (+16) ions acquired on three independent production-grade hardware assemblies (E–G). (H) CIU difference plot indicating the areas of greatest difference between the CIU fingerprints from PG1–3 (E–G), resulting in an interhardware RMSD of 5%.

feature (F2) in the BSA CIU fingerprint produced at TAMU, wherein F2 never achieved sufficient signal for feature detection (Figure 4-4B, Figure V-3, Table V-5). Our analysis instead detected the first feature at ~45 nm^2 (F1) and the third feature at ~58 nm^2 (F3), only populating F2 transiently enroute during the F1-to-F3 transition (Figure V-3D). While our interlaboratory measurements of BSA +16 were found to be consistent, the observed CIU50 values once again varied. For example, F1 unfolds into F2 at ~180 V in the UM fingerprint (Figure 4-4A), however, F2 is undetected in the TAMU data (Figure 4-4B) and the same transition occurs at a lower volage (~140 V) in the VU fingerprint (Figure 4-4C). These differences appeared to be systematic within a given CIU dataset. This effect is particularly apparent when comparing feature F5 in our BSA CIU experiments. This final unfolded feature appears at ~440 V in UM data, while the TAMU and VU fingerprints show F5 appearing at ~370 V, suggesting that the TAMU and VU prototype sources are more activating than the UM source. As was noted in our analysis of Figure 4-3, CIU50 differences are the primary contributor to the high interlaboratory CIU differences detected in our BSA CIU data (Figure 4-4D, Table V-4).

Based on the interlaboratory evaluation of CIU reproducibility for 4 proteins (8-66 kDa), we concluded that CIU experiments obtained from different laboratories sample similar CIU features; however, the prototype source assemblies used in our experiments presented challenges associated with carrying out a rigorous interlaboratory comparison of CIU50 values. Limiting the interlaboratory CIU comparisons to unfolding features alone, eliminates 50% of the structural descriptors typically extracted from CIU data (Figure 4-1), and recovering this information content thus motivates our development of improved ion activation hardware capable of higher degrees of CIU reproducibility.

4.4.3 Evaluation of Production Grade Hardware for BSA

To overcome the lack of CIU50 reproducibility observed in our interlaboratory study, three updated production-grade source assemblies (PG1, PG2, PG3) were constructed using high-precision tolerances to define the dimensions and inter-lens distances within the source assemblies constructed. In addition, the Fragmentor counter electrode was repositioned, improving both the effective activation capabilities of the production-grade source assemblies, as well as the reproducibility of CIU experiments. To test the reproducibility of these new source assemblies independent of other instrument variables, the same DTIM-MS instrument, in Santa Clara, CA was used for all measurements across all three production-grade source assemblies. The instrument was vented completely after completing all measurements with each production-grade source, and the source assemblies were exchanged. This decision was also justified by the findings of the interlaboratory evaluation which established that the CIU feature CCS is highly reproducible across multiple DTIM-MS instruments and geographic locations. The production-grade sources were evaluated in terms of their CIU reproducibility using BSA and SigmaMAb IgG1 standard samples.

CIU collected for BSA +16 ions on PG1, PG2, and PG3 was highly reproducible with intrahardware replicates achieving an RMSDs ≤2.6% (Figure 4-4E-G). Furthermore, an interhardware RMSD of 4.7% was obtained by comparing CIU data collected across all three production-grade sources (PG1 vs. PG2 vs. PG3), which represents a ~4-fold improvement over the 18.3% RMSD measured for interlaboratory comparisons of BSA +16 CIU fingerprints using prototype hardware (Figure 4-4H, Table V-4, Table V-6). Features F1-F5 were detected in all three production- grade hardware tests, addressing the previous inconsistencies in CIU feature detection during our prototype source evaluation (Figure 4-4B, Figure V-3D).

Each CIU feature CCS had an interhardware replicate RSD of ≤0.3%, indicating that the features associated with low-energy structures and those related to gas phase unfolding intermediates were highly reproducible across the hardware assemblies tested. The greatest improvement was observed in the reproducibility of CIU50 voltages, which resulted in an RSD of ≤3% in our interhardware evaluation (Table V-6). CIU50-1, and CIU50-3 displayed some variation; however, producing RSDs of ~3%. In contrast, the CIU50-2 and CIU50-4 values were highly reproducible across our production-grade hardware tests, leading to RSDs of 0.2% and 1%, respectively. The slight differences in CIU50s for CIU50-1 and CIU50-3 are likely a result of the PG2 source requiring ~10V more in-source CE to induce feature transitions compared to PG1 and PG3. CIU50-1 and CIU50-3 are the two highest intensity regions in the CIU difference plot (Figure 4-4H), indicating that they are the main contributors to the slightly higher RSMD calculated for the interhardware tests compared to our intrahardware data. Overall, the production-grade source assemblies outperformed prototype source hardware in terms of CIU reproducibility improving upon the interlaboratory reproducibility of BSA CIU by approximately ~4-fold.

4.4.4 Immunoglobulin G1 (IgG1)

Throughout the pharmaceutical industry, stability measurements act as critical elements in the development of biotherapeutic monoclonal antibodies (mAbs). CIU has long been proposed as an ideal approach for inclusion in biotherapeutic pipelines, with a substantial body of work supporting its ability to characterize relevant mAb structures.[12,14,15,46,52,53] A high level of technical reproducibility is required to conduct comparative analyses across mAb subtypes. Although the BSA results discussed above can be used to positively project the reproducibility of such CIU experiments for protein-based pharmaceuticals, mAbs are over two times larger (~150 kDa), and thus pose unique challenges for high-precision IM-MS and CIU.

CIU of SigmaMAb was conducted across each of the three production prototype hardware assemblies (PG1, PG2, PG3), and replicate RMSDs were calculated for each hardware assembly independently, as well as for all three assemblies. Representative mass spectra from our CIU experiments were plotted against the in-source CE potential values demonstrating an increase in signal intensity as the activation level increased (Figure 4-5A). The increase in signal intensity is due to both an associated improvement in ion transmission efficiency and improved desolvation of the large IgG1 ions at elevated source potentials. Seven mAb charge states (+25 to +31) of intact IgG1 were observed in these mass spectra, and the 5 highest intensity charge states (+26 to +30) were extracted for CIU analysis. Three technical replicates were acquired from each hardware assembly, resulting in nine CIU fingerprints which were averaged to produce the interhardware CIU fingerprint displayed here (Figure 4-5B-F). Corresponding CIU difference plots were also produced for each charge state, indicating that most of the differences between individual CIU fingerprints are the result of variations in CIU50 values (Figure 4-5G-K). The intrahardware RMSDs ranged from 1.8- 5.0% (Table V-7), with interhardware RMSDs of 2.6-

4.4% (Figure 4-5G-K). In both instances the magnitude of the RMSDs recorded was inversely correlated with the intensities of the charge states selected for CIU analysis. The slightly higher interhardware RMSD observed for the CIU data extracted from +26 and +30 mAb ions is likely attributable to the relatively low abundances of these (Table V-7, Figure 4-5A), however such RMSD values are <5%.

Our CIU data for SigmaMAb yields fingerprints similar to those reported previously,[12] with ions across all charge states producing a similarly gradual transition from the CIU first feature to the second. All fingerprints were fit to two (+27, +29), or three (+26, +28, +30) features (Figure V-4). In CIU data acquired for +29 mAb ions, a third feature is apparent at ~124 nm^2; however, it was not included in our fits due to lack of sufficient sampling of the associated voltage slices where these structures are observed in our CIU data. We record an average interhardware feature CCS reproducibility value for SigmaMAb of 0.2%, similar to the ~0.3% feature RSD measured for BSA (Table V-7). Continuing with this trend, we observe an average CIU50 RSD 1.5%, which is comparable to the ~2% measured for BSA (Table V-7). If we filter our data to search for the most reproducible CIU fingerprints within our mAb dataset, we obtain interhardware RSDs across CIU features and CIU50s of 0.03%, and 1.2% respectively (28+ and 29+ data only), representing exceptional interhardware CIU reproducibility for such a large, structurally dynamic protein ion.

4.5 Conclusion

We evaluated the interlaboratory reproducibility of CIU data acquired using prototype source hardware for a variety of small proteins (8-66 kDa). These measurements were performed at 3 independent sites to rigorously assess the interlaboratory reproducibility of CIU data. Our analysis of this prototype hardware revealed the CIU experiments were generally reproducible, with all three laboratories reporting similar CCS measurements (RSD<3%) for gas-phase unfolding intermediates observed during CIU experiments. However, the results also indicated that prototype source construction tolerances were insufficient to produce high-precision CIU50 measurements across the different test sites.

These results spurred the development of the production-grade CIU hardware which performs ion activation equally across DTIM-MS platforms. Three production prototype hardware assemblies were built to final commercial specifications and were evaluated for their ability to reproduce CIU experiments for larger proteins such as BSA and SigmaMAb (66-150 kDa). We found that the production prototype hardware assemblies were capable of conducting CIU experiments with a high level of overall interhardware CIU reproducibility (≤4.4% RMSD). Furthermore, we observed improved feature reproducibility, to a value of <0.5%, and critically collected CIU50 measurements with a reproducibility of <2% RSD using our calibrated activation source optics.

With CIU becoming a more commonly utilized technology for applications in structural biology and the pharmaceutical sciences, the reproducibility of such data is paramount to achieving its full potential as a laboratory-independent comparative technique. Presently, most CIU practitioners only compare CIU data with other datasets acquired in the same laboratory. The reproducibility of CIU data reported here opens the door to broader interlaboratory comparisons of CIU fingerprints, including the creation of CIU databases, potentially enabling broader uses of such data extending to protein identification and protein biomarker tracking.[51]

4.6 References

(1) Leney, A. C.; Heck, A. J. R. Native Mass Spectrometry: What Is in the Name? *J Am Soc Mass Spectrom* **2017**, *28* (1), 5–13. https://doi.org/10.1007/s13361-016-1545-3.

(2) Wilm, M.; Mann, M. Analytical Properties of the Nanoelectrospray Ion Source. *Anal. Chem.* **1996**, *68* (1), 1–8. https://doi.org/10.1021/ac9509519.

(3) Tahallah, N.; Pinkse, M.; Maier, C. S.; Heck, A. J. R. The Effect of the Source Pressure on the Abundance of Ions of Noncovalent Protein Assemblies in an Electrospray Ionization Orthogonal Time-of-Flight Instrument. *Rapid Communications in Mass Spectrometry* **2001**, *15* (8), 596–601. https://doi.org/10.1002/rcm.275.

(4) Sobott, F.; Hernández, H.; McCammon, M. G.; Tito, M. A.; Robinson, C. V. A Tandem Mass Spectrometer for Improved Transmission and Analysis of Large Macromolecular Assemblies. *Anal. Chem.* **2002**, *74* (6), 1402–1407. https://doi.org/10.1021/ac0110552.

(5) Li, H.; Wolff, J. J.; Van Orden, S. L.; Loo, J. A. Native Top-down Electrospray Ionization-Mass Spectrometry of 158 KDa Protein Complex by High-Resolution Fourier Transform Ion Cyclotron Resonance Mass Spectrometry. *Anal. Chem.* **2014**, *86* (1), 317–320. https://doi.org/10.1021/ac4033214.

(6) May, J. C.; Goodwin, C. R.; Lareau, N. M.; Leaptrot, K. L.; Morris, C. B.; Kurulugama, R. T.; Mordehai, A.; Klein, C.; Barry, W.; Darland, E.; Overney, G.; Imatani, K.; Stafford, G. C.; Fjeldsted, J. C.; McLean, J. A. Conformational Ordering of Biomolecules in the Gas Phase: Nitrogen Collision Cross Sections Measured on a Prototype High Resolution Drift Tube Ion Mobility-Mass Spectrometer. *Anal. Chem.* **2014**, *86* (4), 2107–2116. https://doi.org/10.1021/ac4038448.

(7) May, J. C.; Dodds, J. N.; Kurulugama, R. T.; Stafford, G. C.; Fjeldsted, J. C.; Mclean, J. A. Broadscale Resolving Power Performance of a High Precision Uniform Field Ion Mobility-Mass Spectrometer †. *Analyst* **2015**, *140*, 6824. https://doi.org/10.1039/c5an00923e.

(8) Dyachenko, A.; Wang, G.; Belov, M.; Makarov, A.; De Jong, R. N.; Van Den Bremer, E. T. J.; Parren, P. W. H. I.; Heck, A. J. R. Tandem Native Mass-Spectrometry on Antibody-Drug Conjugates and Submillion Da Antibody-Antigen Protein Assemblies on an Orbitrap EMR Equipped with a High-Mass Quadrupole Mass Selector. *Anal. Chem.* **2015**, *87* (12), 6095–6102. https://doi.org/10.1021/acs.analchem.5b00788.

(9) Gadkari, V. v.; Ramírez, C. R.; Vallejo, D. D.; Kurulugama, R. T.; Fjeldsted, J. C.; Ruotolo, B. T. Enhanced Collision Induced Unfolding and Electron Capture Dissociation of Native-like Protein Ions. *Anal. Chem.* **2020**, *92* (23), 15489–15496. https://doi.org/10.1021/acs.analchem.0c03372.

(10) Mallis, C. S.; Zheng, X.; Qiu, X.; McCabe, J. W.; Shirzadeh, M.; Lyu, J.; Laganowsky, A.; Russell, D. H. Development of Native MS Capabilities on an Extended Mass Range Q-TOF MS. *International Journal of Mass Spectrometry* **2020**, *458*, 116451. https://doi.org/10.1016/j.ijms.2020.116451.

(11) Giles, K.; Ujma, J.; Wildgoose, J.; Pringle, S.; Richardson, K.; Langridge, D.; Green, M. A Cyclic Ion Mobility-Mass Spectrometry System. *Anal. Chem.* **2019**, *91* (13), 8564–8573. https://doi.org/10.1021/acs.analchem.9b01838.

(12) Tian, Y.; Han, L.; Buckner, A. C.; Ruotolo, B. T. Collision Induced Unfolding of Intact Antibodies: Rapid Characterization of Disulfide Bonding Patterns, Glycosylation, and Structures. *Anal. Chem.* **2015**, *87* (22), 11509–11515. https://doi.org/10.1021/acs.analchem.5b03291.

(13) Tian, Y.; Lippens, J. L.; Netirojjanakul, C.; Campuzano, I. D. G.; Ruotolo, B. T. Quantitative Collision-Induced Unfolding Differentiates Model Antibody–Drug Conjugates. *Protein Science* **2019**, *28* (3), 598–608. https://doi.org/10.1002/pro.3560.

(14) Hernandez-Alba, O.; Wagner-Rousset, E.; Beck, A.; Cianférani, S. Native Mass Spectrometry, Ion Mobility, and Collision-Induced Unfolding for Conformational Characterization of IgG4 Monoclonal Antibodies. *Anal. Chem.* **2018**, *90* (15), 8865–8872. https://doi.org/10.1021/acs.analchem.8b00912.

(15) Vallejo, D. D.; Polasky, D. A.; Kurulugama, R. T.; Eschweiler, J. D.; Fjeldsted, J. C.; Ruotolo, B. T. A Modified Drift Tube Ion Mobility-Mass Spectrometer for Charge-Multiplexed Collision-Induced Unfolding. *Anal. Chem.* **2019**, *91* (13), 8137–8146. https://doi.org/10.1021/acs.analchem.9b00427.

(16) Laganowsky, A.; Reading, E.; Allison, T. M.; Ulmschneider, M. B.; Degiacomi, M. T.; Baldwin, A. J.; Robinson, C. v. Membrane Proteins Bind Lipids Selectively to Modulate Their Structure and Function. *Nature* **2014**, *510* (7503), 172–175. https://doi.org/10.1038/nature13419.

(17) Hopper, J. T. S.; Yu, Y. T. C.; Li, D.; Raymond, A.; Bostock, M.; Liko, I.; Mikhailov, V.; Laganowsky, A.; Benesch, J. L. P.; Caffrey, M.; Nietlispach, D.; Robinson, C. V. Detergent-Free Mass Spectrometry of Membrane Protein Complexes. *Nature Methods* **2013**, *10* (12), 1206–1208. https://doi.org/10.1038/nmeth.2691.

(18) Laganowsky, A.; Reading, E.; Hopper, J. T. S.; Robinson, C. V. Mass Spectrometry of Intact Membrane Protein Complexes. *Nature Protocols* **2013**, *8* (4), 639–651. https://doi.org/10.1038/nprot.2013.024.

(19) Fantin, S. M.; Parson, K. F.; Niu, S.; Liu, J.; Polasky, D. A.; Dixit, S. M.; Ferguson-Miller, S. M.; Ruotolo, B. T. Collision Induced Unfolding Classifies Ligands Bound to the Integral Membrane Translocator Protein. *Anal. Chem* **2019**, *91*, 38. https://doi.org/10.1021/acs.analchem.9b03208.

(20) Fantin, S. M.; Huang, H.; Sanders, C. R.; Ruotolo, B. T. Collision-Induced Unfolding Differentiates Functional Variants of the KCNQ1 Voltage Sensor Domain. *J Am Soc Mass Spectrom* **2020**, *01*, 13. https://doi.org/10.1021/jasms.0c00288.

(21) Hutchison, J. M.; Shih, K. C.; Scheidt, H. A.; Fantin, S. M.; Parson, K. F.; Pantelopulos, G. A.; Harrington, H. R.; Mittendorf, K. F.; Qian, S.; Stein, R. A.; Collier, S. E.; Chambers, M. G.; Katsaras, J.; Voehler, M. W.; Ruotolo, B. T.; Huster, D.; McFeeters, R. L.; Straub, J. E.; Nieh, M. P.; Sanders, C. R. Bicelles Rich in Both Sphingolipids and Cholesterol and Their Use in Studies of Membrane Proteins. *J Am Chem Soc* **2020**, *142* (29), 12715–12729. https://doi.org/10.1021/jacs.0c04669.

(22) Fantin, S. M.; Parson, K. F.; Yadav, P.; Juliano, B.; Li, G. C.; Sanders, C. R.; Ohi, M. D.; Ruotolo, B. T. Ion Mobility–Mass Spectrometry Reveals the Role of Peripheral Myelin Protein Dimers in Peripheral Neuropathy. *Proceedings of the National Academy of Sciences* **2021**, *118* (17). https://doi.org/10.1073/PNAS.2015331118.

(23) Sobott, F.; Benesch, J. L. P.; Vierling, E.; Robinson, C. v. Subunit Exchange of Multimeric Protein Complexes: REAL-TIME MONITORING OF SUBUNIT EXCHANGE BETWEEN SMALL HEAT SHOCK PROTEINS BY USING ELECTROSPRAY MASS SPECTROMETRY. *Journal of Biological Chemistry* **2002**, *277* (41), 38921–38929. https://doi.org/10.1074/JBC.M206060200.

(24) Aquilina, J. A.; Benesch, J. L. P.; Bateman, O. A.; Slingsby, C.; Robinson, C. V. Polydispersity of a Mammalian Chaperone: Mass Spectrometry Reveals the Population of

Oligomers in AB-Crystallin. *Proceedings of the National Academy of Sciences* **2003**, *100* (19), 10611–10616. https://doi.org/10.1073/PNAS.1932958100.

(25) Mitra, R.; Gadkari, V. v.; Meinen, B. A.; van Mierlo, C. P. M.; Ruotolo, B. T.; Bardwell, J. C. A. Mechanism of the Small ATP-Independent Chaperone Spy Is Substrate Specific. *Nature Communications* **2021**, *12* (1), 1–13. https://doi.org/10.1038/s41467-021-21120-8.

(26) Uetrecht, C.; Barbu, I. M.; Shoemaker, G. K.; van Duijn, E.; Heck, A. J. R. Interrogating Viral Capsid Assembly with Ion Mobility-Mass Spectrometry. *Nature Chemistry* **2011**, *3* (2), 126–132. https://doi.org/10.1038/nchem.947.

(27) Mason, E. A.; McDaniel, E. W. *Transport Properties of Ions in Gases*; 1988. https://doi.org/10.1107/97809553602060000907.

(28) Marklund, E. G.; Degiacomi, M. T.; Robinson, C. V; Baldwin, A. J.; Benesch, J. L. P. Collision Cross Sections for Structural Proteomics. *Structure* **2015**, *23* (4), 791–799. https://doi.org/10.1016/j.str.2015.02.010.

(29) Ewing, S. A.; Donor, M. T.; Wilson, J. W.; Prell, J. S. Collidoscope: An Improved Tool for Computing Collisional Cross-Sections with the Trajectory Method. *J Am Soc Mass Spectrom* **2017**, *28* (4), 587–596. https://doi.org/10.1007/S13361-017-1594-2/SUPPL_FILE/JS8B05514_SI_001.PDF.

(30) Bleiholder, C.; Contreras, S.; Bowers, M. T. A Novel Projection Approximation Algorithm for the Fast and Accurate Computation of Molecular Collision Cross Sections (IV). Application to Polypeptides. *International Journal of Mass Spectrometry* **2013**, *354–355*, 275–280. https://doi.org/10.1016/J.IJMS.2013.06.011.

(31) Anderson, S. E.; Bleiholder, C.; Brocker, E. R.; Stang, P. J.; Bowers, M. T. A Novel Projection Approximation Algorithm for the Fast and Accurate Computation of Molecular Collision Cross Sections (III): Application to Supramolecular Coordination-Driven Assemblies with Complex Shapes. *International Journal of Mass Spectrometry* **2012**, *330–332*, 78–84. https://doi.org/10.1016/J.IJMS.2012.08.024.

(32) Bleiholder, C.; Contreras, S.; Do, T. D.; Bowers, M. T. A Novel Projection Approximation Algorithm for the Fast and Accurate Computation of Molecular Collision Cross Sections (II). Model Parameterization and Definition of Empirical Shape Factors for Proteins. *International Journal of Mass Spectrometry* **2013**, *345–347*, 89–96. https://doi.org/10.1016/J.IJMS.2012.08.027.

(33) Bleiholder, C.; Wyttenbach, T.; Bowers, M. T. A Novel Projection Approximation Algorithm for the Fast and Accurate Computation of Molecular Collision Cross Sections (I). Method. *International Journal of Mass Spectrometry* **2011**, *308* (1), 1–10. https://doi.org/10.1016/J.IJMS.2011.06.014.

(34) Shvartsburg, A. A.; Jarrold, M. F. An Exact Hard-Spheres Scattering Model for the Mobilities of Polyatomic Ions. *Chemical Physics Letters* **1996**, *261* (1–2), 86–91. https://doi.org/10.1016/0009-2614(96)00941-4.

(35) Mesleh, M. F.; Hunter, J. M.; Shvartsburg, A. A.; Schatz, G. C.; Jarrold, M. F. Structural Information from Ion Mobility Measurements: Effects of the Long-Range Potential. *Journal of Physical Chemistry* **1996**, *100* (40), 16082–16086. https://doi.org/10.1021/JP961623V.

(36) Shvartsburg, A. A.; Hudgins, R. R.; Dugourd, P.; Jarrold, M. F. Structural Information from Ion Mobility Measurements: Applications to Semiconductor Clusters. *Chemical Society Reviews* **2001**, *30* (1), 26–35. https://doi.org/10.1039/A802099J.

(37) Shvartsburg, A. A.; Jarrold, M. F. An Exact Hard-Spheres Scattering Model for the Mobilities of Polyatomic Ions. *Chemical Physics Letters* **1996**, *261* (1–2), 86–91. https://doi.org/10.1016/0009-2614(96)00941-4.

(38) Davidson, K. L.; Oberreit, D. R.; Hogan, C. J.; Bush, M. F. Nonspecific Aggregation in Native Electrokinetic Nanoelectrospray Ionization. *International Journal of Mass Spectrometry* **2017**, *420*, 35–42. https://doi.org/10.1016/J.IJMS.2016.09.013.

(39) Stow, S. M.; Causon, T. J.; Zheng, X.; Kurulugama, R. T.; Mairinger, T.; May, J. C.; Rennie, E. E.; Baker, E. S.; Smith, R. D.; McLean, J. A.; Hann, S.; Fjeldsted, J. C. An Interlaboratory Evaluation of Drift Tube Ion Mobility-Mass Spectrometry Collision Cross Section Measurements. *Anal. Chem.* **2017**, *89* (17), 9048–9055. https://doi.org/10.1021/acs.analchem.7b01729.

(40) Dixit, S. M.; Polasky, D. A.; Ruotolo, B. T. Collision Induced Unfolding of Isolated Proteins in the Gas Phase: Past, Present, and Future. *Current Opinion in Chemical Biology* **2018**, *42*, 93–100. https://doi.org/10.1016/j.cbpa.2017.11.010.

(41) Rabuck, J. N.; Hyung, S. J.; Ko, K. S.; Fox, C. C.; Soellner, M. B.; Ruotolo, B. T. Activation State-Selective Kinase Inhibitor Assay Based on Ion Mobility-Mass Spectrometry. *Anal. Chem.* **2013**, *85* (15), 6995–7002. https://doi.org/10.1021/ac4012655.

(42) Dong, S.; Wagner, N. D.; Russell, D. H. Collision-Induced Unfolding of Partially Metalated Metallothionein-2A: Tracking Unfolding Reactions of Gas-Phase Ions. *Anal. Chem.* **2018**, *90* (20), 11856–11862. https://doi.org/10.1021/ACS.ANALCHEM.8B01622.

(43) Dong, S.; Shirzadeh, M.; Fan, L.; Laganowsky, A.; Russell, D. H. Ag+ Ion Binding to Human Metallothionein-2A Is Cooperative and Domain Specific. *Anal. Chem.* **2020**, *92* (13), 8923–8932. https://doi.org/10.1021/ACS.ANALCHEM.0C00829.

(44) Hernandez-Alba, O.; Wagner-Rousset, E.; Beck, A.; Cianférani, S. Native Mass Spectrometry, Ion Mobility, and Collision-Induced Unfolding for Conformational Characterization of IgG4 Monoclonal Antibodies. *Anal. Chem.* **2018**, *90* (15), 8865–8872. https://doi.org/10.1021/acs.analchem.8b00912.

(45) Zheng, X.; Kurulugama, R. T.; Laganowsky, A.; Russell, D. H. Collision-Induced Unfolding Studies of Proteins and Protein Complexes Using Drift Tube Ion Mobility-Mass Spectrometer. *Anal. Chem* **2020**, *92*, 23. https://doi.org/10.1021/acs.analchem.0c00772.

(46) Vallejo, D. D.; Kang, J.; Coghlan, J.; Ramírez, C. R.; Polasky, D. A.; Kurulugama, R. T.; Fjeldsted, J. C.; Schwendeman, A. A.; Ruotolo, B. T. Collision-Induced Unfolding Reveals Stability Differences in Infliximab Therapeutics under Native and Heat Stress Conditions. *Anal. Chem.* **2021**, *93* (48), 16166–16174. https://doi.org/10.1021/ACS.ANALCHEM.1C03946/SUPPL_FILE/AC1C03946_SI_001.PDF.

(47) Harrison, J. A.; Kelso, C.; Pukala, T. L.; Beck, J. L. Conditions for Analysis of Native Protein Structures Using Uniform Field Drift Tube Ion Mobility Mass Spectrometry and Characterization of Stable Calibrants for TWIM-MS. *J. Am. Soc. Mass Spectrom* **2019**, *30* (2), 256–267. https://doi.org/10.1007/s13361-018-2074-z.

(48) May, J. C.; Jurneczko, E.; Stow, S. M.; Kratochvil, I.; Kalkhof, S.; McLean, J. A. Conformational Landscapes of Ubiquitin, Cytochrome c, and Myoglobin: Uniform Field Ion Mobility Measurements in Helium and Nitrogen Drift Gas. *International Journal of Mass Spectrometry* **2018**, *427*, 79–90. https://doi.org/10.1016/j.ijms.2017.09.014.

(49) Gabelica, V.; Livet, S.; Rosu, F. Optimizing Native Ion Mobility Q-TOF in Helium and Nitrogen for Very Fragile Noncovalent Structures. *J Am Soc Mass Spectrom* **2018**, *29* (11), 2189–2198. https://doi.org/10.1007/s13361-018-2029-4.
(50) Polasky, D. A.; Dixit, S. M.; Fantin, S. M.; Ruotolo, B. T. CIUSuite 2: Next-Generation Software for the Analysis of Gas-Phase Protein Unfolding Data. *Anal. Chem* **2019**. https://doi.org/10.1021/acs.analchem.8b05762.
(51) Ruotolo, B. T. Collision Cross Sections for Native Proteomics: Challenges and Opportunities. *Journal of Proteome Research* **2021**, *21* (1), 2–8. https://doi.org/10.1021/ACS.JPROTEOME.1C00686.
(52) Pisupati, K.; Tian, Y.; Okbazghi, S.; Benet, A.; Ackermann, R.; Ford, M.; Saveliev, S.; Hosfield, C. M.; Urh, M.; Carlson, E.; Becker, C.; Tolbert, T. J.; Schwendeman, S. P.; Ruotolo, B. T.; Schwendeman, A. A Multidimensional Analytical Comparison of Remicade and the Biosimilar Remsima. *Anal. Chem.* **2017**, *89* (9), 4838–4846. https://doi.org/10.1021/ACS.ANALCHEM.6B04436.
(53) Botzanowski, T.; Hernandez-Alba, O.; Malissard, M.; Wagner-Rousset, E.; Deslignière, E.; Colas, O.; Haeuw, J.-F.; Beck, A.; Cianférani, S. Middle Level IM–MS and CIU Experiments for Improved Therapeutic Immunoglobulin Subclass Fingerprinting. *Anal. Chem.* **2020**, *92* (13), 8827–8835. https://doi.org/10.1021/ACS.ANALCHEM.0C00293.

Chapter 5 Collision Induced Unfolding Enable the Quantitation of Isomass Biotherapeutics in Complex Biological Matrices

Brock R. Juliano and Brandon T. Ruotolo

5.1 Abstract

Quantitative mass spectrometry has been widely deployed to evaluate the concentrations of molecules within a variety of biological matrices. Typically, such quantitative mass spectrometry analyses are predicated upon the production of mass resolved precursor or fragment ions, leading to challenges surrounding the quantification of isomeric or conformationally distinct analytes. As such, new approaches are required for the label-free quantitation of isomass proteins. Native ion-mobility MS (nIM-MS) in combination with collision induced unfolding (CIU) is a potentially enabling approach for such quantitative mass spectrometry methods, as the technique can rapidly separate and detect many biomacromolecule isoforms. CIU uses collisional activation to capture the unfolding trajectory of ions in the gas phase, producing different intermediate structures that can be leveraged to distinguish protein structures that exhibit identical sizes at lower energies. Here we describe the deployment of Quantitative CIU methodology to measure the concentrations of isomass pairs of biotherapeutics and sequence homologues in both standard and biological matrices. Our results cover three antibody pairs and include examples of mixed therapies where multiple biologics are commonly provided to patients. In all cases, CIU enables the production of resolved features for each antibody mixture probed, producing calibration curves with correlation coefficients ranging from 0.92-0.99, limits of detection ranging from 300-5000 nM and sensitivities ranging from 8.7×10^{-5} nM^{-1} – 6×10^{-3}

μM^{-1}. We conclude our report by projecting the future utility of CIU-enabled quantitative MS methods.

5.2 Introduction

Quantitative mass spectrometry (qMS) assays have been widely deployed to determine the concentrations for a wide array biological molecules including: lipids[1], metabolites[2], peptides[3], proteins[4–6], glycans[7] and oligonucleotides[8]. Such qMS approaches are commonly interfaced with multiple ionization approaches including electrospray ionization (ESI) and matrix assisted laser desorption ionization (MALDI)[9], and can be coupled to mass spectrometry-based imaging (MSI) technologies to measure localized concentrations of analytes from *ex vivo* tissue samples[10]. In most cases, qMS analyses are predicated upon the adequate separation of the analytes of interest in m/z space. If the analytes of interest are not mass resolved *ab initio*, tags may be added to the analytes to improve the effective mass resolution observed. This approach is often deployed in order to quantify proteins[11,12]. Analytes can also be labeled using isotopically encoded tagging reagents in order to enable massively parallelized quantitative evaluations of proteins, peptides and metabolites[13,14]. While such tagging methodologies can be adroitly used to quantify a wide range of compounds within complex matrices, they can be inadequate when working with isomass analytes that cannot be modified with a tag prior to an experiment, such as large proteins extracted from tissues or sera, in addition to cases where specific biomolecular conformations are the intended targets of qMS.

For qMS assays targeting proteins, many approaches utilize a liquid chromatography tandem MS approach similar to those used routinely in bottom-up proteomics, relying upon the enzymatic digestion of proteins into peptides, which are the direct analytes of the qMS method[15,16]. While effective in many cases, such approaches are typically unable to track specific proteoforms or conformational states. In addition, in cases where proteins targets of qMS methods collocate with interferant proteins that exhibit strong sequence homologies, enzymatically-produced peptides may prove insufficient to quantify the protein of interest. For qMS methods that utilize intact protein ions for quantitation, organic solvents are often used which act to disrupt native protein folds, thus rendering such qMS approaches unable to track critical elements of protein structure for quantitative purposes[17].

Native mass spectrometry (nMS) is uniquely positioned to contribute to qMS assays, as such methods can preserve native-like protein structures for the duration of the experiment. Such nMS experiments require careful tuning of the solution phase and instrument conditions to minimize ion activation[18]. For a direct evaluation of protein conformation, nMS can be coupled with ion mobility (IM), which separates ions according to their collision cross-sections (CCSs) and charge. The ability of IM to resolve isomass analytes could be particularly useful for qMS experiments, as differences in the drift times of protein analytes could be used for quantitation; thereby enabling the quantitation of protein analytes that would otherwise not be quantifiable using standard qMS methodologies.

The amount of information obtained in an IM-MS experiment can be increased using collision induced unfolding (CIU). In a CIU experiment, protein ion populations are collisionally activated prior to the ion mobility separation, causing the proteins to adopt different conformational unfolding states. CIU has been widely deployed to gain insight into protein structure and stability for a wide array of proteins and protein complexes[19–22]. While proteins that are similar and isomass may have similar baseline drift times, as they are activated they may adopt slightly different drift times at differing collision voltages, allowing for the collision voltages at which the analytes are most differentiated to be identified. While CIU has been used previously to quantitatively evaluate a wide range of features associated with protein structure and stability, including the determining the number of appended chemical moieties on intact monoclonal antibodies (mAbs)[23], CIU methods for assessing the concentrations of protein biomarkers have yet to be described.

Here we describe the development of quantitative CIU workflows, used to evaluate mixtures of isomass proteins, including three mAb pairs and one pair of albumin sequence homologues. Our work demonstrates that CIU can be used to perform quantitative analyses not only under standard buffer conditions, but also from samples containing complex biological matrices such as sera. Quantitative CIU can produce highly linear calibration curves with correlation coefficients ranging from 0.92-0.99. Our quantitative CIU curves have sensitivities ranging from $8.7\text{x}10^{-5}$ nM to $6\text{x}10^{-3}$ μM^{-1} and limits of detection from 300 to 5000 nM. Importantly, the LODs determined for our CIU assays encompass the range of the concentrations where biotherapeutics can be found in patient serum[24,25]. As such, our data suggests that nMS and CIU can be more widely deployed as a quantitative tool for a wide range of protein systems where standard separation methods cannot be used or fragmentation cannot be achieved, or in cases where biomolecular conformation is an important criterion in the quantitative assay to be carried out.

5.3 Materials and Methods

5.3.1 Sample Preparation

Ammonium acetate, bovine serum, IgG1 λ, IgG2 κ, Adalimumab, Infliximab, Pembrolizumab, Vedolizumab, Bovine Serum Albumin (BSA) and Leporine Serum Albumin (LSA) were all obtained from MilliporeSigma (St. Louis, MO). IgG1, IgG2, Adalimumab, Pembrolizumab, and Vedolizumab were buffer exchanged into 200 mM ammonium acetate (pH=6.8-7) using Bio-Spin P-6 columns (Bio-Rad, Hercules, CA) and diluted to working concentrations of 1 mg/mL (~7 µM). BSA and LSA were prepared in 100 mM ammonium acetate and analyzed at concentrations of 10 µM. Protein samples were also spiked into bovine serum. Prior to adding protein to the serum, proteins greater than 30 kDa were filtered out of the serum using Amicon 30 kDa MWCO ultracentrifugal filters (MilliporeSigma). After incubation within the serum, proteins were then buffer exchanged into ammonium acetate prior to analysis by MS. For the serum studies, mAbs were analyzed at concentrations of 0.5 mg/mL in 200 mM ammonium acetate and serum albumins were analyzed at concentrations of 5 µM in 100 mM ammonium acetate.

5.3.2 Synapt G2

Native IM-MS and CIU data with IgG1, IgG2, and the serum albumins was collected on the Waters Synapt G2 (Milford, MA) quadrupole-ion mobility-time-of-flight MS (q-IM-TOF). Samples (7.5 µL) were transferred to a borosilicate capillary needle coated in gold, and ions were then generated by direct infusion with a nanoelectrospray (nESI) source in positive mode. The capillary voltages were set to 1.3-1.5 kV. For all proteins, the sampling cone was set to 20-30 V and the backing pressure was adjusted to 6 mbar. The helium cell was operated at 200 mL/min at a pressure 1.00×10^{-3} mbar. The traveling wave IM separator (TWIMS) was run at about 3.6 mbar and the IM separation was conducted with a wave velocity of 600 m/s and a wave height of 40 V. The TOF operated over at 2000-10000 Th mass range with a pressure of 2.4×10^{-6} mbar. To perform CIU, ions were collisionally activated in the trap prior to the IM separation. CIU data were collected in broadband fashion, without quadrupole selecting particular charge states. The collision voltages were then ramped from 10 to 200 V in 10 V increments.

5.3.3 Select Series cIM

nIM-MS and CIU data with IgG1, IgG2, Adalimumab, Infliximab, Pembrolizumab and Vedolizumab were collected using Waters SelectSeries IMS q-cyclic IM-TOF (Milford, MA). Similarly to the G2 analyses, samples (7.5 μL) were ionized using nESI in positive mode through direct infusion via a gold coated borosilicate capillary emitter. The capillary voltage was set to 1.3 kV, with the sample cone operating at 20 V and the backing pressure at 2.40 mbar. The TOF operated over 50-8000 Th with a pressure of 4.95×10^{-7} mbar. The cyclic TWIMS was run at 1.77 mbar with a wave velocity of 375 m/s and a wave height of 27 V. CIU data were collected in manner analogous to data collection on the G2, with ions being collisionally activated in the trap and CIU data were collected in 10 V increments from 10-200 V.

5.3.4 Data Processing

nIM-MS data were visualized using MassLynx and DriftScope (Waters). Mass deconvolution was performed using UniDec[26,27]. Drift times for the proteins at each step of the voltage gradient were extracted using TWIMExtract[28]. The extract drift times were compiled into CIU fingerprints using CIUSuite 2[29]. CIU fingerprints were then smoothed using a two-dimensional Savitzky-Golay function, including a smoothing window of 5 with 2 smoothing iterations. Root-mean-square-deviation (RMSD) analyses of the CIU data were performed using the compare function within CIUSuite 2. Univariate Feature Selection (UFS) was used to assist in the identification of the maximally differentiating collision voltages of the CIU fingerprints for certain protein systems. The Gaussian fitting feature of CIUSuite 2 was also utilized to construct Gaussian fits of the drift time data in order to perform the quantitative analysis by comparing the ratio of the intensities between the two peaks. All CIU fingerprints displayed in the paper are the result of three replicates. OriginPro (OriginLab, Northampton, MA) was also used for data processing.

5.4 Results and Discussion

5.4.1 Quantitative CIU of Model IgG Mixtures

IgG1 and IgG2 are subclasses of immunoglobulin G, the most prevalent immunoglobulin isotype in serum, with IgG1 and IgG2 being the first and second most prevalent subtypes of IgG respectively[30]. IgG1 and IgG2 primarily differ in the number of disulfide bonds that link the halfmers of the antibodies[31]. In addition to their analogous structures, IgG1 and IgG2 have highly similar molecular weights. Our nMS data demonstrates that these two subtypes possess molecular weights within 600 Da of one another (Figure VI-1) when analyzed *in vitro*. Given the charge states that are observed, this often results in there being a difference of less than 30 Th between the respective signals associated with each subclass, making them difficult to resolve in m/z space using standard nMS techniques (Figure VI-1). As such, IgG1 and IgG2 were analyzed using CIU (Figure 5-1a,b). Across all of the charge states studied, 23+ was

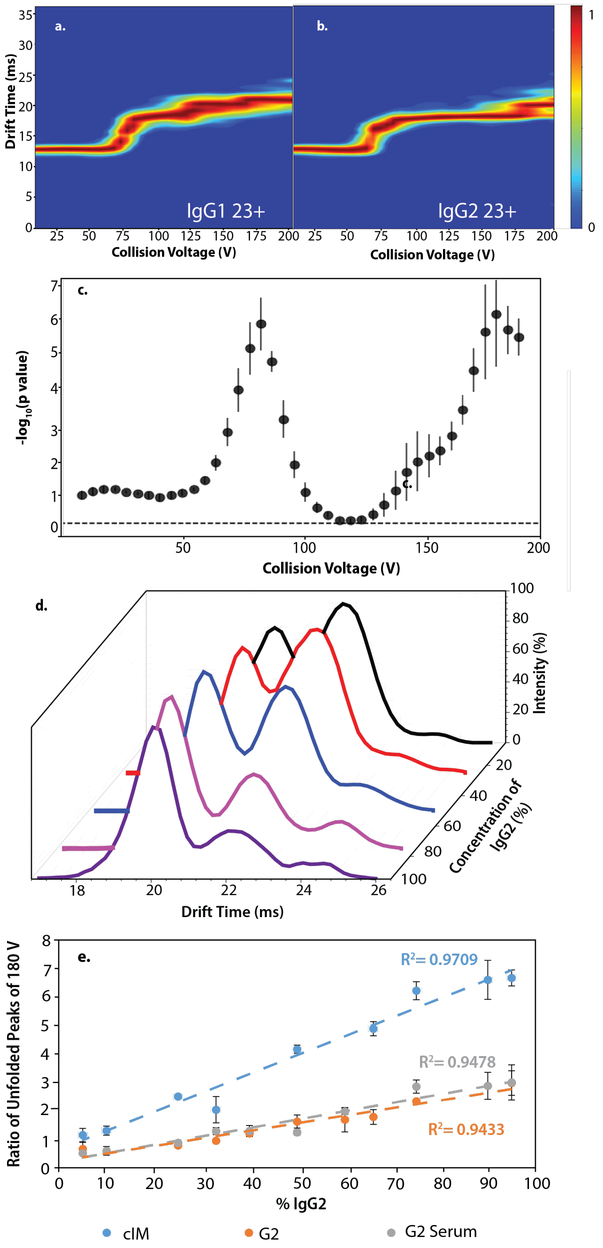

Figure 5-1 Averaged CIU fingerprints of 23+ IgG1 (a) and IgG2 (b). A univariate feature selection plot denoting the collision voltages that are most differentiating based on the CIU fingerprints of IgG1 and IgG2 (c). A plot of the drift times extracted from various concentrations of mixtures of IgG1 and IgG2 at 180 V for the 23+ charge states (d). A plot of linear calibration curves generated for mixtures of IgG1 and IgG2 on the G2 in ammonium acetate and serum, as well as on the cIM (e)

determined to produce the most different CIU fingerprints for each isotype, producing a fingerprint-wide RMSD of 20.53 when the two datasets were compared (Figure VI-2a), a value 6 times greater than that acquired for replicate CIU fingerprint comparisons[32]. A Univariate Feature Selection (UFS) analysis was performed using CIUSuite 2 by constructing a classifier for the IgG1 and IgG2 CIU data collected (Figure 5-1c). Based on our UFS analysis, the CIU slices at 180 V and 75 V were the most differentiated for IgG1 and IgG2 CIU data. At 180 V, IgG 1 exhibits two features, at 20 and 22ms respectively, whereas CIU data for IgG 2 lacks measurable intensity for a 22ms feature entirely. We chose to focus our quantitative method on 180 V, as this slice produced stable features, whereas CIU data captured at 75 V represented a transition between features.

Given the analysis framework described above, we constructed a variety of mixtures of IgG1 and IgG2 of various relative concentrations. We then analyzed these samples using nIM-MS using 180 V in the trap region of the instrument in order to generate the resolved transitions at 20 and 22 ms described above using mixtures where the IgG1 ranged in relative concentration from 5% to 95% by volume. Drift times for the 23+ charge states were then extracted for each mixture and subsequently fit to Gaussian functions in CIUSuite 2. As described above, following activation at 180V signals at 20 ms are common to both IgGs; however, signals observed at 22 ms are specific IgG1 (Figure 5-1d). As a result, the ratio of the intensities of these two features can be utilized to compute the relative amount of IgG2 within the sample. This procedure generates a for a highly linear calibration curve, exhibiting a correlation coefficient (R^2) of 0.94 (Figure 5-1e). Similar results can be obtained for data collected from IgG1 and IgG2 mixtures that have been spiked into serum, despite the increase in chemical noise from such an environment, we obtained calibration plots with and R^2 of 0.95 (Figure 5-1e). Results from serum demonstrate that similar calibration curves to be constructed with nearly identical levels of linearity. In addition, levels of sensitivity are nearly identical between quantitative CIU data collected from both matrices, where both experiments produced values of nominally 8x10^{-4} nM^{-1}. Similarly, the limits of detection obtained in these datasets were ~500 nM for both experiments, further indicating the robustness of our quantitative CIU methods.

While the data collected using a standard, linear TWIMS instrument generated a useful quantitative CIU method for our model IgGs, we moved our efforts to a cyclic ion mobility (cIM) system in order to leverage its improved IM resolution for quantitative CIU [33,34]. Similar to our linear TWIMS data described above, the cIM CIU fingerprints acquired for 23+ ions generated for IgG1 and IgG2 were significantly different, producing an RMSD of 28.67 on comparison, a value 9 times higher than RMSD values generated for control replicates for this system (Figure VI-2b)[32]. As above, we utilized 180 V of collision voltage in the cIM instrument in order to generate the CIU features tracked in our linear TWIMS data, and these features were readily observed, allowing us to produce an IgG calibration curve using the same procedure as developed for our linear TWIMS dataset. A UFS analysis indicated that 180 V is among the most differentiating voltages on the cIM as well. Greater linearity was obtained from IgG1/IgG2 mixtures in ammonium acetate on the cIM platform versus those analyzed on the linear TWIMS instrument, with calibration plots producing an R^2 of 0.97 (Figure 1e). Also, the cIM data exhibited twice the sensitivity (2.0x10^{-3} nM^{-1}) and an improved LOD (440 nM) when compared to analyses carried out via linear TWIMS. In general, these improvements can be explained by the superior IM resolution of the cIM instrument, which proved to be approximately 50 percent higher than our linear TWIMS data. Given the superior performance obtained on the cIM, we elected to collect quantitative CIU data for isomass biotherapeutic pairs exclusively on this platform.

5.4.2 Quantitative CIU of Biotherapeutics

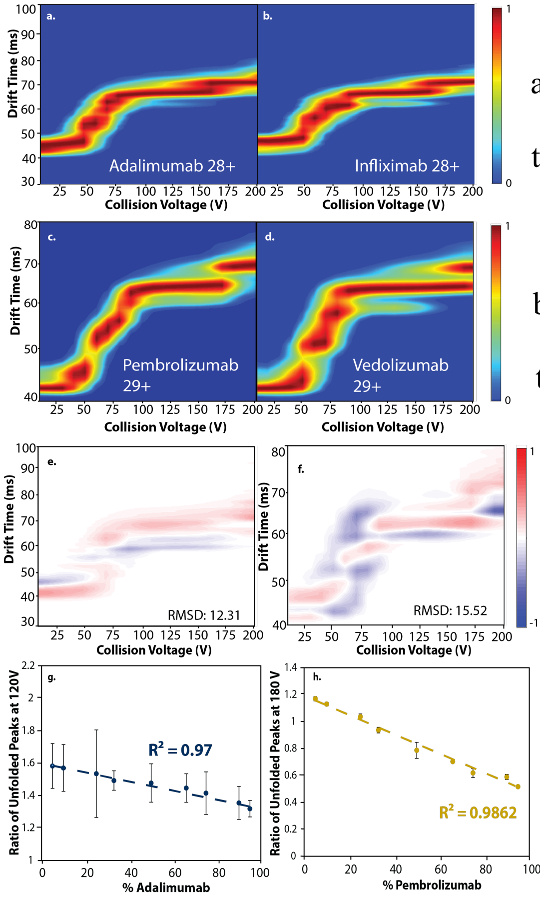

Figure 5-2 CIU fingerprints of the 28+ charges states of Adalimumab (a) and Infliximab (b) and CIU fingerprints of the 29+ charge states of Pembrolizumab (c) and Vedolizumab (d). Comparison plots between the fingerprints of Adalimumab and Infliximab (e) and Pembrolizumab and Vedolizumab (f). Linear calibration curves generated for mixtures of Adalimumab and Infliximab (g) and Pembrolizumab and Vedolizumab (h) in ammonium acetate.

Adalimumab and Infliximab are both IgG1 based therapeutics that serve as TNF-α inhibitors that are utilized for the treatment of autoimmune disorders[35]. While not typically taken together due to their similar pharmacological properties, Adalimumab and Infliximab may often be taken after one another in instances where one of therapeutic fails[36]. In such cases, tracking the effective concentrations of each therapeutic in patient serum is necessary in order establish future treatment plans. Adalimumab (ADA) and Infliximab (INF) differ in molecular weight by ~ 0.2% (300 Da). In the resultant MS data, this would yield differences of less than 10 Th between the MS signals recorded (Figure VI-3). Following a survey across mAb charge states, CIU data collected for 28+ ions was determined to be maximally differentiating between the two biotherapeutics, although the comparative RMSD value obtained for ADA and INF 28+ CIU data (12.31) is significantly less than the equivalent value recorded for our IgG analysis described above (Figure 5-2a,b).

This RMSD value is 3 times higher than control replicate RMSD values collected for these proteins on the cIM. A UFS analysis of our biotherapeutic CIU data identified 120 V as the optimal voltage for our quantitative CIU analysis. As above, IM data recorded at 120V reveals two features, 63 and 67ms, with the latter unique to INF at this activation voltage (Figure VI-4). Like the work with IgG1 and IgG2, the ratio of the intensities of these two features were used to produce a calibration curve, revealing strong linearity for experiments conducted in ammonium acetate ($R^2 = 0.97$) and bovine serum (Figure 5-2g and 5-3a). Sensitivity values determined for our calibration curves were similar between both data sets ($8.7\text{x}10^{-5}$ nM^{-1} in ammonium acetate and $1.7\text{x}10^{-4}$ nM^{-1} in serum) with LODs of 340 nM and 430 nM determined respectively.

Pembrolizumab (PEM) is an IgG4 based therapeutic that is used in immunotherapy treatments for various cancers[37–39], whereas Vedolizumab (VED) is an IgG1 based antirheumatic therapeutic[40]. PEM and VED can also be taken concurrently for certain cancer treatment regimens[41]. Despite being derived from different IgG subclasses, they differ in molecular weight by 0.4% (600 Da, Figure VI-5). We identified CIU fingerprints recorded for the 29+ as maximally differentiating for PEM and VED (RMSD of 15.52) as observed by cIM (Figure 5-2c-d, f). The RMSD here is 5 times higher than control replicate RMSD values collected for these species on the cIM. In this case, we determined 180 V as the optimal level of activation, producing features at 66ms and

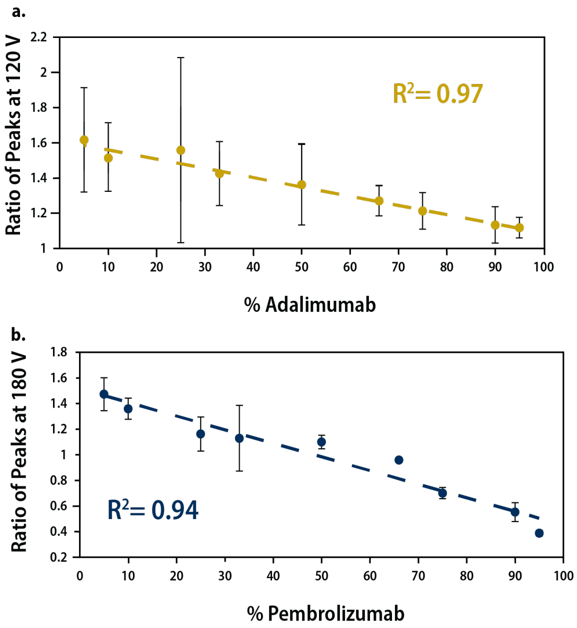

Figure 5-3 . Linear calibration curves generated for mixtures of Adalimumab and Infliximab (a) and Pembrolizumab and Vedolizumab (b) in bovine serum.

70ms, the latter of which is strongly correlated with PEM (Figure VI-6). Calibration curves were constructed for samples both in ammonium acetate and serum. The quantitative CIU calibration curves obtained under these conditions were strongly linear, with R^2 values of 0.99 and 0.94 obtained in ammonium acetate and serum respectively (Figure5-2h and Figure 5-3b), whereas the LODs obtained for these experiments were 290 nM and 500 nM respectively. Sensitivities of $2.3\text{x}10^{-4}$ nM^{-1} in ammonium acetate and $1.7\text{x}10^{-4}$ nM^{-1} in serum were determined during these quantitative CIU experiments. Taken together, our quantitative CIU experiments targeting mAbs illustrate the capabilities of this approach for determining the concentrations of isomass, iso-CCS (at low activation energies) biotherapeutics without the need for extensive sample preparation, digestion, or chemical modification.

5.4.3 Quantitative CIU of Sequence Homologues

Quantitative CIU can extend to separate and quantify protein sequence homologues. For example, previous studies have revealed that serum albumin homologues, such as BSA and LSA, can be differentiated by CIU despite their high sequence homology[42]. LSA and BSA differ in molecular weight by less than 300 Da, generating highly similar mass spectra with only a difference of a few Th between the MS signals recorded (Figure VI-7). Using the workflow introduced in Figure 1 (see above), we elected to collect and analyze CIU fingerprints for 16+ BSA/LSA charge states using linear TWIMS-MS, and a difference analysis of these data produced a fingerprint-wide RMSD value of 15.73 (Figure VI-8a-c). Our UFS analysis highlighted an activation potential 120 V, producing features at 24 ms (unique to BSA at this potential) and 26ms (unique to LSA at this potential) which enabled us to construct calibration curves for mixtures of BSA and LSA (5-50% BSA) based on a ratioing of these signals as described above (Figure VI-9). Calibration curves constructed from this CIU data were highly linear ($R^2 = 0.95$, Figure S6d), exhibiting a LOD and sensitivity of 5 μM and 6×10^{-3} μM^{-1} respectively. This example highlights the potential future applications of quantitative CIU methods to assess the concentrations of sequence variants and related proteoforms. Prior CIU analyses suggest that point mutants and the addition of single PTMs can significantly alter protein CIU in a manner that would enable the quantitative approaches discussed in this report[20,42–44].

5.5 Conclusions

Quantitative CIU is a promising methodology that can be deployed to track the concentrations of isomass protein biomarkers that would prove challenging to study using traditional qMS approaches. Quantitative CIU leverages the ability of CIU to sample the unique unfolding trajectory of each protein ion in order to identify subtle differences in drift time and thus resolve structurally similar protein systems. This is especially important for iso-CCS proteoforms which occupy identical drift times when not collisionally activated. Our data show that quantitative CIU can be deployed for multiple pairs of protein targets, including those associated with biotherapeutics and protein sequence homologues, achieving strong linearity for the calibration curves developed in each experiment. In addition, the sensitivities of these quantitative CIU analyses ranged between $8.7*10^{-5}$ nM^{-}-$6*10^{-3}$ μM^{-1}, with LODs between 300-5000 nM, which is within standard clinical concentration of mAbs in serum[24]. Our data demonstrate that quantitative CIU approaches can be used for systems both in standard matrices and complex biological matrices, such as sera, highlighting the potential application of quantitative CIU for clinical pharmacological applications[24,25]. While our approaches do not involve separations prior to nESI, on-line chromatography or electrophoretic separations would clearly act to extend the sensitivities and LODs of our quantitative CIU methods even further when analyzing samples from biological matrices. While this study focused on serum, it is possible that Quantitative CIU methodologies could be applied to analytes extracted from other matrices, such as tissues sampled by liquid extraction surface analysis coupled to nIM-MS[45,46].

By extension, the quantitative CIU methods discussed in this report will also benefit from further advances in IM and CIU technologies. Recent innovations in IM-MS with the cIM system have allowed for multidimensional IM^n-MS experiments to be performed, suggesting that features of the CIU fingerprints may be selected for further activation and separation. Such methodologies could be leveraged to track the concentrations of biomarkers in the future, especially for proteins that may have particularly similar CIU fingerprints[34]. Our data shows that the higher IM resolution offered by cIM can be instrumental in achieve stronger results with higher degrees of linearity. Prior reports have also demonstrated how nIM-MS can be adapted to enable high-throughput assays, with complete CIU fingerprints acquired in 30 seconds and with as little as a 40 nanoliters consumed per sample, thus making it conceivable that quantitative CIU could be similarly automated and used in a high throughput fashion[47]. Improving the throughput of quantitative CIU would be critically important for clinical assays, in which quantitative CIU could be deployed to measure the concentrations of isomass proteins extracted from biological matrices

5.6 References

(1) Koivusalo, M.; Haimi, P.; Heikinheimo, L.; Kostiainen, R.; Somerharju, P. Quantitative Determination of Phospholipid Compositions by ESI-MS: Effects of Acyl Chain Length, Unsaturation, and Lipid Concentration on Instrument Response. *Journal of Lipid Research* **2001**, *42* (4), 663–672. https://doi.org/10.1016/S0022-2275(20)31176-7.

(2) Oberson, J. M.; Bénet, S.; Redeuil, K.; Campos-Giménez, E. Quantitative Analysis of Vitamin D and Its Main Metabolites in Human Milk by Supercritical Fluid Chromatography Coupled to Tandem Mass Spectrometry. *Anal Bioanal Chem* **2020**, *412* (2), 365–375. https://doi.org/10.1007/s00216-019-02248-5.

(3) Schweppe, D. K.; Prasad, S.; Belford, M. W.; Navarrete-Perea, J.; Bailey, D. J.; Huguet, R.; Jedrychowski, M. P.; Rad, R.; McAlister, G.; Abbatiello, S. E.; Woulters, E. R.; Zabrouskov,

V.; Dunyach, J.-J.; Paulo, J. A.; Gygi, S. P. Characterization and Optimization of Multiplexed Quantitative Analyses Using High-Field Asymmetric-Waveform Ion Mobility Mass Spectrometry. *Anal. Chem.* **2019**, *91* (6), 4010–4016. https://doi.org/10.1021/acs.analchem.8b05399.

(4) Sim, K. H.; Liu, L. C.-Y.; Tan, H. T.; Tan, K.; Ng, D.; Zhang, W.; Yang, Y.; Tate, S.; Bi, X. A Comprehensive CHO SWATH-MS Spectral Library for Robust Quantitative Profiling of 10,000 Proteins. *Sci Data* **2020**, *7* (1), 263. https://doi.org/10.1038/s41597-020-00594-z.

(5) Bian, Y.; Zheng, R.; Bayer, F. P.; Wong, C.; Chang, Y.-C.; Meng, C.; Zolg, D. P.; Reinecke, M.; Zecha, J.; Wiechmann, S.; Heinzlmeir, S.; Scherr, J.; Hemmer, B.; Baynham, M.; Gingras, A.-C.; Boychenko, O.; Kuster, B. Robust, Reproducible and Quantitative Analysis of Thousands of Proteomes by Micro-Flow LC–MS/MS. *Nat Commun* **2020**, *11* (1), 157. https://doi.org/10.1038/s41467-019-13973-x.

(6) Rosati, S.; Yang, Y.; Barendregt, A.; Heck, A. J. R. Detailed Mass Analysis of Structural Heterogeneity in Monoclonal Antibodies Using Native Mass Spectrometry. *Nat Protoc* **2014**, *9* (4), 967–976. https://doi.org/10.1038/nprot.2014.057.

(7) Zhao, X.; Guo, C.; Huang, Y.; Huang, L.; Ma, G.; Liu, Y.; He, Q.; Wang, H.; Chen, K.; Pan, Y. Combination Strategy of Reactive and Catalytic Matrices for Qualitative and Quantitative Profiling of N-Glycans in MALDI-MS. *Anal. Chem.* **2019**, *91* (14), 9251–9258. https://doi.org/10.1021/acs.analchem.9b02144.

(8) Taoka, M.; Nobe, Y.; Hori, M.; Takeuchi, A.; Masaki, S.; Yamauchi, Y.; Nakayama, H.; Takahashi, N.; Isobe, T. A Mass Spectrometry-Based Method for Comprehensive Quantitative Determination of Post-Transcriptional RNA Modifications: The Complete Chemical Structure of Schizosaccharomyces Pombe Ribosomal RNAs. *Nucleic Acids Research* **2015**, *43* (18), e115. https://doi.org/10.1093/nar/gkv560.

(9) Unsihuay, D.; Mesa Sanchez, D.; Laskin, J. Quantitative Mass Spectrometry Imaging of Biological Systems. *Annu Rev Phys Chem* **2021**, *72*, 307–329. https://doi.org/10.1146/annurev-physchem-061020-053416.

(10) Ye, H.; Wang, J.; Tian, Z.; Ma, F.; Dowell, J.; Bremer, Q.; Lu, G.; Baldo, B.; Li, L. Quantitative Mass Spectrometry Reveals Food Intake-Induced Neuropeptide Level Changes in Rat Brain: Functional Assessment of Selected Neuropeptides as Feeding Regulators *. *Molecular & Cellular Proteomics* **2017**, *16* (11), 1922–1937. https://doi.org/10.1074/mcp.RA117.000057.

(11) Muntel, J.; Kirkpatrick, J.; Bruderer, R.; Huang, T.; Vitek, O.; Ori, A.; Reiter, L. Comparison of Protein Quantification in a Complex Background by DIA and TMT Workflows with Fixed Instrument Time. *J. Proteome Res.* **2019**, *18* (3), 1340–1351. https://doi.org/10.1021/acs.jproteome.8b00898.

(12) Ahrné, E.; Glatter, T.; Viganò, C.; Schubert, C. von; Nigg, E. A.; Schmidt, A. Evaluation and Improvement of Quantification Accuracy in Isobaric Mass Tag-Based Protein Quantification Experiments. *J. Proteome Res.* **2016**, *15* (8), 2537–2547. https://doi.org/10.1021/acs.jproteome.6b00066.

(13) Chahrour, O.; Cobice, D.; Malone, J. Stable Isotope Labelling Methods in Mass Spectrometry-Based Quantitative Proteomics. *Journal of Pharmaceutical and Biomedical Analysis* **2015**, *113*, 2–20. https://doi.org/10.1016/j.jpba.2015.04.013.

(14) Jang, C.; Chen, L.; Rabinowitz, J. D. Metabolomics and Isotope Tracing. *Cell* **2018**, *173* (4), 822–837. https://doi.org/10.1016/j.cell.2018.03.055.

(15) Gillette, M. A.; Carr, S. A. Quantitative Analysis of Peptides and Proteins in Biomedicine by Targeted Mass Spectrometry. *Nat Methods* **2013**, *10* (1), 28–34. https://doi.org/10.1038/nmeth.2309.

(16) Pino, L. K.; Searle, B. C.; Bollinger, J. G.; Nunn, B.; MacLean, B.; MacCoss, M. J. The Skyline Ecosystem: Informatics for Quantitative Mass Spectrometry Proteomics. *Mass Spectrometry Reviews* **2017**, *39* (3), 229–244. https://doi.org/10.1002/mas.21540.

(17) Chen, Y.; Mao, P.; Wang, D. Quantitation of Intact Proteins in Human Plasma Using Top-Down Parallel Reaction Monitoring-MS. *Anal. Chem.* **2018**, *90* (18), 10650–10653. https://doi.org/10.1021/acs.analchem.8b02699.

(18) Heck, A. J. R. Native Mass Spectrometry: A Bridge between Interactomics and Structural Biology. *Nat Methods* **2008**, *5* (11), 927–933. https://doi.org/10.1038/nmeth.1265.

(19) Tian, Y.; Han, L.; Buckner, A. C.; Ruotolo, B. T. Collision Induced Unfolding of Intact Antibodies: Rapid Characterization of Disulfide Bonding Patterns, Glycosylation, and Structures. *Anal. Chem.* **2015**, *87* (22), 11509–11515. https://doi.org/10.1021/acs.analchem.5b03291.

(20) Fantin, S. M.; Parson, K. F.; Yadav, P.; Juliano, B.; Li, G. C.; Sanders, C. R.; Ohi, M. D.; Ruotolo, B. T. Ion Mobility–Mass Spectrometry Reveals the Role of Peripheral Myelin Protein Dimers in Peripheral Neuropathy. *Proceedings of the National Academy of Sciences* **2021**, *118* (17), e2015331118.

(21) Hernandez-Alba, O.; Wagner-Rousset, E.; Beck, A.; Cianférani, S. Native Mass Spectrometry, Ion Mobility, and Collision-Induced Unfolding for Conformational Characterization of IgG4 Monoclonal Antibodies. *Anal. Chem.* **2018**, *90* (15), 8865–8872. https://doi.org/10.1021/acs.analchem.8b00912.

(22) Huang, Y.; Salinas, N. D.; Chen, E.; Tolia, N. H.; Gross, M. L. Native Mass Spectrometry, Ion Mobility, and Collision-Induced Unfolding Categorize Malaria Antigen/Antibody Binding. *J. Am. Soc. Mass Spectrom.* **2017**, *28* (11), 2515–2518. https://doi.org/10.1007/s13361-017-1782-0.

(23) Tian, Y.; Lippens, J. L.; Netirojjanakul, C.; Campuzano, I. D. G.; Ruotolo, B. T. Quantitative Collision-Induced Unfolding Differentiates Model Antibody–Drug Conjugates. *Protein Science* **2019**, *28* (3), 598–608. https://doi.org/10.1002/pro.3560.

(24) Adedokun, O. J.; Sandborn, W. J.; Feagan, B. G.; Rutgeerts, P.; Xu, Z.; Marano, C. W.; Johanns, J.; Zhou, H.; Davis, H. M.; Cornillie, F.; Reinisch, W. Association Between Serum Concentration of Infliximab and Efficacy in Adult Patients With Ulcerative Colitis. *Gastroenterology* **2014**, *147* (6), 1296-1307.e5. https://doi.org/10.1053/j.gastro.2014.08.035.

(25) Kolho, K.-L. Therapeutic Drug Monitoring and Outcome of Infliximab Therapy in Pediatric Onset Inflammatory Bowel Disease. *Frontiers in Pediatrics* **2021**, *8*.

(26) Marty, M. T.; Baldwin, A. J.; Marklund, E. G.; Hochberg, G. K. A.; Benesch, J. L. P.; Robinson, C. V. Bayesian Deconvolution of Mass and Ion Mobility Spectra: From Binary Interactions to Polydisperse Ensembles. *Anal. Chem.* **2015**, *87* (8), 4370–4376. https://doi.org/10.1021/acs.analchem.5b00140.

(27) Kostelic, M. M.; Marty, M. T. Deconvolving Native and Intact Protein Mass Spectra with UniDec. In *Proteoform Identification: Methods and Protocols*; Sun, L., Liu, X., Eds.; Methods in Molecular Biology; Springer US: New York, NY, 2022; pp 159–180. https://doi.org/10.1007/978-1-0716-2325-1_12.

(28) Haynes, S. E.; Polasky, D. A.; Dixit, S. M.; Majmudar, J. D.; Neeson, K.; Ruotolo, B. T.; Martin, B. R. Variable-Velocity Traveling-Wave Ion Mobility Separation Enhancing Peak Capacity for Data-Independent Acquisition Proteomics. *Anal. Chem.* **2017**, *89* (11), 5669–5672. https://doi.org/10.1021/acs.analchem.7b00112.

(29) Polasky, D. A.; Dixit, S. M.; Fantin, S. M.; Ruotolo, B. T. CIUSuite 2: Next-Generation Software for the Analysis of Gas-Phase Protein Unfolding Data. *Anal. Chem.* **2019**, *91* (4), 3147–3155. https://doi.org/10.1021/acs.analchem.8b05762.

(30) Vidarsson, G.; Dekkers, G.; Rispens, T. IgG Subclasses and Allotypes: From Structure to Effector Functions. *Frontiers in Immunology* **2014**, *5*.

(31) Napodano, C.; Marino, M.; Stefanile, A.; Pocino, K.; Scatena, R.; Gulli, F.; Rapaccini, G. L.; Delli Noci, S.; Capozio, G.; Rigante, D.; Basile, U. Immunological Role of IgG Subclasses. *Immunological Investigations* **2021**, *50* (4), 427–444. https://doi.org/10.1080/08820139.2020.1775643.

(32) Gadkari, V. V.; Juliano, B. R.; Mallis, C. S.; May, J. C.; Kurulugama, R. T.; Fjeldsted, J. C.; McLean, J. A.; Russell, D. H.; Ruotolo, B. T. Performance Evaluation of In-Source Ion Activation Hardware for Collision-Induced Unfolding of Proteins and Protein Complexes on a Drift Tube Ion Mobility-Mass Spectrometer. *Analyst* **2023**, *148* (2), 391–401. https://doi.org/10.1039/D2AN01452A.

(33) Giles, K.; Ujma, J.; Wildgoose, J.; Pringle, S.; Richardson, K.; Langridge, D.; Green, M. A Cyclic Ion Mobility-Mass Spectrometry System. *Anal. Chem.* **2019**, *91* (13), 8564–8573. https://doi.org/10.1021/acs.analchem.9b01838.

(34) Eldrid, C.; Ujma, J.; Kalfas, S.; Tomczyk, N.; Giles, K.; Morris, M.; Thalassinos, K. Gas Phase Stability of Protein Ions in a Cyclic Ion Mobility Spectrometry Traveling Wave Device. *Anal. Chem.* **2019**, *91* (12), 7554–7561. https://doi.org/10.1021/acs.analchem.8b05641.

(35) Murdaca, G.; Spanò, F.; Contatore, M.; Guastalla, A.; Penza, E.; Magnani, O.; Puppo, F. Immunogenicity of Infliximab and Adalimumab: What Is Its Role in Hypersensitivity and Modulation of Therapeutic Efficacy and Safety? *Expert Opinion on Drug Safety* **2016**, *15* (1), 43–52. https://doi.org/10.1517/14740338.2016.1112375.

(36) Chaparro, M.; Andreu, M.; Barreiro-de Acosta, M.; García-Planella, E.; Ricart, E.; Domènech, E.; Esteve, M.; Merino, O.; Nos, P.; Peñalva, M.; Gisbert, J. P. Effectiveness of Infliximab after Adalimumab Failure in Crohn's Disease. *World J Gastroenterol* **2012**, *18* (37), 5219–5224. https://doi.org/10.3748/wjg.v18.i37.5219.

(37) André, T.; Shiu, K.-K.; Kim, T. W.; Jensen, B. V.; Jensen, L. H.; Punt, C.; Smith, D.; Garcia-Carbonero, R.; Benavides, M.; Gibbs, P.; de la Fouchardiere, C.; Rivera, F.; Elez, E.; Bendell, J.; Le, D. T.; Yoshino, T.; Van Cutsem, E.; Yang, P.; Farooqui, M. Z. H.; Marinello, P.; Diaz, L. A. Pembrolizumab in Microsatellite-Instability–High Advanced Colorectal Cancer. *New England Journal of Medicine* **2020**, *383* (23), 2207–2218. https://doi.org/10.1056/NEJMoa2017699.

(38) Gandhi, L.; Rodríguez-Abreu, D.; Gadgeel, S.; Esteban, E.; Felip, E.; De Angelis, F.; Domine, M.; Clingan, P.; Hochmair, M. J.; Powell, S. F.; Cheng, S. Y.-S.; Bischoff, H. G.; Peled, N.; Grossi, F.; Jennens, R. R.; Reck, M.; Hui, R.; Garon, E. B.; Boyer, M.; Rubio-Viqueira, B.; Novello, S.; Kurata, T.; Gray, J. E.; Vida, J.; Wei, Z.; Yang, J.; Raftopoulos, H.; Pietanza, M. C.; Garassino, M. C. Pembrolizumab plus Chemotherapy in Metastatic Non–Small-Cell Lung Cancer. *New England Journal of Medicine* **2018**, *378* (22), 2078–2092. https://doi.org/10.1056/NEJMoa1801005.

(39) Schmid, P.; Cortes, J.; Pusztai, L.; McArthur, H.; Kümmel, S.; Bergh, J.; Denkert, C.; Park, Y. H.; Hui, R.; Harbeck, N.; Takahashi, M.; Foukakis, T.; Fasching, P. A.; Cardoso, F.; Untch, M.; Jia, L.; Karantza, V.; Zhao, J.; Aktan, G.; Dent, R.; O'Shaughnessy, J. Pembrolizumab for Early Triple-Negative Breast Cancer. *New England Journal of Medicine* **2020**, *382* (9), 810–821. https://doi.org/10.1056/NEJMoa1910549.

(40) Feagan, B. G.; Rutgeerts, P.; Sands, B. E.; Hanauer, S.; Colombel, J.-F.; Sandborn, W. J.; Van Assche, G.; Axler, J.; Kim, H.-J.; Danese, S.; Fox, I.; Milch, C.; Sankoh, S.; Wyant, T.; Xu, J.; Parikh, A. Vedolizumab as Induction and Maintenance Therapy for Ulcerative Colitis. *New England Journal of Medicine* **2013**, *369* (8), 699–710. https://doi.org/10.1056/NEJMoa1215734.

(41) Frohne, C. C.; Llano, E. M.; Perkovic, A.; Cohen, R. D.; Luke, J. J. Complete Response of Metastatic Melanoma in a Patient with Crohn's Disease Simultaneously Receiving Anti-A4β7 and Anti-PD1 Antibodies. *Journal for ImmunoTherapy of Cancer* **2019**, *7* (1), 1. https://doi.org/10.1186/s40425-018-0484-x.

(42) Eschweiler, J. D.; Martini, R. M.; Ruotolo, B. T. Chemical Probes and Engineered Constructs Reveal a Detailed Unfolding Mechanism for a Solvent-Free Multidomain Protein. *J. Am. Chem. Soc.* **2017**, *139* (1), 534–540. https://doi.org/10.1021/jacs.6b11678.

(43) Bellamy-Carter, J.; O'Grady, L.; Passmore, M.; Jenner, M.; Oldham, N. J. Decoding Protein Gas-Phase Stability with Alanine Scanning and Collision-Induced Unfolding Ion Mobility Mass Spectrometry. *Analysis & Sensing* **2021**, *1* (1), 63–69. https://doi.org/10.1002/anse.202000019.

(44) Tian, Y.; Ruotolo, B. T. Collision Induced Unfolding Detects Subtle Differences in Intact Antibody Glycoforms and Associated Fragments. *International Journal of Mass Spectrometry* **2018**, *425*, 1–9. https://doi.org/10.1016/j.ijms.2017.12.005.

(45) Hale, O. J.; Cooper, H. J. Native Mass Spectrometry Imaging and In Situ Top-Down Identification of Intact Proteins Directly from Tissue. *J. Am. Soc. Mass Spectrom.* **2020**, *31* (12), 2531–2537. https://doi.org/10.1021/jasms.0c00226.

(46) Mikhailov, V. A.; Griffiths, R. L.; Cooper, H. J. Liquid Extraction Surface Analysis for Native Mass Spectrometry: Protein Complexes and Ligand Binding. *International Journal of Mass Spectrometry* **2017**, *420*, 43–50. https://doi.org/10.1016/j.ijms.2016.09.011.

(47) D'Amico, C. I.; Polasky, D. A.; Steyer, D. J.; Ruotolo, B. T.; Kennedy, R. T. Ion Mobility-Mass Spectrometry Coupled to Droplet Microfluidics for Rapid Protein Structure Analysis and Drug Discovery. *Anal. Chem.* **2022**. https://doi.org/10.1021/acs.analchem.2c02307.

Chapter 6 The Development of an Automated, High-Throughput Methodology for Native Mass Spectrometry and Collision Induced Unfolding

Brock R. Juliano, Joseph W. Keating, Henry W. Li, Anna G. Anders, Zhuoer Xie and Brandon T. Ruotolo

6.1 Abstract

Native ion mobility mass spectrometry (nIM-MS) has emerged as a powerful technology for the determination of native-like biomolecular structure in the gas phase. When combined with collisional activation in a collision induced unfolding (CIU) experiment, nIM-MS experimentation can be leveraged to gain greater insight into biomolecular structure, as well as allowing for the structural effects of ligand binding to be probed. However, nIM-MS remains a throughput limited technique, due to bottlenecks associated with sample preparation and introduction. Here we explore the use of a RapidFire (RF) system to develop an automated, high-throughput methodology for nMS. Native RF-MS (nRF-MS) can perform online desalting and sample introduction in as little as 10 s per well. When combined with CIU, nRF-MS can be used to collect some of the fastest CIU data reported, with fingerprints being acquired in 30 s. When compared to nMS and CIU data collected with standard approaches, nRF-MS data is highly similar capturing the same conformational ensembles as measured by collision cross section (CCS). nRF-MS is extensible to a variety of biomolecular systems of interest, including proteins and protein complexes ranging from 5-150 kDa and oligonucleotides. nRF-MS data with biotherapeutics, including monoclonal antibodies and siRNA, suggest that nRF-MS could be a powerful tool for enabling high-throughput nMS analyses in biopharma and academia. Future

work will focus on improving the throughput of this assay and reducing the sample volume requirements.

6.2 Introduction

Native mass spectrometry (nMS) has emerged as a transformative technique for structural biology. In a nMS experiment, conditions both in solution and in the gas phase are carefully tuned such that the native-like biomolecular ions are preserved for the duration of the measurement. Typically, this is done by preparing samples in aqueous solutions containing volatile salts and prepared at neutral pH, before gently ionizing the biomolecules such that transient, non-covalent interactions may be preserved throughout the ionization process[1]. Such nMS methods have been widely deployed to gain structural insights into many diverse systems of interest including: oligonucleotides, membrane proteins, monoclonal antibodies (mAbs), chaperones, and intact viruses[2–14]. In order to provide structural information content, nMS is often combined with ion mobility (IM) spectrometry to perform native IM-MS (nIM-MS) experiments that allow for biomolecular ions to separated according to their size, shape, and charge [15–19]. The measured drift times can then be converted to collision cross section (CCS) values that described the 3D rotationally average size of the ion, which can be validated against measurements from other biophysical techniques through calibration[20–25].

However, since biomolecules typically adopt an ensemble of conformational states, CCS measurements of native-like ions alone are often insufficient to detect subtle structural differences between samples[26,27]. Accordingly, biomolecules can be collisionally activated and unfolded to sample different conformational states that can be used to resolve iso-CCS ions and evaluate biomolecular stabilities via collision induced unfolding (CIU). CIU data are typically treated as fingerprints, where changes in CCS produced during activation can be mapped and quantified in order to produce multivariate classifiers capable of identifying and evaluating of subtly different protein states. [28]. For example, CIU data has been deployed to study a variety of protein systems including biotherapeutics, membrane proteins and kinases[6,29–32]. CIU features are generally reproducible between laboratories when collected using a drift tube instrument, enabling future databasing efforts for CIU data for the identification of proteoforms and conformationally-distinct biomarker conformers[33].

While nMS and CIU have been widely deployed, they largely remain throughput limited technologies due to bottlenecks associated with pre-analysis desalting and sample introduction using nanoelectrospray ionization (nESI) at low flow rates. Typically, samples must be desalted prior to analysis by MS, a process which can take up to 25 minutes[34]. Beyond this, the nESI emitters often used in nMS experiments are typically single use and are prone to clogging and unstable signal[35]. Multiple prior reports have described methods to improve the throughput nMS. Examples include, the Advion Nanomate [36–40], and standard autosamplers coupled to fast desalting or separation technologies [41–44]. In addition to nMS, recent efforts have been made to increase the throughput of CIU measurements, including droplet microfluidics for sample introduction and online SEC that requires several minutes per sample[42,43,45].

The RapidFire (RF) automated, high-throughput robotic system enables the analysis of samples from a well plate format and performs online sample clean-up, with standard RF utilizing solid phase extraction (SPE) with a reverse phase (RP) cartridge before eluting samples onto the MS instrument[36]. RF-MS has been widely deployed to perform high-throughput analyses of small molecules including peptides, lipids and metabolites[46–52]. Experiments have also been performed with RF-MS wherein denatured biomolecules were analyzed in as little as 20 seconds per sample[53–55]. Here, we present modifications to the standard RF layout to accommodate nMS and CIU experiments, by using a size exclusion chromatography (SEC) cartridge for online desalting and non-denaturing solvents for nMS. Furthermore, we interface the RF with drift tube IM-q-TOF for the first time, and verify the ability of the RF ion source to enable nMS and CIU data collection [29,33,56]. We find that nMS experiments on the RF require seconds per sample, and CIU data can be collected in an automated fashion in 30 seconds per fingerprint, and we present CIU data for a variety of standard proteins and protein complexes. In addition, we collected nRF-MS and CIU data for biotherapeutics, including mAbs and a siRNA duplex, suggesting the potential of nRF-MS for enabling high-throughput CIU screens for biopharma applications. Overall, we find that nRF-MS data produces ion CCSs without significant difference to infusion-based values, and CIU fingerprints with root-mean-squared difference (RMSD) values similar to infusion-mode replicates, indicating that the ions produced by nRF-MS share the same conformational states with those produced using standard nESI-MS sources. We conclude by discussing the future use of nRF-MS for enabling high-throughput CIU screens of biotherapeutic targets, as well as enabling the rapid collection of structural measurements, such as CCSs and CIU fingerprints in service of integrative structural biology campaigns.

6.3 Materials and Methods

6.3.1 Sample Preparation

Ammonium acetate, triethylammonium acetate (TEAA), bovine serum album (BSA), insulin, alcohol dehydrogenase (ADH), concanavalin A (ConA), β-lactoglobulin (β-lac), myoglobin, NIST mAb, Cytochrome C (Cyt C), IgG1 Universal Antibody Standard (Sigma mAb), NIST mAb, Streptavidin, Vedolizumab, Pembrolizumab, IgG2 and IgG4 were all obtained from MilliporeSigma (St. Louis, MO). Sodium chloride and acetonitrile was obtained from Fisher Scientific (Pittsburgh, PA). GDX was also purified from *Escherichia coli* into β-n-decyl maltoside micelles (4 mM), 100 mM NaCl, and 10 mM HEPES (pH=8.0). Information the preparation of about the siRNA duplex is available in the supplementary information. The siRNA duplex and mitochondrial $^{LEU(UUR)}$tRNA (mt-tRNA) were obtained from Integrated DNA Technologies (Coralville, IA). Except for mAbs, all samples were prepared at 10 μM concentrations in the appropriate solvent prior to RF-MS analysis. mAbs were prepared at 0.5 mg/mL concentrations (~3.5 μM) Typically samples were prepared in 200 mM ammonium acetate, but Insulin samples were also prepared directly in bovine serum (MilliporeSigma) filtered with a 30 kDa ultracentrifugal filter (MilliporeSigma) to deplete it of extraneous proteins) and 0.001-1 M NaCl.

6.3.2 RapidFire Operation

Samples were run using a RapidFire 400 (Agilent Technologies, Santa Clara, CA). RapidFire pumps 1, 2 and 3 supplied 200 mM ammonium acetate. Experimentation with streptavidin used 160 mM ammonium acetate and 40 mM TEAA on pumps 1, 2 and 3 to accomplish charge reduction. The peristaltic pump supplied acetonitrile and water to the RF. All solvents were LC-MS grade and degassed prior to being loaded to the RF. Protein and oligonucleotide stocks were pipetted directly onto the 96-well plate. Samples were drawn into the 35 μL sample loop, prior to being loaded onto a cartridge packed with Sepharose 6 Fast Flow resin (Optimize Technologies, Oregon City, OR), before ultimately being eluted onto the MS. Pump 1 was operated at 0.5 mL/min and Pumps 2 and 3 were set to 0.42 mL/min. Lower flow rates than typical were deployed to be compatible with a microelectrospray ionization source. The aspiration step was programmed to take 1.8 s with the cartridge wash taking 4.5 s and the reequilibration step completing in 3 s, with the whole cycle completing in less than 10 s (Figure 6-1a). The sipper was washed with organic and aqueous solvent immediately before and each sample run, with discrete peaks in the chromatogram corresponding to solvent and sample injections (Figure VII-1). The plumbing was altered from the standard configuration with valve 2 ports 2 and 5 being reversed to allow for biomolecules to reach the MS after being desalted on the SEC cartridge (Figures VII-2 and 6-1b).

6.3.3 Direct Infusion Methods

Samples were aspirated into a GasTight #1750 (Hamilton Companies, Reno, NV) syringe connected to the nebulizer source through 0.0625" outer diameter PEEK tubing. Samples were infused with a syringe pump at 750 μL/hr with a syringe pump (kD Scientific, Holliston, MA).

6.3.4 nIM-MS and CIU

Samples were eluted directly onto an Agilent 6560c using the micronebulizer (Agilent Technologies) source which is more compatible with RF flow rates than nESI. The micronebulizer source has been previously used to collect nMS data and has been demonstrated to be comparable to nESI-MS for nMS applications[33]. The following positive polarity ESI settings were used based on previous studies on the micronebulizer: transfer capillary voltage, 3 kV; fragmentor, 450 V; nozzle voltage, 2 kV; drying gas flow 5 L/min; drying gas temperature, 140-300°; sheath gas flow 11 L/min; sheath gas temperature, 140° [33]. Additional tuning parameters may be viewed in Table VII-1. The drying gas temperature was adjusted based on several factors, largely based on the size of the biomolecules. Proteins less than 65 kDa were sprayed at 140° drying gas temperature, while larger proteins were sprayed at 250° to be effectively desolvated. RNA species were sprayed between 250 and 300°. The drift tube was operated under ambient temperature with a 18.5 V/cm gradient. The high-pressure funnel, ion trap funnel and drift tube were operated with high purity N_2 and under pressures of 4.5 mbar, 3.95 mbar and 3.8 mbar respectively. $^{DT}CCS_{N2}$ measurements were collected based on a single field calibration with tune mix (Agilent Technologies), which is derived from the Mason-Schamp equation as described previously[21]. Mass spectra were visualized using MassHunter (Agilent Technologies) and mMass[57–59].

CIU has been extensively characterized on the 6560c[29,33,56]. The 6560c unfolds ions by ramping a potential difference between the fragmentor lens and the capillary exit. When performed in N_2, protein and oligonucleotide ions can be successfully unfolded in the front funnel prior to IM separation. CIU ramps were programmed in using the time segment feature in MassHunter (Agilent Technologies), with the voltage ramp programmed to run as the molecules elute off the RF. For mAb CIU, sulfur hexafluoride was doped into the drying gas at 10% v/v concentration. CIU data were created by plotting the $^{DT}CCS_{N2}$ of the molecule as a function of the capillary exit voltage, referred to hereafter as the collision voltage. CIU data were plotted and analyzed using CIUSuite 2, which allowed for the identification of features and CIU50s in the data[28]. Sample CIU plotting parameters are available in Table VII-2. All CIU data were collected in triplicate and averaged in CIUSuite 2.

6.3.5 mAb Deglycosylation and Stress

mAb samples were deglycosylated using PNGase-F (New England Biolabs, Ipswich, MA). 10 μL of mAb stock (0.5 mg/ml) were mixed with 2 μL of 10x Glycobuffer 2 (New England Biolabs) before being diluted with 8 μL of H_2O. Then, 1 μL of PNGase-F were added to the mixture and incubated at 37° overnight. pH stressed samples were formed by exchanging 0.5 mg/mL mAb stocks into 200 mM ammonium acetate at pH 4 and 10, using BioSpin P-6 columns (Bio-Rad, Hercules, CA). Statistical analyses to assess significance by unpaired t-test were performed in GraphPad Prism (Dotmatics, Boston, MA).

6.4 Results and Discussion

6.4.1 Online Desalting by RF-MS

To evaluate the efficiency SEC cartridges for online desalting in the context of nRF-MS, we utilized insulin samples prepared using a variety of different matrices containing a range of chemical interferents. Control insulin samples prepared in 200 mM ammonium acetate when analyzed using nRF-MS produce insulin spectra exhibiting the same charge states detected by standard infusion nESI experiments[60] (Figure VII-3a). When Insulin was prepared in bovine serum, desalted, and analyzed by nRF-MS, we again detect a native-like charge state distribution, albeit detected with some residual noise from the serum sample matrix (Figure 6-1c). We then infused the sample containing serum and insulin directly for nESI, and observed no clear insulin signals, suggesting that SEC cartridge-based desalting carried out during nRF-MS is an effective method of desalting samples housed within biological matrices and buffers (Figure VII-3b). We observed similar nRF-MS

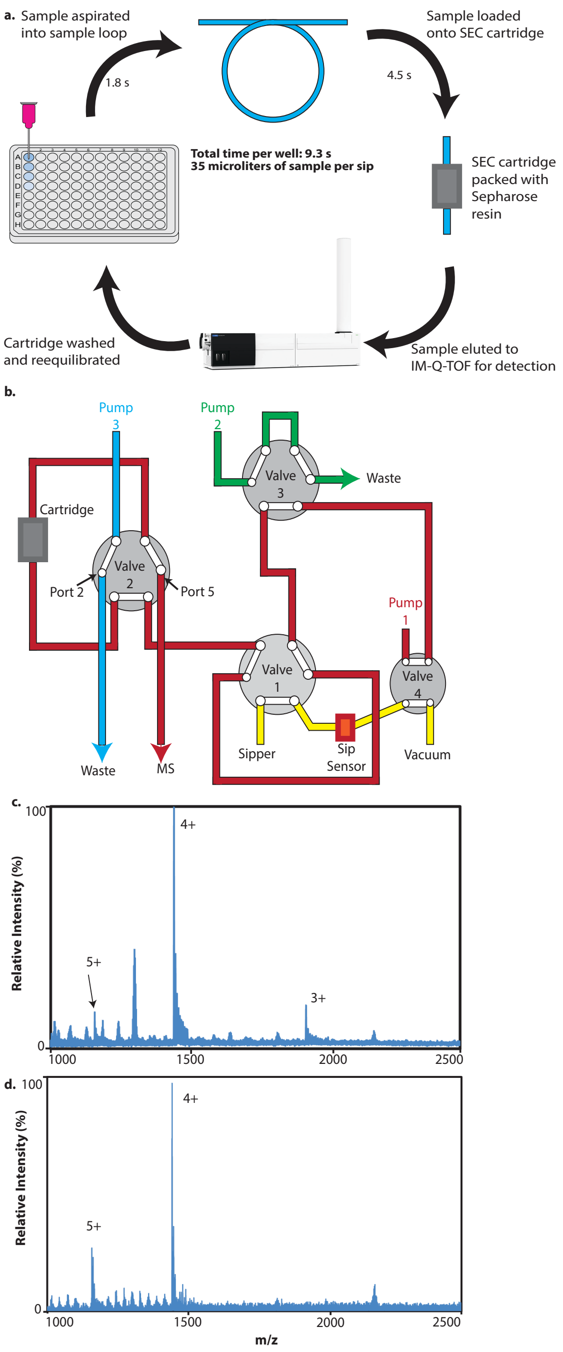

Figure 6-1 An overview of the RapidFire methodology for nMS (a). A schematic of the modified plumbing employed for RF-MS for online desalting with the SEC cartridge during the wash step (b). RF-MS data for insulin samples spiked into complex matrices: bovine serum (c) and 1 M NaCl (d).

results for insulin prepared in 1 M NaCl, wherein we observe clear insulin signals in the resulting mass spectrum, although salt clusters signals can also be observed (Figure 6-1d). In experiments where no desalting was performed, insulin signals were not detected in samples containing 1 M NaCl data, underscoring the effectiveness of online desalting by nRF-MS (Figure VII-3c). When IM is employed to select only the drift time regions where insulin signal is observed, nRF-MS data acquired from 1 M NaCl-containing buffer results in a mass spectrum free of any salt cluster related noise (Figure VII-3d). Finally, data acquired using nRF-MS for Insulin samples prepared using lower amounts of NaCl (5 mM) resulted in no observable salt cluster related noise, whereas direct injection of the same sample produced significant chemical noise signals related to NaCl cluster ions (Figures VII-3e,f). Taken together, our data illustrates the effectiveness and efficiency of SEC cartridge-based desalting, enabling nRF-MS analysis of protein samples housed within a wide range of challenging matrices.

6.4.2 nRF-MS of Standard Proteins

To evaluate the performance of the nRF-MS, we evaluated the CCSs and distribution of charge states produced for standard protein systems using the ESI source conditions and flow rates used for our modified instrument platform. For example, nRF-MS data collected for samples of myoglobin and BSA exhibit identical charge state distributions and CCSs when compared to data collected using standard nESI (Figure 6-2a-h). We have observed similar trends in data collected for standard protein systems ranging in size from 5 to 150 kDa, including protein complexes such as streptavidin, ADH, and ConA tetramers, (Figure VII-4). These data suggest that the protein ions produced and analyzed by nRF-MS adopt native-like structures in the gas phase[61]. Furthermore, the preservation of protein complexes, such as the above-referenced tetramers, lends additional support to the conclusion that nRF-MS can produce native-like protein ions. We extended our nRF-MS data to include GDX, an integral membrane protein, demonstrating that nRF-MS is tolerant of the detergents commonly used for nMS of membrane proteins. To further validate native-like status of the ions produced by nRF-MS, we recorded $^{DT}CCS_{N2}$ values for all the model protein ions analyzed in this study across across all charge states observed. In all cases, the nRF CCS values produced were within 3% relative standard deviation (RSD) of published $^{SF\text{-}DT}CCS_{N2}$ values collected by standard nMS using nESI on the same instrument (Table VII-3, Figure 6-2i)[29,56]. Altogether, these data strongly suggest that nRF-MS, with its automated, online desalting is capable of producing native-like ions in a manner similar to standard nMS approaches (Figure 6-2i).

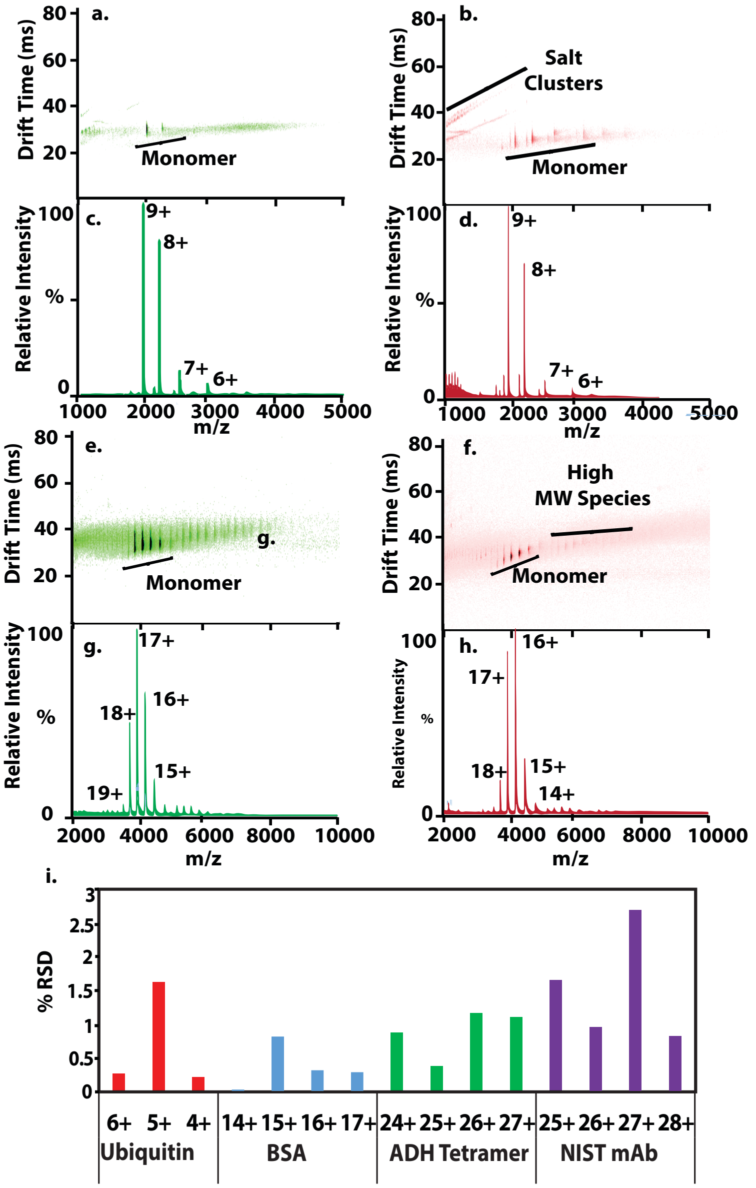

Figure 6-2 . Ion mobility data for myoglobin collected by direct infusion (a) and RF-MS (b). Mass spectra for myoglobin collected by direct infusion (c) and RF-MS (d). Ion mobility data for BSA collected by direct infusion (d) and RF-MS (e). Mass spectra for BSA collected by direct infusion (f) and RF-MS (g). A bar chart depicting the RSD (%) differences in $^{DT}CCS_{N2}$ values between proteins collected with standard direct infusion approaches with proteins collected by RF-MS(i).

6.4.3 Automated CIU using nRF

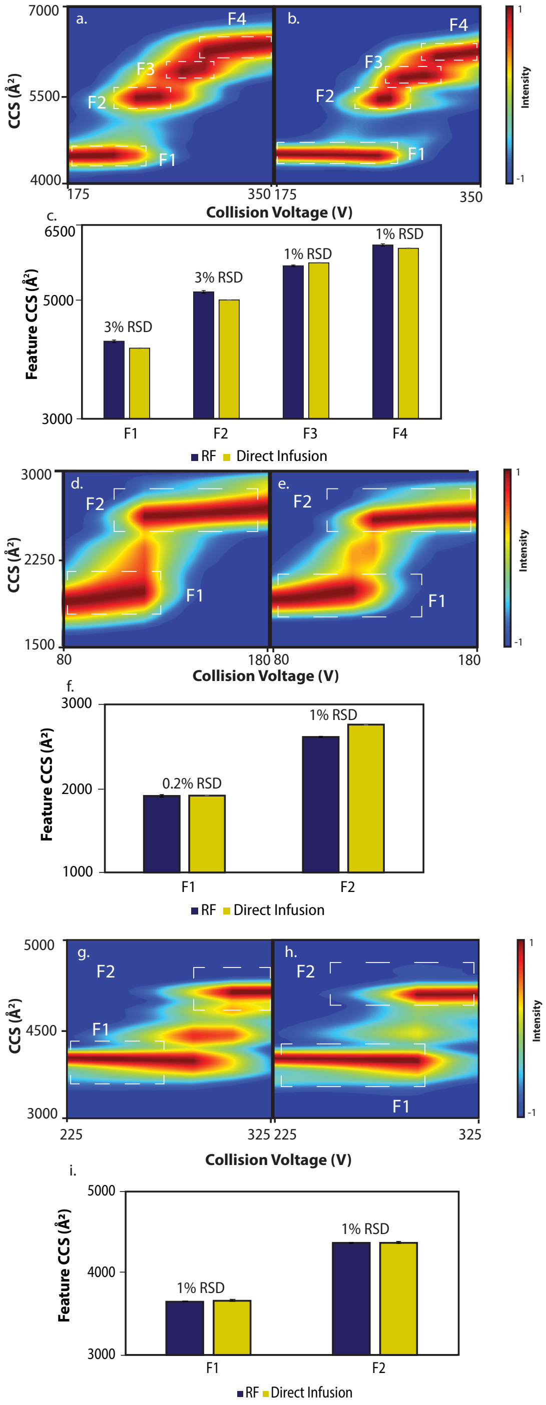

Figure 6-3 . CIU data collected with direct infusion for BSA 16+ (a), Myoglobin 8+ (d) and Streptavidin 11+ (g). RF-CIU data collected with BSA 16+ (b), Myoglobin 8+ (e) and Streptavidin 11+ (h). Bar charts depicting the DTCCSN2 values of the features observed in both the direct infusion and RF CIU fingerprints (c, f, i).

In order to collect CIU data using nRF-MS, voltage ramps were programmed to run as proteins eluted off of the nRF. Complete voltage ramps were completed in 30 s, using 3 s per voltage step, representing a substantial increase in CIU throughput for drift tube-based methodologies described previously [29,33,56]. We collected CIU data for several standard proteins and protein complexes in this high-throughput mode, including streptavidin, BSA, and myoglobin, and these data were then compared to CIU data collected by standard direct infusion ESI source. For CIU data recorded for16+ BSA, we observe four features in both our direct infusion and nRF-CIU fingerprints, similar to prior CIU data reported for these ions (Figure 6-3a-b). Despite the higher flow rates employed by nRF-MS, we found the CIU features recorded to be highly similar, producing an overall RSD of 3%. Similarly, we found the CIU50s values extracted from nRF-MS to be quantitatively similar to CIU data collected by standard nESI, except for CIU50-3 which we find to be slightly destabilized in nRF-CIU data (Figures 6-3c, VII-5a, Table VII-4,5). Similar trends were observed for nRF-CIU data collected for 11+ Streptavidin tetramer ions. CIU features recorded using nRF and direct infusion for the tetramer were highly similar, exhibiting an RSD within 1%, including a transient intermediate feature observed at 2300 $Å^2$, whilst the CIU50 values were all within error (Figures 3d-f, S5b, Table VII-4,5). Similarly, we observe strong correlation between CIU data collected in nRF and standard infusion mode for myoglobin 8+ ions, again producing an inter-fingerprint RSD of 1% RSD (Figures 3g-i, VII-5c, Table VII-3, VII-4). Our nRF-CIU dataset includes proteins with molecular weights ranging from 8-150 kDa (Figure VII-6). The similarity of the unfolding trajectories between our fast nRF-CIU and standard infusion CIU data further underscores that nRF-MS captures native-like ions in a manner similar to standard nMS workflows while simultaneously enabling high-throughput nMS and CIU data acquisition.

6.4.4 nRF-MS of Protein Biotherapeutics

Given the ability of nRF-MS to perform automated, rapid nMS experiments with proteins and protein complexes, we then moved to extend nRF-MS to monoclonal antibodies (mAbs). As discussed above for other model proteins, our nRF-MS data for mAbs includes the charge state distribution as observed in data acquired using standard nESI approaches, whilst also resolving same mAb glycoform populations (Figure 6-4a-d). Overall, our nRF-MS dataset includes six mAbs, including both model antibodies and FDA-approved biotherapeutics, all of which produce similar nRF-MS data quality (Figure VII-7).

In order to generate nRF-CIU for mAbs we added SF_6 to the front funnel region of the 6560C platform to impart sufficient ion activation for CIU. Our data reveals a complete CIU fingerprint for NIST mAb across several charge states (Figure 6-4i and VII-8). The same features can be observed in direct infusion CIU data, although at the feature at 9500 Å^2 appears with greater intensity in nRF-CIU data, which suggests that nRF-CIU produces marginally increased activation under these conditions (Figure VII-9). When comparing the CCSs of the CIU features captured in our 27+ NIST mAb data acquired through nRF-MS and standard nMS conditions, we note that all features are within 3% RSD (Figure VII-9). High-throughput nRF-CIU data was also collected on 39+ NIST mAb dimer ions, suggesting that nRF-MS operation can extend to 300 kDa, and be utilized to evaluate mAb degradation in process development[62] (Figure VII-10a). A broader dataset including mAb fragments (Figure VII-10b,c and VII-11), biotherapeutic mAbs (Figure VII-12), deglycosylated mAbs [63,64] (Figure VII-7, and Figures VII-8d-g, VII-11d-f) all indicate the strong similarities between nRF-CIU and standard infusion-mode CIU data. An

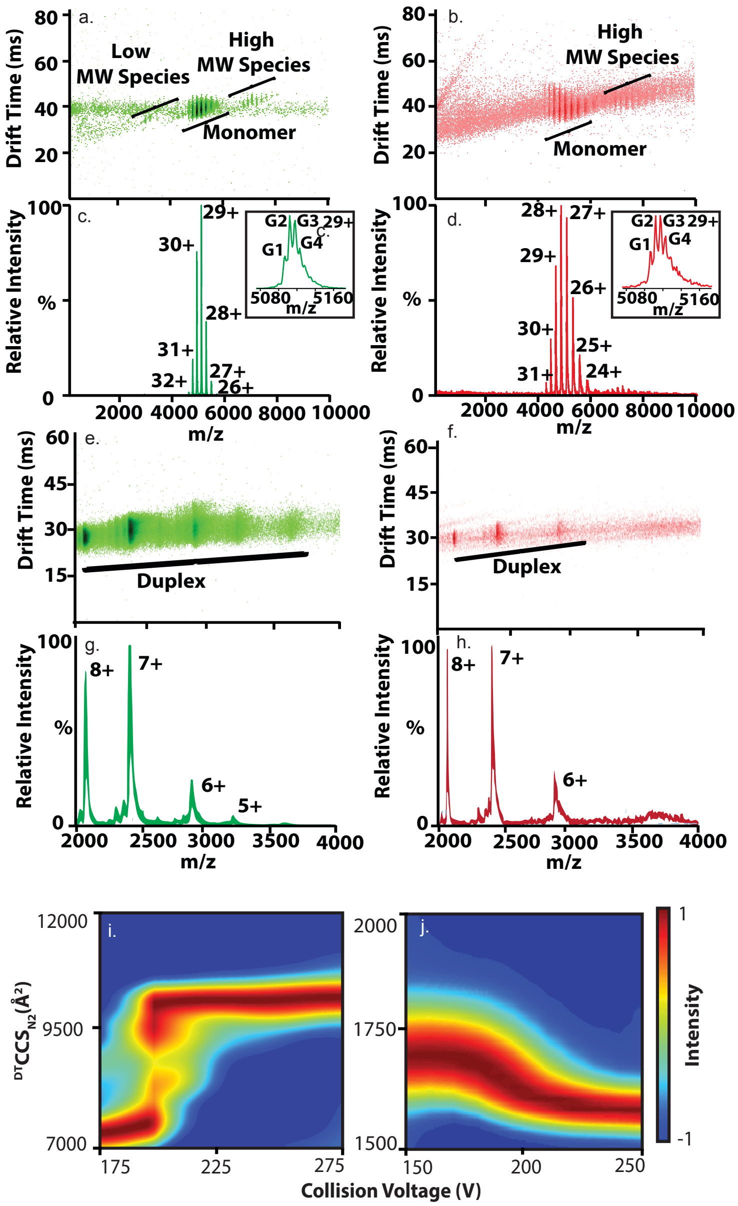

Figure 6-4 Ion mobility data for NIST mAB collected by direct infusion (a) and RF-MS (b). Mass spectra for NIST mAb collected by direct infusion (c) and RF-MS (d) with insets depicting the glycoform populations observed. Ion mobility data for an siRNA duplex collected by direct infusion (d) and RF-MS (e). Mass spectra for siRNA duplex collected by direct infusion (f) and RF-MS (g). RF-CIU data for 27+ NIST mAb (i) and 7+ siRNA duplex (j).

exception to this statement are CIU50 value comparisons recorded for deglycosylated and intact mAbs, which reveal statistically significant differences for the 26+ of Sigma mAb, wherein the deglycosylated form was destabilized when compared to intact NIST mAb. (Figure VII-13a). Additional nRF-MS studies targeting pH stressed mAbs were able capture significant differences between mAbs under acidic pH stressed conditions and standard conditions which was consistent with direct infusion data for the same systems (Figure VII-13b and Figure VII-14).

6.4.5 nRF-MS of Oligonucleotides

Prior reports have demonstrated the utility of nMS for the study of oligonucleotide structure, sequence and modification state[2,9]. To evaluate nRF-MS performance for this biomolecular class, we collected nRF-MS for samples containing both a 16 kDa therapeutic siRNA duplex and a 25 kDa mt-tRNA (Figure 6-4 f,h and VII-5). Notably, we observed that RNA samples required greater drying gas temperatures when compared to samples containing proteins of similar size, with siRNA duplex and mt-tRNA samples requiring 250° and 300° respectively. As observed in our protein nRF-MS data, when compared to direct infusion data, nRF-MS for siRNA exhibits identical charge states distributions and IM drift times, suggesting that the nRF can be used for the nMS analysis of oligonucleotide samples (Figure 6-4e-h). Additionally, we collected high-throughput nRF-CIU data, observing a compaction of approximately 115 Å^2 for 7+ siRNA, a value within 3% of direct infusion data CIU data (Figure 6-4j, VII-16). When we extended our comparisons of nRF-MS and direct infusion CIU data for oligonucleotide ions, similar trends were observed for 8+ and 9+ siRNA and 9+ mt-tRNA ions (Figure VII-17). Taken together, our nRF-MS rapidly collected over multiple oligonucleotides, highlights the versatility of this platform for automated, high-throughput nMS and CIU assay development.

6.5 Conclusions

In this report, we demonstrate that nRF-MS can be deployed to collect automated nIM-MS and CIU data on a subminute time scale, highlighting the potential for nRF-MS to be leveraged for high-throughput nMS applications. Online desalting using nRF-MS significantly reduces bottlenecks associated with sample preparation, reducing typical desalting procedures from requiring nearly a half hour to seconds. The flow rates used in our nRF-MS experiments are low enough to be compatible with a fixed micronebulizer source, allowing sample introduction to be automated, reducing inefficiencies necessitated by single use nESI emitters. Our nRF-MS data further indicates that the ions produced in our experiments that are highly similar to those produced using standard infusion-based nESI nMS, as the ions adopt nearly identical charge states and CCS values. Furthermore, nRF-MS can be employed to conduct high-throughput nMS and CIU analyses for a diverse array of biomolecular ions of interest including protein complexes, membrane proteins, mAbs and oligonucleotides. Given the ability to store multiple plates under temperature-controlled conditions within the RF platform, our nRF-MS could be leveraged in the future to perform extensive nMS screens, analyzing a complete 96 well plate in as little as 15 minutes, and several 96 well plates within an hour.

In addition, we envision that nRF-MS could become a transformative tool in the pharmaceutical sciences more generally. The nRF-MS data presented here suggest that our methodology can be used to collect automated, high-throughput CIU data for a variety of therapeutic biomolecules such as mAbs and siRNA. In the future, nRF-MS could be leveraged to collect high-throughput drug binding assays, where CIU could be deployed to quickly identify potential drug candidates and characterize them based on their mechanism of action[28,45]. Beyond biopharma, nRF could be of wide interest in structural biology research more generally, by improving the throughput and efficiency of routine nMS analyses. Given the high level of reproducibility of CIU, high-throughput nRF-CIU could even be deployed to facilitate the creation of a CIU database[33]. In removing some of the bottlenecks around nMS experimentation, nRF-MS makes it easier for non-expert groups to perform nMS experimentation and could expand the adoption of nMS to more diverse users. Our nRF-MS method does present some limitations; for example, each analysis requires 35 µL of sample, which is larger volume than typically required for standard nMS. However, adjustments to the connective tubing used in the RF can conceivably reduce the per-sample volume requirements to 10 µL. Additionally, CIU on the 6560c is currently limited by the scan speeds allowed by the activation potential used to initiate CIU, which is restricted to 3 s per voltage step. Overall, nRF-MS is a promising methodology than can be deployed to collect nMS and CIU data in an automated, high-throughput compatible manner for a variety of biomolecules. The use of the nRF-MS as a *bona fide* high-throughput and automated technology for nMS research has the potential for transformative impacts in the deployment of nMS research across the biosciences.

6.6 References

(1) Heck, A. J. R. Native Mass Spectrometry: A Bridge between Interactomics and Structural Biology. *Nat Methods* **2008**, *5* (11), 927–933. https://doi.org/10.1038/nmeth.1265.

(2) Marchand, A.; Gabelica, V. Native Electrospray Mass Spectrometry of DNA G-Quadruplexes in Potassium Solution. *J. Am. Soc. Mass Spectrom.* **2014**, *25* (7), 1146–1154. https://doi.org/10.1007/s13361-014-0890-3.

(3) Cong, X.; Liu, Y.; Liu, W.; Liang, X.; Russell, D. H.; Laganowsky, A. Determining Membrane Protein–Lipid Binding Thermodynamics Using Native Mass Spectrometry. *J. Am. Chem. Soc.* **2016**, *138* (13), 4346–4349. https://doi.org/10.1021/jacs.6b01771.

(4) Fantin, S. M.; Parson, K. F.; Yadav, P.; Juliano, B.; Li, G. C.; Sanders, C. R.; Ohi, M. D.; Ruotolo, B. T. Ion Mobility–Mass Spectrometry Reveals the Role of Peripheral Myelin Protein Dimers in Peripheral Neuropathy. *Proceedings of the National Academy of Sciences* **2021**, *118* (17), e2015331118.

(5) Tian, Y.; Han, L.; Buckner, A. C.; Ruotolo, B. T. Collision Induced Unfolding of Intact Antibodies: Rapid Characterization of Disulfide Bonding Patterns, Glycosylation, and Structures. *Anal. Chem.* **2015**, *87* (22), 11509–11515. https://doi.org/10.1021/acs.analchem.5b03291.

(6) Botzanowski, T.; Erb, S.; Hernandez-Alba, O.; Ehkirch, A.; Colas, O.; Wagner-Rousset, E.; Rabuka, D.; Beck, A.; Drake, P. M.; Cianférani, S. Insights from Native Mass Spectrometry Approaches for Top- and Middle- Level Characterization of Site-Specific Antibody-Drug Conjugates. *mAbs* **2017**, *9* (5), 801–811. https://doi.org/10.1080/19420862.2017.1316914.

(7) Hale, O. J.; Hughes, J. W.; Sisley, E. K.; Cooper, H. J. Native Ambient Mass Spectrometry Enables Analysis of Intact Endogenous Protein Assemblies up to 145 KDa Directly from Tissue. *Anal. Chem.* **2022**, *94* (14), 5608–5614. https://doi.org/10.1021/acs.analchem.1c05353.

(8) Harvey, S. R.; O'Neale, C.; Schey, K. L.; Wysocki, V. H. Native Mass Spectrometry and Surface Induced Dissociation Provide Insight into the Post-Translational Modifications of Tetrameric AQP0 Isolated from Bovine Eye Lens. *Anal. Chem.* **2022**, *94* (3), 1515–1519. https://doi.org/10.1021/acs.analchem.1c04322.

(9) Abi-Ghanem, J.; Rabin, C.; Porrini, M.; Rosu, F.; Gabelica, V. Compaction of RNA Hairpins and Their Kissing Complexes in Native Electrospray Mass Spectrometry. *J. Am. Soc. Mass Spectrom.* **2020**, *31* (10), 2035–2043. https://doi.org/10.1021/jasms.0c00060.

(10) Largy, E.; König, A.; Ghosh, A.; Ghosh, D.; Benabou, S.; Rosu, F.; Gabelica, V. Mass Spectrometry of Nucleic Acid Noncovalent Complexes. *Chemical Reviews* **2021**, *122* (8), 7720–7839.

(11) Sobott, F.; Benesch, J. L. P.; Vierling, E.; Robinson, C. V. Subunit Exchange of Multimeric Protein Complexes: REAL-TIME MONITORING OF SUBUNIT EXCHANGE BETWEEN SMALL HEAT SHOCK PROTEINS BY USING ELECTROSPRAY MASS SPECTROMETRY*. *Journal of Biological Chemistry* **2002**, *277* (41), 38921–38929. https://doi.org/10.1074/jbc.M206060200.

(12) Aquilina, J. A.; Benesch, J. L. P.; Bateman, O. A.; Slingsby, C.; Robinson, C. V. Polydispersity of a Mammalian Chaperone: Mass Spectrometry Reveals the Population of Oligomers in AB-Crystallin. *Proceedings of the National Academy of Sciences* **2003**, *100* (19), 10611–10616. https://doi.org/10.1073/pnas.1932958100.

(13) Uetrecht, C.; Barbu, I. M.; Shoemaker, G. K.; van Duijn, E.; Heck, A. J. R. Interrogating Viral Capsid Assembly with Ion Mobility–Mass Spectrometry. *Nature Chem* **2011**, *3* (2), 126–132. https://doi.org/10.1038/nchem.947.

(14) Allison, T. M.; Reading, E.; Liko, I.; Baldwin, A. J.; Laganowsky, A.; Robinson, C. V. Quantifying the Stabilizing Effects of Protein–Ligand Interactions in the Gas Phase. *Nat Commun* **2015**, *6* (1), 8551. https://doi.org/10.1038/ncomms9551.

(15) Stojko, J.; Fieulaine, S.; Petiot-Bécard, S.; Dorsselaer, A. V.; Meinnel, T.; Giglione, C.; Cianférani, S. Ion Mobility Coupled to Native Mass Spectrometry as a Relevant Tool to Investigate Extremely Small Ligand-Induced Conformational Changes. *Analyst* **2015**, *140* (21), 7234–7245. https://doi.org/10.1039/C5AN01311A.

(16) Wu, R.; Metternich, J. B.; Tiwari, P.; Benzenberg, L. R.; Harrison, J. A.; Liu, Q.; Zenobi, R. Structural Studies of a Stapled Peptide with Native Ion Mobility-Mass Spectrometry and Transition Metal Ion Förster Resonance Energy Transfer in the Gas Phase. *J. Am. Chem. Soc.* **2022**, *144* (32), 14441–14445. https://doi.org/10.1021/jacs.2c02776.

(17) Chen, S.-H.; Russell, D. H. How Closely Related Are Conformations of Protein Ions Sampled by IM-MS to Native Solution Structures? *J. Am. Soc. Mass Spectrom.* **2015**, *26* (9), 1433–1443. https://doi.org/10.1007/s13361-015-1191-1.

(18) McCabe, J. W.; Hebert, M. J.; Shirzadeh, M.; Mallis, C. S.; Denton, J. K.; Walker, T. E.; Russell, D. H. The Ims Paradox: A Perspective on Structural Ion Mobility-Mass Spectrometry. *Mass Spectrometry Reviews* **2021**, *40* (3), 280–305. https://doi.org/10.1002/mas.21642.

(19) Borotto, N. B.; Osho, K. E.; Richards, T. K.; Graham, K. A. Collision-Induced Unfolding of Native-like Protein Ions Within a Trapped Ion Mobility Spectrometry Device. *J. Am. Soc. Mass Spectrom.* **2022**, *33* (1), 83–89. https://doi.org/10.1021/jasms.1c00273.

(20) Stow, S. M.; Causon, T. J.; Zheng, X.; Kurulugama, R. T.; Mairinger, T.; May, J. C.; Rennie, E. E.; Baker, E. S.; Smith, R. D.; McLean, J. A.; Hann, S.; Fjeldsted, J. C. An Interlaboratory Evaluation of Drift Tube Ion Mobility–Mass Spectrometry Collision Cross Section Measurements. *Anal. Chem.* **2017**, *89* (17), 9048–9055. https://doi.org/10.1021/acs.analchem.7b01729.

(21) Marklund, E. G.; Degiacomi, M. T.; Robinson, C. V.; Baldwin, A. J.; Benesch, J. L. P. Collision Cross Sections for Structural Proteomics. *Structure* **2015**, *23* (4), 791–799. https://doi.org/10.1016/j.str.2015.02.010.

(22) Ruotolo, B. T. Collision Cross Sections for Native Proteomics: Challenges and Opportunities. *J. Proteome Res.* **2022**, *21* (1), 2–8. https://doi.org/10.1021/acs.jproteome.1c00686.

(23) Stiving, A. Q.; Jones, B. J.; Ujma, J.; Giles, K.; Wysocki, V. H. Collision Cross Sections of Charge-Reduced Proteins and Protein Complexes: A Database for Collision Cross Section Calibration. *Anal. Chem.* **2020**, *92* (6), 4475–4483. https://doi.org/10.1021/acs.analchem.9b05519.

(24) Pukala, T. Importance of Collision Cross Section Measurements by Ion Mobility Mass Spectrometry in Structural Biology. *Rapid Communications in Mass Spectrometry* **2019**, *33* (S3), 72–82. https://doi.org/10.1002/rcm.8294.

(25) Gabelica, V.; Shvartsburg, A. A.; Afonso, C.; Barran, P.; Benesch, J. L. P.; Bleiholder, C.; Bowers, M. T.; Bilbao, A.; Bush, M. F.; Campbell, J. L.; Campuzano, I. D. G.; Causon, T.; Clowers, B. H.; Creaser, C. S.; De Pauw, E.; Far, J.; Fernandez-Lima, F.; Fjeldsted, J. C.; Giles, K.; Groessl, M.; Hogan Jr, C. J.; Hann, S.; Kim, H. I.; Kurulugama, R. T.; May, J. C.; McLean, J. A.; Pagel, K.; Richardson, K.; Ridgeway, M. E.; Rosu, F.; Sobott, F.; Thalassinos, K.; Valentine, S. J.; Wyttenbach, T. Recommendations for Reporting Ion Mobility Mass Spectrometry Measurements. *Mass Spectrometry Reviews* **2019**, *38* (3), 291–320. https://doi.org/10.1002/mas.21585.

(26) Nash, S.; Vachet, R. W. Gas-Phase Unfolding of Protein Complexes Distinguishes Conformational Isomers. *J. Am. Chem. Soc.* **2022**, *144* (48), 22128–22139. https://doi.org/10.1021/jacs.2c09573.

(27) Dixit, S. M.; Polasky, D. A.; Ruotolo, B. T. Collision Induced Unfolding of Isolated Proteins in the Gas Phase: Past, Present, and Future. *Current Opinion in Chemical Biology* **2018**, *42*, 93–100. https://doi.org/10.1016/j.cbpa.2017.11.010.

(28) Polasky, D. A.; Dixit, S. M.; Fantin, S. M.; Ruotolo, B. T. CIUSuite 2: Next-Generation Software for the Analysis of Gas-Phase Protein Unfolding Data. *Anal. Chem.* **2019**, *91* (4), 3147–3155. https://doi.org/10.1021/acs.analchem.8b05762.

(29) Vallejo, D. D.; Polasky, D. A.; Kurulugama, R. T.; Eschweiler, J. D.; Fjeldsted, J. C.; Ruotolo, B. T. A Modified Drift Tube Ion Mobility-Mass Spectrometer for Charge-Multiplexed Collision-Induced Unfolding. *Analytical chemistry* **2019**, *91* (13), 8137–8146.

(30) Fantin, S. M.; Huang, H.; Sanders, C. R.; Ruotolo, B. T. Collision-Induced Unfolding Differentiates Functional Variants of the KCNQ1 Voltage Sensor Domain. *J. Am. Soc. Mass Spectrom.* **2020**, *31* (11), 2348–2355. https://doi.org/10.1021/jasms.0c00288.

(31) Polasky, D. A.; Dixit, S. M.; Vallejo, D. D.; Kulju, K. D.; Ruotolo, B. T. An Algorithm for Building Multi-State Classifiers Based on Collision-Induced Unfolding Data. *Analytical chemistry* **2019**, *91* (16), 10407–10412.

(32) Liu, Y.; Cong, X.; Liu, W.; Laganowsky, A. Characterization of Membrane Protein–Lipid Interactions by Mass Spectrometry Ion Mobility Mass Spectrometry. *J. Am. Soc. Mass Spectrom.* **2017**, *28* (4), 579–586. https://doi.org/10.1007/s13361-016-1555-1.

(33) Gadkari, V. V.; Juliano, B. R.; Mallis, C. S.; May, J. C.; Kurulugama, R. T.; Fjeldsted, J. C.; McLean, J. A.; Russell, D. H.; Ruotolo, B. T. Performance Evaluation of In-Source Ion Activation Hardware for Collision-Induced Unfolding of Proteins and Protein Complexes on a Drift Tube Ion Mobility-Mass Spectrometer. *Analyst* **2023**, *148* (2), 391–401. https://doi.org/10.1039/D2AN01452A.

(34) Kondrat, F. D. L.; Struwe, W. B.; Benesch, J. L. P. Native Mass Spectrometry: Towards High-Throughput Structural Proteomics. In *Structural Proteomics: High-Throughput Methods*; Owens, R. J., Ed.; Methods in Molecular Biology; Springer: New York, NY, 2015; pp 349–371. https://doi.org/10.1007/978-1-4939-2230-7_18.

(35) Wilm, M.; Mann, M. Analytical Properties of the Nanoelectrospray Ion Source. *Anal. Chem.* **1996**, *68* (1), 1–8. https://doi.org/10.1021/ac9509519.

(36) Kempa, E. E.; Hollywood, K. A.; Smith, C. A.; Barran, P. E. High Throughput Screening of Complex Biological Samples with Mass Spectrometry – from Bulk Measurements to Single Cell Analysis. *Analyst* **2019**, *144* (3), 872–891. https://doi.org/10.1039/C8AN01448E.

(37) Zhong, Y.; Feng, J.; Ruotolo, B. T. Robotically-Assisted Titration Coupled to Ion Mobility-Mass Spectrometry Reveals the Interface Structures and Analysis Parameters Critical for Multiprotein Topology Mapping. *Anal. Chem.* **2013**, *85* (23), 11360–11368. https://doi.org/10.1021/ac402276k.

(38) Miliara, X.; Tatsuta, T.; Berry, J.-L.; Rouse, S. L.; Solak, K.; Chorev, D. S.; Wu, D.; Robinson, C. V.; Matthews, S.; Langer, T. Structural Determinants of Lipid Specificity within Ups/PRELI Lipid Transfer Proteins. *Nat Commun* **2019**, *10*, 1130. https://doi.org/10.1038/s41467-019-09089-x.

(39) Keetch, C. A.; Hernández, H.; Sterling, A.; Baumert, M.; Allen, M. H.; Robinson, C. V. Use of a Microchip Device Coupled with Mass Spectrometry for Ligand Screening of a Multi-Protein Target. *Anal. Chem.* **2003**, *75* (18), 4937–4941. https://doi.org/10.1021/ac034251c.

(40) Schultz, G. A.; Corso, T. N.; Prosser, S. J.; Zhang, S. A Fully Integrated Monolithic Microchip Electrospray Device for Mass Spectrometry. *Anal. Chem.* **2000**, *72* (17), 4058–4063. https://doi.org/10.1021/ac000325y.

(41) VanAernum, Z. L.; Busch, F.; Jones, B. J.; Jia, M.; Chen, Z.; Boyken, S. E.; Sahasrabuddhe, A.; Baker, D.; Wysocki, V. H. Rapid Online Buffer Exchange for Screening of Proteins, Protein Complexes, and Cell Lysates by Native Mass Spectrometry. *Nat Protoc* **2020**, *15* (3), 1132–1157. https://doi.org/10.1038/s41596-019-0281-0.

(42) Deslignière, E.; Ehkirch, A.; Botzanowski, T.; Beck, A.; Hernandez-Alba, O.; Cianférani, S. Toward Automation of Collision-Induced Unfolding Experiments through Online Size

Exclusion Chromatography Coupled to Native Mass Spectrometry. *Anal. Chem.* **2020**, *92* (19), 12900–12908. https://doi.org/10.1021/acs.analchem.0c01426.

(43) van Schaick, G.; Domínguez-Vega, E.; Castel, J.; Wuhrer, M.; Hernandez-Alba, O.; Cianférani, S. Online Collision-Induced Unfolding of Therapeutic Monoclonal Antibody Glyco-Variants through Direct Hyphenation of Cation Exchange Chromatography with Native Ion Mobility–Mass Spectrometry. *Anal. Chem.* **2023**. https://doi.org/10.1021/acs.analchem.2c03163.

(44) Nguyen, G. T. H.; Bennett, J. L.; Liu, S.; Hancock, S. E.; Winter, D. L.; Glover, D. J.; Donald, W. A. Multiplexed Screening of Thousands of Natural Products for Protein–Ligand Binding in Native Mass Spectrometry. *J. Am. Chem. Soc.* **2021**, *143* (50), 21379–21387. https://doi.org/10.1021/jacs.1c10408.

(45) D'Amico, C. I.; Polasky, D. A.; Steyer, D. J.; Ruotolo, B. T.; Kennedy, R. T. Ion Mobility-Mass Spectrometry Coupled to Droplet Microfluidics for Rapid Protein Structure Analysis and Drug Discovery. *Anal. Chem.* **2022**. https://doi.org/10.1021/acs.analchem.2c02307.

(46) Dodds, J. N.; Baker, E. S. Improving the Speed and Selectivity of Newborn Screening Using Ion Mobility Spectrometry–Mass Spectrometry. *Anal. Chem.* **2021**, *93* (51), 17094–17102. https://doi.org/10.1021/acs.analchem.1c04267.

(47) Butler, K. E.; Dodds, J. N.; Flick, T.; Campuzano, I. D. G.; Baker, E. S. High-Resolution Demultiplexing (HRdm) Ion Mobility Spectrometry-Mass Spectrometry for Aspartic and Isoaspartic Acid Determination and Screening. *Anal Chem* **2022**, *94* (16), 6191–6199. https://doi.org/10.1021/acs.analchem.1c05533.

(48) Maksymiuk, C.; Balakrishnan, A.; Bryk, R.; Rhee, K. Y.; Nathan, C. F. E1 of α-Ketoglutarate Dehydrogenase Defends Mycobacterium Tuberculosis against Glutamate Anaplerosis and Nitroxidative Stress. *Proceedings of the National Academy of Sciences* **2015**, *112* (43), E5834–E5843. https://doi.org/10.1073/pnas.1510932112.

(49) Clausse, V.; Fang, Y.; Tao, D.; Tagad, H. D.; Sun, H.; Wang, Y.; Karavadhi, S.; Lane, K.; Shi, Z.-D.; Vasalatiy, O.; LeClair, C. A.; Eells, R.; Shen, M.; Patnaik, S.; Appella, E.; Coussens, N. P.; Hall, M. D.; Appella, D. H. Discovery of Novel Small-Molecule Scaffolds for the Inhibition and Activation of WIP1 Phosphatase from a RapidFire Mass Spectrometry High-Throughput Screen. *ACS Pharmacol. Transl. Sci.* **2022**, *5* (10), 993–1006. https://doi.org/10.1021/acsptsci.2c00147.

(50) Bretschneider, T.; Ozbal, C.; Holstein, M.; Winter, M.; Buettner, F. H.; Thamm, S.; Bischoff, D.; Luippold, A. H. RapidFire BLAZE-Mode Is Boosting ESI-MS Toward High-Throughput-Screening. *SLAS TECHNOLOGY: Translating Life Sciences Innovation* **2019**, *24* (4), 386–393. https://doi.org/10.1177/2472630318822449.

(51) Hutchinson, S. E.; Leveridge, M. V.; Heathcote, M. L.; Francis, P.; Williams, L.; Gee, M.; Munoz-Muriedas, J.; Leavens, B.; Shillings, A.; Jones, E.; Homes, P.; Baddeley, S.; Chung, C.-W.; Bridges, A.; Argyrou, A. Enabling Lead Discovery for Histone Lysine Demethylases by High-Throughput RapidFire Mass Spectrometry. *J Biomol Screen* **2012**, *17* (1), 39–48. https://doi.org/10.1177/1087057111416660.

(52) Veach, B. T.; Mudalige, T. K.; Rye, P. RapidFire Mass Spectrometry with Enhanced Throughput as an Alternative to Liquid–Liquid Salt Assisted Extraction and LC/MS Analysis for Sulfonamides in Honey. *Anal. Chem.* **2017**, *89* (6), 3256–3260. https://doi.org/10.1021/acs.analchem.6b04889.

(53) Campuzano, I. D. G.; San Miguel, T.; Rowe, T.; Onea, D.; Cee, V. J.; Arvedson, T.; McCarter, J. D. High-Throughput Mass Spectrometric Analysis of Covalent Protein-Inhibitor Adducts for the Discovery of Irreversible Inhibitors: A Complete Workflow. *J Biomol Screen* **2016**, *21* (2), 136–144. https://doi.org/10.1177/1087057115621288.

(54) Sawyer, W. S.; Srikumar, N.; Carver, J.; Chu, P. Y.; Shen, A.; Xu, A.; Williams, A. J.; Spiess, C.; Wu, C.; Liu, Y.; Tran, J. C. High-Throughput Antibody Screening from Complex Matrices Using Intact Protein Electrospray Mass Spectrometry. *Proc Natl Acad Sci U S A* **2020**, *117* (18), 9851–9856. https://doi.org/10.1073/pnas.1917383117.

(55) Campuzano, I. D. G.; Pelegri-O'Day, E. M.; Srinivasan, N.; Lippens, J. L.; Egea, P.; Umeda, A.; Aral, J.; Zhang, T.; Laganowsky, A.; Netirojjanakul, C. High-Throughput Mass Spectrometry for Biopharma: A Universal Modality and Target Independent Analytical Method for Accurate Biomolecule Characterization. *J. Am. Soc. Mass Spectrom.* **2022**, *33* (11), 2191–2198. https://doi.org/10.1021/jasms.2c00138.

(56) Gadkari, V. V.; Ramírez, C. R.; Vallejo, D. D.; Kurulugama, R. T.; Fjeldsted, J. C.; Ruotolo, B. T. Enhanced Collision Induced Unfolding and Electron Capture Dissociation of Native-like Protein Ions. *Anal. Chem.* **2020**, *92* (23), 15489–15496. https://doi.org/10.1021/acs.analchem.0c03372.

(57) Strohalm, M.; Hassman, M.; Košata, B.; Kodíček, M. MMass Data Miner: An Open Source Alternative for Mass Spectrometric Data Analysis. *Rapid Communications in Mass Spectrometry* **2008**, *22* (6), 905–908. https://doi.org/10.1002/rcm.3444.

(58) Strohalm, M.; Kavan, D.; Novák, P.; Volný, M.; Havlíček, V. MMass 3: A Cross-Platform Software Environment for Precise Analysis of Mass Spectrometric Data. *Anal. Chem.* **2010**, *82* (11), 4648–4651. https://doi.org/10.1021/ac100818g.

(59) Niedermeyer, T. H. J.; Strohalm, M. MMass as a Software Tool for the Annotation of Cyclic Peptide Tandem Mass Spectra. *PLoS One* **2012**, *7* (9), e44913. https://doi.org/10.1371/journal.pone.0044913.

(60) Cole, H.; Porrini, M.; Morris, R.; Smith, T.; Kalapothakis, J.; Weidt, S.; Mackay, C. L.; MacPhee, C. E.; Barran, P. E. Early Stages of Insulin Fibrillogenesis Examined with Ion Mobility Mass Spectrometry and Molecular Modelling. *Analyst* **2015**, *140* (20), 7000–7011. https://doi.org/10.1039/C5AN01253H.

(61) Kafader, J. O.; Melani, R. D.; Schachner, L. F.; Ives, A. N.; Patrie, S. M.; Kelleher, N. L.; Compton, P. D. Native vs Denatured: An in Depth Investigation of Charge State and Isotope Distributions. *J. Am. Soc. Mass Spectrom.* **2020**, *31* (3), 574–581. https://doi.org/10.1021/jasms.9b00040.

(62) Vallejo, D. D.; Jeon, C. K.; Parson, K. F.; Herderschee, H. R.; Eschweiler, J. D.; Filoti, D. I.; Ruotolo, B. T. Ion Mobility–Mass Spectrometry Reveals the Structures and Stabilities of Biotherapeutic Antibody Aggregates. *Anal. Chem.* **2022**, *94* (18), 6745–6753. https://doi.org/10.1021/acs.analchem.2c00160.

(63) Vallejo, D. D.; Kang, J.; Coghlan, J.; Ramírez, C. R.; Polasky, D. A.; Kurulugama, R. T.; Fjeldsted, J. C.; Schwendeman, A. A.; Ruotolo, B. T. Collision-Induced Unfolding Reveals Stability Differences in Infliximab Therapeutics under Native and Heat Stress Conditions. *Anal. Chem.* **2021**, *93* (48), 16166–16174. https://doi.org/10.1021/acs.analchem.1c03946.

(64) Tian, Y.; Ruotolo, B. T. Collision Induced Unfolding Detects Subtle Differences in Intact Antibody Glycoforms and Associated Fragments. *International Journal of Mass Spectrometry* **2018**, *425*, 1–9. https://doi.org/10.1016/j.ijms.2017.12.005.

Chapter 7 Conclusions and Future Directions

7.1 Conclusions

nMS is a valuable technique for the evaluation of biomolecular sequence and structure. While nMS is not able to produce atomic level biomolecular structures, it can yield valuable insights into biomolecular sequence and conformation, within a much-reduced experimental time frame when compared to more established techniques like X-Ray diffraction. As such, nMS is a versatile technique for performing structural biology assays in both academic and industrial laboratories. Despite the progress in expanding nMS applications, some gaps remain, especially in designing high-throughput nMS methods and applying nMS methods to more challenging targets, such as membrane proteins. This thesis develops new methodologies for nMS that can expand the breadth of its applications whilst also validating existing methodologies to evaluate their experimental rigor.

In Chapters 2 and 3 we work to improve nMS applications for MP systems. Based on previous work that revealed that IR photoactivation can be used to liberate proteins from proteomicelles, we critically evaluated the mechanism by which IR activation breaks down detergent micelles[1]. Using a variety of detergents from several detergent classes, we revealed that IR photoactivation does not need a particular chromophore to elicit the fission of detergent micelles, rather weak absorption in the 950 cm^{-1} region is sufficient to break apart these weakly associated clusters in a processive manner. We also revealed that IR photoactivation can be utilized to liberate MPs from a wide variety of mimetics due to the presence of phospholipids, which have P-O stretches that strongly absorb 10.6 μm IR light[2]. Finally, we coupled IR photoactivation to native top-down experiments, using the IR photoactivation to liberate proteins from the micelle prior to activation. With this method, we observed ~20% higher sequence coverages with PMP22, a model transmembrane system, and we also observed that IR photoactivation was critical for performing native top-down experiments with GDX dimer.

When analyzing data for Chapter 2, we observed that large amounts of DM detergent remained in samples even after detergent exchange procedures were performed, suggesting that existing exchange methodologies are inefficient in performing this exchange. In Chapter 3, we then evaluated the detergent exchange efficiencies of several proteins exchanged into various common detergents using three detergent exchange methods. In all cases, we observed that detergent exchange remained incomplete, indicating that these protocols should be revised. The most efficient exchange procedure was performing exchange by FPLC using an SEC column; however, this is impractical for quotidian experimentation. To evaluate improved methodologies for detergent exchange, we found that iterative exchanges with a SEC spin cartridge could notably improve exchange efficiency, albeit imperfectly. Further method development is required to evaluate whether a more efficient form of detergent exchange is possible.

As CIU becomes more widely used, including by non-expert labs, it is important to benchmark the reproducibility of CIU data collected in distinct laboratories. Previous work suggest that $^{DT}CCS_{N2}$ values are quite reproducible across laboratories, but CIU data had never been evaluated in this manner[3]. In order to address this, we worked with partner laboratories that had the same instrument to evaluate the reproducibility of CIU measurements taken with our platforms as detailed in Chapter 4. We observed that while the features of the CIU fingerprints were generally reproducible within a few percent RSD, the transitions between the features were less reproducible, suggesting that there were differences in gas phase activation between the sources on the platforms. As the MS systems were non-commercial prototypes, a new version of the source was generated with stricter engineering controls to produce more reproducible collisional activation. With this improved system, transitions between features became much more reproducible, suggesting that when carefully tuned CIU can be quite reproducible across geographically distinct versions of the same MS platform.

While CIU is primarily deployed as a structural assay, in Chapter 5 we investigated its suitability for quantitative applications. Canonical quantitative MS approaches are predicated on the analytes being mass resolved[4]. However, many similar systems, such as mAb biotherapeutics, are not mass resolved due to their similarly. These systems are also often isocross-sectional, with a simple IM separation unable to completely resolve them. We utilized CIU to identify slight differences in unfolding patterns for several pairs of isomass mAbs and a pair of sequence homologues. By using CIU to identify at which collision voltages the proteins exhibit differences in drift time, we were able to quantitate these proteins in mixtures by using the ratio between the discreet drift time peaks that occurred at select voltages. We were able to quantitate these systems with nanomolar LODs in both ammonium acetate and serum matrices, within clinically relevant concentrations, suggesting future clinical applications of quantitative CIU[5].

In Chapter 6, we develop an automated, high-throughput compatible methodology for nMS. We adapted the RapidFire high-throughput MS system for nMS by using an SEC cartridge for online desalting, with ammonium acetate as the solvent system for the experiment. When employed for nMS, we were able to develop a RapidFire method that can acquire automated nMS data in as little as 30 seconds for a complete CIU fingerprint. We compared the ${}^{DT}CCS_{N2}$ values of protein analytes collected with the RF to published values collected on the same system using nanoelectrospray and found them to be replicable with <3% RSD[6,7]. Similarly, the $^{DT}CCS_{N2}$ of the features of RF-CIU fingerprints, as well as the CIU50s, were found to be reproducible between RF-CIU data and data collected with a standard CIU approach, suggesting that the RF method is producing the same native, compact ion populations. Finally, we extended the RF methodology to more challenging systems, such as mAb and oligonucleotides to collect fast, automated CIU for these systems, highlighting the potential application of native RF-MS to high-throughput screens in the pharmaceutical industry.

7.2 Future Directions

7.2.1 Further Applications of Infrared Photoactivation for Native Mass Spectrometry of Membrane Proteins

Chapter 2 was limited to performing native top-down experimentation with CID. However, several other fragmentation methods exist, making it conceivable that this IR photoactivation based methodology could be interfaced with other fragmentation methodologies such as ETD or ECD. Previous studies have demonstrated that combining multiple fragmentation techniques can be advantageous in improving the sequence coverage obtained[8,9]. While the sequence coverages obtained for PMP22 and GDX in Chapter 2 are high relative to other native top-down studies, they are not 100%, leaving room to improve the methodology[10]. Given that the Orbitrap Fusion Lumos can perform ETD experiments alongside HCD, we attempted an EThcD experiment with PMP22 after it had been liberated from a micelle by IR photoactivation. Initial results demonstrate that EThcD can improve the fragmentation of PMP22, compared to HCD alone, yielding 70% sequence coverage (Figure 7-1). Optimization of the ETD parameters is difficult here, as these experiments often yield electron transfer without dissociation. Signal loss is also a challenge as ions must be trapped in the ion trap for IR photoactivation, and then trapped even longer (up to 1 s) in the ion trap for ETD to occur. Additionally, the intensity of the

ETD fragments is quite low, requiring the fragmentation spectra to been annotated by hand, which is quite time consuming.

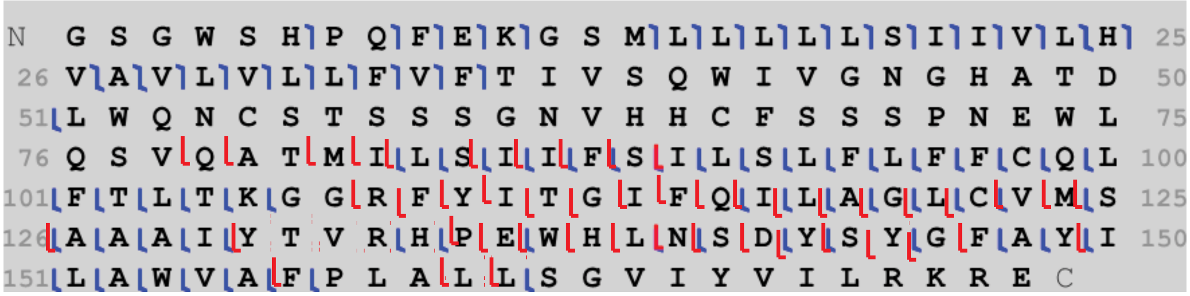

Figure 7-1 A sequence coverage map for PMP22 obtained for an EThcD experiment coupled to liberation through IR activation. A sequence coverage of 69% was obtained. While most ETD fragments are redundant to HCD fragments, this redundancy increases confidence in the sequence that is identified.

Despite the challenges with performing EThcD coupled with IR photoactivation with membrane proteins on the Lumos, it would be worthwhile to investigate building out such a method, especially as ETD is better able to preserve labile modifications[11]. An ideal target for this approach would be PMP22 purified from insect Sf9 (*Spodoptera frugiperda)* and HEK (Human embryonic kidney) cell lines, which are expected to have PTMs as the protein is expressed in eukaryotic cell line. Collaborators from Vanderbilt University have indicated that they are interested in using native top-down to explore differences in PTMs across PMP22 mutants, making IR-activated EThcD potentially an ideal method for this system. Native EThcD methods for membrane protein systems would be also particularly impactful, as there is currently no published native ETD data for membrane proteins.

While the IR-activated methodology described in Chapter 2 has been implemented on a Orbitrap Fusion system, it is conceivable that IR photoactivation can also be leveraged on other mass spectrometers. The Orbitrap Fusion Lumos is a powerful platform, but it has a limited mass range that makes it incompatible for typical nMS MP targets such as G-coupled protein receptors, and channels such as the ammonium channel (AmtB) and Aquaporin Z[12,13]. For example, it would be particularly advantageous to implement IR photoactivation on an IM-MS platform, which often have more expansive mass ranges. For example, he IR laser could irradiate the trap of a Synapt G2, similarly to a Waters Q-TOF that was modified with an IR laser[1]. It is important to note that modifying an instrument to accommodate infrared photoactivation with a CO_2 laser is a not a trivial matter, given the need for significant engineering safety controls to be implemented, as well has requiring the instrument to be physically modified with an IR transparent window, such as CaF_2.

Coupling IR photoactivation to IM-MS could allow for more detailed studies of proteins liberated from mimetics by IR activation. For example, IM-MS could further validate that proteins liberated from mimetics retain their native-like structure, by measuring the CCS of proteins liberated in this manner, which would more conclusively demonstrate that the proteins themselves are unperturbed by IR photoactivation. Data collected from GDX in Chapter 2 suggests that this is the case, as GDX dimer and lipid bound GDX species remain intact after IR photoactivation, but it would be most ideal to validate this experimentally by direct measurement. It would also be interesting to observe the structural changes that micelles undergo as they are activated with IR photons, potentially offering further insight into the mechanisms of IR photoactivation based fission of detergent micelles. While orbitrap systems can be used to measure CCS, only specialist groups have access to the settings necessary to perform these measurements on orbitrap systems[14].

Additionally, IR photoactivation could be particularly advantageous for nIM-MS experimentation. When using collisional activation to both liberate and unfold membrane proteins, it is possible that the collisional activation could disrupt labile ligand binding interactions, making it difficult to observe these interactions and measure their stability effects by CIU[15]. Given that the data in Chapter 2 suggest that IR activation seems to be selective and preserves native-like ligand binding, this could allow for CIU to be performed with a more tunable means of liberating the MPs from the mimetic, without worrying about disrupting native oligomeric states or native ligand binding. Beyond this challenge of collisional activation perturbing native ligand binding, it is often difficult to liberate MPs from more complex mimetics, such as liposomes and nanodiscs, as a significant amount of the accessible collisional energy is used up trying to liberate the protein from these mimetics[16]. IR activation could potentially surmount this challenge, as the use of infrared photoactivation could be used to completely liberate MP from the mimetic, as demonstrated in Chapter 2, leaving more collisional activation available to unfold the protein system of interest more completely, potentially yielding more unfolding features and more informative CIU fingerprints.

Furthermore, CIU data collected on MPs are often noisy, due to the detergent and mimetic noise that results from collisional activation, and subsequently often requires significant mathematical denoising approaches to interpret the unfolding trajectories that were obtained[15]. IR activation could potentially improve this, as the data in Chapter 2 suggest that IR photoactivation breaks down detergent micelles and mimetics into smaller discrete clusters of lipids and detergent that could potentially be more easily be separated from larger proteins, potentially reducing the amount of noise in the CIU data collected. While difficult to implement, it would be worthwhile to implement IR photoactivation based approaches on an IM-MS platform like a Synapt G2 to evaluate improvements in nIM-MS methodologies that could arise with IR photoactivation, while also gaining more insights into the structural effects of IR photoactivation on MPs.

7.2.2 High-Throughput CIU Approaches with RF-MS

Chapter 6 discusses the development of automated and high-throughput compatible nMS methodologies that can collect CIU data in as little as 30 seconds. However, the studies conducted in Chapter 6 only demonstrated that such assays were compatible with potential high-throughput approaches, a large high-throughput screen, such as assaying the binding of a drug library to a protein target has yet to be done on the RF. Performing a screen with a drug compound library against Sirtuin proteins would be a good start to validate the RF-MS methodology. Previous studies with droplet microfluidics have shown that high-throughput CIU drug binding screens of this system are possible and replicating these results by RF-MS would be a good start[17]. However, there are several informatics challenges that would need to be surmounted for the RapidFire-MS methodology to be employed in this way.

Firstly, data collection would be a challenge as there is currently no way to run multiple voltage ramps in succession on the 6560c with one method file in a way that is analogous to work with the method editor on the Synapt G2 [17]. This would make a high-throughput RF-MS screen challenging as one would have to manually begin all voltage ramps in order to collect the CIU data. Further software development in collaboration with Agilent would be needed to resolve this challenge. An alternative approach could use one long voltage ramp in a single method file to collect multiple voltage ramps in one acquisition. However, CIUSuite 2 cannot separate data files based on discrete timepoints[18]. Future iterations of CIUSuite 2 should address this by including retention time based parameters for extracting CIU data, especially as CIU begins to be coupled more widely to native separations[19,20].

Further investigation should also investigate the possibility that RF-MS methodologies could be even faster. The MassHunter acquisition software from Agilent limits CIU voltage steps to be as a fast as 3 seconds per voltage step. However, conversations with scientists at Agilent, suggest that this is only a limitation of the MassHunter software, and that voltage ramps of as fast as 1 second per step should be possible with the RapidFire. This would allow for CIU fingerprints of 10 steps to be collected in as little as 10 seconds, improving the throughput of RF-MS analyses threefold, allowing for CIU fingerprints to be taken with less sample required. This is particularly important for precious samples, such as mAbs, that can be very costly even for standardized, model mAb systems. Increasing voltage ramp speeds would require collaboration with Agilent to modify the software, but this would be worthwhile for improving the potential throughput of RF-MS.

Initial work with RF-MS was limited to being interfaced with the RapidFire with 6560c. While this is the most obvious pairing, given that the two systems are from the same vendor and have supported compatibility, it is conceivable that the RF could be interfaced with other mass spectrometers. One potentially advantageous pairing would be of the RapidFire with the cIM. The cIM has been demonstrated to allow for CIU fingerprints to be collected with subsecond voltage steps. Pairing the RapidFire with the cIM could allow for RF-CIU data to be acquired in less than 10 seconds, which is substantially faster than the 6560c, potentially allowing for even faster RF-MS methodologies to be developed.

For a RF-MS method interfaced with the cyclic to be successful, one would have to identify a Waters source that would be compatible with RF-MS flow rates. The Waters Universal Sprayer is somewhat analogous to the Agilent micronebulizer and would likely be compatible with RF-MS flowrates. However, the universal sprayer is slightly smaller (20 µm I.D.) when compared to the micronebulizer (50 µm I.D.), so some further modifications to the RF-MS flow rates would likely need to be made to generate stable spray with the universal sprayer coupled to the RF. Interfacing the RF to the cIM would be advantageous not only for theoretical improvements in throughput, but would also be helpful as the cIM has higher IM and mass resolving power than the 6560c. These improvements in resolution could be particularly useful when performing RF-MS analyses on highly similar analytes, such as the mixtures of biotherapeutics as discussed in Chapter 5. Additionally, demonstrating that RF-MS workflows are not limited to being coupled with the 6560c would be helpful for users who may be implementing such a workflow on a MS from a different vendor, potentially increasing the uptake of native RF-MS technology.

Additionally, while data in Chapter 4 suggest that CIU data can be collected reproducibly on the same instrument using the same parameters, further investigation into the sources of CIU variability is needed. The establishment of RF-CIU and CIU coupled to droplet microfluidics methodologies suggest that the advent of high-throughput CIU is upon us. With these methodologies, it will be possible to amass large amounts of CIU data in relatively short time frames, necessitating means of distributing and making these large CIU datasets publicly available for use in the community, such as a CIU database. For databased CIU data to be most informative, it will be necessary to expand upon the analysis done in Chapter 4 to more critically examine how factors such as flow rate, source gas temperatures, and emitter orifice size can affect the gas phase activation employed to perform CIU. Such a critical analysis would be better able to rationalize the barriers that may exist to reproducing CIU data across different instrument platforms, with several now commercially available[6,21–23], as well as establishing the potential to utilize CIU data to be able to classify unknown proteins and proteoforms.

7.2.3 Developing Native Top-Down Mass Spectrometry Methods for Membrane Proteins on Additional Mass Spectrometry Platforms

While the methodology described in Chapter 2 yields excellent results, it is important to develop methodologies for MPs for additional mass spectrometers in order to leverage the unique benefits of each system for membrane protein research. While platforms such as the QE UHMR and the Waters Synapt G2 have been extensively published upon with MPs [15,24–26], there are no published methodologies for MP research with the Agilent 6560c and the Water Select Series Cyclic IMS. The utility of these systems for MP research is worth exploring in order to understand their advantages for these experiments.

The IR photoactivation based methodology developed in Chapter 2 underscores that there are advantages to liberating MPs from their mimetics prior to fragmenting them. The design of the 6560c can be leveraged for this purpose, with collision energy being imparted in the front funnel to liberate MPs from the source prior to fragmentation in the collision cell by CID[6]. Data for GDX suggests that the 6560c performs well for this purpose, with sequence coverages of ~65% being obtained (Figure 7-2a). However, data with PMP22 suggests that fragmenting larger MP systems may be a challenge, with lackluster sequence coverages of ~20% being obtained (Figure 7-2a). Future work in this space should investigate using the ECD cell to perform ECD in combination with CID for membrane proteins on the 6560c, as combined fragmentation methods can yield improvements in sequence coverage[8]. Some challenges associated with performing this work would include the continued difficulties in obtaining acceptable levels of ECD performance with the current ECD cell, as well as the low CID efficiencies that are obtained whilst the ECD cell is installed. Hopefully, future collaboration with Agilent and eMSion will resolve these problems to make these experiments more feasible, especially given the recent acquisition of eMSion by Agilent.

Initial data taken with the 6560c suggest that the front funnel alone is sufficient to liberate and unfold proteins such as GDX from detergent micelles, with CIU data collected for GDX dimeric in both apo and detergent bound forms (Figure 7-2b-c). Coupling CIU on the

6560c with ECD could allow for combined CIU-ECD experiments These experiments have been previously performed with proteins such as ADH tetramer to annotate domain correlated unfolding patterns[6]. However, such studies have never performed on MP systems, so it would be worthwhile doing this experiment to gain greater insight into how MPs unfold in a domain correlated manner. These CIU-ECD experiments could be especially useful in probing how ligand binding affects MP structure, especially for MP systems that are particularly important drug targets such as cytochrome P450[27].

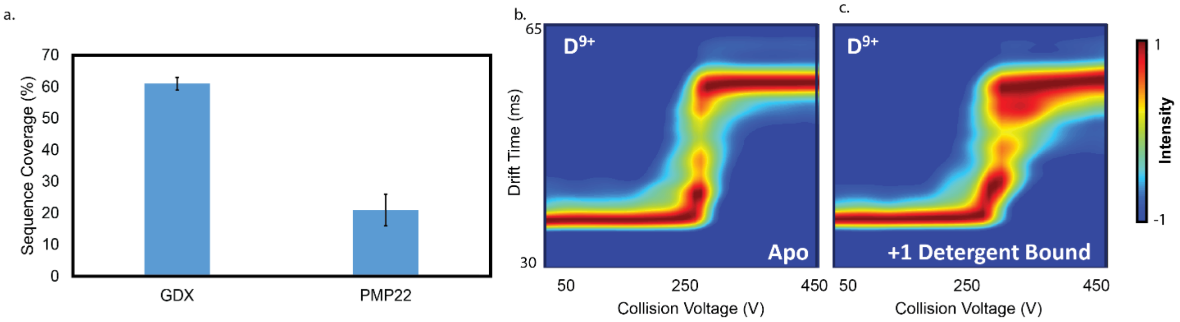

Figure 7-2 Sequence coverage obtained for GDX and PMP22 by CID on the 6560c (a). CIU fingerprints collected for apo (b) and detergent bound (c) GDX 9+ Dimer collected on the 6560c.

The Waters Select Series Cyclic IMS also has the potential to be a powerful platform for nMS MP research. Initial research with PMP22 and GDX shows that the stepwave ion guide on the cyclic is sufficiently activating to liberate these proteins from their detergent micelles, without the need for supplementary trap activation (Figure 7-3a). Subsequent activation in the trap engenders CID based fragmentation for both systems. Sequence coverages for both PMP22 and GDX compare favorably with data collected on the Lumos, with sequence coverages as high as 60% being obtained (Figure 7-3b). For PMP22 fragments common to both platforms, the cIM has higher mass resolution than the 6560c, but less than the Lumos, whilst having higher IM resolution than the 6560c, potentially explaining the improved performance observed with the cIM relative to the 6560c (Table 7-1). Future research in this space should investigate the extent to which improvements in sequence coverage are due to improvements in IM resolution or mass resolution when compared to older IM-MS platforms such as the Synapt G2. While these limited investigations were focused on using the trap for CID, future research should also investigate the use of reinjection into the separator in order to provide supplementary collisional activation in the cyclic separator to determine if sequence coverage can be improved by those means as well[28].

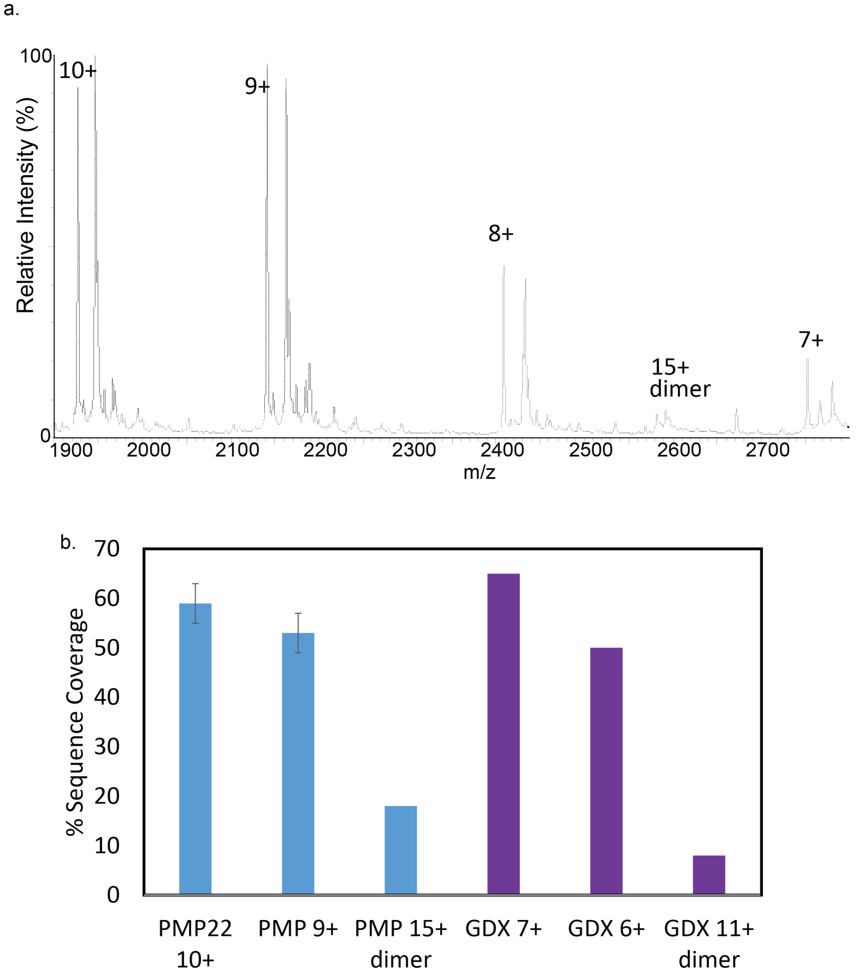

Figure 7-3 Mass spectrum of PMP22 collected on the cIM, demonstrating that PMP22 monomer and dimer are liberated in the stepwave without supplemental activation in the trap (a). Sequence coverage of various charge and oligomeric states of PMP22 and GDX obtained by CID in the trap of the cIM (b).

Additional investigations with the cIM system should also evaluate its performance for MP CIU. The initial observations support that the stepwave ion guide is sufficiently activating to liberate MPs from their mimetic environments. This leaves the collisional activation in the trap to be solely utilized for unfolding. This could be especially important for CIU experiments with MPs ensconced in more complex mimetics such as bicelles and nanodiscs which are more difficult to remove[29]. Future investigation should explore whether the cIM could be used to improve CIU for MPs in these mimetics by increasing the amount of unfolding that occurs, making the CIU fingerprints more informative. Additionally, the ability to eject and reinject could potentially be used to remove noise from mimetics to improve CIU fingerprint quality[21].

Table 7-1 Comparison of mass and IM resolution for PMP22 fragments observed on the Lumos, 6560c and cIM systems. The highest values for each category are bolded.

Fragment ion	Instrument	Mass Resolution	IM Resolution
b_{32}	Agilent 6560c	15000	5
	Waters cIM	35800	**6.3**
	Thermo Fusion Lumos	**46585**	NA
y_{40}	Agilent 6560c	9800	**4.5**
	Waters cIM	28500	3
	Thermo Fusion Lumos	**38476**	NA
b_8	Agilent 6560c	10200	5.6
	Waters cIM	21400	**9.8**
	Thermo Fusion Lumos	**31789**	NA

7.3 References

(1) Mikhailov, V. A.; Liko, I.; Mize, T. H.; Bush, M. F.; Benesch, J. L. P.; Robinson, C. V. Infrared Laser Activation of Soluble and Membrane Protein Assemblies in the Gas Phase. *Anal. Chem.* **2016**, *88* (14), 7060–7067. https://doi.org/10.1021/acs.analchem.6b00645.

(2) Potel, C. M.; Lemeer, S.; Heck, A. J. R. Phosphopeptide Fragmentation and Site Localization by Mass Spectrometry: An Update. *Anal. Chem.* **2019**, *91* (1), 126–141. https://doi.org/10.1021/acs.analchem.8b04746.

(3) Stow, S. M.; Causon, T. J.; Zheng, X.; Kurulugama, R. T.; Mairinger, T.; May, J. C.; Rennie, E. E.; Baker, E. S.; Smith, R. D.; McLean, J. A.; Hann, S.; Fjeldsted, J. C. An Interlaboratory Evaluation of Drift Tube Ion Mobility–Mass Spectrometry Collision Cross Section Measurements. *Anal. Chem.* **2017**, *89* (17), 9048–9055. https://doi.org/10.1021/acs.analchem.7b01729.

(4) Gillette, M. A.; Carr, S. A. Quantitative Analysis of Peptides and Proteins in Biomedicine by Targeted Mass Spectrometry. *Nat Methods* **2013**, *10* (1), 28–34. https://doi.org/10.1038/nmeth.2309.

(5) Adedokun, O. J.; Sandborn, W. J.; Feagan, B. G.; Rutgeerts, P.; Xu, Z.; Marano, C. W.; Johanns, J.; Zhou, H.; Davis, H. M.; Cornillie, F.; Reinisch, W. Association Between Serum Concentration of Infliximab and Efficacy in Adult Patients With Ulcerative Colitis. *Gastroenterology* **2014**, *147* (6), 1296-1307.e5. https://doi.org/10.1053/j.gastro.2014.08.035.

(6) Gadkari, V. V.; Ramírez, C. R.; Vallejo, D. D.; Kurulugama, R. T.; Fjeldsted, J. C.; Ruotolo, B. T. Enhanced Collision Induced Unfolding and Electron Capture Dissociation

of Native-like Protein Ions. *Anal. Chem.* **2020**, *92* (23), 15489–15496. https://doi.org/10.1021/acs.analchem.0c03372.

(7) Vallejo, D. D.; Polasky, D. A.; Kurulugama, R. T.; Eschweiler, J. D.; Fjeldsted, J. C.; Ruotolo, B. T. A Modified Drift Tube Ion Mobility-Mass Spectrometer for Charge-Multiplexed Collision-Induced Unfolding. *Anal. Chem.* **2019**, *91* (13), 8137–8146.

(8) Wongkongkathep, P.; Han, J. Y.; Choi, T. S.; Yin, S.; Kim, H. I.; Loo, J. A. Native Top-Down Mass Spectrometry and Ion Mobility MS for Characterizing the Cobalt and Manganese Metal Binding of α-Synuclein Protein. *J. Am. Soc. Mass Spectrom.* **2018**, *29* (9), 1870–1880. https://doi.org/10.1007/s13361-018-2002-2.

(9) Gomes, F. P.; Diedrich, J. K.; Saviola, A. J.; Memili, E.; Moura, A. A.; Yates, J. R. I. EThcD and 213 Nm UVPD for Top-Down Analysis of Bovine Seminal Plasma Proteoforms on Electrophoretic and Chromatographic Time Frames. *Anal. Chem.* **2020**, *92* (4), 2979–2987. https://doi.org/10.1021/acs.analchem.9b03856.

(10) Konijnenberg, A.; Bannwarth, L.; Yilmaz, D.; Koçer, A.; Venien-Bryan, C.; Sobott, F. Top-down Mass Spectrometry of Intact Membrane Protein Complexes Reveals Oligomeric State and Sequence Information in a Single Experiment. *Protein Science* **2015**, *24* (8), 1292–1300. https://doi.org/10.1002/pro.2703.

(11) Mikesh, L. M.; Ueberheide, B.; Chi, A.; Coon, J. J.; Syka, J. E. P.; Shabanowitz, J.; Hunt, D. F. The Utility of ETD Mass Spectrometry in Proteomic Analysis. *Biochimica et Biophysica Acta (BBA) - Proteins and Proteomics* **2006**, *1764* (12), 1811–1822. https://doi.org/10.1016/j.bbapap.2006.10.003.

(12) Cong, X.; Liu, Y.; Liu, W.; Liang, X.; Russell, D. H.; Laganowsky, A. Determining Membrane Protein–Lipid Binding Thermodynamics Using Native Mass Spectrometry. *J. Am. Chem. Soc.* **2016**, *138* (13), 4346–4349. https://doi.org/10.1021/jacs.6b01771.

(13) Yen, H.-Y.; Jazayeri, A.; Robinson, C. V. G Protein-Coupled Receptor Pharmacology - Insights from Mass Spectrometry. *Pharmacol Rev* **2023**. https://doi.org/10.1124/pharmrev.120.000237.

(14) James, V. K.; Sanders, J. D.; Aizikov, K.; Fort, K. L.; Grinfeld, D.; Makarov, A.; Brodbelt, J. S. Advancing Orbitrap Measurements of Collision Cross Sections to Multiple Species for Broad Applications. *Anal. Chem.* **2022**, *94* (45), 15613–15620. https://doi.org/10.1021/acs.analchem.2c02146.

(15) Fantin, S. M.; Parson, K. F.; Niu, S.; Liu, J.; Polasky, D. A.; Dixit, S. M.; Ferguson-Miller, S. M.; Ruotolo, B. T. Collision Induced Unfolding Classifies Ligands Bound to the Integral Membrane Translocator Protein. *Anal. Chem.* **2019**, *91* (24), 15469–15476. https://doi.org/10.1021/acs.analchem.9b03208.

(16) Keener, J. E.; Zhang, G.; Marty, M. T. Native Mass Spectrometry of Membrane Proteins. *Anal. Chem.* **2021**, *93* (1), 583–597. https://doi.org/10.1021/acs.analchem.0c04342.

(17) D'Amico, C. I.; Polasky, D. A.; Steyer, D. J.; Ruotolo, B. T.; Kennedy, R. T. Ion Mobility-Mass Spectrometry Coupled to Droplet Microfluidics for Rapid Protein Structure Analysis and Drug Discovery. *Anal. Chem.* **2022**. https://doi.org/10.1021/acs.analchem.2c02307.

(18) Polasky, D. A.; Dixit, S. M.; Fantin, S. M.; Ruotolo, B. T. CIUSuite 2: Next-Generation Software for the Analysis of Gas-Phase Protein Unfolding Data. *Anal. Chem.* **2019**, *91* (4), 3147–3155. https://doi.org/10.1021/acs.analchem.8b05762.

(19) Deslignière, E.; Ehkirch, A.; Botzanowski, T.; Beck, A.; Hernandez-Alba, O.; Cianférani, S. Toward Automation of Collision-Induced Unfolding Experiments through Online Size

Exclusion Chromatography Coupled to Native Mass Spectrometry. *Anal. Chem.* **2020**, *92* (19), 12900–12908. https://doi.org/10.1021/acs.analchem.0c01426.

(20) van Schaick, G.; Domínguez-Vega, E.; Castel, J.; Wuhrer, M.; Hernandez-Alba, O.; Cianférani, S. Online Collision-Induced Unfolding of Therapeutic Monoclonal Antibody Glyco-Variants through Direct Hyphenation of Cation Exchange Chromatography with Native Ion Mobility–Mass Spectrometry. *Anal. Chem.* **2023**. https://doi.org/10.1021/acs.analchem.2c03163.

(21) Eldrid, C.; Ujma, J.; Kalfas, S.; Tomczyk, N.; Giles, K.; Morris, M.; Thalassinos, K. Gas Phase Stability of Protein Ions in a Cyclic Ion Mobility Spectrometry Traveling Wave Device. *Anal. Chem.* **2019**, *91* (12), 7554–7561. https://doi.org/10.1021/acs.analchem.8b05641.

(22) Borotto, N. B.; Osho, K. E.; Richards, T. K.; Graham, K. A. Collision-Induced Unfolding of Native-like Protein Ions Within a Trapped Ion Mobility Spectrometry Device. *J. Am. Soc. Mass Spectrom.* **2022**, *33* (1), 83–89. https://doi.org/10.1021/jasms.1c00273.

(23) Zhong, Y.; Hyung, S.-J.; T. Ruotolo, B. Characterizing the Resolution and Accuracy of a Second-Generation Traveling-Wave Ion Mobility Separator for Biomolecular Ions. *Analyst* **2011**, *136* (17), 3534–3541. https://doi.org/10.1039/C0AN00987C.

(24) Chorev, D. S.; Baker, L. A.; Wu, D.; Beilsten-Edmands, V.; Rouse, S. L.; Zeev-Ben-Mordehai, T.; Jiko, C.; Samsudin, F.; Gerle, C.; Khalid, S.; Stewart, A. G.; Matthews, S. J.; Grünewald, K.; Robinson, C. V. Protein Assemblies Ejected Directly from Native Membranes Yield Complexes for Mass Spectrometry. *Science* **2018**, *362* (6416), 829–834. https://doi.org/10.1126/science.aau0976.

(25) Harvey, S. R.; White, W.; Schey, K. L.; Wysocki, V. H. Native Mass Spectrometry for the Study of Membrane Proteins. *J Biomol Tech* **2019**, *30* (Suppl), S56–S57.

(26) Fantin, S. M.; Parson, K. F.; Yadav, P.; Juliano, B.; Li, G. C.; Sanders, C. R.; Ohi, M. D.; Ruotolo, B. T. Ion Mobility–Mass Spectrometry Reveals the Role of Peripheral Myelin Protein Dimers in Peripheral Neuropathy. *Proceedings of the National Academy of Sciences* **2021**, *118* (17), e2015331118.

(27) Nebert, D. W.; Wikvall, K.; Miller, W. L. Human Cytochromes P450 in Health and Disease. *Philosophical Transactions of the Royal Society B: Biological Sciences* **2013**, *368* (1612), 20120431. https://doi.org/10.1098/rstb.2012.0431.

(28) Giles, K.; Ujma, J.; Wildgoose, J.; Pringle, S.; Richardson, K.; Langridge, D.; Green, M. A Cyclic Ion Mobility-Mass Spectrometry System. *Anal. Chem.* **2019**, *91* (13), 8564–8573. https://doi.org/10.1021/acs.analchem.9b01838.

(29) Marty, M. T.; Hoi, K. K.; Robinson, C. V. Interfacing Membrane Mimetics with Mass Spectrometry. *Acc. Chem. Res.* **2016**, *49* (11), 2459–2467. https://doi.org/10.1021/acs.accounts.6b00379.

Appendices

Appendix I Quantifying Protamine Proteoforms from Patients with Sperm Abnormalities

I.1 Overview

Protamines are proteins found in the nuclei of sperm cells, that serve to condense the the genome of the spermatazoon, in a manner similar to the histones found in somatic cells[1]. Protamines pack the genome more tightly than somatic histones in order to protect better protect the genetic material during fertilization[2]. Previous studies with mass spectrometry demonstrated that protamines in mice are modified by PTMs similarly to histones, suggesting that these PTMs could play roles in epigenetic regulation like they do with histones[3]. However, no studies have sought to explore how these PTMs in human samples. In collaboration with Samantha Schon and Sue Hammoud in the Departments of Human Genetics, Urology, and Obstetrics and Gynecology, we studied protamines extracted from samples collected from patients at Michigan Medicine. We sought to compare the PTMs present in people with normal sperm to those of patients with abnormal sperm to investigate if protamine PTMs may affect the etiology of male factor fertility. The abnormal sperm samples were from people with ashtenozoospermia, a condition in which spermatozoa have reduced motility, and oligoasthenoteratozoospermia, a condition in which spermatozoa have low count, reduced motility and abnormal morphology[4]. Both asthenozoospermia and oligoasthenoteratozoospermia can result in male factor infertility[4].

I.2 Materials and Methods

A total of 29 purified protamine samples were obtained from our collaborators: 14 from people with normal sperm quality, 11 from people with asthenozoospermia and 4 from people with oligoasthenoteratozoospermia. PRM samples were dialyzed into 200 mM ammonium acetate (MilliporeSigma, St. Louis, MO) using dialysis cassettes with a 2 kDa MWCO and 0.5 mL capacity (ThermoFisher, San Jose, CA). The ammonium acetate buffer was exchanged twice: at 2 hours and 4 hours. PRM samples were extracted from the cartridge after 24 hours of dialysis at 4 degrees. PRM samples were then analyzed using an Orbitrap Fusion Lumos mass spectrometer (ThermoFisher). Samples were ionized using nanoelectrospray ionization in positive polarity using the NanoSpray Flex source (ThermoFisher). 1.6 kV of capillary voltage was applied to a borosilicate emitter coated in gold. These emitters were fabricated using a P-97 pipette puller (Sutter Instruments, Novato, CA). Data was collected with a mass resolution of 120000 at 300 Th. MS data were collected with an extended mass range up to 3000 Th and with a radio frequency amplitude of 30%. The transfer tube temperature was set to 275 degrees. MS data were visualized using FreeStyle (ThermoFisher) and deconvoluted using the Xtract algorithm to measure the intact masses of the PRMs present. The intensities of all identified protamines in the samples were then summed to calculate the relative abundance of each protamine detected in the sample. Statistical analyses were performed in Prism (Dotmatics, Boston, MA).

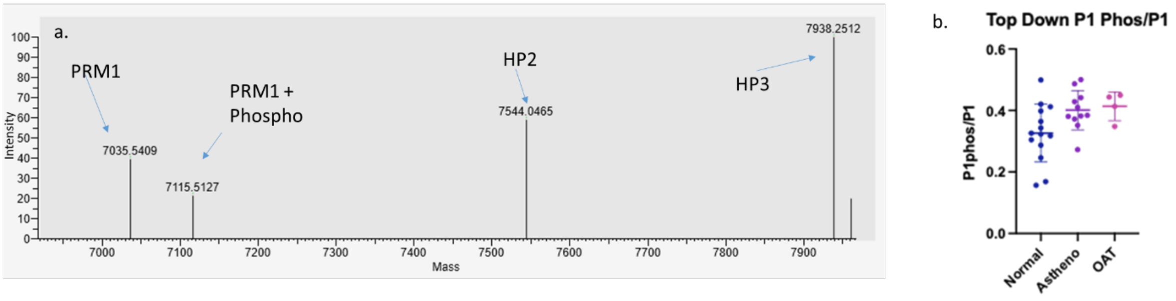

Figure I-1 A deconvoluted mass spectrum from a typical protamine experiment (a). Several isoforms of protamine are present including PRM1, HP2, and HP3. Phosphorylated PRM1 is also detected. Ratios of phosphorylated PRM1 to PRM1 in samples from patients with normal sperm, asthenozoospermia and oligoasthenoteratozoospermia (b). The ratio of phosphorylated PRM1 to PRM1 was found to be statistically significant between people with normal and abnormal sperm quality by a one-way ANOVA test.

I.3 Results

Several proteoforms of protamine were typically identified in these samples, including several isoforms of protamine that form from differential enzymatic cleavage: P1 and P2 (Figure I-1a). HP2, HP3 and HP4 are all forms of P2. P1 with a phosphorylation was the most common PTM observed in these species, so it was included in the comparison. The relative abundancies of HP3, HP2, P1 and P1 with the phosphorylation were tracked across all 29 samples and the ratios of the isoforms to one another were analyzed by one-way ANOVA. Of the data analyzed, there was a statistically significant difference in the ratio of Phosphorylated P1 to P1 in samples from people with sperm abnormalities (Figure I-1b). These data suggest that the phosphorylation of P1 is upregulated in people with sperm abnormalities, suggesting that this phosphorylation may affect the etiology of these disease states. Additionally, the ratio of P1+Phosphorylation to P1 could also be potentially utilized as a diagnostic measurement to assay sperm abnormalities and male factor infertility in the clinic, in addition to the P1:P2 ratio that is currently used in the clinic[5].

I.4 References

(1) Björndahl, L.; Kvist, U. Human Sperm Chromatin Stabilization: A Proposed Model Including Zinc Bridges. *Mol Hum Reprod* **2010**, *16* (1), 23–29. https://doi.org/10.1093/molehr/gap099.

(2) Okada, Y. Sperm Chromatin Structure: Insights from in Vitro to in Situ Experiments. *Current Opinion in Cell Biology* **2022**, *75*, 102075. https://doi.org/10.1016/j.ceb.2022.102075.

(3) Brunner, A. M.; Nanni, P.; Mansuy, I. M. Epigenetic Marking of Sperm by Post-Translational Modification of Histones and Protamines. *Epigenetics & Chromatin* **2014**, *7* (1), 2. https://doi.org/10.1186/1756-8935-7-2.

(4) Ray, P. f.; Toure, A.; Metzler-Guillemain, C.; Mitchell, M. j.; Arnoult, C.; Coutton, C. Genetic Abnormalities Leading to Qualitative Defects of Sperm Morphology or Function. *Clinical Genetics* **2017**, *91* (2), 217–232. https://doi.org/10.1111/cge.12905.

(5) Carrell, D. T.; Emery, B. R.; Hammoud, S. The Aetiology of Sperm Protamine Abnormalities and Their Potential Impact on the Sperm Epigenome. *Int J Androl* **2008**, *31* (6), 537–545. https://doi.org/10.1111/j.1365-2605.2008.00872.x.

Appendix II Identifying Unknown Metal Binding in a Bacterial α-Amylase

II.1 Overview

The gut microbiota is essential to human health as these microorganisms are essential to the processing of complex carbohydrates so that they may be further metabolized[1]. While the microbiota is composed of various microorganisms such as archaea, viruses and fungi, bacteria are the most studied constituents of the gut flora, digesting up 10% of calories directly from bacterial fermentation[2,3]. In the colon, bacteria are known to interact directly with epithelial tissue, mediating health and disease states[4]. *Bacteriodes thetaiotaomicron* is a colonic bacterium whose genome encodes for multiple enzymes that process starches, including BoGH13A$_{\text{Sus}}$ [5]. Initial structural projections based on data from X-Ray diffraction suggested that BoGH13A$_{\text{Sus}}$ may contain an Mn^{2+} binding site; however, Mn^{2+} binding is not typically observed in α-amylases like BoGH13A$_{\text{Sus}}$. In collaboration with the laboratory of Nicole Koropatkin in the Department of Microbiology and Immunology, native MS and inductively coupled plasma (ICP)-MS studies were conducted on BoGH13A$_{\text{Sus}}$ to validate the presence of Mn^{2+} binding in this protein.

II.2 Materials and Methods

II.2.1 Native Intact Mass Analysis of BoGH13A$_{\text{Sus}}$

Native mass spectrometry data on purified BoGH13A$_{\text{Sus}}$ were collected on a Q Exactive Ultra-High Mass Range (UHMR) orbitrap system (ThermoFisher, San Jose, CA). Tune settings were carefully selected such that the protein would remain intact for the duration of the experiment. Prior to MS, samples were buffer exchanged into 200 mM ammonium acetate (pH=8) (MilliporeSigma, St. Louis, MO) using P-6 Biospin Columns (Bio-Rad, Hercules, CA). Ions were generated using nanoelectrospray ionization in positive polarity through direct infusion with the NanoSpray FlexIon source (ThermoFisher). 1.5 kV of capillary voltage was applied to a borosilicate emitter that was coated in gold and fabricated in house using a P-97 pipette puller (Sutter Instruments, Novato, CA). The capillary temperature was set to 275° and the S-lens RF was set to 80. Data were collected with a resolution of 200000 at 200 Th and were visualized with FreeStyle (ThermoFisher) and deconvoluted with UniDec[6].

II.2.2 ICP-MS

ICP-MS data were collected with a Nexion 2000 ICP-MS (PerkinElmer, Waltham, MA) that utilizes Argon plasma. BoGH13A$_{Sus}$ samples were diluted with 2% Nitric Acid (MilliporeSigma) prior to analysis and ionization. Internal standards (PerkinElmer), namely Bismuth, Holmium, Indium, Lithium-6, Scandium, Terbium and Yttrium, were employed to ensure data reproducibility. Calibration curves were constructed for ^{55}Mn and ^{44}Ca, ranging from 1 to 50 ppb via ICP-MS, with a blank sample also being run. ICP-MS data for BoGH13A$_{Sus}$ samples were collected in triplicate by autosampling. Data were analyzed with Synergistix (PerkinElmer) and Excel (Microsoft, Redmond, WA).

II.3 Results

II.3.1 Intact Mass Measurement of BoGH13A$_{Sus}$

Native MS data collected on the QE-UHMR platform were consistent with Mn^{2+} binding to BoGH13A$_{Sus}$. The intact mass of the deconvoluted BoGH13A$_{Sus}$ native MS was 84213 +/- .04 Da, whereas the sequence mass of BoGH13A$_{Sus}$ is 83975 Da (Figure II-1). The discrepancy between the observed and expected mass can be explained by the presence of Ca^{2+}, 3 H_2O, and Mn^{2+} binding to the enzyme as predicted, with the masses of these individual species summing to

148 Da mass discrepancy. While this observation lends credence to the idea that Mn^{2+} is binding BoGH13A$_{Sus}$, it is not conclusive as Mn^{2+} was not directly observed being ejected from BoGH13A$_{Sus}$ in the mass spectra. This is because the m/z ratio of Mn^{2+} was too low to be detected on the UHMR and the other MS platforms that were accessible to us.

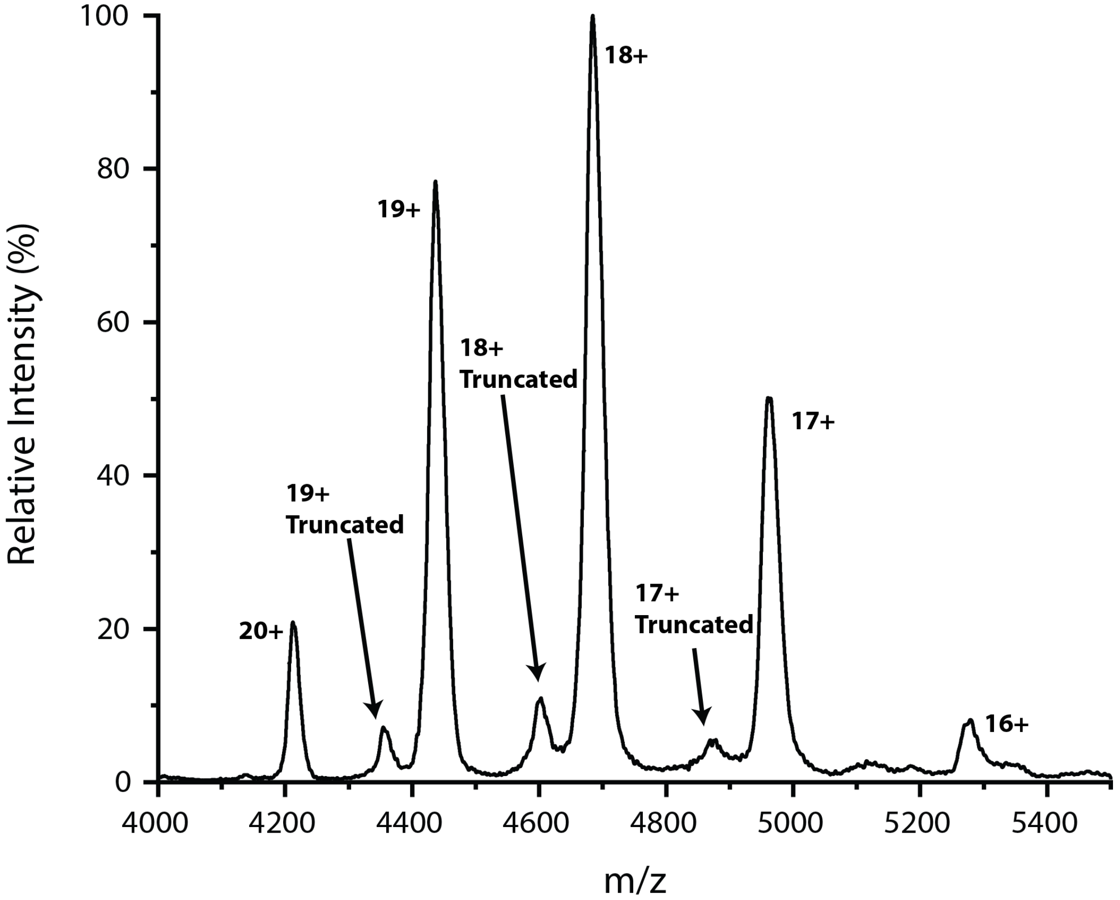

Figure II-1 Native mass spectrum obtained for BoGH13A$_{Sus}$ on the UHMR that was then deconvoluted by UniDec. A truncated form of BoGH13A$_{Sus}$ is also visible in the spectrum, this truncation is likely enzymatic in origin.

II.3.2 ICP-MS Validation of Mn^{2+} Presence in BoGH13A$_{Sus}$

To surmount this challenge, we performed ICP-MS studies on BoGH13A$_{Sus}$ to see if Mn^{2+} could be observed in that sample. Mn^{2+} was present in addition to Ca^{2+}, at concentrations of 38 ppb and 2 ppb respectively (Table II-1). These data suggests that Mn^{2+} is present in the sample and does bind to the active site of BoGH13A$_{Sus}$. These data correlated with other enzymology data that suggest that Mn^{2+} presence is necessary for enzymatic activity with

$\text{BoGH13A}_{\text{Sus}}$. Altogether, the MS data describe herein aided in establishing that $\text{BoGH13A}_{\text{Sus}}$ does bind Mn^{2+}. $\text{BoGH13A}_{\text{Sus}}$ is the first α-amylase to be discovered that Mn^{2+} dependent, suggesting that Mn^{2+} may be more influential in the function of the gut microbiome than is currently appreciated.

Table II-1 Concentrations of Calcium and Manganese present in $\text{BoGH13A}_{\text{Sus}}$ sample as determined by ICP-MS.

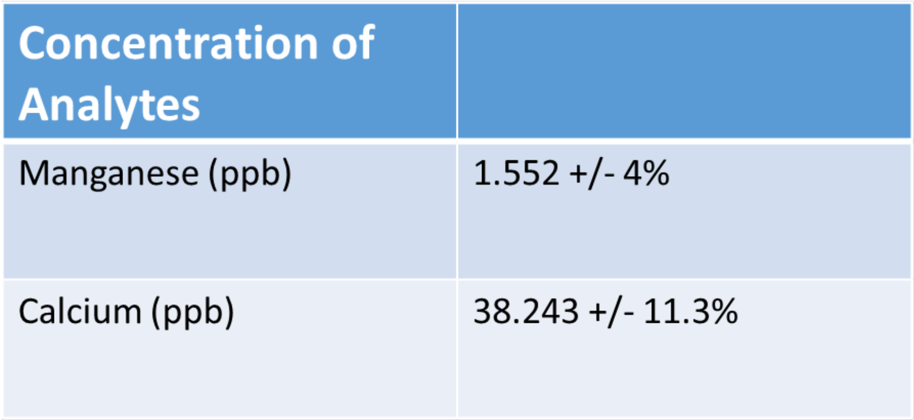

Concentration of Analytes	
Manganese (ppb)	1.552 +/- 4%
Calcium (ppb)	38.243 +/- 11.3%

II.4 References

(1) Reyes, A.; Semenkovich, N. P.; Whiteson, K.; Rohwer, F.; Gordon, J. I. Going Viral: Next-Generation Sequencing Applied to Phage Populations in the Human Gut. *Nat Rev Microbiol* **2012**, *10* (9), 607–617. https://doi.org/10.1038/nrmicro2853.

(2) Wilson, A. S.; Koller, K. R.; Ramaboli, M. C.; Nesengani, L. T.; Ocvirk, S.; Chen, C.; Flanagan, C. A.; Sapp, F. R.; Merritt, Z. T.; Bhatti, F.; Thomas, T. K.; O'Keefe, S. J. D. Diet and the Human Gut Microbiome: An International Review. *Dig Dis Sci* **2020**, *65* (3), 723–740. https://doi.org/10.1007/s10620-020-06112-w.

(3) N i, M. The Contribution of the Large Intestine to Energy Supplies in Man. *The American Journal of Clinical Nutrition* **1984**, *39* (2), 338–342. https://doi.org/10.1093/ajcn/39.2.338.

(4) Hansson, G. C. Mucins and the Microbiome. *Annu Rev Biochem* **2020**, *89*, 769–793. https://doi.org/10.1146/annurev-biochem-011520-105053.

(5) Koropatkin, N. M.; Smith, T. J. SusG: A Unique Cell-Membrane-Associated Alpha-Amylase from a Prominent Human Gut Symbiont Targets Complex Starch Molecules. *Structure* **2010**, *18* (2), 200–215. https://doi.org/10.1016/j.str.2009.12.010.

(6) Marty, M. T.; Baldwin, A. J.; Marklund, E. G.; Hochberg, G. K. A.; Benesch, J. L. P.; Robinson, C. V. Bayesian Deconvolution of Mass and Ion Mobility Spectra: From Binary Interactions to Polydisperse Ensembles. *Anal. Chem.* **2015**, *87* (8), 4370–4376. https://doi.org/10.1021/acs.analchem.5b00140.

Appendix III Chapter 2 Supporting Information

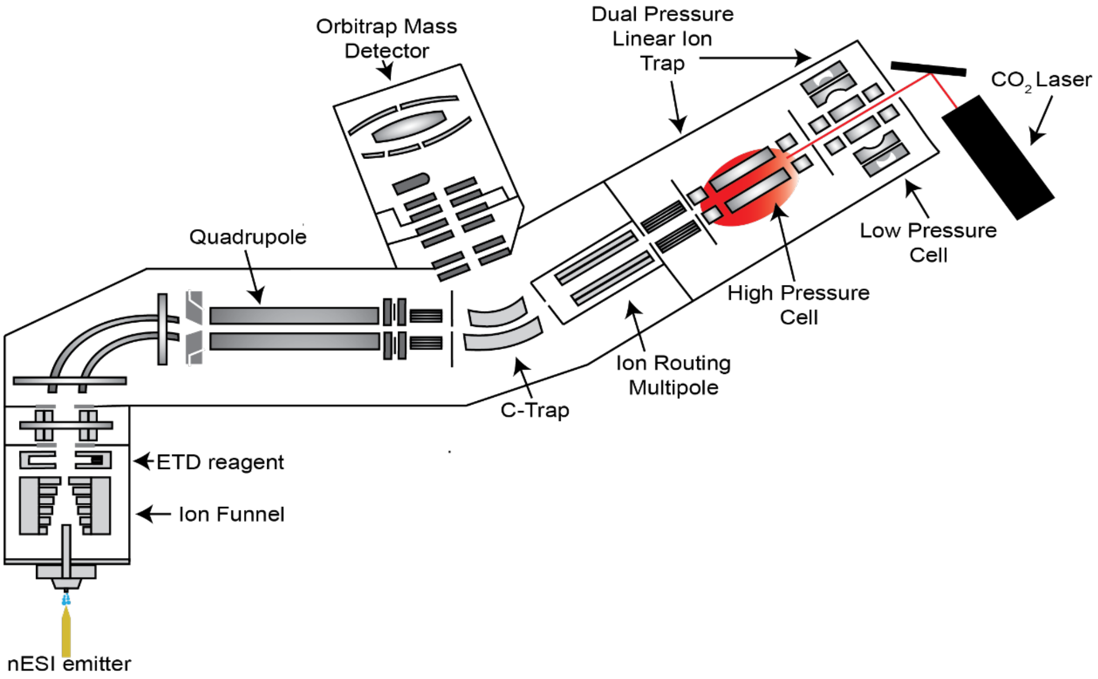

Figure III-1A schematic of the Orbitrap Fusion Lumos Tribrid MS with the 60 W Synrad CO$_2$ laser. The laser is external to the instrument and is controlled by software. The laser beam enters the instrument through an infrared transparent window and irradiates the high pressure cell of the linear ion trap.

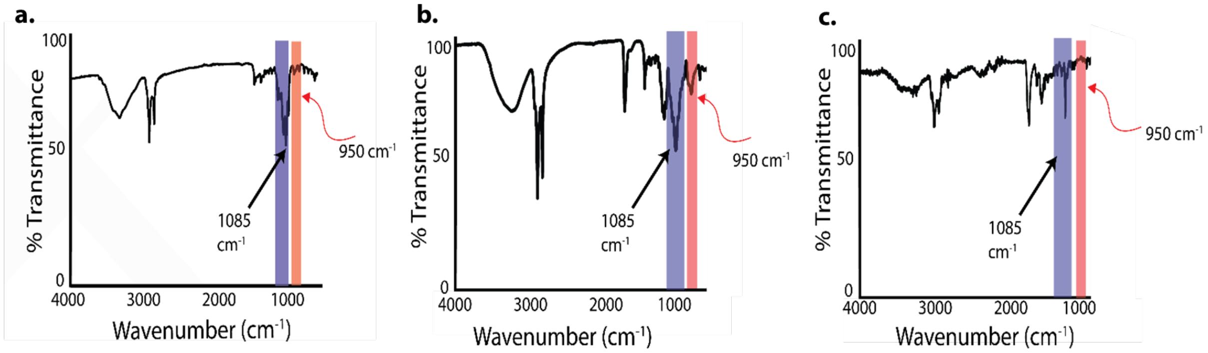

Figure III-2 Infrared spectra for DM (a), LMPG (b) and DC (c). The regions of the IR sepctra where the laser operates at are highlighted in red. The region where the C-O stretch at 1085 cm^{-1} is prominent is highlighted in blue.

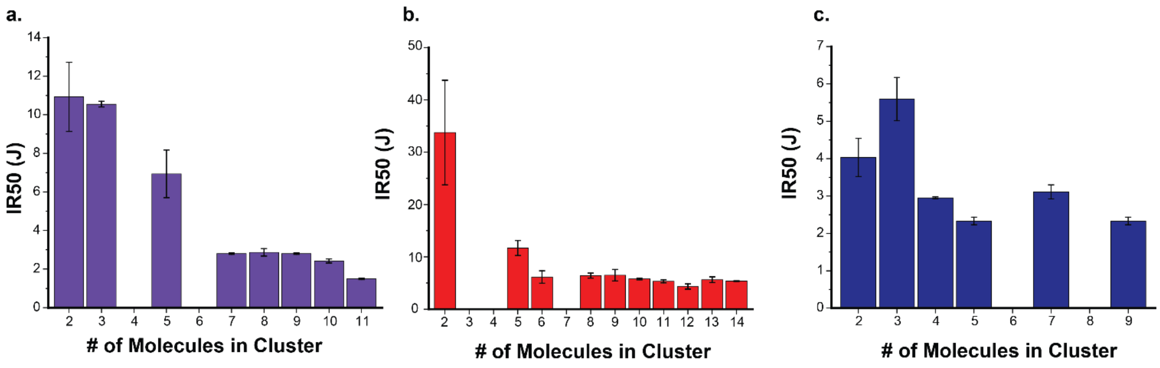

Figure III-3 Histograms depicting the IR50 values for LMPG (a), DM (b), and DC (c) clusters of various sizes.

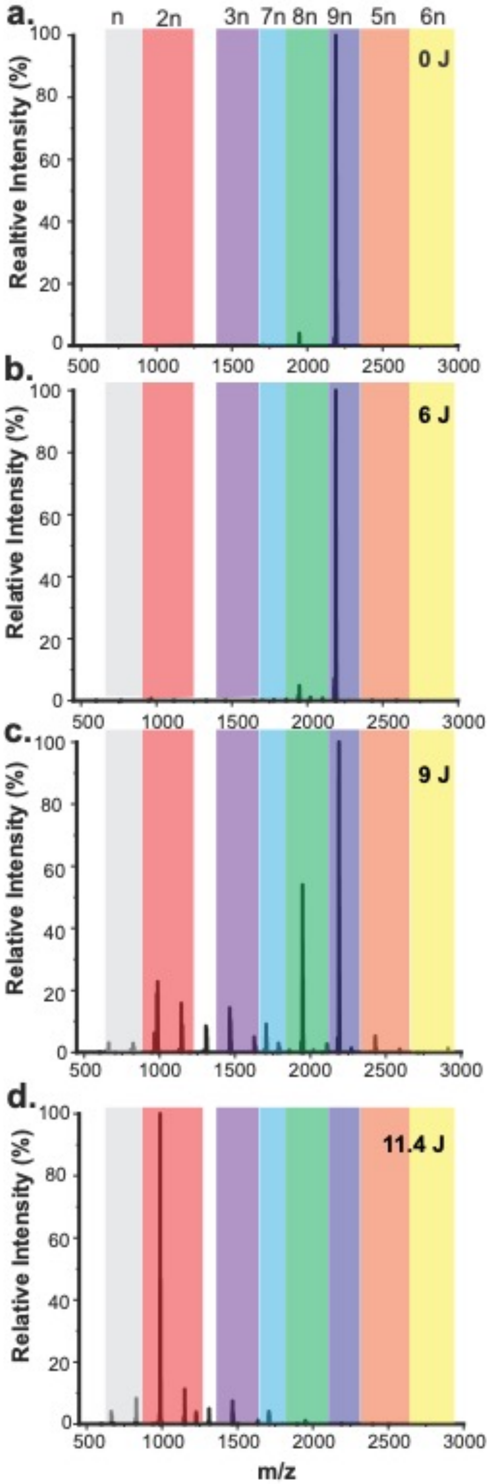

Figure III-4 A stackplot of mass spectra obtained from DM 9mer that has been mass selected and exposed to 0 J (a), 6 J (b), 9 J (c), and 11.4 J (d) of IR activation in the ion trap.

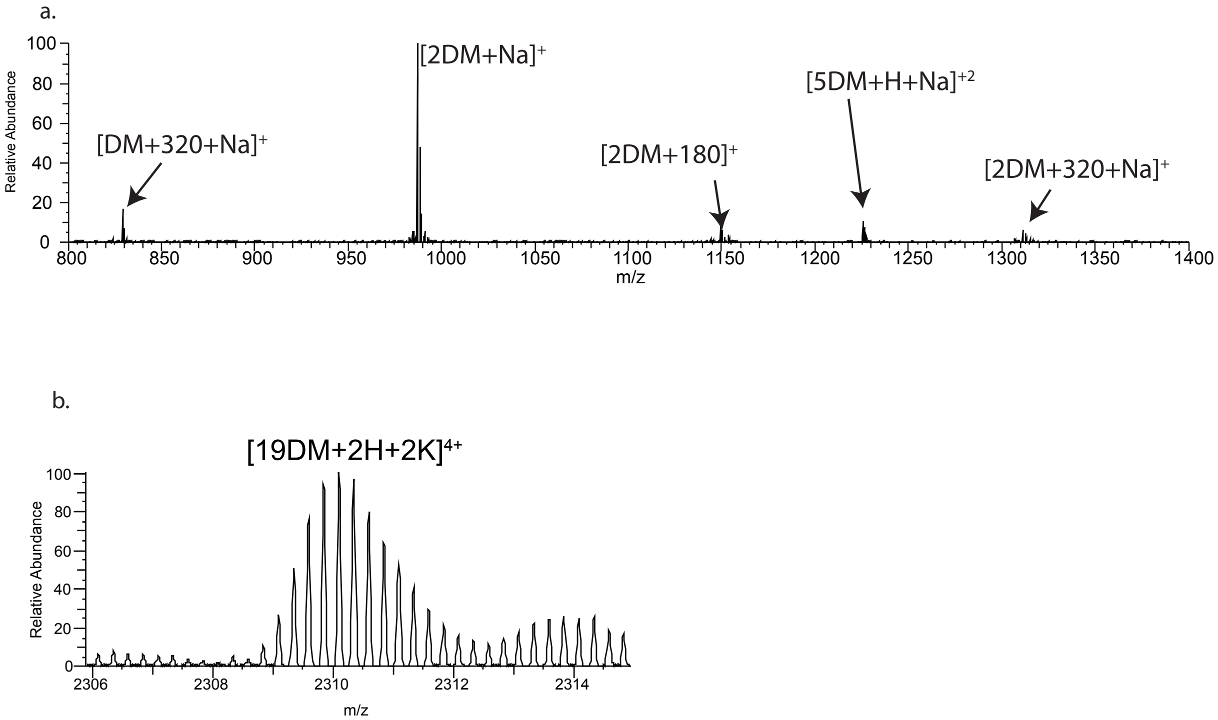

Figure III-5 An inset of a region the mass spectrum depicted in Figure 2-1a (a). In this mass spectrum we observe adducted DM 2mer and 5mer. Additionally, we observe DM clusters with additions of 180 and 320 Da, respectively. These mass additions are from DM molecules which have had their glycosidic bonds hydrolyzed, yielding fragments of 320.2 Da and 180.1 Da that cluster with intact DM molecules. A mass spectrum highlighting a peak resulting from an adducted 19mer of DM with a charge of 4.

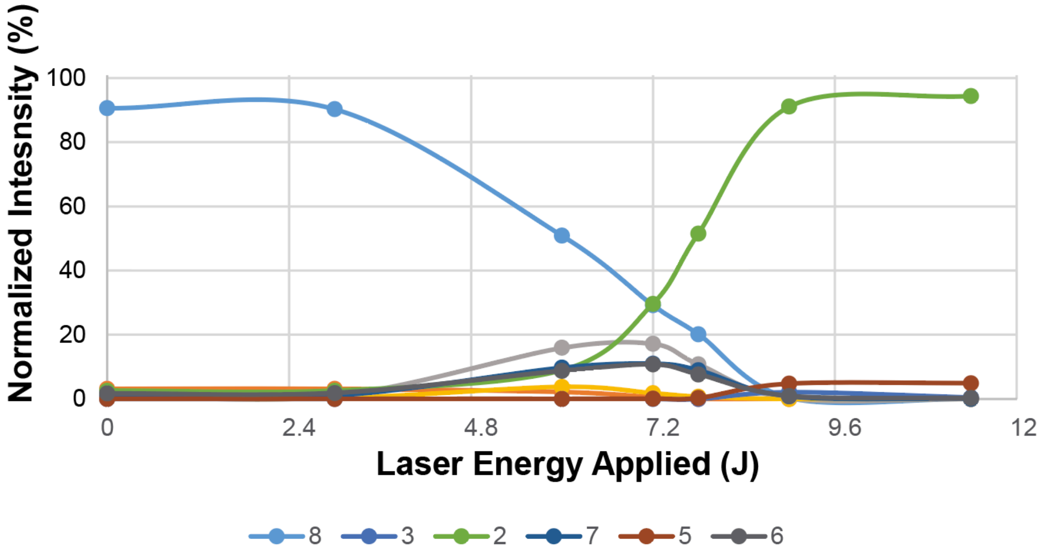

Figure III-6 The relative intensities of a quadrupole selected DM 8mer and its products as infrared activation was applied.

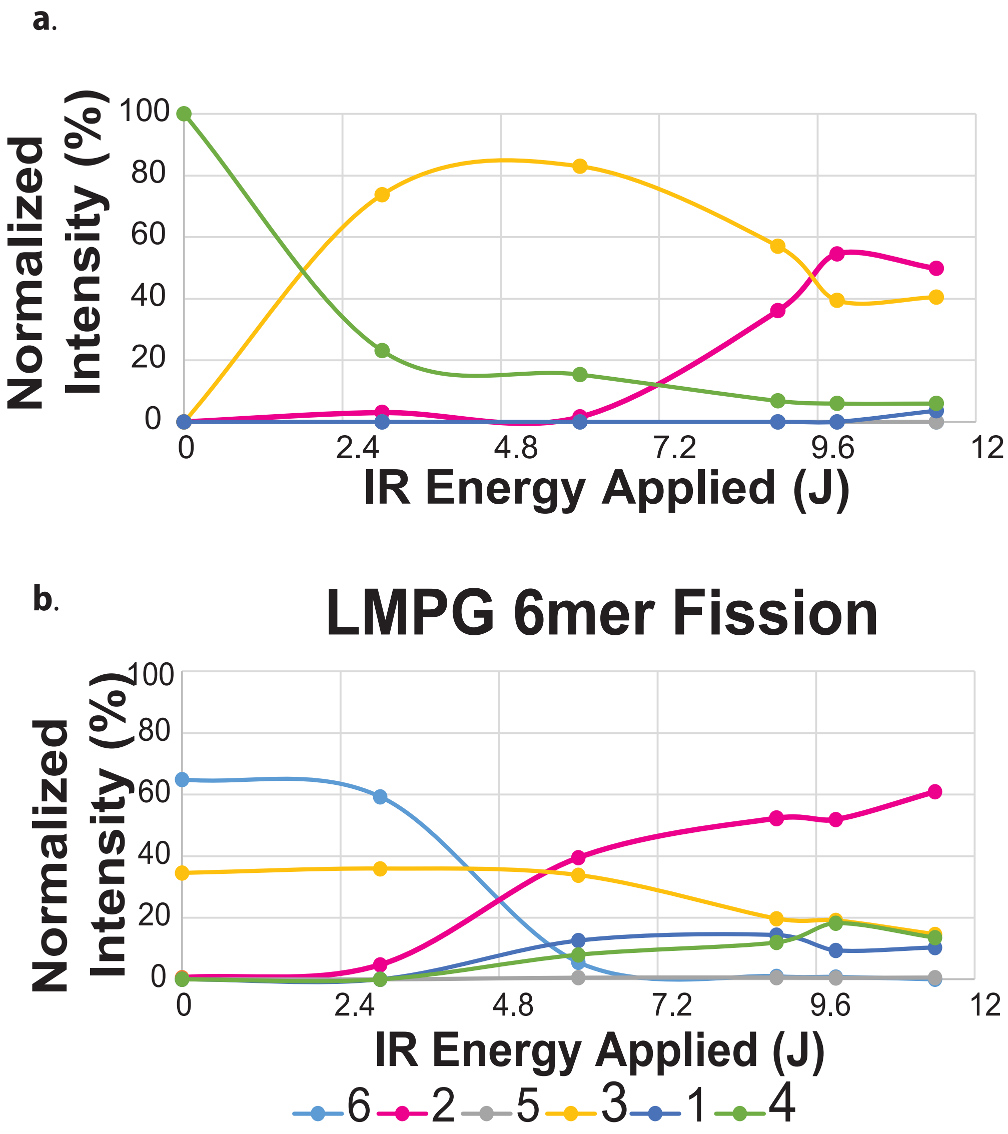

Figure III-7 The relative intensities of quadrupole selected DC 4mer (a) and LMPG 6mer (b) clusters and their products as infrared activation was applied.

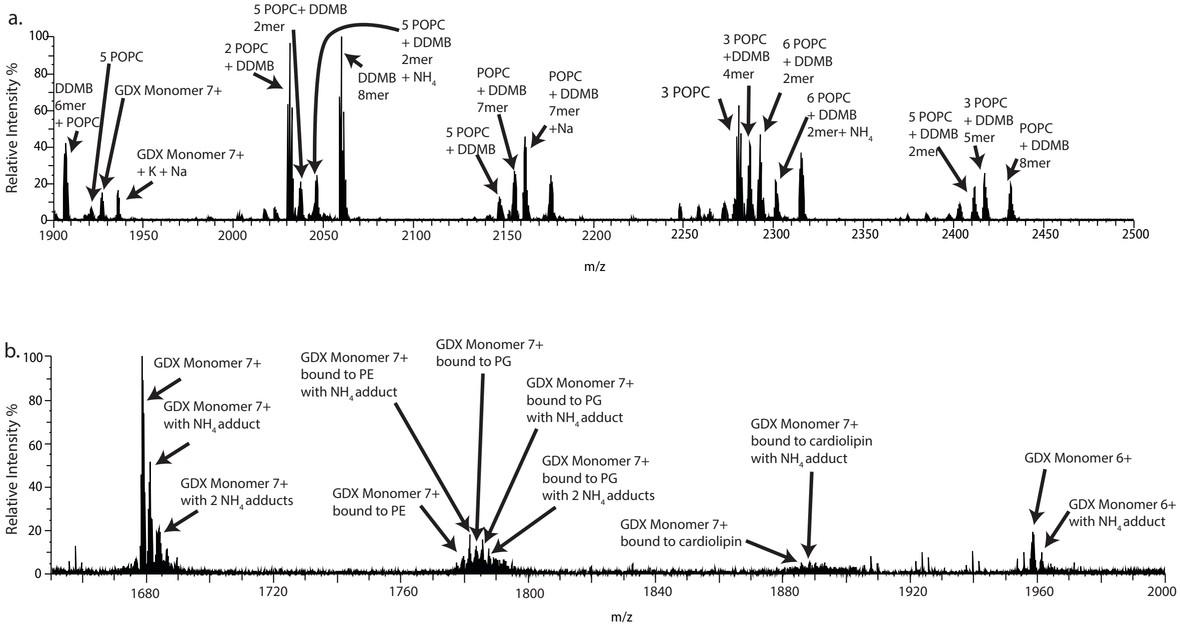

Figure III-8 The mass spectra displayed in in Figures 2-2a (a) and f (b), annotated with additional detail. In panel a, depicting a GDX bicelle sprayed without any IR photoactivation, various lipid, detergent, and mixed lipid detergent clusters are observed. In panel b, from GDX liberated out of a liposome with 11.4 J of IR photoactivation, adducted GDX monomer peaks are observed along with &+ GDX monomers which are bound to PG, PE, cardiolipin with adducts.

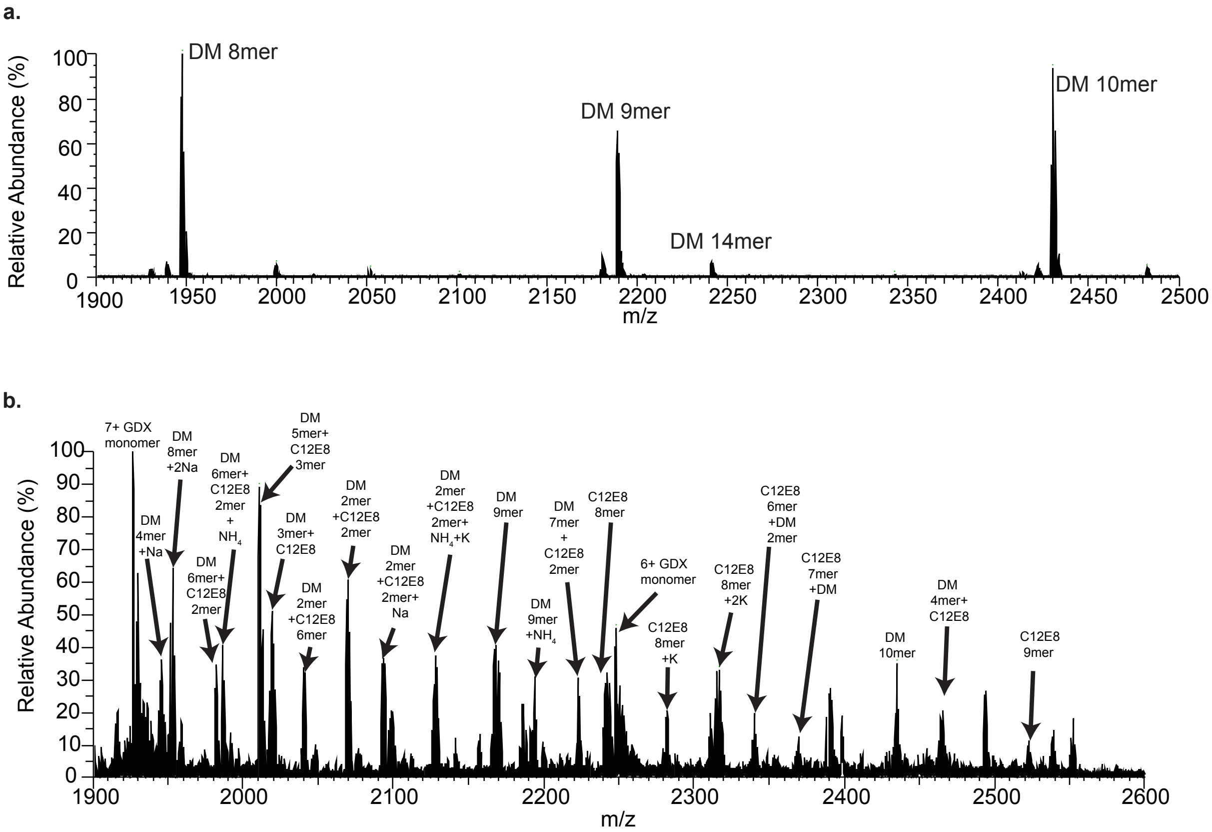

Figure III-9 Mass spectra of PMP22 (a) and GDX (b) before IR activation has been applied displaying the detergent clusters that predominate before activation.

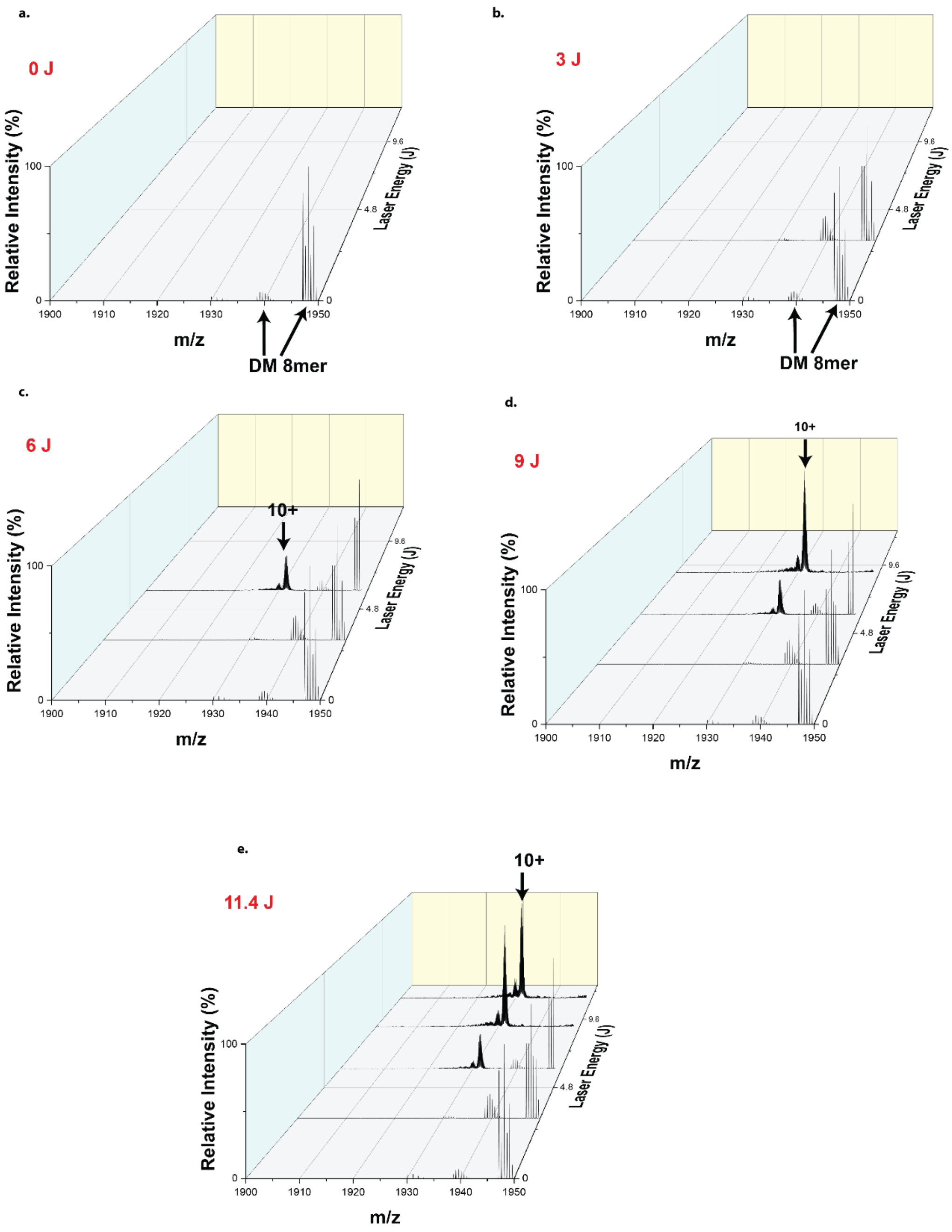

Figure III-10 A selected portion of the mass spectra obtained from PMP22 in micelles as infrared activation was applied, 0 J (a), 3 (b), 6 (c), 9 J (d) and 11.4 J (e). As IR activation increased, the 10+ charge state becomes visible and the most intense species in the spectra.

a.

PMP22 without laser activation **(36% Residue Cleavages)**

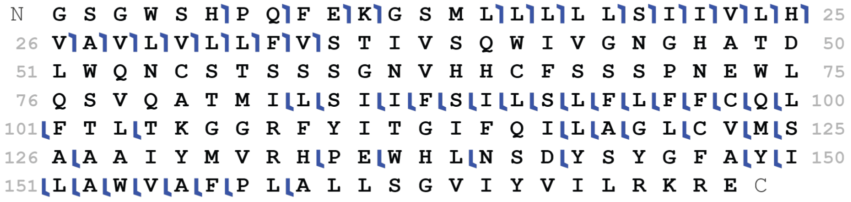

b.

PMP22 with 11.4 J of laser activation **(71% Residue Cleavages)**

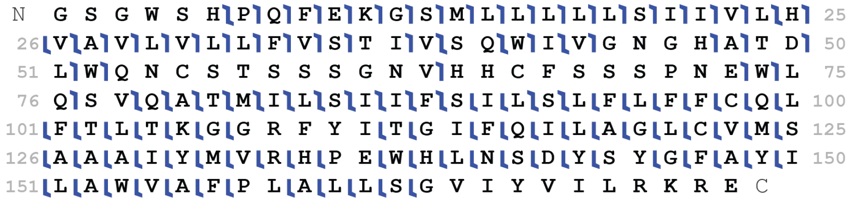

c.

PMP22 8+ wth 11.4 J of laser activation **(64% Residue Cleavages)**

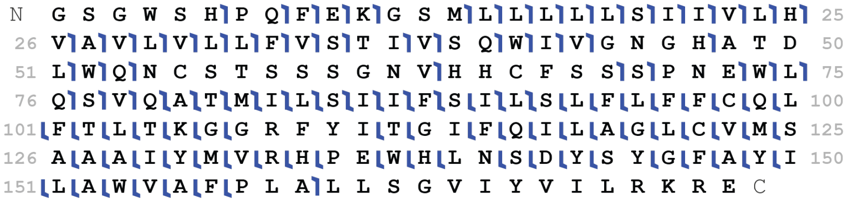

d.

PMP22 9+ wth 11.4 J of laser activation **(67% Residue Cleavages)**

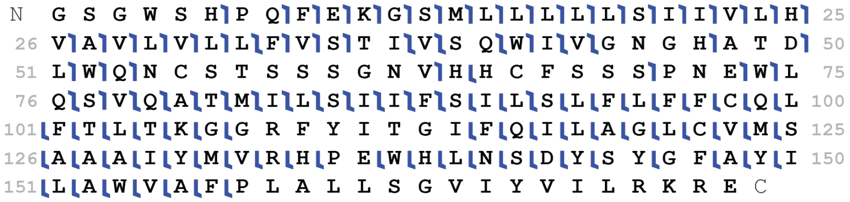

e.

PMP22 10+ wth 11.4 J of laser activation **(67% Residue Cleavages)**

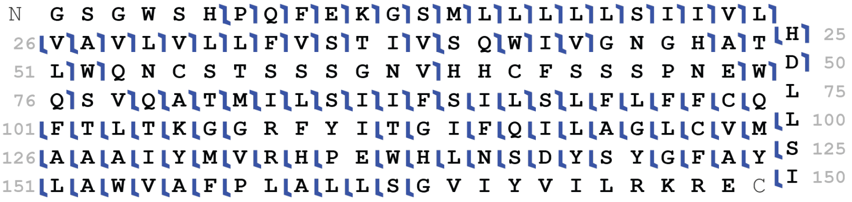

Figure III-11 Representative sequence coverage maps for PMP22 all charge state data without (a) and with (b) IR activation. As well as representative sequence coverage maps for PMP22 8+ (c), 9+ (d), and 10 + (e) monomers after IR activation.

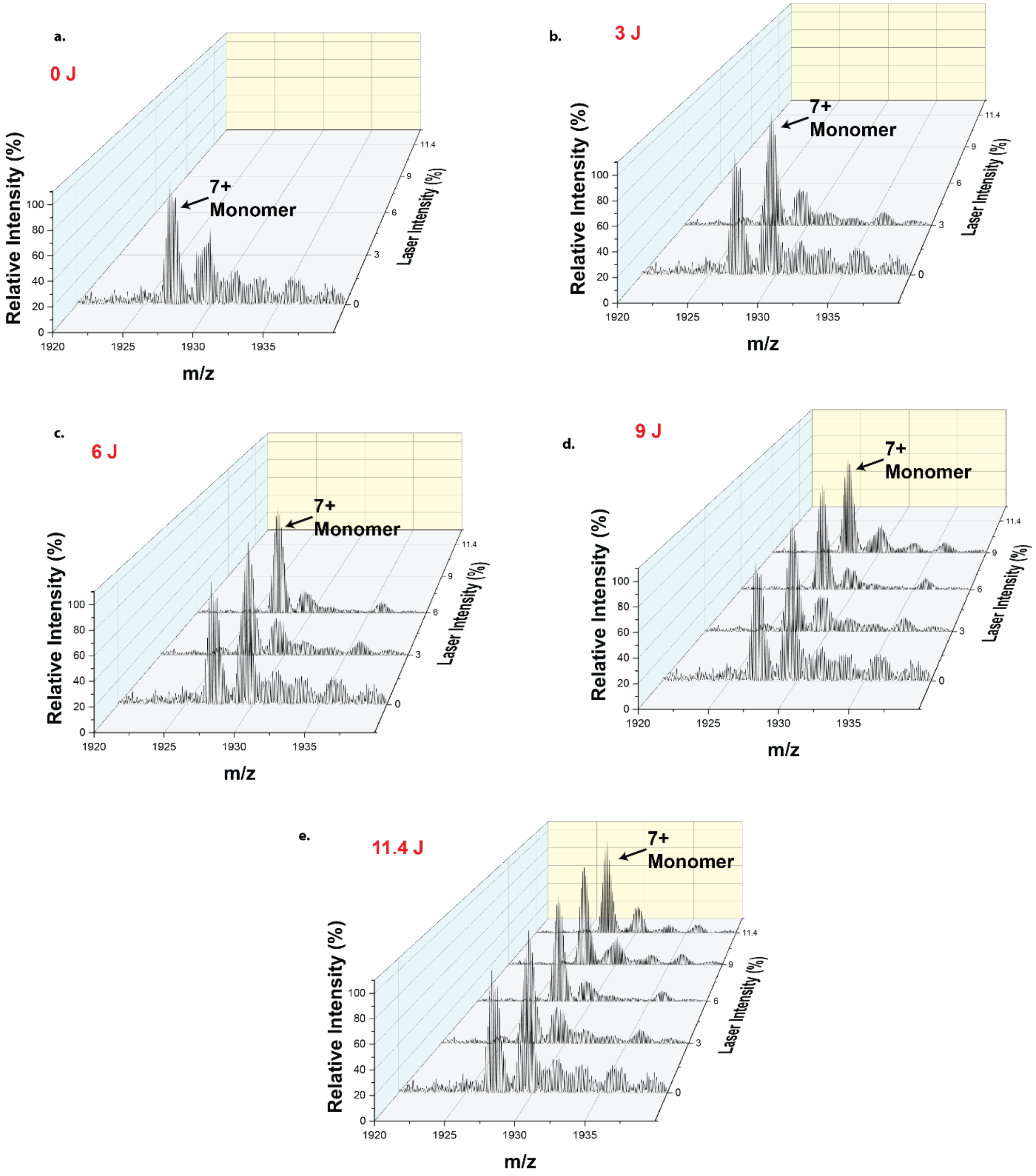

Figure III-12 A selected portion of the mass spectra obtained from GDX in micelles as infrared activation was applied. The 7+ monomer of GDX was liberated prior to IR activation, and the 7+ monomer signal remains unchanged as IR activation increases.

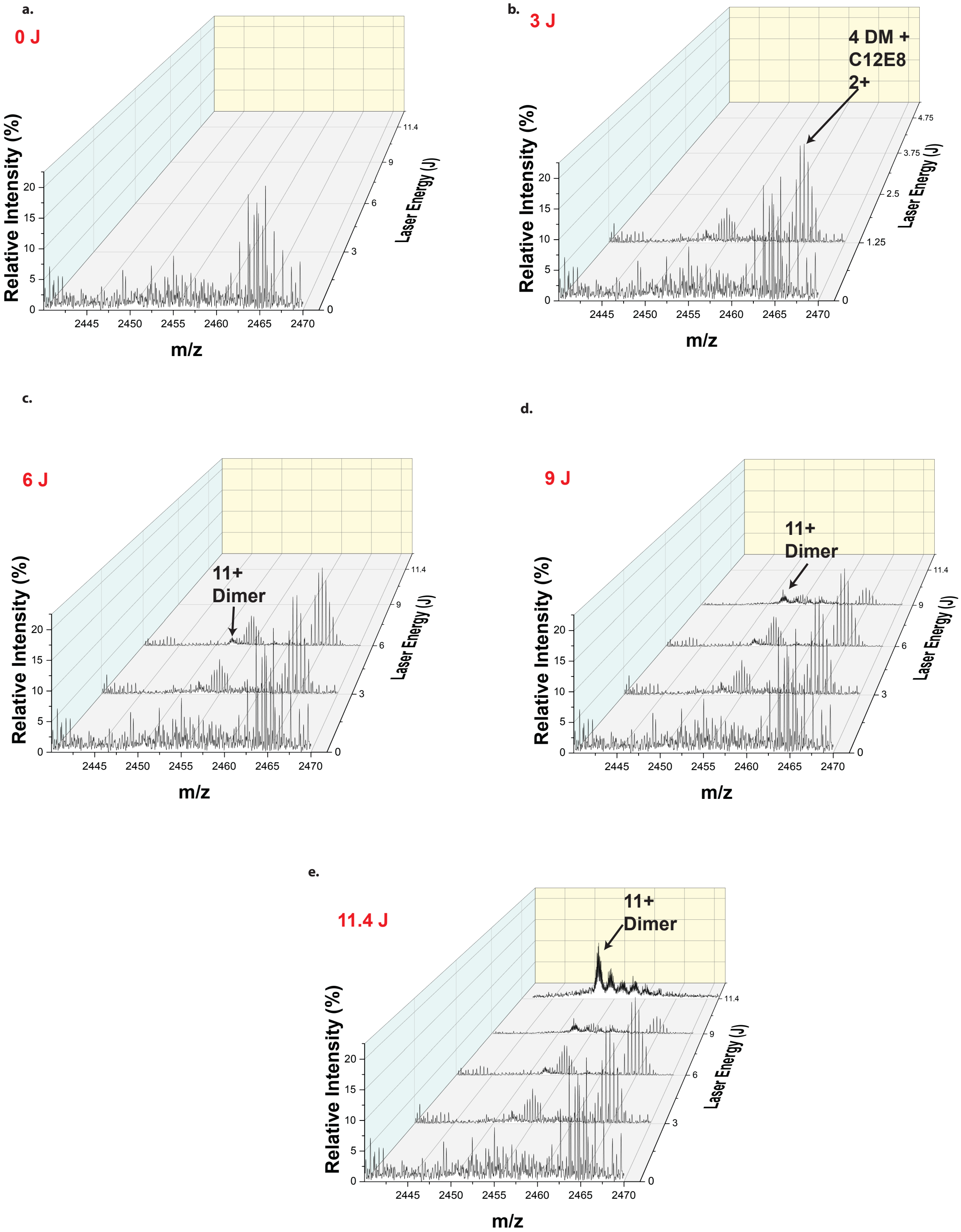

Figure III-13 A selected portion of the mass spectra obtained from GDX in micelles as infrared activation was applied. The 11+ dimer of GDX is liberated from the micelle as IR activation is applied.

a.

7+ Monomer with 11.4 J of IR activation **(46% Residues Cleavage)**

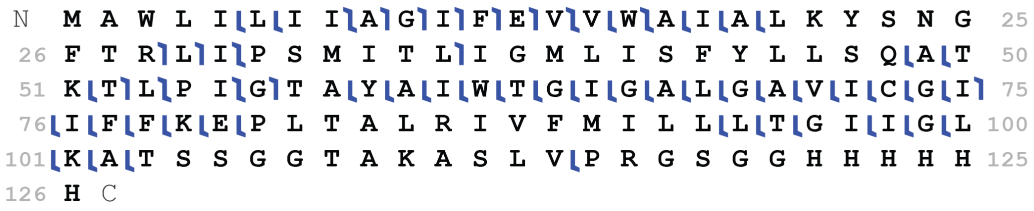

b. 7+ Monomer without IR activation (**62% Residues Cleavage)**

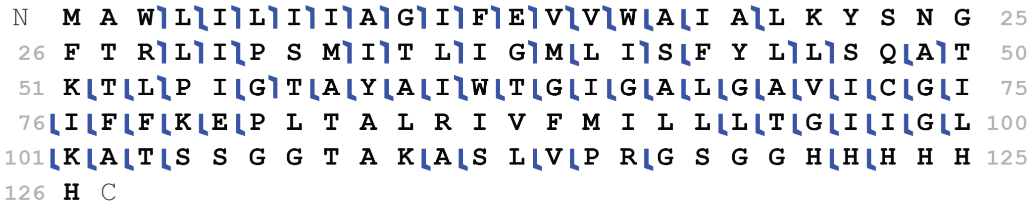

c. 6+ Monomer with 11.4 J of IR activation **(67% Residues Cleavage)**

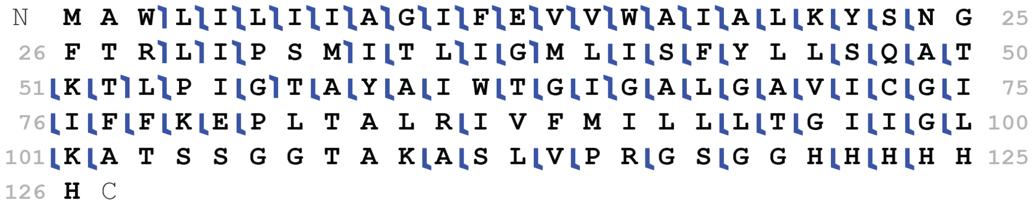

d.

6+ Monomer without IR activation **(46% Residues Cleavage)**

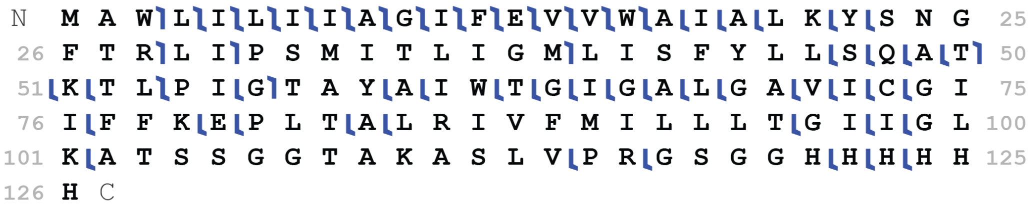

e. 11+ Monomer with 11.4 J of IR activation **(62% Residues Cleavage)**

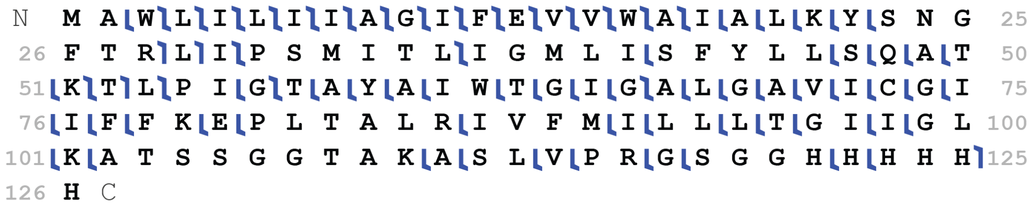

Figure III-14 Representative sequence coverage maps for GDX 7+ monomer with (a) and without (b) IR activation, as well as data for the 11+ dimer with IR activation (c).

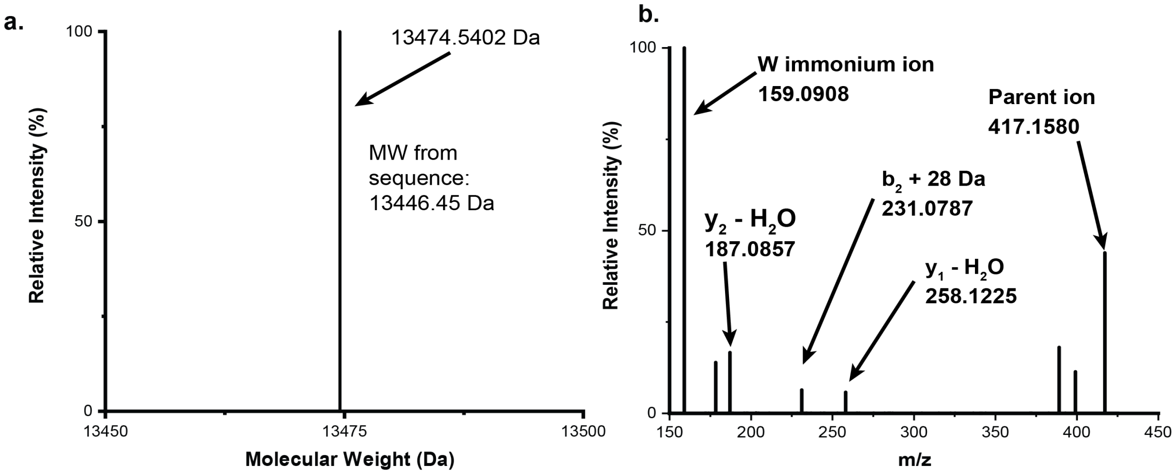

Figure III-15 The deconvoluted spectrum (a) of GDX that was produced by Xtract. The deconvoluted mass of GDX is 28 Da higher than the mass predicted from sequence (b). The fragmentation spectrum when b_3 was subjected to additional fragmentation in MS^3. The parent ion (b_3) produced a series of fragments including an immonium ion, b_2 and y_2 and y_1 with the loss of water. Only b_2 contained the 28 Da addition, therefore M1 is the most likely site of the modification.

Appendix IV Chapter 3 Supporting Information

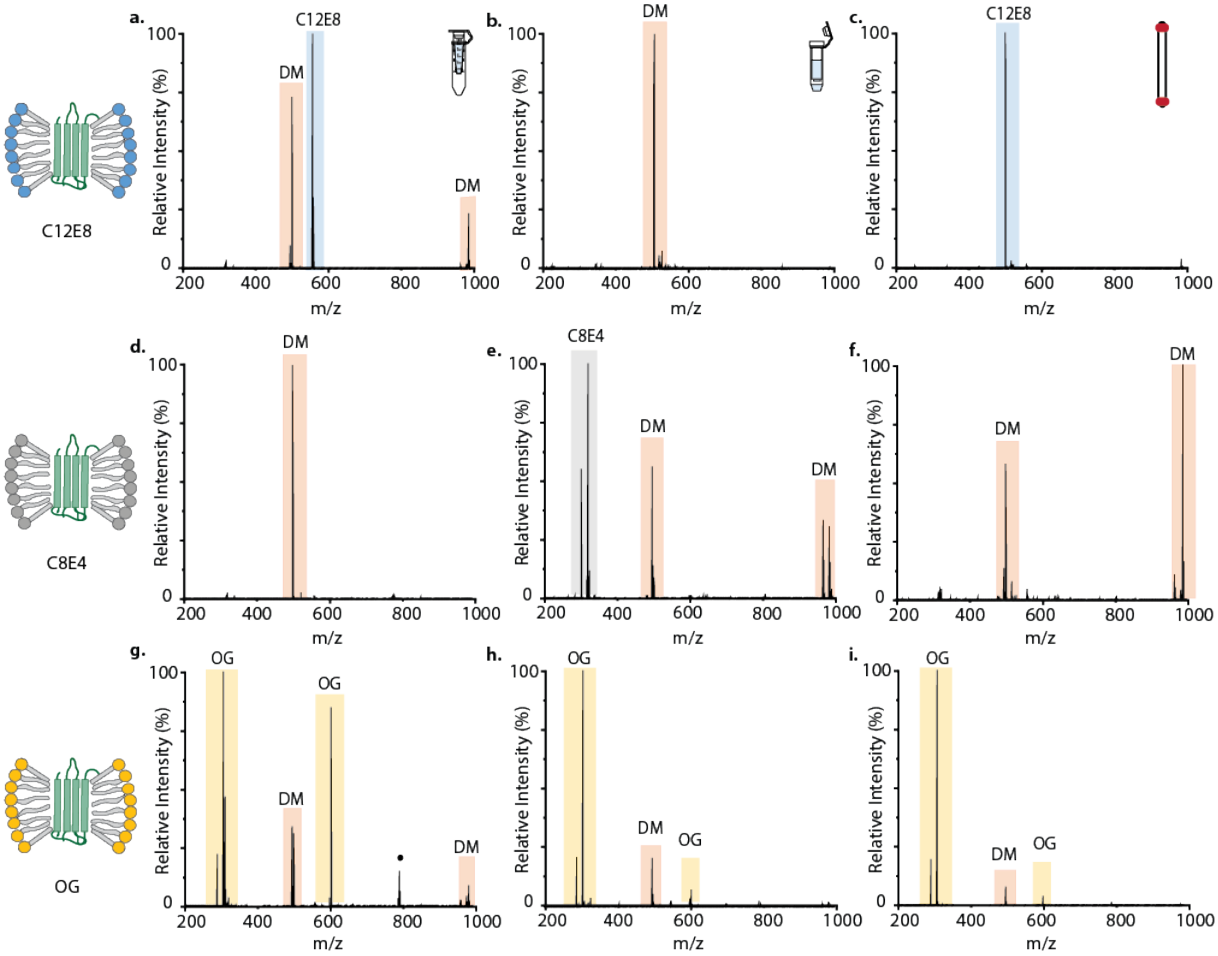

Figure IV-1 nMS spectra of PMP22 WT detergent exchanged from DM into (a-c) C12E8 (d-f) C8E4 and (g-i) OG by Amicon, BioSpin, and SEC methods each (left to right) at 0% HCD. DM signals are highlighted in orange. C12E8 signals are highlighted in blue and C8E4 signals are highlighted in grey, some signals are not apparent in some spectra due to their relative low abundance in comparison to DM signals. OG signals can be observed and are highlighted in yellow. Additional signals seen in the spectra annotated with a circle were found to be unrelated contaminant signals.

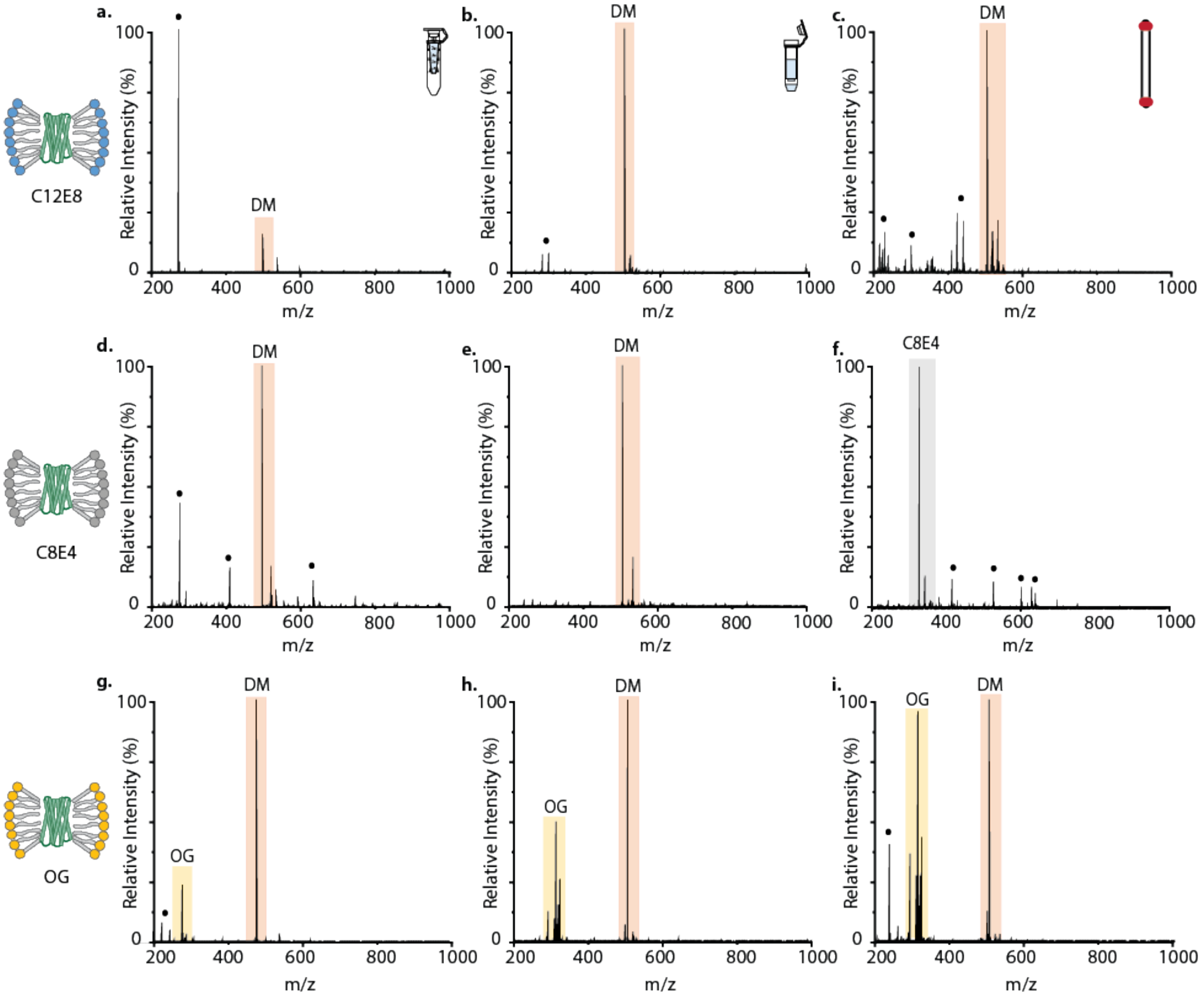

Figure IV-2 nMS spectra of GDX detergent exchanged from DM into (a-c) C12E8
(d-f) C8E4 and (g-i) OG by Amicon, BioSpin, and SEC methods each (left to right) at 30% HCD. DM signals are highlighted in orange. C12E8 signals are not apparent in the spectra due to their relative low abundance in comparison to DM signals. C8E4 signals are highlighted in grey. OG signals can be observed and are highlighted in yellow. Additional signals seen in the spectra annotated with a circle were found to be unrelated contaminant signals.

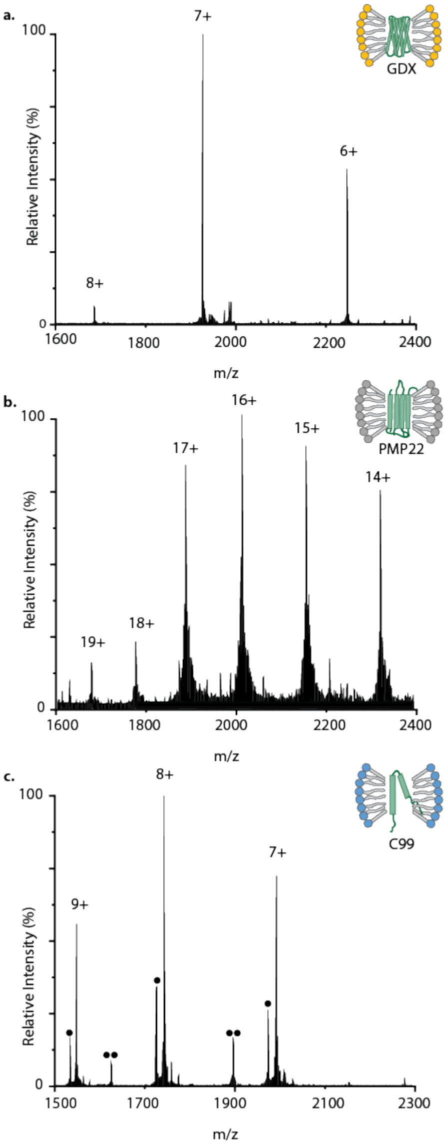

Figure IV-3 nMS spectra of intact MPs at 12.5% HCD to remove detergent molecules and dissociate micelles while keeping the protein relatively compact. (a) GDX 6+-8+ charge states following a detergent exchange into OG with the BioSpin method. (b) PMP WT 14+-18+ charge states following a detergent exchange into C8E4 with the BioSpin method. This version of PMP22 has additional soluble tags that make it larger than previously published constructs of PMP22. (c) C99 7+-9+ charge states following a detergent exchange into C12E8 with the BioSpin method. Additional peaks annotated with circles are of a truncated form of C99.

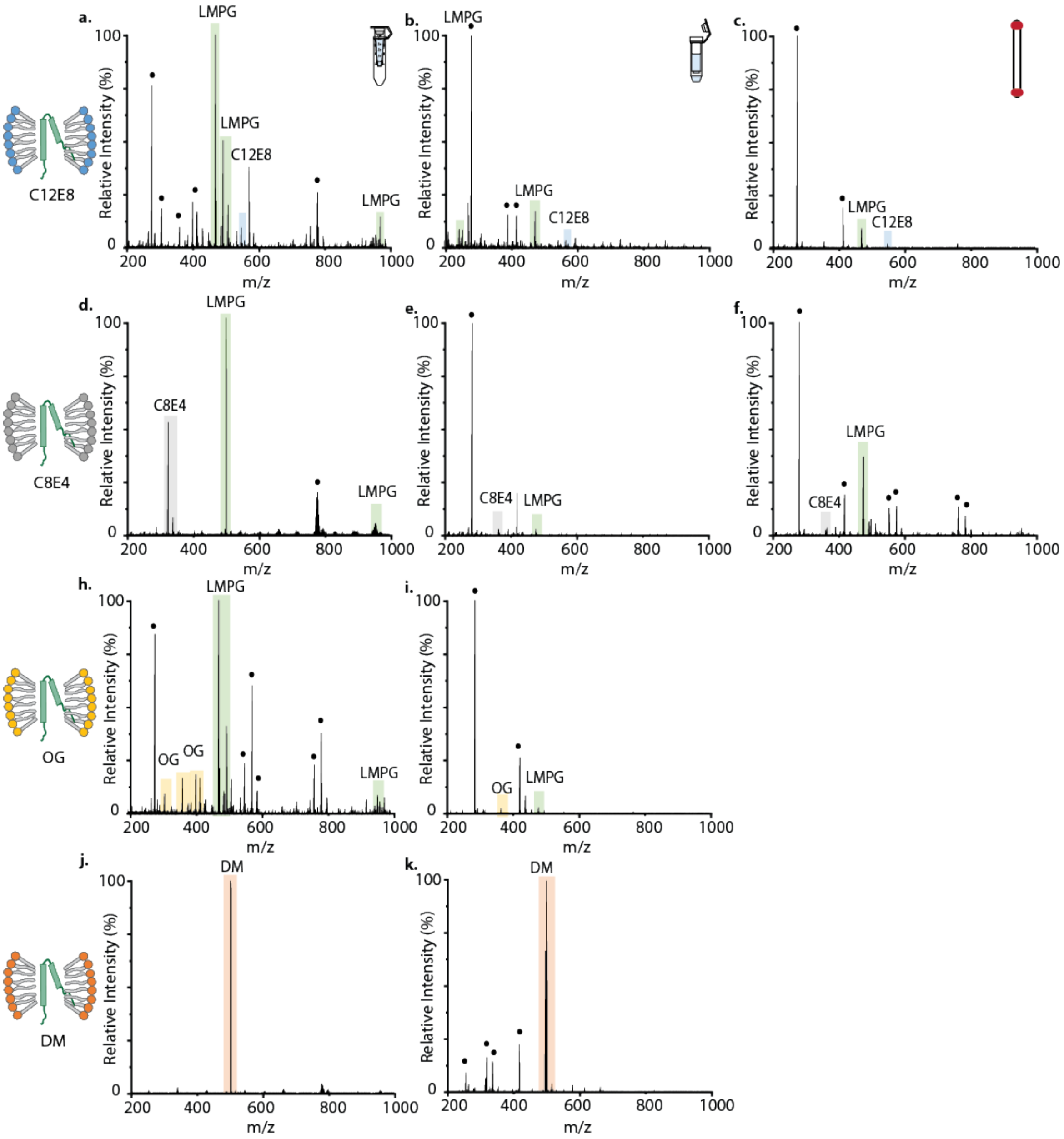

Figure IV-4 nMS spectra of C99 detergent exchanged from LMPG into (a-c) C12E8 (d-f) C8E4 by Amicon, BioSpin, and SEC methods each (left to right), (h-i) OG and (j-k) DM were exchanged by Amicon and BioSpin only (left to right) only. All measurements were obtained at 30% HCD. LMPG signals are highlighted in green. C12E8 signals are highlighted in blue. C8E4 signals are highlighted in gray. OG signals can be observed and are highlighted in yellow. DM signals are highlighted in orange. Additional signals seen in the spectra annotated with a circle were found to be unrelated contaminant signals. In some cases, the relative abundance of LMPG and secondary detergent were suppressed because of the high abundance of contaminants most likely attributed to the instrument.

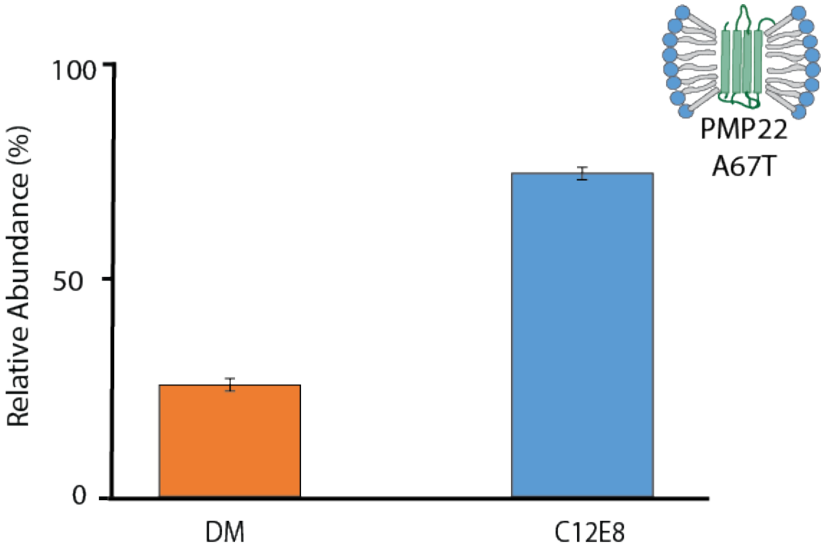

Figure IV-5 Bar graph of PMP22 A67T detergent exchanged from DM into 100X CMC C12E8 at 30% HCD by the Amicon ultracentrifugal filter method, we observed only 26% of DM remaining in the sample compared to 74% of C12E8. When compared to PMP22 WT exchanged from DM into 2X CMC C12E8 (Figure 3), we saw 100% DM remaining in the sample and no C12E8 signals detected, the 50X increase in CMC resulted in a significant increase in detergent exchange.

Table IV-1 Representative Intensities of Empty Detergent Clusters Acquired at HCD 0 at equivalent concentrations.

Detergent	**Intensity**
LMPG	$1.2*10^{8}$ +/- $0.3*10^{8}$
OG	$3.7*10^{8}$ +/- $4*10^{8}$
DM	$3.4*10^{7}$ +/- $0.3*10^{7}$
C12E8	$3.7*10^{7}$ +/- $4.2*10^{7}$
C8E4	$1.1*10^{7}$ +/- $0.1*10^{7}$

Table IV-2 Unknown contaminants seen consistently throughout many samples regardless of the detergents used, these signals could not be confidently identified but are most likely associated with experiments from previous users on the Orbitrap Fusion Lumos (ThermoFisher, San Jose, CA).

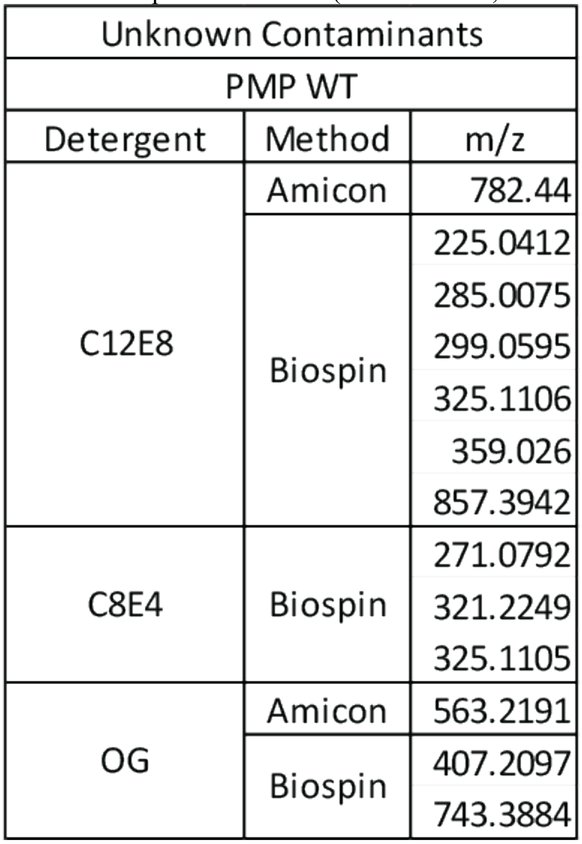

Unknown Contaminants		
PMP WT		
Detergent	Method	m/z
C12E8	Amicon	782.44
	Biospin	225.0412
		285.0075
		299.0595
		325.1106
		359.026
		857.3942
C8E4	Biospin	271.0792
		321.2249
		325.1105
OG	Amicon	563.2191
	Biospin	407.2097
		743.3884

Appendix V Chapter 4 Supporting Information

Table V-1 Protein Standards Used in This Work

Protein	**Product Number**	**Molecular Weight (kDa)**
SiLu Lite SigmaMAb Standard antibody	MSQC4	150
Bovine Serum Albumin	A2153	66.5
Streptavidin from *Streptomyces Avidinii*	S0677	52.8
Myoglobin from equine heart	M1182	17.6
Ubiquitin from bovine erythrocytes	U6253	8.6

Table V-2 Optimized Instrument Parameters for Native Conditions

Region	**Setting Name**	**Default**	**Native Ubiquitin**	**Native Myoglobin, Streptavidin, BSA**
Source	Sample Infusion Rate (µL/min)	n/a	2-5	2-5
	Gas Temp (deg. C)	325	140	140
	Drying Gas (L/min)	5	5	5
	Nebulizer Pressure (psi)	20	35	20
	Sheath Gas Temp (deg. C)	275	140	140
	Sheath Gas Flow (L/min)	10	8	11
	VCap, Capillary Voltage (V)	4000	3000	2500-3000
	Nozzle Voltage (V)	2000	2000	2000
	Fragmentor (V)	400	400	400
Pressures	High Pressure Funnel (Torr)	4.00	4.80	4.80
	Trapping Funnel (Torr)	3.80	3.80	3.80
	Drift Tube (Torr)	3.95	3.95	3.95
Acquisition	Max Drift Time (ms)	n/a	90	90
	Trap Fill Time (µs)	20000	80000	80000
	Trap Release Time (µs)	150	1000	1000
Advanced Parameters	In-Source CE (V)	20	10 - 200	10 - 450
	High Pressure Funnel Delta (V)	150	50	150
	High Pressure Funnel Radio Frequency (Vpp)	150	50	150
	Trapping Funnel Delta (V)	180	160	164
	Trapping Funnel Radio Frequency (Vpp)	150	180	150

Table V-3 CIUSuite2 Data Processing Parameters

		Ubiquitin +6	**Myoglobin +8**	**Streptavidin +11**	**BSA +16**	**SigmaMAb**
Data Import	**Smoothing** **Savitzky-Golay**	Window: 5; Iteration: 1 (Default)	Window: 5; Iteration: 1 (Default)	Window: 5; Iteration: 1 (Default)	Window: 5; Iteration: 1 (Default)	Window: 7 Iteration: 1
	Crop	10-200 V 10-20 nm^2	10-240 V 15-35 nm^2	100-440 V 30-50 nm^2	10-410 V 40-70 nm^2	10-410 V 70-140 nm^2
	Plot Options	Default	Default	Default	Default	Default
Feature Fitting	**Mode**	Standard (Default)	Standard (Default)	Standard (Default)	Standard (Default)	Standard (Default)
	Minimum Feature Length [x-axis] (Data Points)	5 (Default)	2	4	2	4-6
	Feature Width [y-axis] Allowed (nm^2)	1	1	1	1.5	2-4
	Max CV Gap	0 (Default)	0 (Default)	0 (Default)	0 (Default)	0 (Default)
CIU50 Fitting	**Mode**	Standard (Default)	Standard (Default)	Standard (Default)	Standard (Default)	Standard (Default)
	Trans. Region Padding	15 (Default)	15 (Default)	15 (Default)	15 (Default)	15 (Default)
	Max CV Gap	0 (Default)	0 (Default)	0 (Default)	0 (Default)	0 (Default)

Table V-4 Inter-Laboratory RMSD Values for Ubiquitin, Myoglobin, Streptavidin, and BSA

Ion	CIU Reproducibility RMSD (%)			
	UM	TAMU	VU	Interlaboratory
Ubiquitin +6	3.8 ± 1.4	2.5 ± 0.6	1.9 ± 0.4	18 ± 2
Myoglobin +8	3.7 ± 0.6	2.9 ± 0.5	1.9 ± 0.2	37 ± 11
Streptavidin +11	1.0 ± 0.1	2.3 ± 0.4	4.4 ± 0.4	20 ± 6
BSA +16	2.2 ± 0.3	2.6 ± 0.3	3.0 ± 0.3	18 ± 4

Table V-5 $^{DT}CCS_{N2}$ Values from this study, and referenced literature

		$^{DT}CCS_{N2}$ values reported for each protein ($Å^2$) [a.]						
		[1]*2018 May et al.*	[2]*2020 Stiving et al.*[b.]	[3]*2020 Zheng et al.*	[4]*2020 Gadkari et al.*[c.]	*Lit. Avg.*	*This work* [d.]	*% Bias* [e.]
Ubiquitin (+6)	F1	1220±10 (3)	--	1210±10 (3)	1190±10 (3)	1210 (3)	1220±10 (4), 0.9%	*0.5%*
	F2	1470±20 (4)	--	--	1350±10 (3)	1410 (2)	1430±40 (4), 2.6%	*1.5%*
	F3	1630±10 (5)	--	--	1470±10 (3)	1550 (2)	1660±10 (3), 0.7%	*6.5%*
	F4	--	1730±10 (3)	--	--	1730 (1)	1730±10 (2), 0.3%	*0.0%*
Myoglobin (+8)	F1	1940±30 (5)	--	--	--	1940 (1)	1970±10 (4), 0.5%	1.6%
	F2	--	--	--	--	--	2110±50 (3), 2.4%	--
	F3	--	--	--	--	--	2730±30 (4), 1.0%	--
Streptavidin (+11)	F1	--	3760±40 (3)	--	--	3760 (1)	3680±10 (4), 0.2%	2.1%
	F2	--	--	--	--	--	3520±10 (3), 0.3%	--
	F3	--	--	--	--	--	4350±20 (4), 0.4%	--
BSA (+16)	F1	--	4510±40 (3)	--	4530±20 (3)	4520 (2)	4520±50 (4), 1.2%	0.0%
	F2	--	--	--	--	--	5360±40 (3), 0.7%	--
	F3	--	--	--	--	--	5760±40 (4), 0.7%	--
	F4	--	--	--	--	--	6150±70 (4), 1.1%	--
	F5	--	--	--	--	--	6410±60 (4), 0.9%	--
IgG1 (+26)	F1	--	--	--	--	--	7980±300 (4), 3.2%	--
	F2	--	--	--	--	--	9000±90 (2), 0.9%	--
	F3	--	--	--	--	--	10000±200 (4), 2.4%	--
	F4	--	--	--	--	--	10410±80 (4), 0.8%	--
	F5	--	--	--	--	--	10700±200 (3), 1.8%	--

a. Number of measurements are indicated in the parenthesis. Percent RSDs, when reported, are converted to standard deviations in $Å^2$.

b. The CCS values reported for ammonium acetate solution are used for ubiquitin, and BSA, and the value measured in TEAA solution is used for streptavidin. For ubiquitin, only one CCS value is reported for the +6 charge state and it is assumed this is the fully-extended conformer. The streptavidin +11 and BSA +16 values are assumed to be the lowest-energy states. CCS measurements were obtained with nano-ESI on a traveling wave ion mobility-mass spectrometer.

c. The CCS values for ubiquitin are assumed to correspond to F1, F2, and F3 in this study. CCS measurements were obtained with nano-ESI.

d. The interlaboratory relative standard deviations are also provided at the end of each entry. In some cases, not all features were observed across all laboratories/hardware configurations.

e. The percent bias is referenced against the CCS values obtained in this study.

Table V-6 Production-grade Source RMSD, Feature and CIU50 Reproducibility of BSA

<table>
<tr><th colspan="2">Production Prototype RMSD Analysis</th></tr>
<tr><th>Source Assembly</th><th>RMSD (%)</th></tr>
<tr><td>Production Prototype 1 (PP1)</td><td>2.4 ± 0.1</td></tr>
<tr><td>Production Prototype 2 (PP2)</td><td>2.3 ± 0.1</td></tr>
<tr><td>Production Prototype 3 (PP3)</td><td>2.6 ± 0.1</td></tr>
<tr><td>Inter-Hardware Reproducibility</td><td>5 ± 1</td></tr>
<tr><th colspan="2">Average Feature $^{DT}CCS_{N2}$ Measurements Across Production Prototype Assemblies
3 Replicates: 3 Averaged CIU Fingerprints from PP1, PP2, PP3; R.S.D. in parentheses</th></tr>
<tr><th>Feature #</th><th>Average $^{DT}CCS_{N2}$ (nm^2)</th></tr>
<tr><td>Feature 1</td><td>45.09 ± 0.02 (0.04%)</td></tr>
<tr><td>Feature 2</td><td>53.8 ± 0.1 (0.2%)</td></tr>
<tr><td>Feature 3</td><td>57.7 ± 0.1 (0.2%)</td></tr>
<tr><td>Feature 4</td><td>61.6 ± 0.2 (0.3%)</td></tr>
<tr><td>Feature 5</td><td>64.6 ± 0.2 (0.3%)</td></tr>
<tr><th colspan="2">Average CIU50 Measurements Across Production Prototype Assemblies
3 Replicates: 3 Averaged CIU Fingerprints from PP1, PP2, PP3; R.S.D. in parentheses</th></tr>
<tr><th>Transition #</th><th>Average CIU50 (V)</th></tr>
<tr><td>CIU50-1</td><td>174 ± 5 (3%)</td></tr>
<tr><td>CIU50-2</td><td>200.0 ± 0.4 (0.2%)</td></tr>
<tr><td>CIU50-3</td><td>251 ± 7 (3%)</td></tr>
<tr><td>CIU50-4</td><td>348 ± 3 (1%)</td></tr>
</table>

Table V-7 Production Production-grade Source RMSD, Feature and CIU50 Reproducibility of SigmaMAb

Production Prototype RMSD Analysis					
Source Assembly	**RMSD (%)**				
	+26	**+27**	**+28**	**+29**	**+30**
Production Prototype 1 (PP1)	4.70 ± 0.30	2.22 ± 0.02	1.92 ± 0.09	2.20 ± 0.10	3.10 ± 0.30
Production Prototype 2 (PP2)	4.60 ± 0.10	2.80 ± 0.10	1.80 ± 0.20	2.00 ± 0.20	3.40 ± 0.40
Production Prototype 3 (PP3)	5.00 ± 0.40	2.70 ± 0.10	1.87 ± 0.09	2.20 ± 0.10	3.20 ± 0.10
Inter-Hardware Reproducibility	4.40 ± 0.50	3.30 ± 0.70	2.60 ± 0.90	2.70 ± 0.40	3.50 ± 0.60
Average Feature $^{DT}CCS_{N2}$ Measurements Across Production Prototype Assemblies 3 Replicates: 3 Averaged CIU Fingerprints from PP1, PP2, PP3; R.S.D. in parentheses					
Feature #	**Average $^{DT}CCS_{N2}$ (nm^2)**				
	+26	**+27**	**+28**	**+29**	**+30**
Feature 1	81.90 ± 0.40 (0.5%)	83.60 ± 0.40 (0.5%)	85.17 ± 0.04 (0.05%)	87.23 ± 0.02 (0.05%)	90.29 ± 0.04 (0.04%)
Feature 2	97.60 ± 0.40 (0.4%)	110.20 ± 0.40 (0.4%)	111.91 ± 0.01 (0.01%)	116.83 ± 0.01 (0.01%)	119.60 ± 0.50 (0.4%)
Feature 3	107.00 ± 0.40 (0.4%)		115.47 ± 0.01 (0.01%)		126.90 ± 0.50 (0.4%)
Average CIU50 Measurements Across Production Prototype Assemblies 3 Replicates: 3 Averaged CIU Fingerprints from PP1, PP2, PP3; R.S.D. in parentheses					
Transition #	**Average CIU50 (V)**				
	+26	**+27**	**+28**	**+29**	**+30**
CIU50-1	201.6 ± 0.6 (0.3%)	211 ± 4 (2%)	203 ± 3 (1%)	200 ± 3 (2%)	191 ± 3 (2%)
CIU50-2	260 ± 8 (3%)		335 ± 3 (1%)		373 ± 4 (1%)

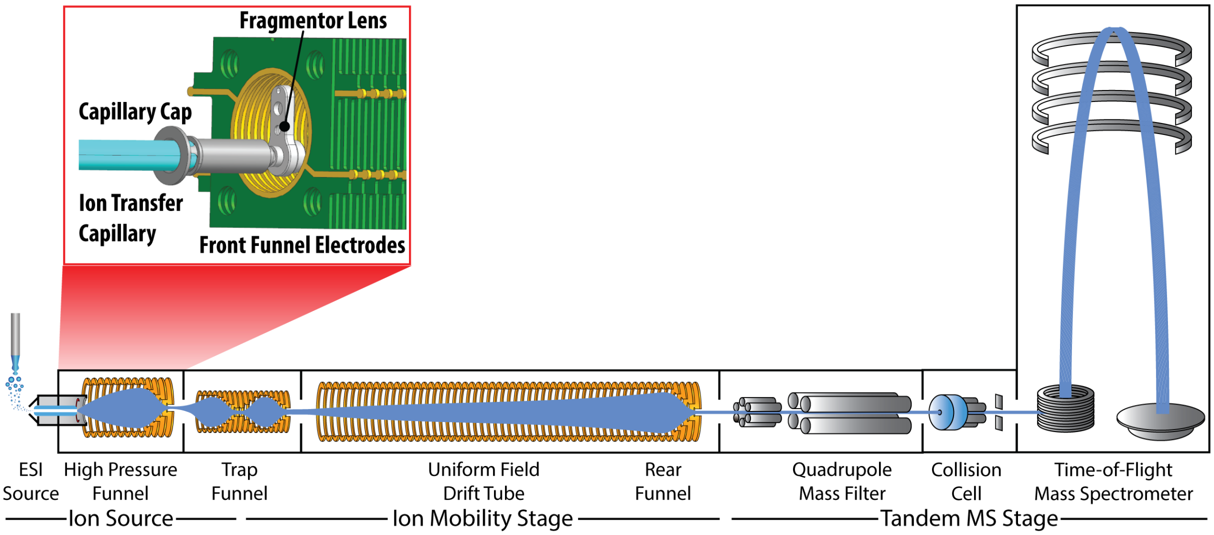

Figure V-1 Full instrument diagram of the Modified Agilent 6560 DTIM-MS, now commercially referred to as the Agilent 6560C (diagram adapted from[4]). The capillary/high pressure funnel (4.8 torr) is modified to enable high-energy in-source activation of biomolecules for collision induced unfolding (CIU), as described in detail in the main text. After ion activation, the ions are accumulated in the trap funnel (3.80 torr) for a fixed amount of time (Trap Fill Time), and then released into the drift tube for mobility separation. The drift tube is operated at ambient temperature, 3.95 torr, and with an electric field of ~18 V/cm. After mobility separation, ions traverse the tandem MS stage of the instrument where they can be isolated by the quadrupole mass filter, further activated in the collision cell, and/or detected by the time-of-flight mass spectrometer. The firmware of this instrument is upgraded to extend the mass range of the time-of-flight mass spectrometer to 20,000 m/z.

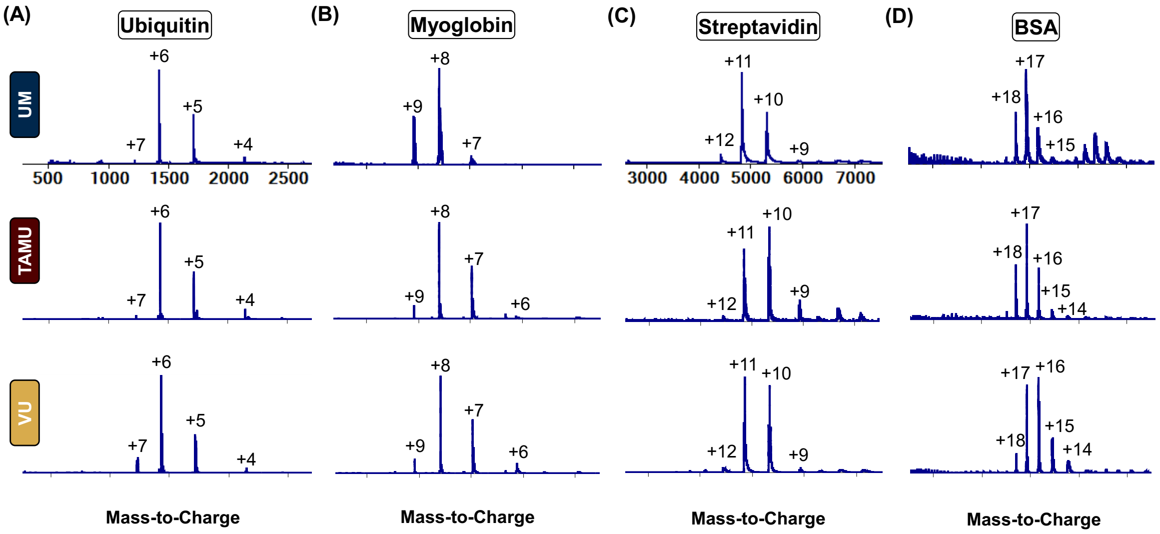

Figure V-2 Native Mass Spectra of (A) Ubiquitin, (B) Myoglobin, (C) Streptavidin, and (D) Bovine Serum Albumin.

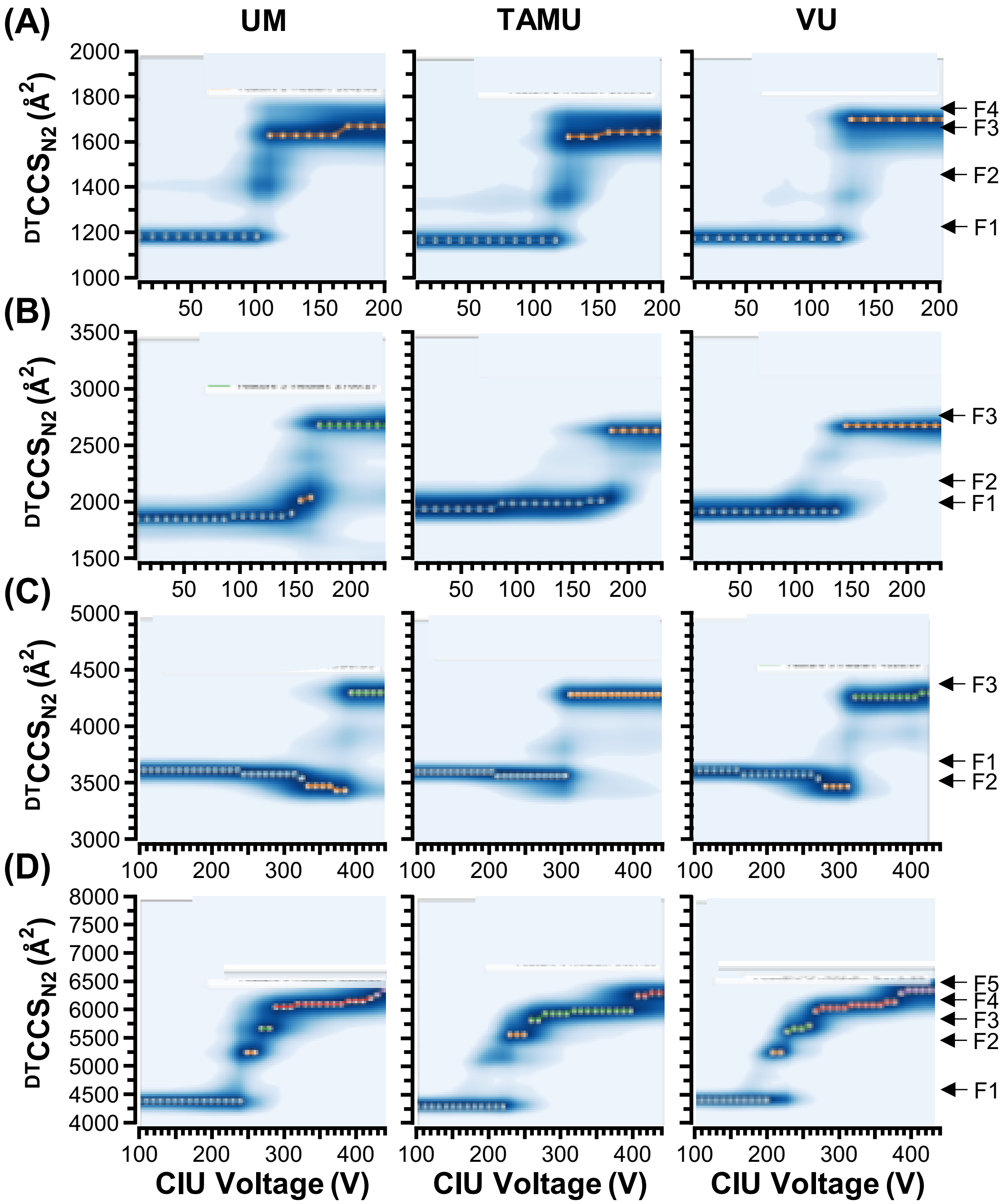

Figure V-3 CIU feature maps. Here, the average map generated from three replicate runs is used for feature annotation, with "significant features" (F1, F2, etc.) determined using specific constraints for the CIU step size and allowable CCS tolerance. These are (A) ubiquitin (+6), 5 steps minimum, 1 nm^2 width tolerance; (B) myoglobin (+8), 2 steps, 1 nm^2; (C) streptavidin (+11), 4 steps 1 nm^2; (D) BSA (+16), 2 steps, 1.5 nm^2.

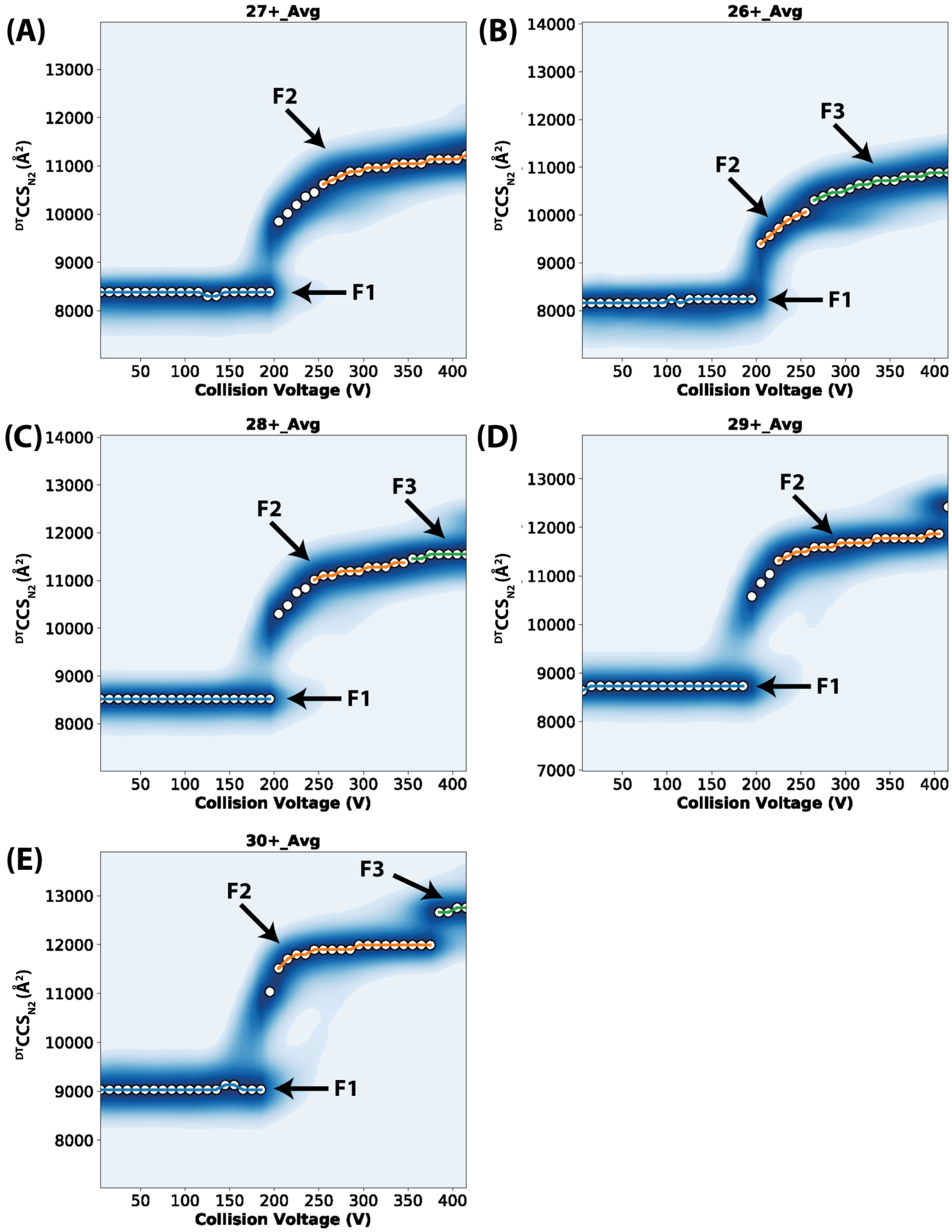

Figure V-4 CIU feature Plots of SigmaMAb. The average CIU fingerprint generated from three replicate runs is used for feature annotation, with "significant features" (F1, F2, etc.) determined using specific constraints for the CIU step size and allowable CCS tolerance. These are **(A)** 26+, 6 steps minimum, 3.5 nm^2 width tolerance; **(B)** 27+, 6 steps minimum, 3.5 nm^2 width tolerance; **(C)** 28+, 4 steps minimum, 2 nm^2 width tolerance; **(D)** 29+, 4 steps minimum, 2 nm^2 width tolerance; **(E)** 30+, 4 steps minimum, 2 nm^2 width tolerance.

V.1 References

(1) May, J. C.; Jurneczko, E.; Stow, S. M.; Kratochvil, I.; Kalkhof, S.; McLean, J. A. Conformational Landscapes of Ubiquitin, Cytochrome c, and Myoglobin: Uniform Field

Ion Mobility Measurements in Helium and Nitrogen Drift Gas. *International Journal of Mass Spectrometry* **2018**, *427*, 79–90. https://doi.org/10.1016/j.ijms.2017.09.014.

(2) Stiving, A. Q.; Vanaernum, Z. L.; Busch, F.; Harvey, S. R.; Sarni, S. H.; Wysocki, V. H. Surface-Induced Dissociation: An Effective Method for Characterization of Protein Quaternary Structure. *Anal. Chem*. American Chemical Society January 2, 2019, pp 190–209. https://doi.org/10.1021/acs.analchem.8b05071.

(3) Zheng, X.; Kurulugama, R. T.; Laganowsky, A.; Russell, D. H. Collision-Induced Unfolding Studies of Proteins and Protein Complexes Using Drift Tube Ion Mobility-Mass Spectrometer. *Anal. Chem.***2020**, *92* (10), 7218–7225. https://doi.org/10.1021/acs.analchem.0c00772.

(4) Gadkari, V. v.; Ramírez, C. R.; Vallejo, D. D.; Kurulugama, R. T.; Fjeldsted, J. C.; Ruotolo, B. T. Enhanced Collision Induced Unfolding and Electron Capture Dissociation of Native-like Protein Ions. *Anal. Chem.* **2020**, *92* (23), 15489–15496. https://doi.org/10.1021/acs.analchem.0c03372.

Appendix VI Chapter 5 Supporting Information

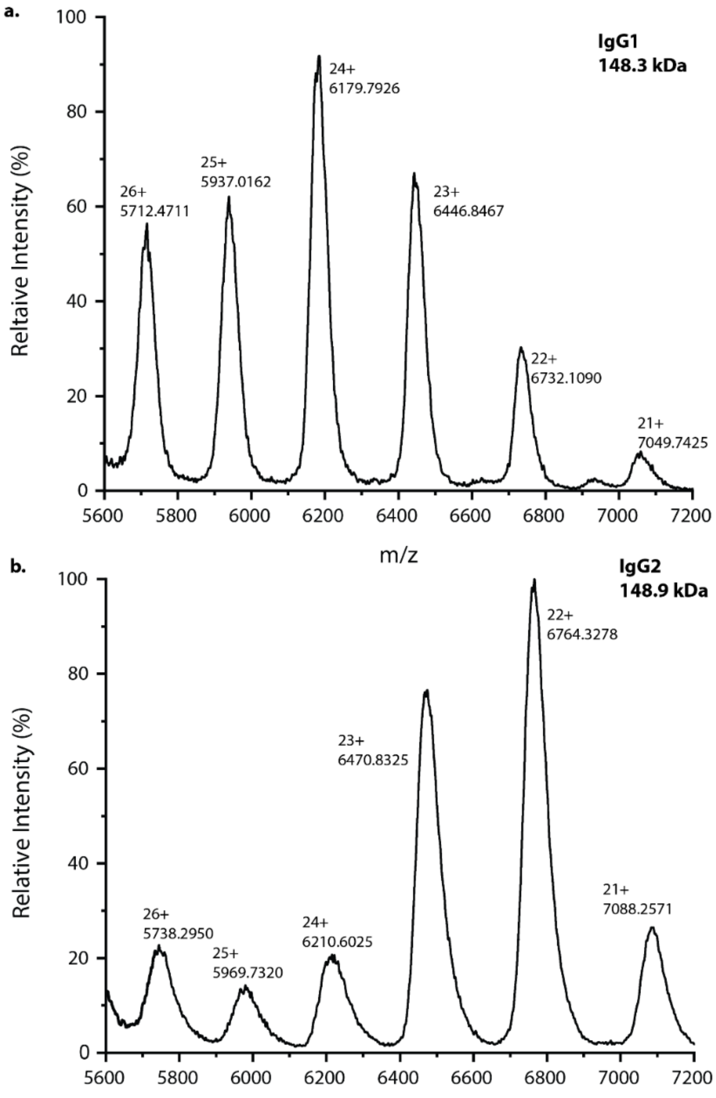

Figure VI-1 Mass spectra of IgG1 (a) and IgG2 (b) collected in ammonium acetate on the G2.

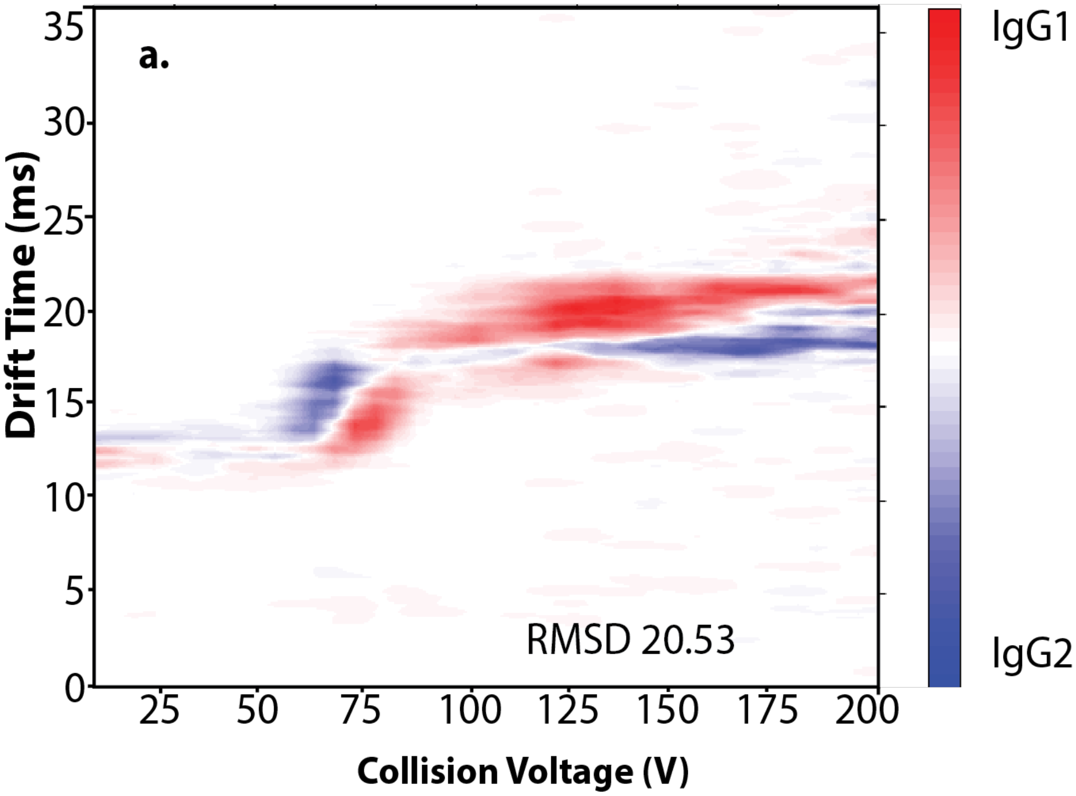

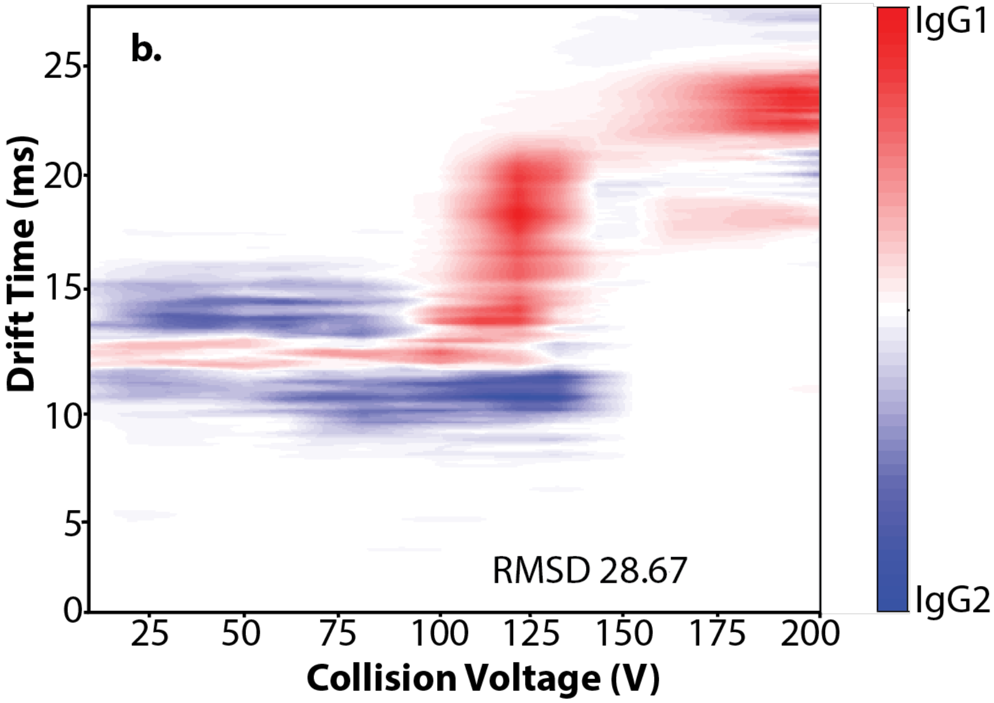

Figure VI-2 Difference plots comparing the 23+ CIU fingerprints of IgG1 and IgG2 on the G2 (a) and cIM (b).

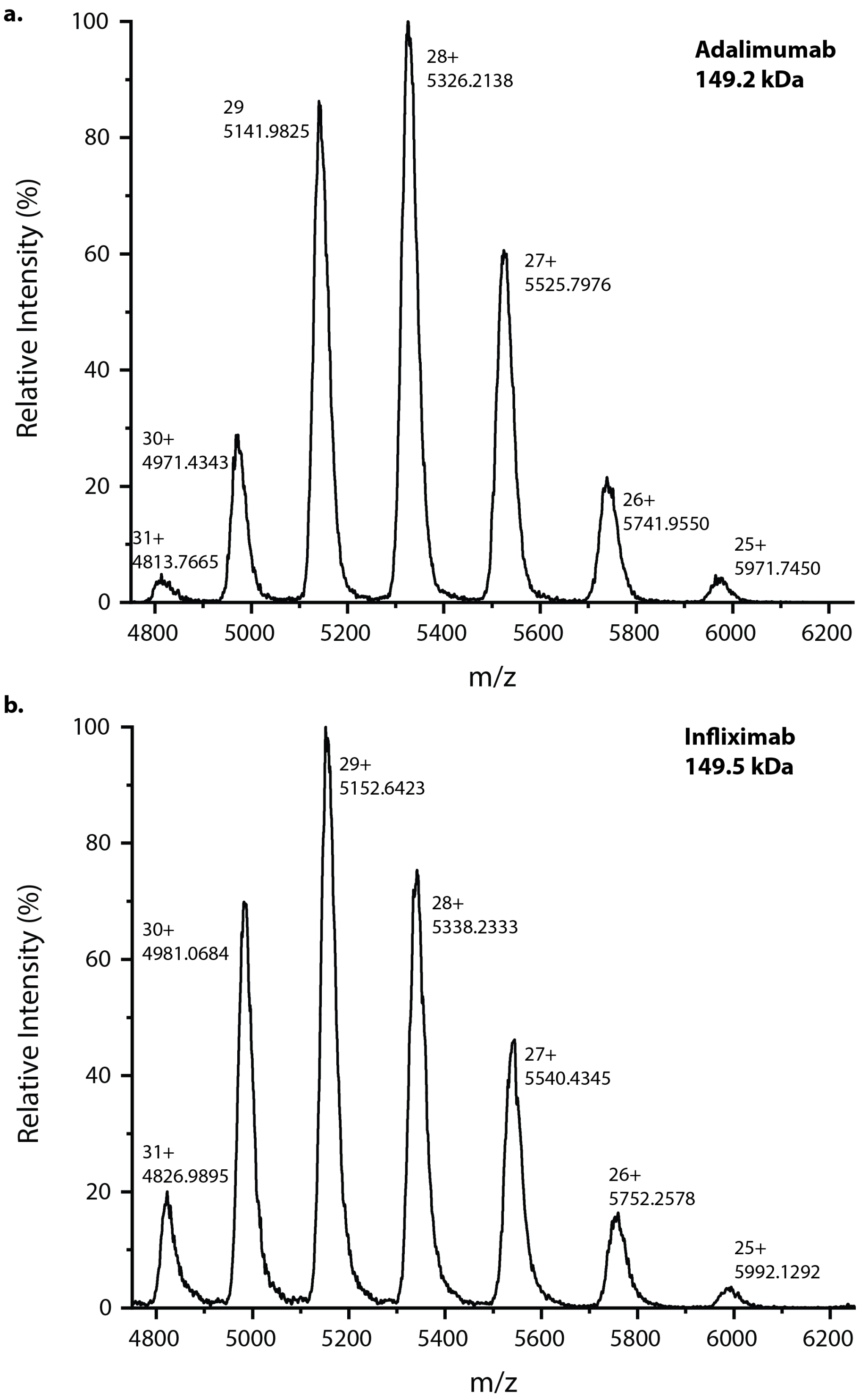

Figure VI-3 Mass spectra of Adalimumab (a) and Infliximab (b) collected on the cIM in ammonium acetate.

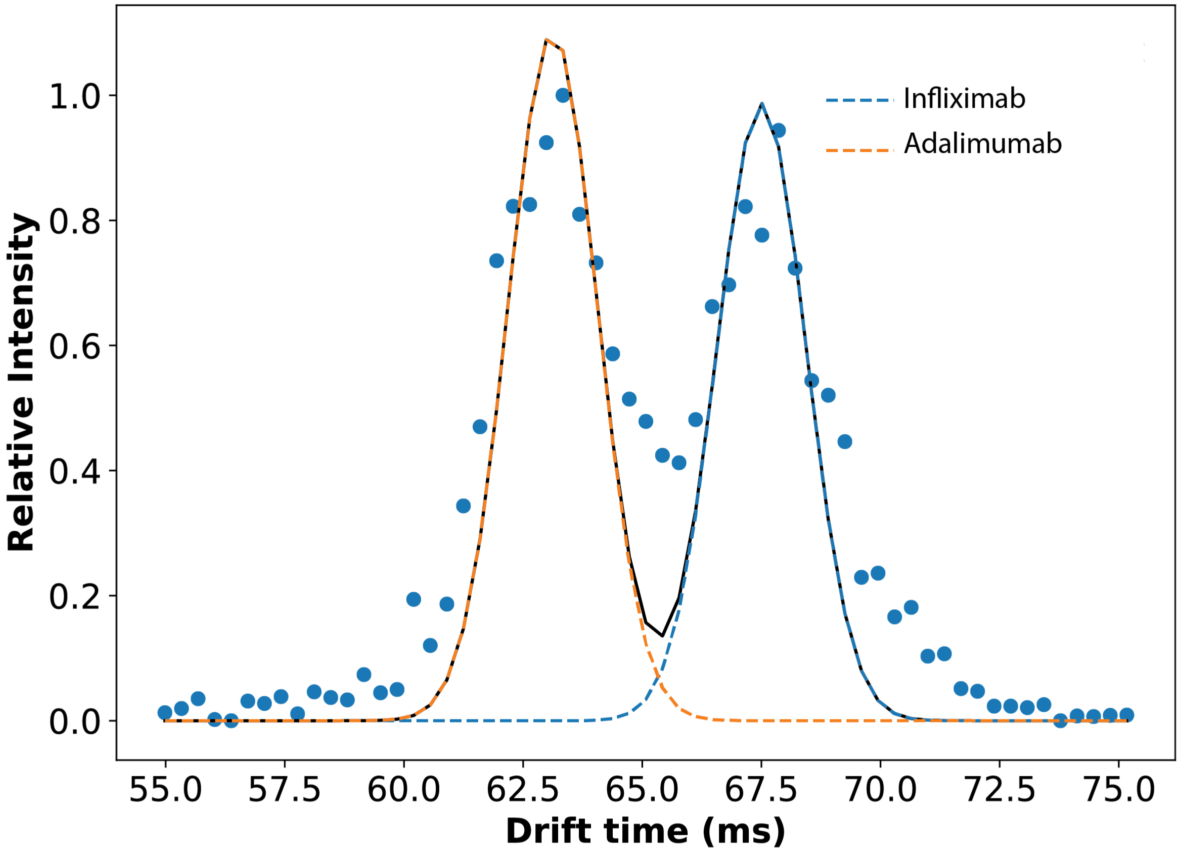

Figure VI-4 Plot highlighting the differences in drift time exhibited by Infliximab and Adalimumab with 120 V of activation in the trap at relative concentrations of 66% Adalimumab and 33 % Infliximab in serum.

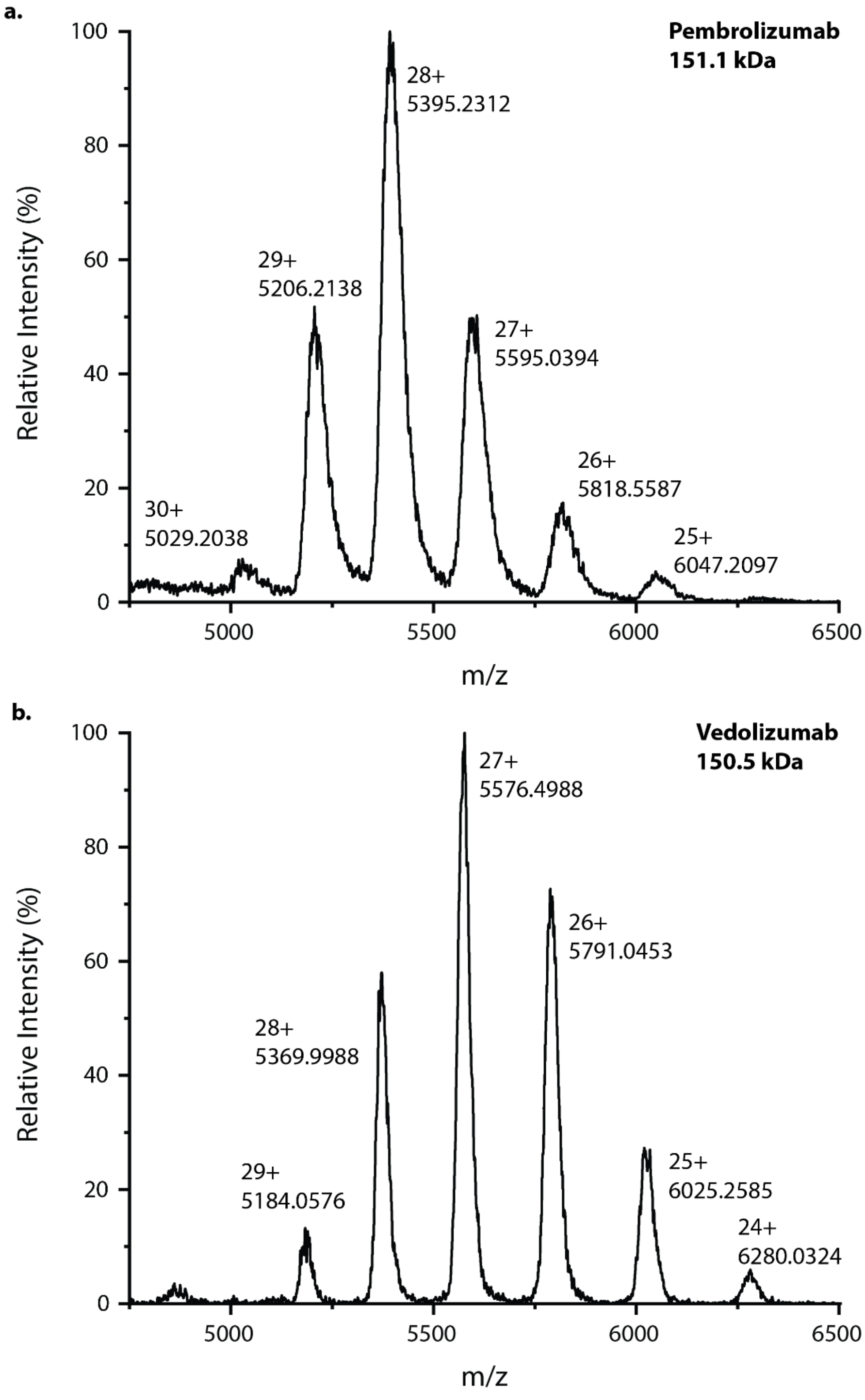

Figure VI-5 Mass spectra of Pembrolizumab (a) and Vedolizumab (b) collected on the cIM in ammonium acetate.

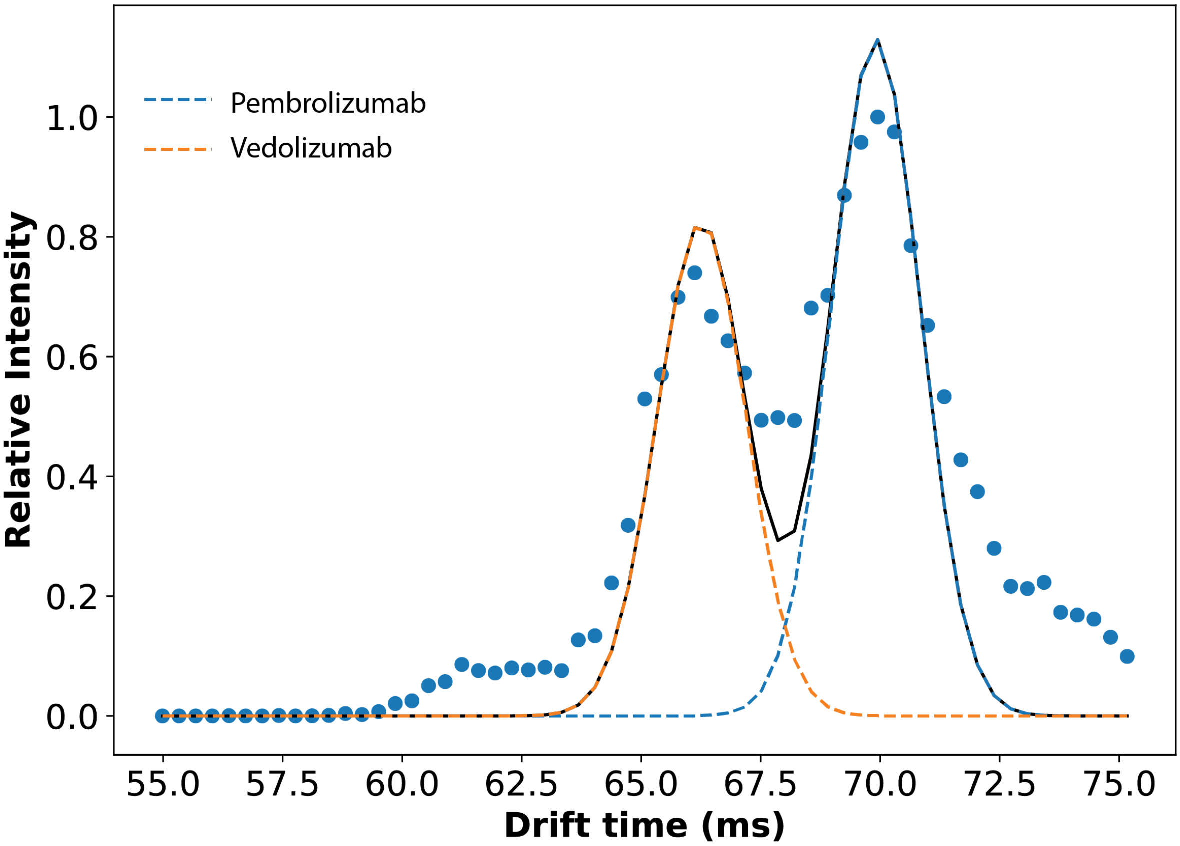

Figure VI-6 Plot highlighting the differences in drift time exhibited by Pembrolizumab and Infliximab with 180 V of activation in the trap at equimolar concentrations in 200 mM ammonium acetate.

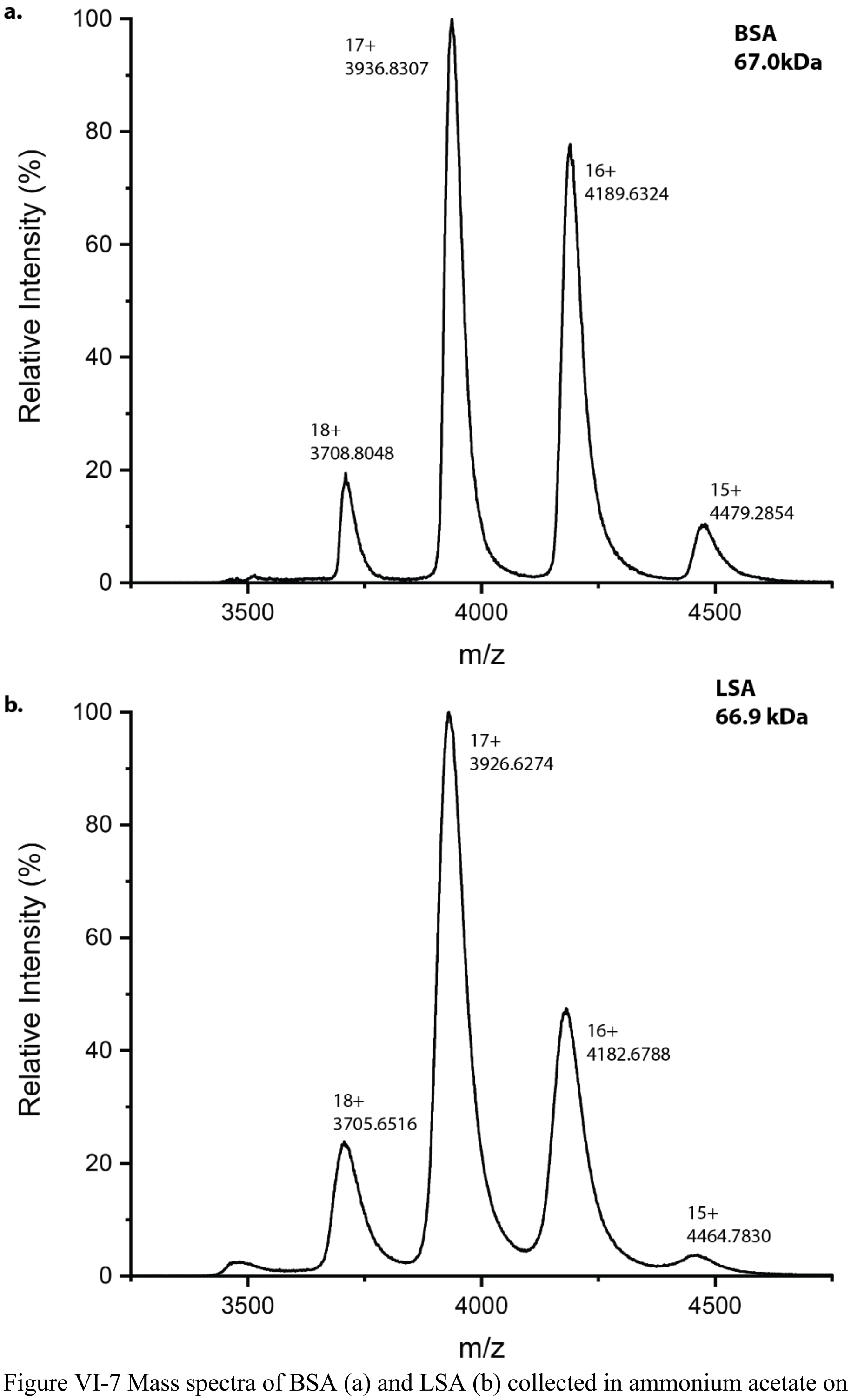

Figure VI-7 Mass spectra of BSA (a) and LSA (b) collected in ammonium acetate on the G2.

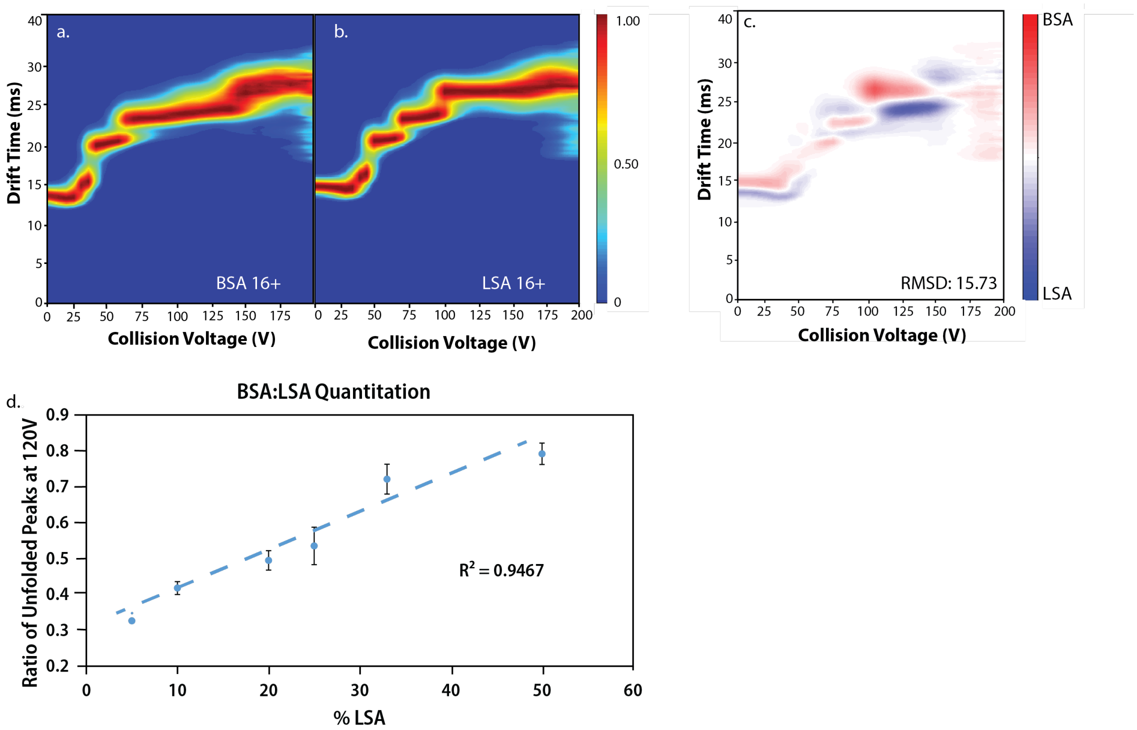

Figure VI-8 CIU fingerprints of the 16+ charge states of BSA (a) and LSA (b), and a difference plot comparing these two fingerprints (c). A linear calibration curve that was generated for BSA and LSA in ammonium acetate using Quantitative CIU (d).

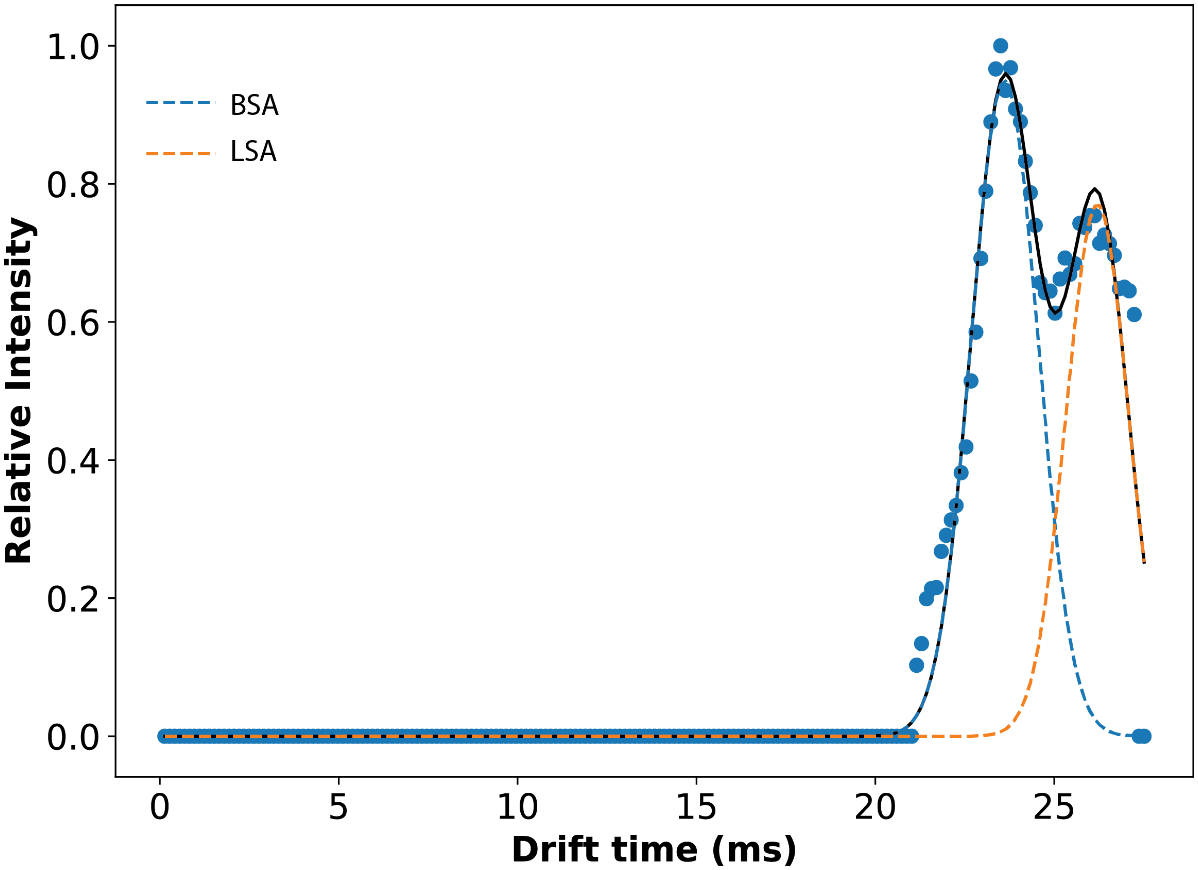

Figure VI-9 Plot highlighting the differences in drift time exhibited by BSA and LSA with 120 V of activation in the trap at equimolar concentrations in 100 mM ammonium acetate.

Appendix VII Chapter 6 Supporting Information

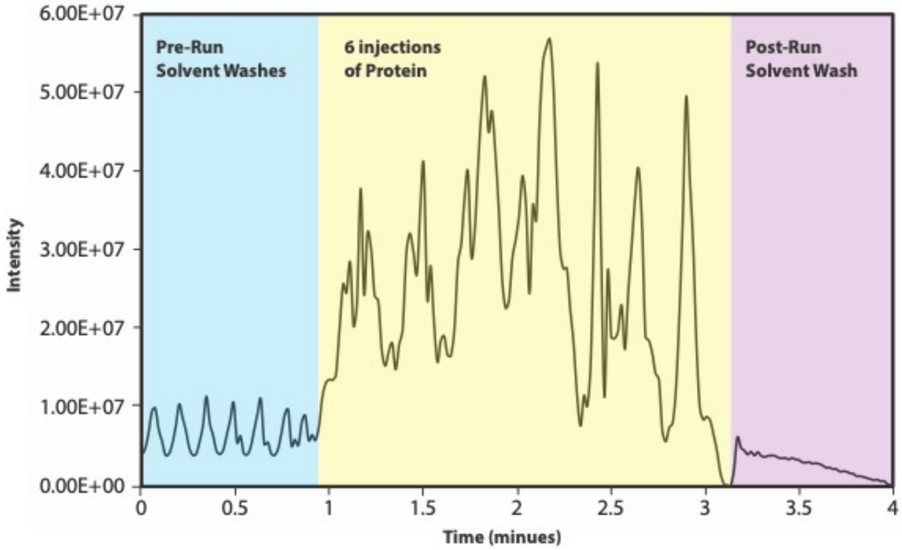

Figure VII-1 Total ion chromatogram for a typical RF experiment, depicting pre-run solvent washes, protein injections from 6 wells, and a post run solvent wash.

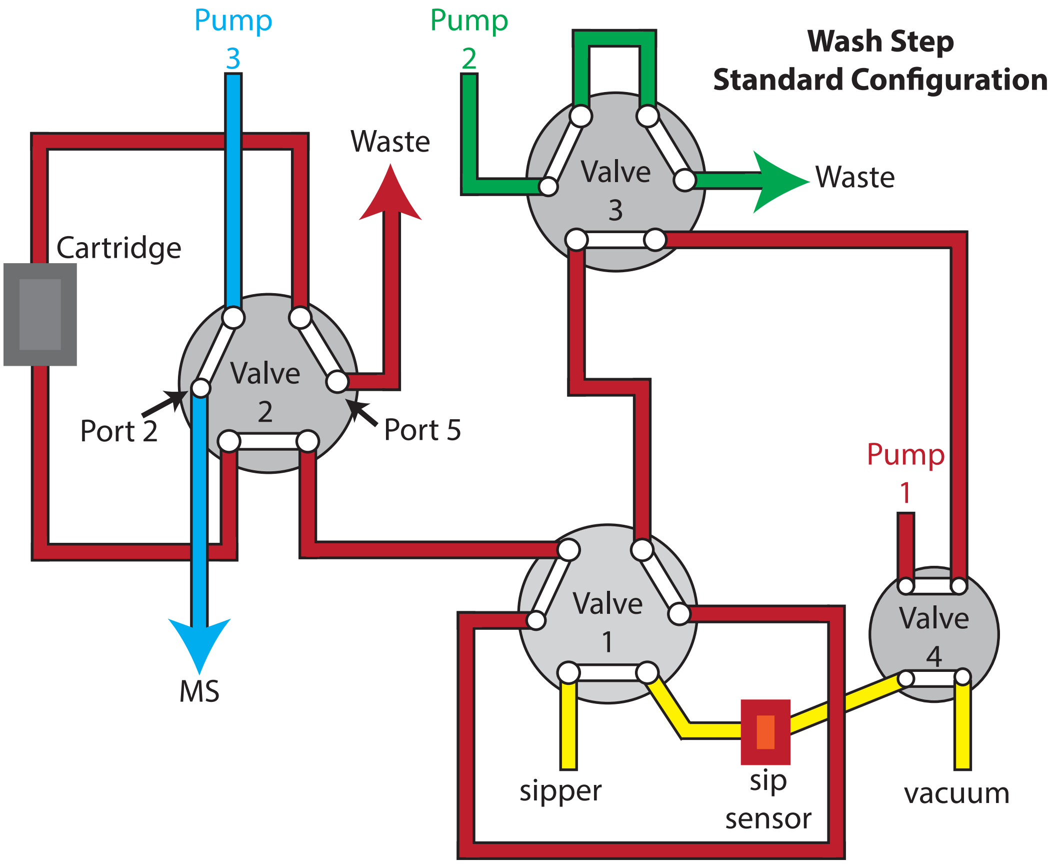

Figure VII-2 A flow diagram of the wash step of the RapidFire under standard plumbing conditions.

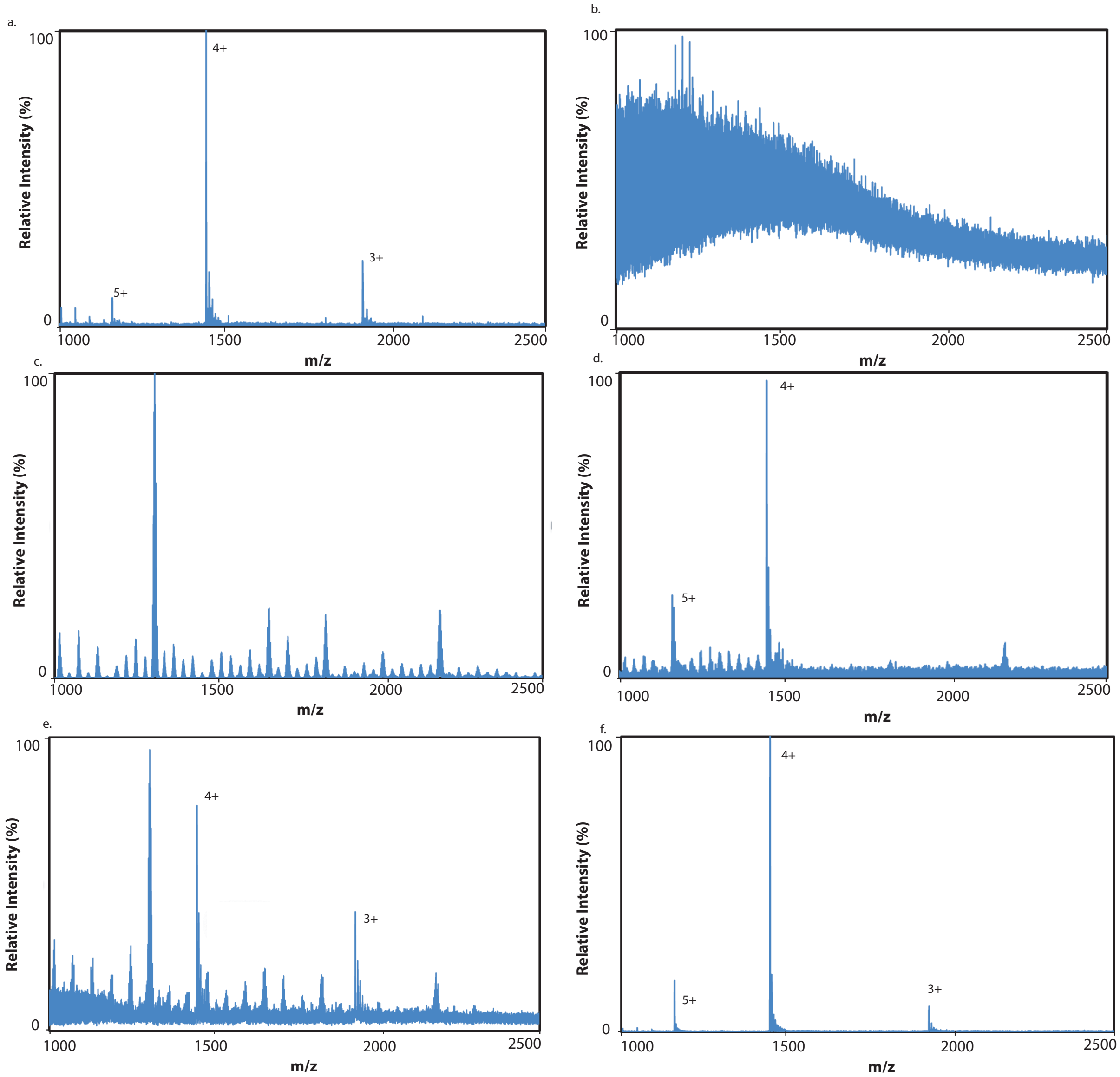

Figure VII-3 Mass spectrum of 10 micromolar insulin sparyed with RF-MS out of 200 mM ammonium acetate (a). Mass spectrum of 10 micromolar insulin in bovine serum directly infused onto MS without online desalting (b). Mass spectrum of 10 micromolar insulin in 1 M NaCl directly infused onto MS without online desalting (c). Mass spectrum of 10 micromolar insulin in 1 M NaCl directly infused onto MS without online desalting (c). Mass spectrum of 10 micromolar insulin in 1 M NaCl directly infused onto MS with online desalting and selecting only for the drift times in which insulin is present (d). Mass spectra of 10 micromolar insulin in 5 mM NaCl (e) and 1 mM NaCl (f) with online desalting on RF.

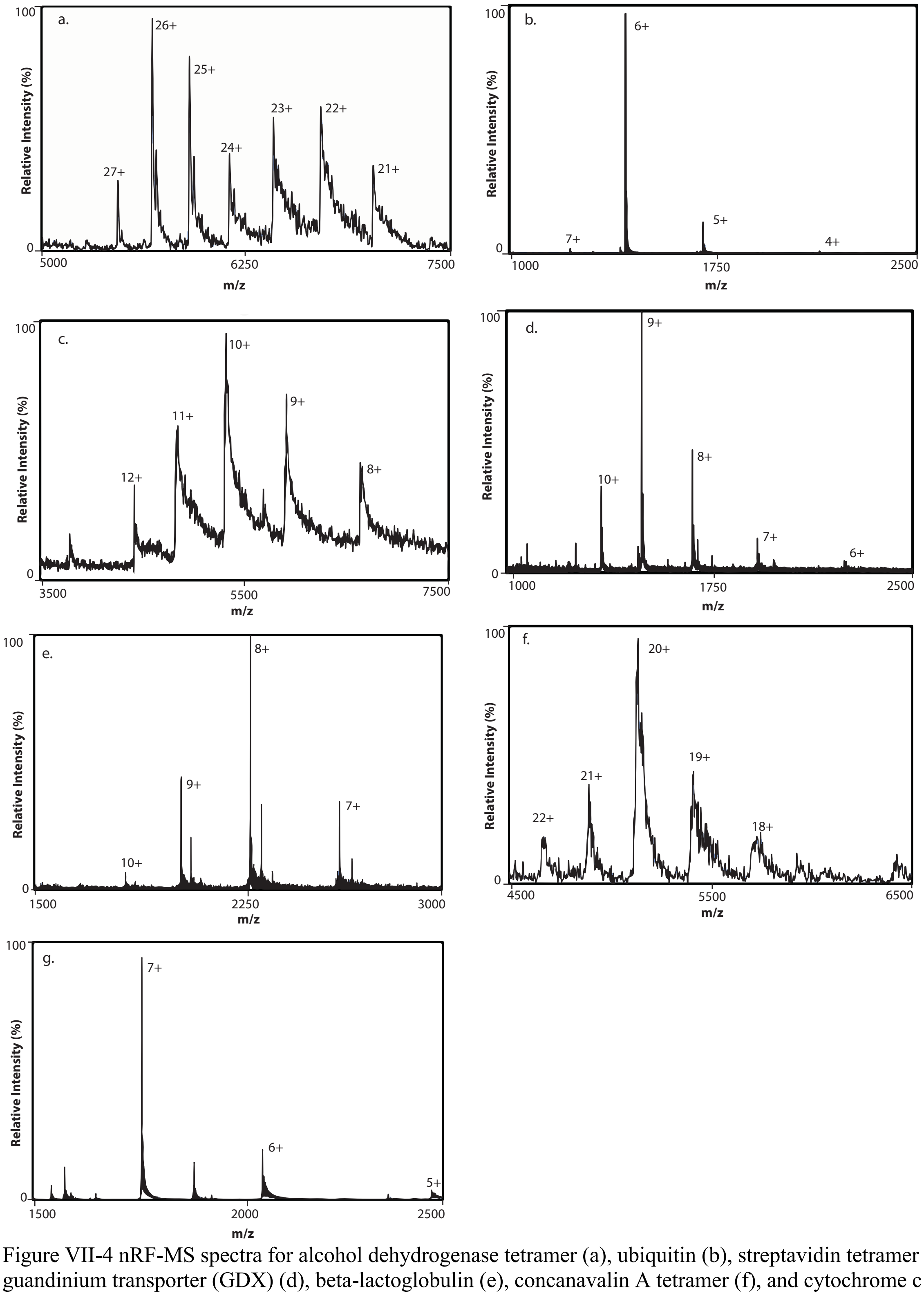

Figure VII-4 nRF-MS spectra for alcohol dehydrogenase tetramer (a), ubiquitin (b), streptavidin tetramer (c), guandinium transporter (GDX) (d), beta-lactoglobulin (e), concanavalin A tetramer (f), and cytochrome c (g).

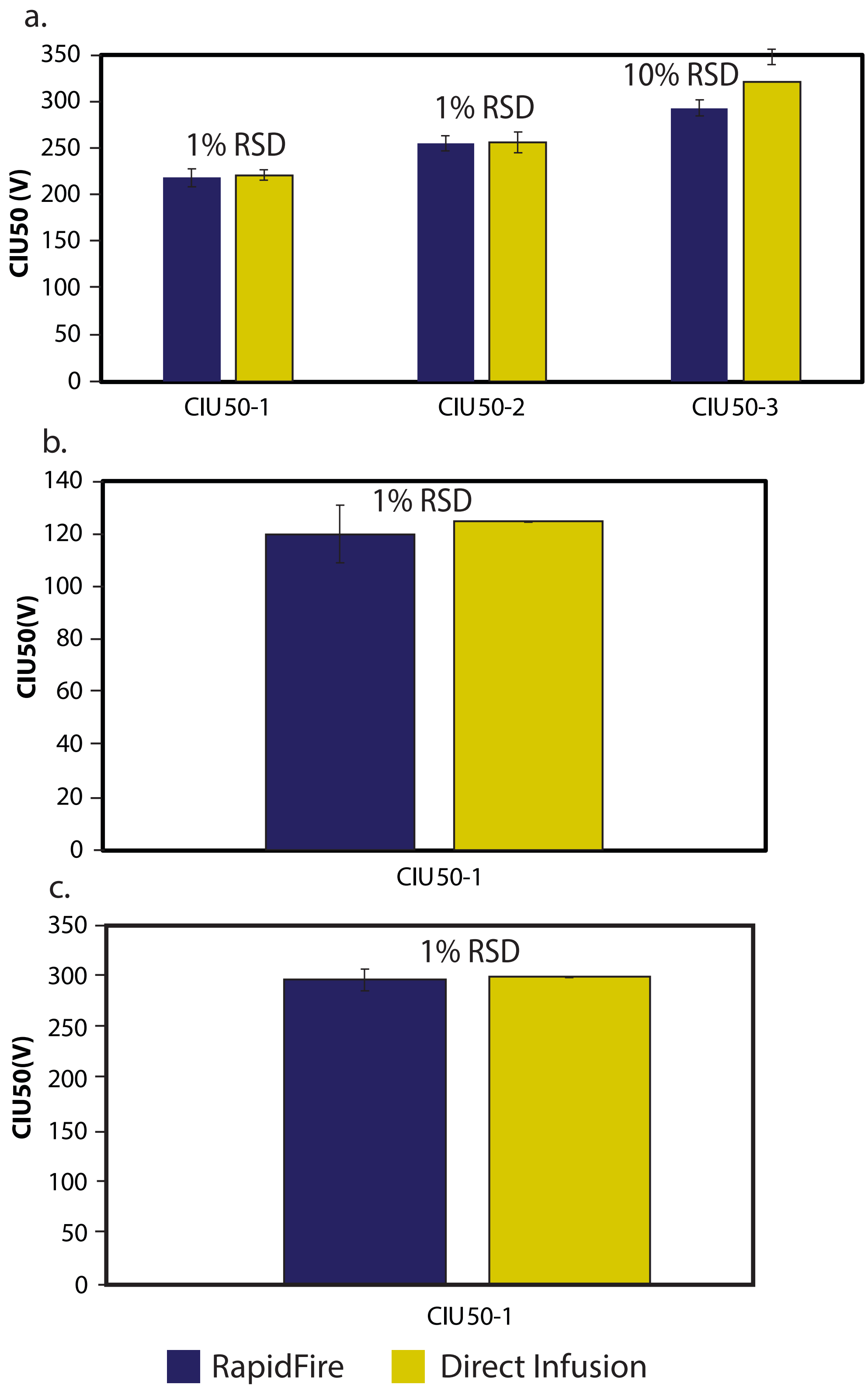

Figure VII-5 Comparison of the CIU50 transitions between RF and direct infusion CIU data collected with BSA (a), myoglobin (b) and streptavidin (c).

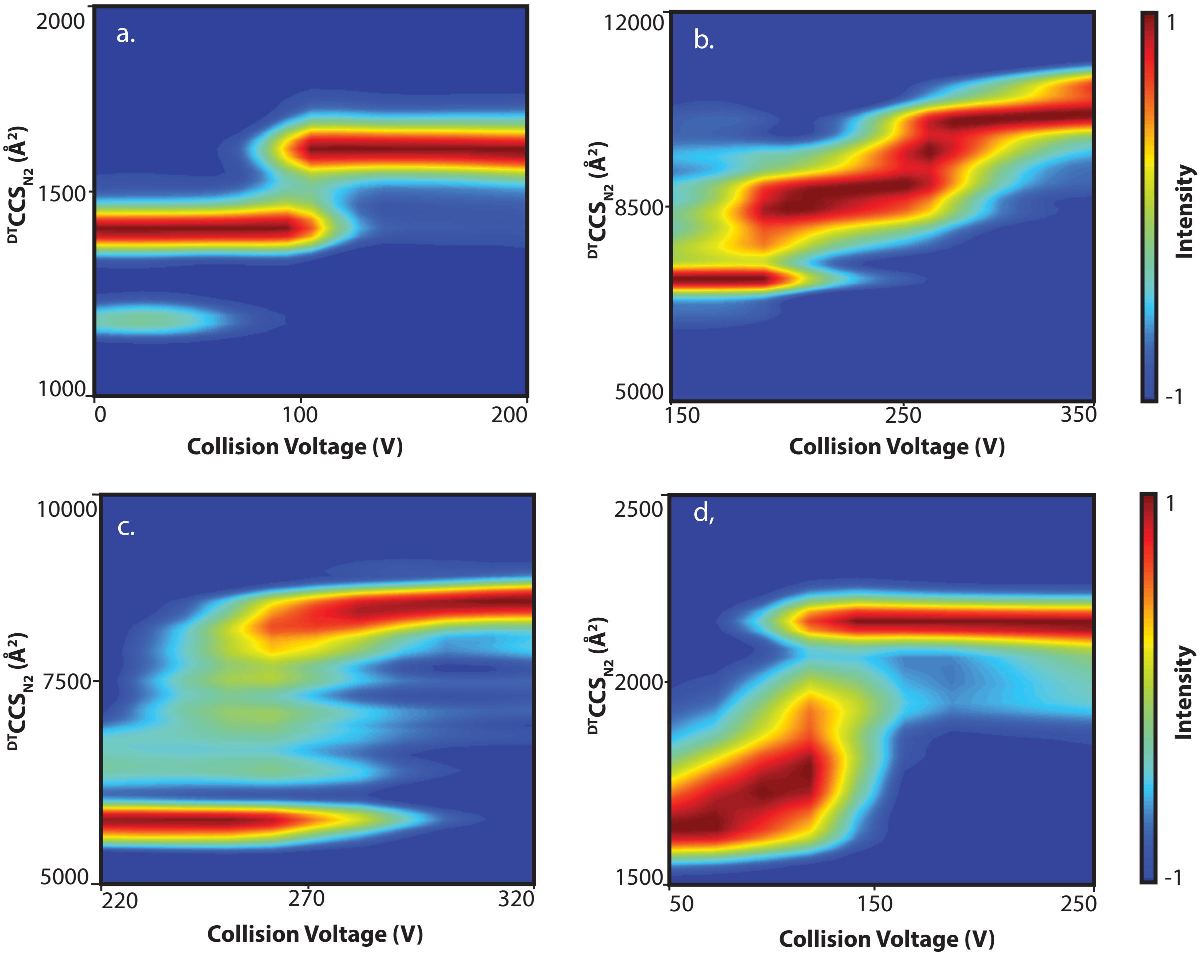

Figure VII-6 RF-CIU data collected for ubiquitin 8+ (a) , alcohol dehydrogenase tetramer 25+ (b), concanavalin A tetramer 20+ (c), and cytochrome c 7+ (d).

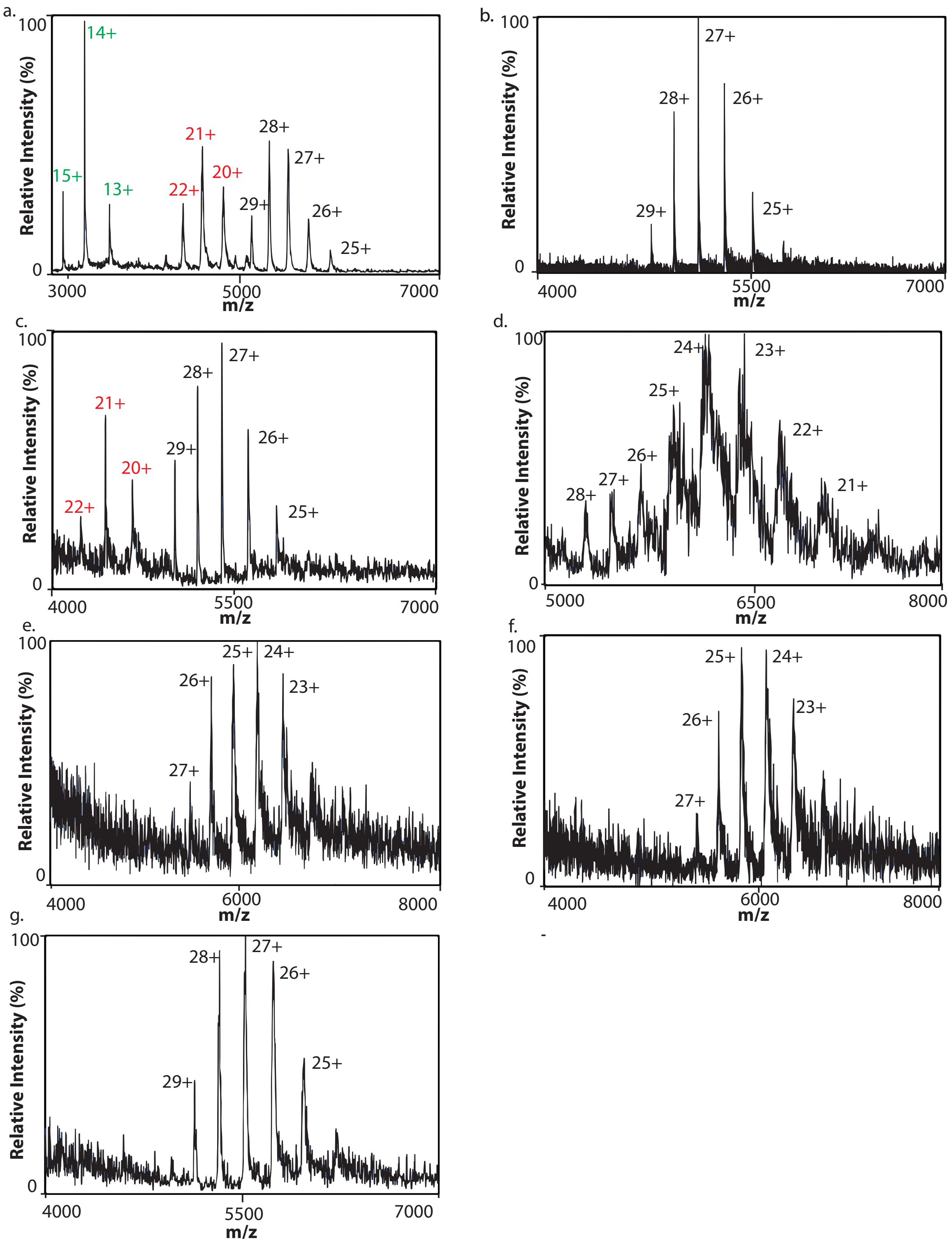

Figure VII-7 RF mass spectra of Sigma mAb, (a) deglycosylated NIST mAb (b), deglycosylated Sigma mAb (c), IgG2 (d), IgG4 (e), Vedolizumab (f) and Pembrolizumab (g). Black annotations denote intact mAb charge states, green annotations are for F(ab')$_2$ domain peaks and red annotations are for Fc domain peaks.

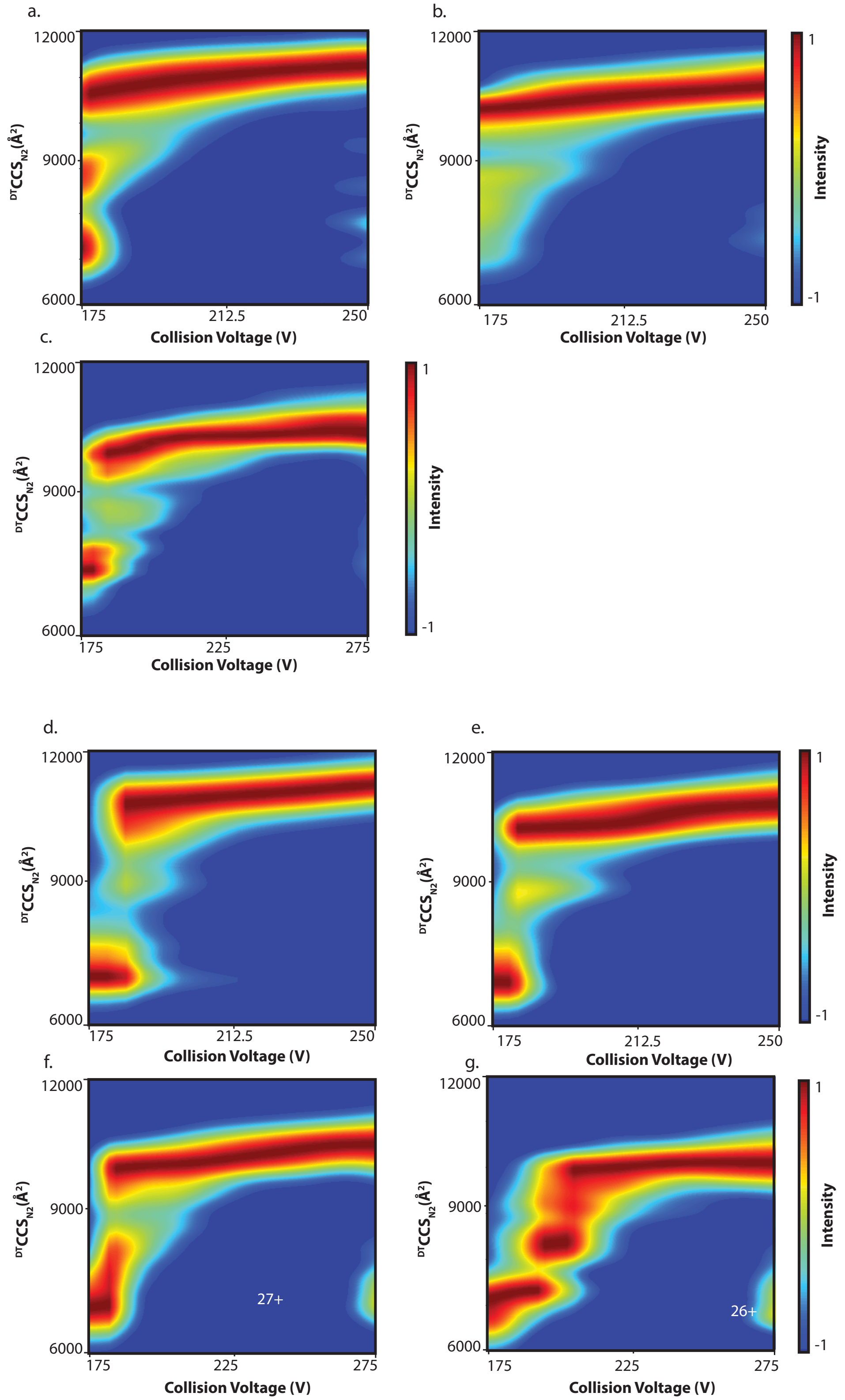

Figure VII-8 RF-CIU of intact NIST mAb 29+ (a), 28+ (b), 27+ (c) and deglycosylated NIST mAb 29+ (d), 28+ (e), 27+ (f), and 26+ (g).

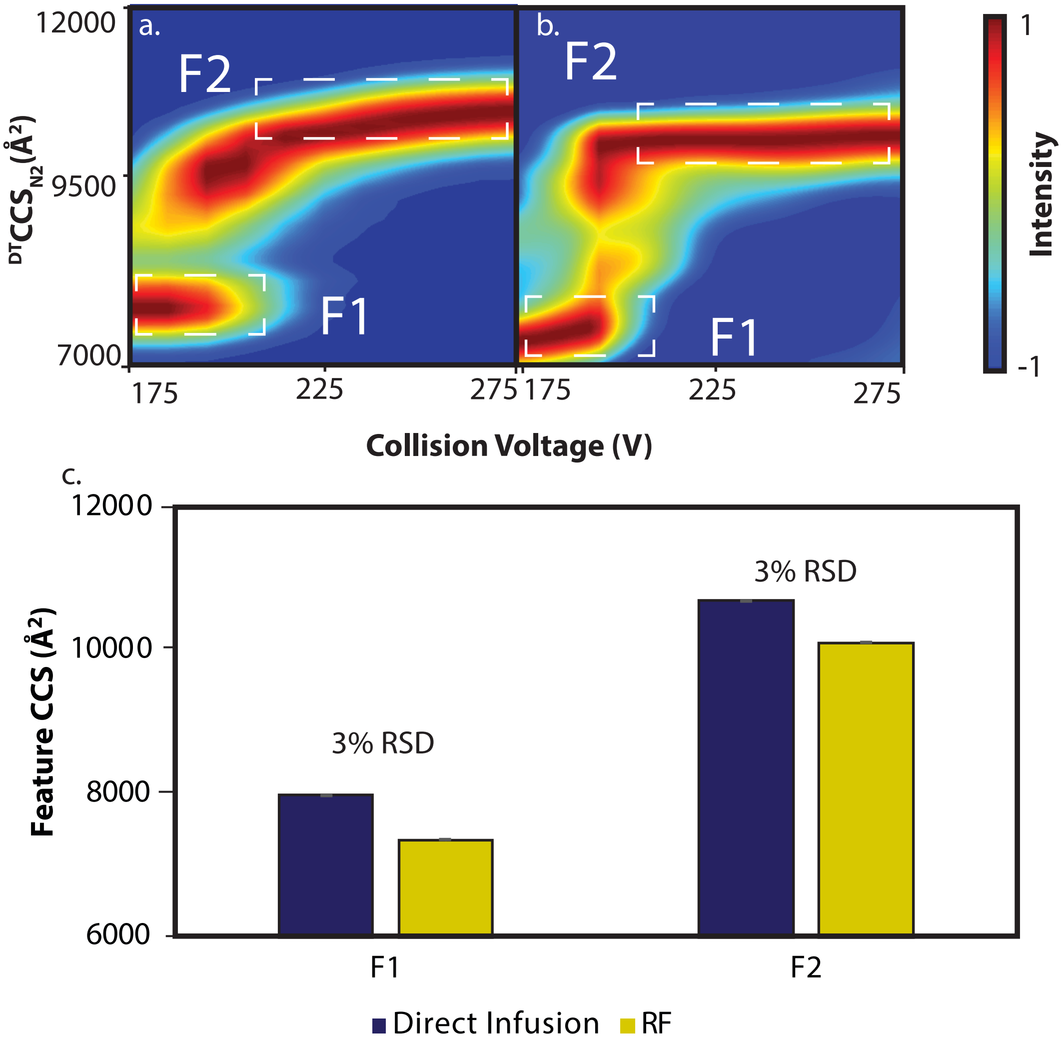

Figure VII-9 CIU for NIST mAb 27+ collected by direct infusion (a) and RF-MS (b). Comparison of Feature CCS values between the two fingerprints (c).

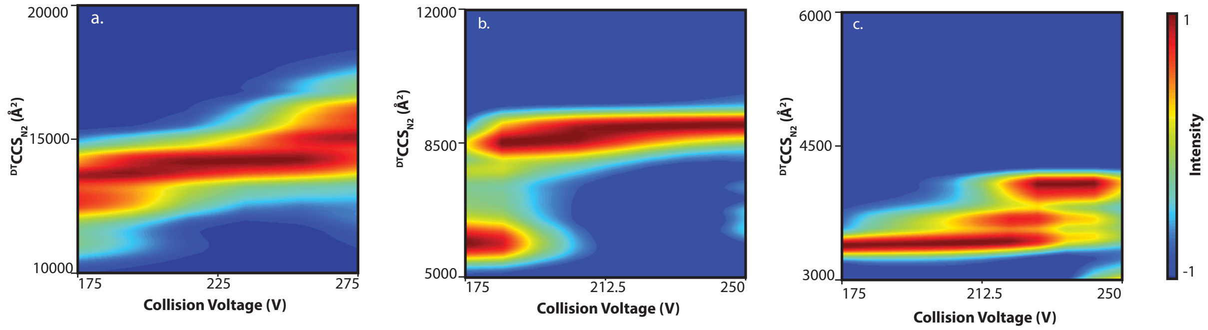

Figure VII-10 RF-CIU of NIST mAb 39+ dimer, Sigma mAb 21+ F(ab')$_2$ and Sigma mAb 11+ Fc.

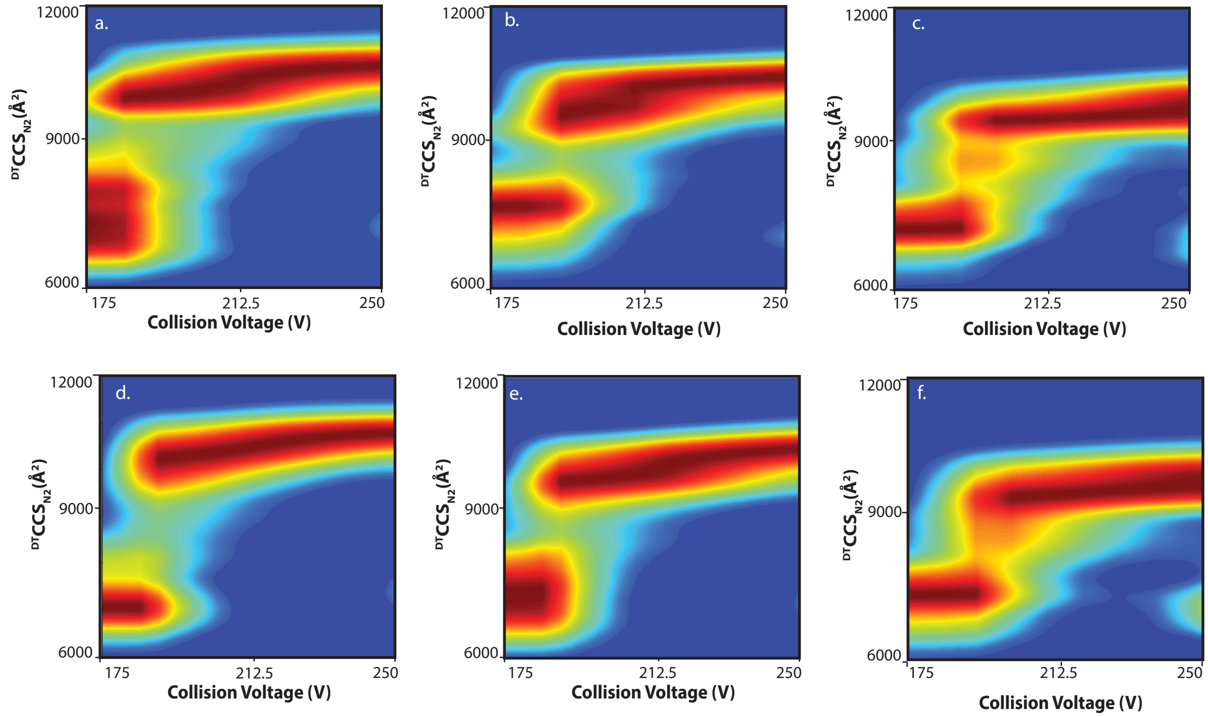

Figure VII-11 RF-CIU for Sigma mAb 28+ (a), 27+ (b) and 26+ (c). RF-CIU for deglycosylated Sigma mAb 28+ (d), 27+ (e), and 26+ (f)

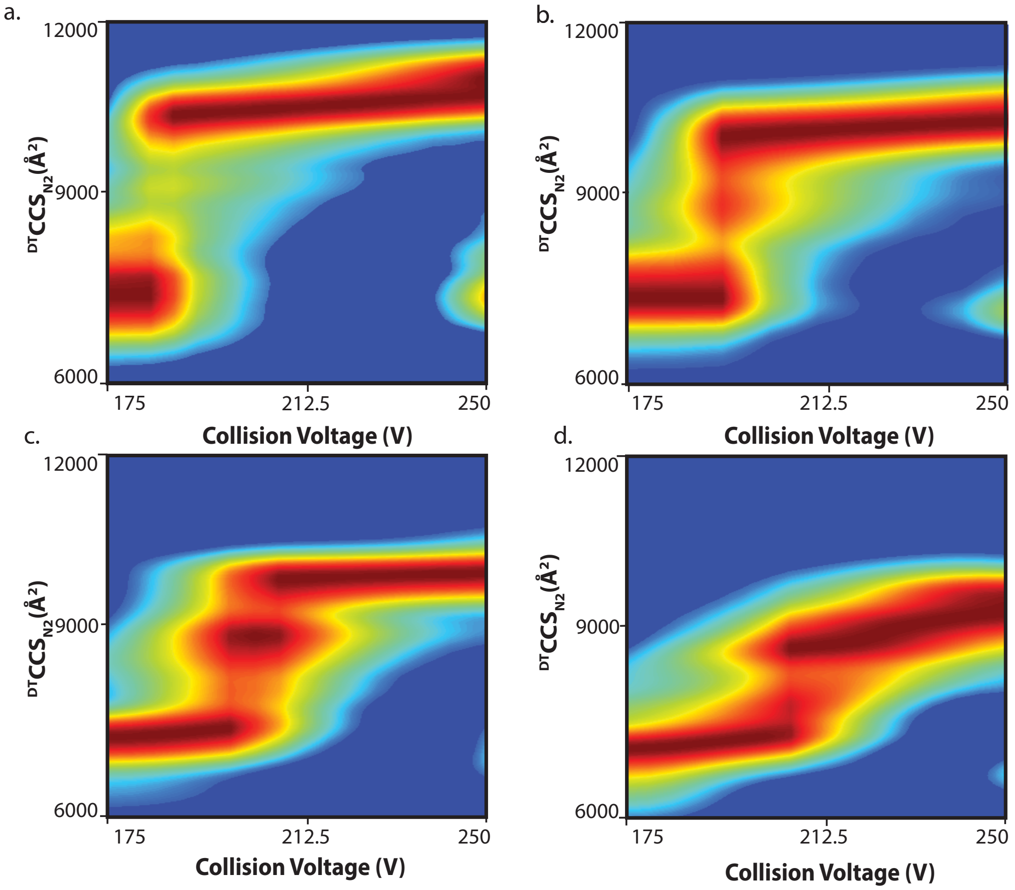

Figure VII-12 RF-CIU for Pembrolizumab 28+ (a), 27+ (b), 26+ (c) and 25+ (d).

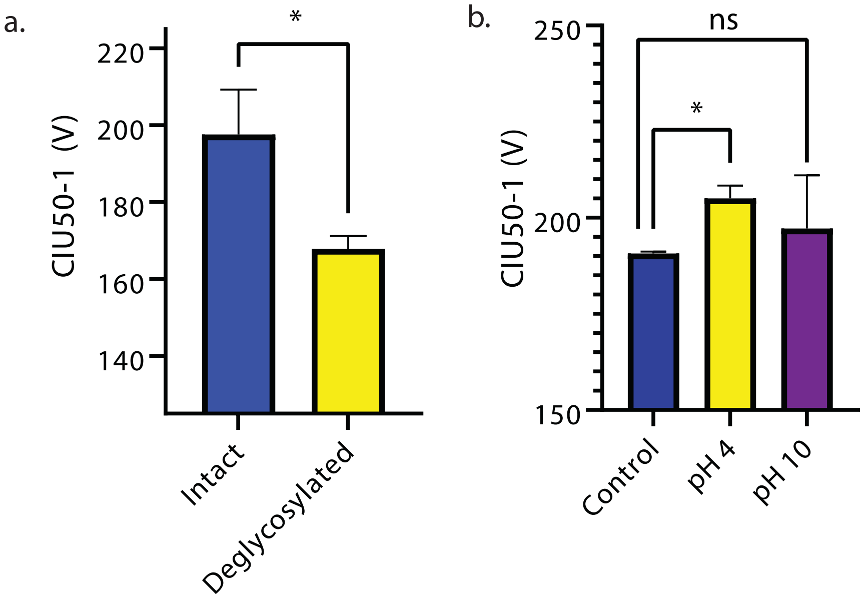

Figure VII-13 CIU-50 comparison for Sigma mAb 26+ under intact and deglycosylated states (a). CIU-50 comparison for Sigma mAb 26+ under control (pH=7) and high and low pH stress states (b).

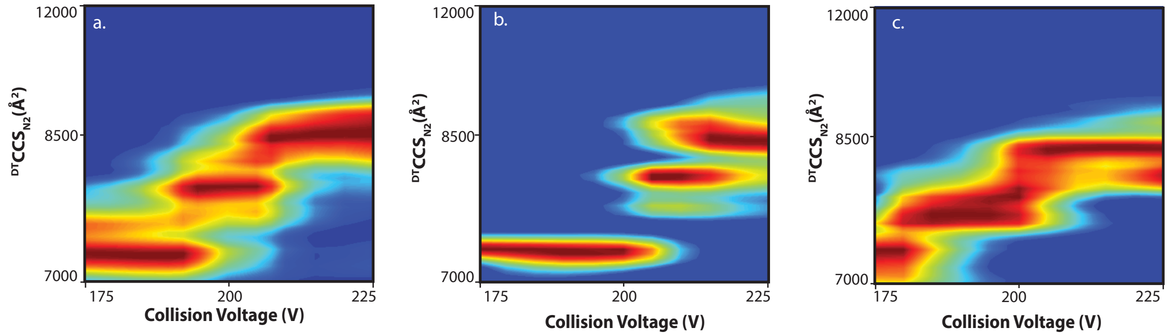

Figure VII-14 RF-CIU for Sigma mAb 26+ at pH 7(a), 4(b), and 10 (c).

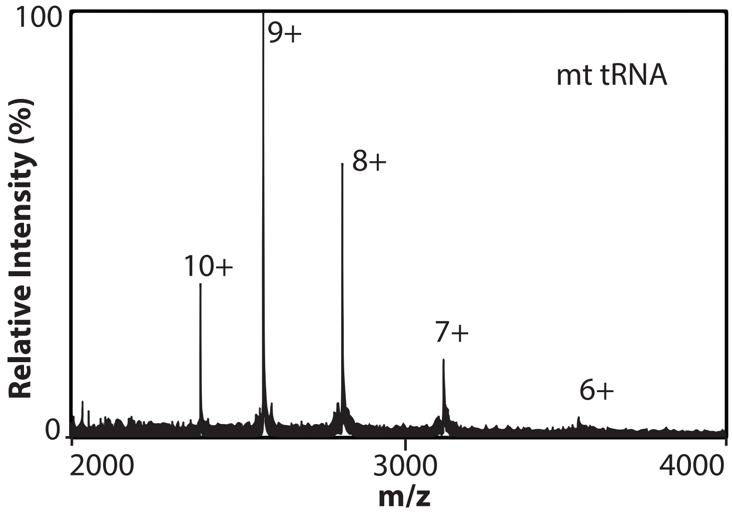

Figure VII-15 RF-MS for mitochondrial $^{LEU(UUR)}$tRNA.

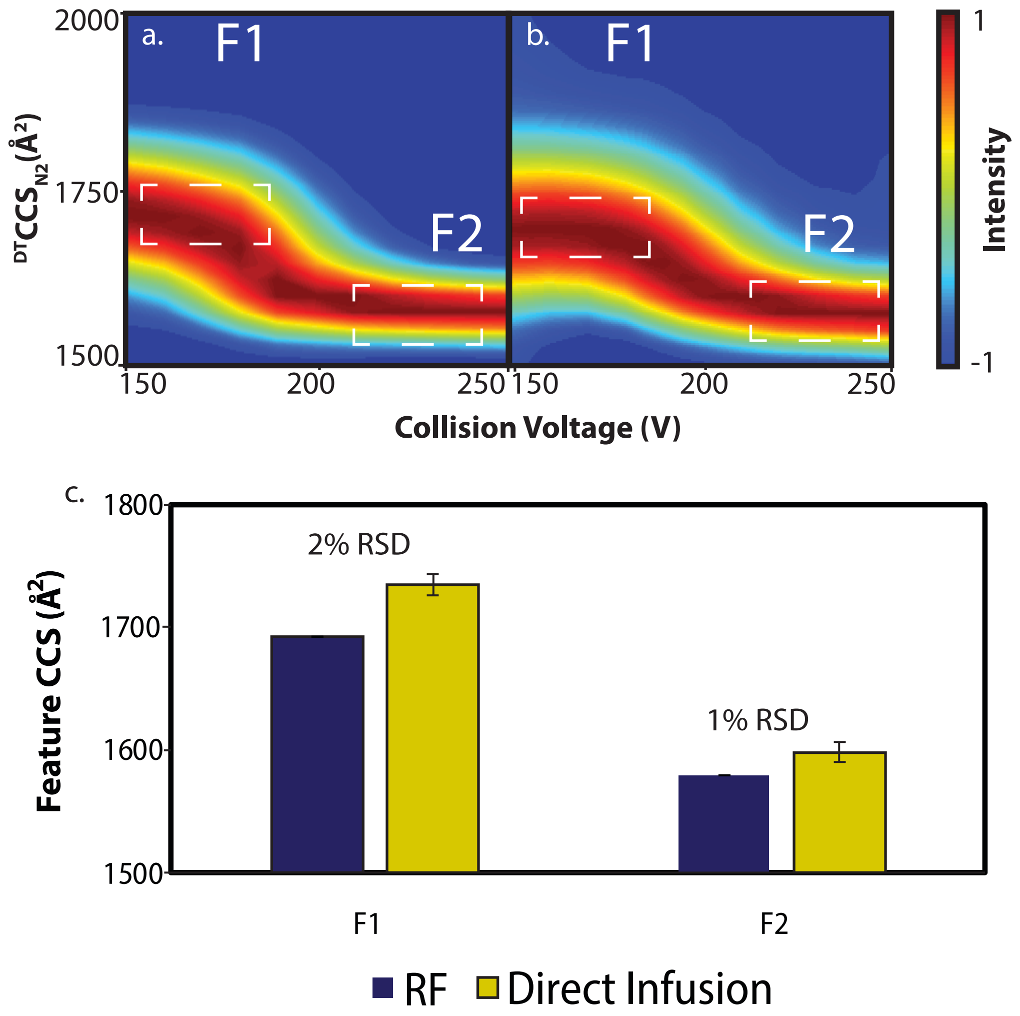

Figure VII-16 CIU for the 7+ siRNA duplex collected with direct infusion (a) and RF-MS (b). Comparing the CCS values for the features of the two CIU aforementioned CIU fingerprints (c).

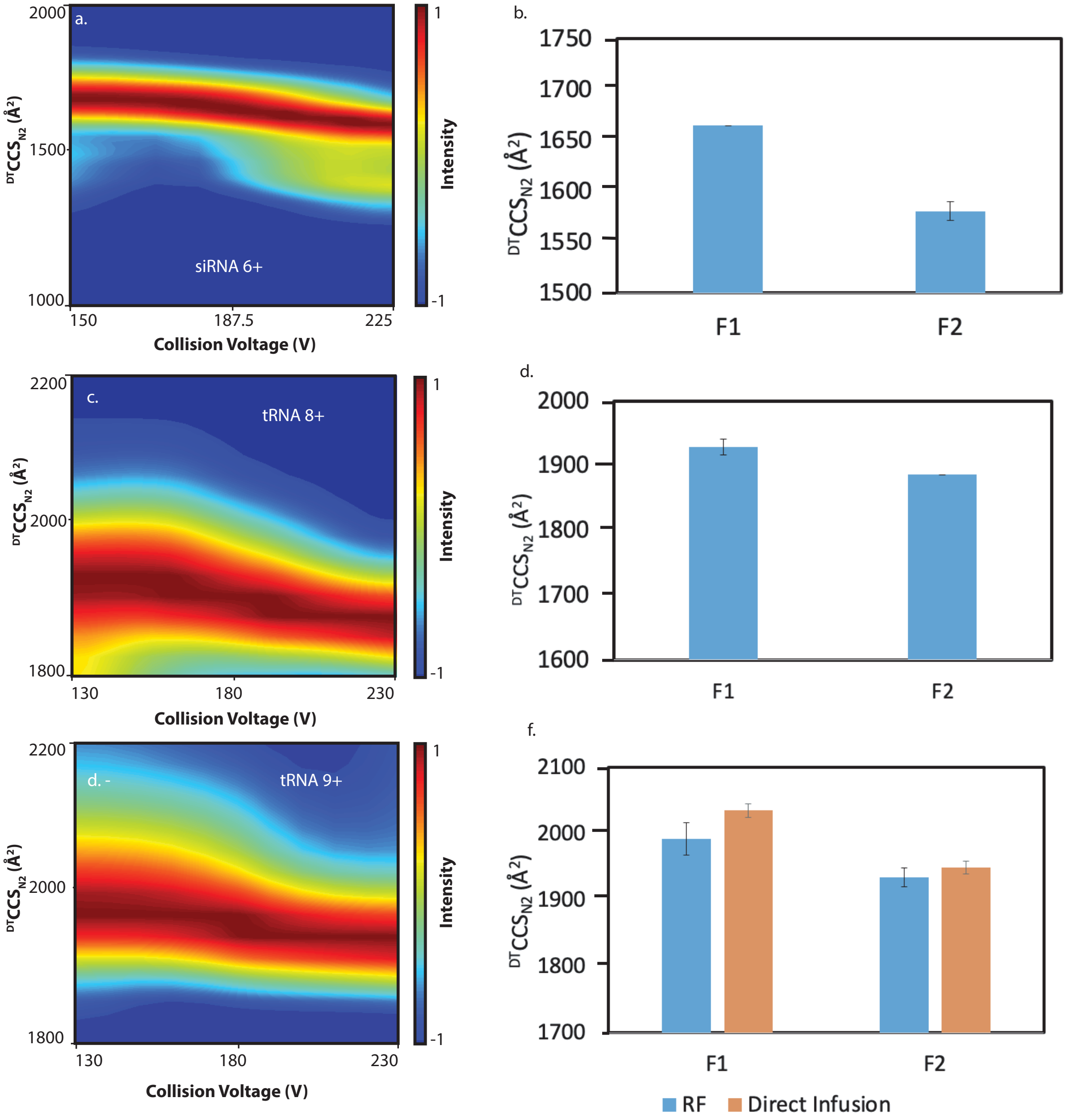

Figure VII-17 RF-CIU of the 6+ siRNA duplex (a) and a bar chart highlighting the level of compaction between the features (b). RF-CIU of the 8+ mitochondrial $^{\mathrm{LEU(UUR)}}$tRNA (c) and a bar chart highlighting the level of compaction between the features (d). RF-CIU of the 9+ mitochondrial $^{\mathrm{LEU(UUR)}}$tRNA (e) and a bar chart highlighting the level of compaction between the features for CIU data collected by RF-MS and direct infusion (f).

Table VII-1 RF-MS Instrument Parameters in Positive Polarity

Region	Setting Name	Setting
Source	Gas Temperature (°)	140-300
	Drying Gas (L/min)	1.5
	Nebulizer pressure (psi)	20
	Sheath Gas Temperature (°)	140
	Sheath Gas Flow (L/min)	11
	Capillary Voltage (V)	3000
	Nozzle Voltage (V)	2000
	Fragmentor (V)	400
Pressures	High Pressure Funnel (Torr)	4.5-4.8
	Trapping Funnel	3.80
	Drift Tube	3.95
Acquisition	Max Drift Time (ms)	90
	Trap fill time (µs)	80000
	Trap release time (µs)	1000
Advanced Parameters	In Source CE	20-400
	High Pressure Funnel Delta (V)	180
	High Pressure Funnel Radio Frequency (Vpp)	200
	Trapping Funnel Delta (V)	164
	Trapping Funnel Radio Frequency (Vpp)	200

Table VII-2 CIU data extraction parameters for standard protein systems.

		Myoglobin 8+	Streptavidin 11+	BSA 16+	NIST mAb 26+
Data Import	Smoothing	Window: 5 Iteration: 2	Window: 5 Iteration: 2	Window: 5 Iteration: 2	Window: 7 Iteration: 2
	Crop	80-180 V 1500-3000 Å^2	150-350 V 3000-5000 Å^2	150-350 V 4000-7000 Å^2	175-275 V 6000-12000 Å^2
Feature Fitting	Minimum Feature Length	4	4	3	4
	Feature Width	100 Å^2	100 Å^2	150 Å^2	250 Å^2
	Max CV Gap (V)	0	0	0	0
CIU50 Calculations	Transition Region Padding	15	15	15	15
	Max CV Gap (V)	15	15	15	15

Table VII-3 A comparison of CCS values determined with RF-MS and those determined by nanoESI on the 6560c.

Protein	**Charge State/ Oligomeric State**	**Avg. RF $^{DT}CCS_{N2}$ (Å^2)**	**Avg. nESI $^{DT}CCS_{N2}$ (Å^2)[1,2]**	**RSD (%)**
Ubiquitin	6+	1207 ± 9	1191	1.36
	6+	1354 ± 15	1345	0.65
	6+	1422 ± 3	1466	3.02
	5+	1177 ± 0	1145	2.73
	4+	1126 ± 0	1113	1.18
Concanavalin A	19+ Tetramer	5540 ± 29	5864	2.84
	20+ Tetramer	5788 ± 1	5904	0.99
	21+ Tetramer	5849 ± 32	5953	0.88
	22+ Tetramer	5960 ± 33	5975	0.12
Alcohol Dehydrogenase	24+ Tetramer	7622 ± 249	7490	0.97
	25+ Tetramer	7478 ± 66	7534	0.36
	26+ Tetramer	7749 ± 79	7571	1.16
	27+ Tetramer	7754 ± 180	7586	1.09
Bovine Serum Albumin	14+	4402 ± 73	4402	0.01
	15+	4525 ± 85	4452	0.81
	16+	4498 ± 24	4526	0.30
	17+	4551 ± 31	4577	0.27
β-Lactoglobulin	7+ Monomer	1902 ± 0	1877	0.66
	8+ Monomer	1964 ± 0	1933	0.81
	12+ Dimer	3259 ± 32	3162	1.52
	13+ Dimer	3299 ± 28	3275	0.37
Insulin	3+ Monomer	875 ± 0	873	0.14
	4+ Monomer	932 ± 0	917	0.79
	5+ Dimer	1381 ± 0.5	1392	0.39
	6+ Dimer	1402 ± 0.7	1451	1.70
NIST mAb	25+	8341 ± 234	8070	1.65
	26+	8419 ± 383	8260	0.95
	27+	8802 ± 253	8340	2.69
	28+	8608 ± 86	8470	0.81

Table VII-4 Comparisons between the CCS values of features determined by RF-CIU and those determined by direct infusion CIU.

Protein	**Charge State / Oligomeric State**	**Feature**	**Avg. RF Feature $^{DT}CCS_{N2}$ (Å^2)**	**Avg. Direct Infusion $^{DT}CCS_{N2}$ (Å^2)**	**RSD (%)**
Bovine Serum Albumin	16+	1	4473 ± 24	4341 ± 0	2.94
		2	5412 ± 26	5258 ± 11	2.84
		3	5907 ± 15	5964 ± 21	0.96
		4	6302 ± 25	6240 ± 0	0.99
Myoglobin	8+	1	1911 ± 14.3	1915 ± 0	0.20
		2	2613 ± 7	2760 ± 5	1.15
Streptavidin	11+ Tetramer	1	3658.66 ± 0	3671 ± 9	0.33
		2	4372.57 ± 8	4378 ± 12	0.83
NIST mAb	26+	1	7360 ± 41	8091	4.04
		2	10117 ± 15	10812	2.80
	27+	1	7478 ± 55	7784	3.93
		2	10486 ± 65	10649	1.52

Table VII-5 Comparisons between the CCS values of features determined by RF-CIU and those determined by direct infusion CIU.

Protein	**Charge State / Oligomeric State**	**Transition**	**Avg. RF CIU-50 (V)**	**Avg. Direct Infusion CIU-50 (V)**	**RSD (%)**
Bovine Serum Albumin	16+	1	218 ± 10	4341 ± 0	2.94
		2	255 ± 8	5258 ± 11	2.84
		3	293 ± 9	5964 ± 21	0.96
Myoglobin	8+	1	120 ± 5	125 ± 0	0.20
Streptavidin	11+ Tetramer	1	297 ± 11	300 ± 1	0.17

VII.1 References

(1) Gadkari, V. V.; Ramírez, C. R.; Vallejo, D. D.; Kurulugama, R. T.; Fjeldsted, J. C.; Ruotolo, B. T. Enhanced Collision Induced Unfolding and Electron Capture Dissociation of Native-like Protein Ions. *Anal. Chem.* **2020**, *92* (23), 15489–15496. https://doi.org/10.1021/acs.analchem.0c03372.

(2) Polasky, D. A.; Dixit, S. M.; Vallejo, D. D.; Kulju, K. D.; Ruotolo, B. T. An Algorithm for Building Multi-State Classifiers Based on Collision-Induced Unfolding Data. *Anal. Chem.* **2019**, *91* (16), 10407–10412.